ASPECTS OF THE PROCESSING, MECHANICAL PROPERTIES AND THERMAL SHOCK BEHAVIOUR OF A DUCTILE PARTICLE TOUGHENED ALUMINA

A THESIS SUBMITTED TO THE UNIVERSITY OF SURREY FOR THE DEGREE OF DOCTOR OF PHILOSOPHY

Matthew Aldridge

December, 1996

SUMMARY

The incorporation of metallic particles in a ceramic matrix is an established method of increasing the fracture toughness of brittle engineering ceramics. The current study is concerned with the effect of the increased fracture toughness of such a ceramic matrix composite on other important material properties, such as strength and thermal shock behaviour.

Composites of Al_2O_3-20 volume % Fe have been fabricated both by sintering and hot pressing. The effect of various processing schedules on the resulting microstructure of the sintered composites has been studied.

The dense hot pressed composite has been found to show a flexure strength of approximately 640 MPa, while the strength of hot pressed monolithic alumina was found to be approximately 400 MPa. The increase has been attributed to the refined microstructure. However, the sintered composite shows a significant decrease in strength (approximately 150 MPa) compared with the hot pressed monolith, resulting from incomplete sintering of the matrix. The sintered composite has been shown to exhibit increasing toughness with increasing crack length (K_R curve behaviour), resulting in a plateau toughness of 8.3 MPa $m^{½}$ for a crack length of 5 mm. Similar behaviour has been observed for the hot pressed composite in a previous study. Examination of crack propagation (during in-situ double cantilever beam testing) and fracture surfaces has indicated that the ceramic/metal interfacial bonding is not sufficient to allow full exploitation of the ductility of the metallic phase.

The thermal shock resistance of the hot pressed composite has been found to be significantly greater than the monolith; a 50 % increase in critcal temperature differential (ΔT_c) has been observed, i.e. from 200 °C to over 300 °C. However, the sintered composite has been shown to behave as a typical low strength refractory ceramic, having no definite ΔT_c and showing a gradual loss of strength. Damage resistance capabilities of both composites has been shown to be superior to the monolith and a commercially available zirconia toughened alumina. The application of a fracture mechanical analysis has enabled the prediction of conditions of crack initiation and propagation, and the associated degradation in flexural strength for a range of temperature differentials. Preliminary analytical estimates broadly support the experimental work, and indicate possible explanations for the differences in thermal shock behaviour observed between the materials studied. The increases in ΔT_c and strength retention following thermal shock have been attributed to the incorporation of the metallic particles into the matrix. However, it is not solely the increased toughness of the composites which is responsible for the improved resistance to thermal shock. Several thermal and mechanical properties of the composites are different to those of the monolith, and these have been shown to have a significant effect on the thermal shock behaviours observed. It is suggested that the decreased Young's modulus of the composites is primarily responsible for the increase in ΔT_c, whilst the increase in damage resistance is due to the increasing toughness with crack length.

ACKNOWLEDGEMENTS

Over the past three years, many contributions to this work have been made by various individuals and institutions. The author would like to take this opportunity to acknowledge these efforts.

The work was performed at the Materials Science and Engineering Department of the University of Surrey, under the supervision of Dr. J. A. Yeomans, with funding provided by the Engineering and Physical Sciences Research Council.

Firstly, and most importantly, I would like to express my sincere thanks to my supervisor Dr. Julie Yeomans. Her continued support, guidance and enthusiasm have been invaluable, especially at those times when my self-confidence and motivation were low.

I am very grateful to Morgan Matroc Ltd. for the provision of raw materials and assistance with aspects of the experimental procedures, in particular Dr. Simon Bradwell and Dr. John Kirk.

The help of Dr. Bill Clegg of the University of Cambridge and Dr. Jon Binner of the University of Nottingham is greatly appreciated, with regard to the processing procedures involved in this project. I am also grateful to Prof. Rees Rawlings of Imperial College, and Dr. Roger Morrell of the National Physical Laboratory.

I would also like to thank the staff and students of the M.S.E. department for making the three year period a pleasure, in both work and play. In particular, my thanks go to Dr. Paul Smith for his guidance and reassuring interest in the work, to all the technical staff, the staff of the Microstructural Studies Unit, and my colleagues, both past and present, in the ceramics group, in particular Dr. Martin Blisset, Dr. Andrew Winn, Mr. Alex Ham and Miss Alison Craig. Special thanks are offered to Mr. Brian Deaville and Dr. Philip Aston of the Mathematics and Computing Sciences Department for their much appreciated help with the mathematical aspects of the work.

Finally, I wish to say a big thank you to my family, Shirley, Dave and Ruth, and my better half, Joanne, for their ever-lasting support throughout my studies.

CONTENTS

SUMMARY		i
ACKNOWLEDGEMENTS		ii
CONTENTS		iii
NOMENCLATURE		viii
1 INTRODUCTION		1
1.1 BACKGROUND		1
1.2 OUTLINE OF THESIS		4
2 REVIEW OF THE LITERATURE		6
2.1 INTRODUCTION		6
2.2 DUCTILE PARTICLE TOUGHENED CERAMIC MATRIX COMPOSITES		6
2.2.1 Introduction		6
2.2.2 Theoretical Considerations		7
	2.2.2.1 Quantification of Toughening Increment	7
	2.2.2.2 Influence of Matrix/Particle Property Mismatch	9
	2.2.2.3 Importance of Ceramic/Metal Interface	11
	2.2.2.4 K_R Curve Behaviour	13
2.2.3 Practical Composite Systems		14
	2.2.3.1 Processing Methods	14
	2.2.3.2 Toughening and Fracture Behaviour	18
2.3 THERMAL SHOCK BEHAVIOUR		21
2.3.1 Introduction		21
2.3.2 Theoretical Considerations Regarding Monoliths		22
2.3.3 Theoretical Considerations Regarding Ceramic Matrix Composites		30
2.3.4 Practical Studies of the Thermal Shock Behaviour of Particulate CMCs		32
2.4 CONCLUDING REMARKS		34

3 MATERIALS AND EXPERIMENTAL TECHNIQUES 49

3.1 INTRODUCTION 49
3.2 FABRICATION OF MATERIALS 49
3.2.1 Introduction 49
3.2.2 Raw Materials 50
3.2.3 Powder Preparation 50
3.2.4 Powder Densification 51
3.2.4.1 Introduction 51
3.2.4.2 Hot Pressing 51
3.2.4.3 Greenbody Production and Conventional Sintering 52
3.3 CHARACTERISATION OF MATERIALS 53
3.3.1 Introduction 53
3.3.2 Density Measurement 53
3.3.3 Microstructural Examination of Polished Surfaces 54
3.3.4 Microstructural Examination of Fracture Surfaces 55
3.4 MECHANICAL PROPERTIES 55
3.4.1 Introduction 55
3.4.2 Fracture Toughness 56
3.4.2.1 Background 56
3.4.2.2 Double Cantilever Beam Method 59
3.4.3 Flexure Strength 60
3.4.3.1 Flexure Testing 60
3.4.3.2 Statistical Analysis 61
3.5 THERMAL SHOCK BEHAVIOUR 63
3.5.1 Introduction 63
3.5.2 Thermal Shock Experiments 63
3.5.3 Water Quenching 66
3.5.4 Measurement of Retained Strength 67
3.5.5 Damage Observation 67
3.5.6 High Temperature Behaviour in the Absence of Thermal Shock 68
3.6 CONCLUDING REMARKS 69

4	**CHARACTERISATION OF MATERIALS**	77
4.1	**INTRODUCTION**	77
4.2	**DENSITY MEASUREMENT**	77
	4.2.1 Hot Pressed Composite	77
	4.2.2 Greenbodies and Sintered Composites	78
	4.2.2.1 Greenbodies	78
	4.2.2.2 Sintered Composites	80
4.3	**MICROSTRUCTURAL EXAMINATION OF POLISHED SURFACES**	81
	4.3.1 Hot Pressed Composite	81
	4.3.2 Sintered Composites	81
4.4	**MICROSTRUCTURAL EXAMINATION OF FRACTURE SURFACES**	82
	4.4.1 Hot Pressed Composite	82
	4.4.2 Greenbodies and Sintered Composites	83
	4.4.2.1 Greenbodies	83
	4.4.2.2 Sintered Composites	83
4.5	**CONCLUSIONS**	85
5	**EVALUATION OF MECHANICAL PROPERTIES**	98
5.1	**INTRODUCTION**	98
5.2	**FRACTURE TOUGHNESS AND K_R CURVE BEHAVIOUR**	98
	5.2.1 Single Edge Notched Beam Method	98
	5.2.2 Double Cantilever Beam Method	99
	5.2.3 Crack/Ductile Particle Interactions	99
	5.2.4 Influence of Microstructure	100
5.3	**FLEXURAL STRENGTH**	103
	5.3.1 Hot Pressed Monolithic Alumina	103
	5.3.2 Hot Pressed Composite	103
	5.3.3 Sintered Composite	104
	5.3.4 Statistical Analysis	105
	5.3.5 Influence of Microstructure	106
5.4	**CONCLUSIONS**	108

6 THERMAL SHOCK BEHAVIOUR AND THEORETICAL ANALYSIS 120

6.1 INTRODUCTION 120
6.2 HIGH TEMPERATURE BEHAVIOUR 121
6.3 RETAINED STRENGTH 123
6.3.1 Hot Pressed Monolithic Alumina 123
6.3.2 Hot Pressed Composite 123
6.3.3 Sintered Composite 124
6.3.4 Zirconia Toughened Alumina 125
6.3.5 Discussion 126
6.4 DAMAGE OBSERVATION 132
6.4.1 Scanning Electron Microscopy 132
6.4.2 Confocal Scanning Laser Microscopy 132
6.4.3 Discussion 133
6.5 SUMMARY OF EXPERIMENTAL OBSERVATIONS OF THERMAL SHOCK BEHAVIOUR 135
6.6 THEORETICAL ANALYSIS OF THERMAL SHOCK BEHAVIOUR 135
6.6.1 Production of K Curves 135
6.6.2 Prediction of Crack Initiation, Crack Propagation and Strength Degradation 138
6.7 CONCLUSIONS 145

7 CONCLUDING REMARKS 173

7.1 CONCLUSIONS FROM CURRENT WORK 173
7.2 PROPOSED FURTHER WORK 177
7.2.1 Processing Development 177
7.2.2 Interfacial Examination 177
7.2.3 Accurate Determination of Thermal Properties 177
7.2.4 Other Properties 178

REFERENCES 179

APPENDICES
APPENDIX 1 ASTM FLEXURE TEST STANDARD 188
APPENDIX 2 COMPUTER ROUTINE 189

NOMENCLATURE

a	Crack length
a_0	Flaw size
a_c	Critical flaw size
a_i	Initial crack length
a_f	Final crack length
a_m	Crack length at maximum K
B_s	Roots to specific Bessel functions
b	Thickness of flexure test specimen
b_c	Distance from crack tip to loading axis in double cantilever beam testing
C	Specific heat capacity
C_l	Total length of test line (linear intercept method)
d	Width of flexure test specimen
d_c	Critical particle size
D	Average grain size
E	Young's modulus
E_0	Young's modulus of fully dense material
E_c	Young's modulus of composite
E_m	Young's modulus of matrix
E_m'	Young's modulus of matrix (modified to account for porosity)
E_p	Young's modulus of particle
f	Area fraction
F	Force
$F(x/a)$	Function of (x/a)
h	Heat transfer coefficient
h_p	Half-width of double cantilever beam specimen
I'	Second moment of area of double cantilever beam cross section
k	Thermal conductivity
K	Stress intensity factor
K_A	Applied stress intensity factor
K_R	Crack growth resistance (K_R curve)
K_{Ic}	Critical mode I stress intensity factor or fracture toughness
l_p	Length of double cantilever beam specimen
m	Weibull modulus
M	Magnification of micrographs
N	Number of cracks per unit volume

N_i	Number of intercepts (linear intercept method)
P	Load
P_s	Probability of survival
r	Characteristic dimension (i.e. half radius of cylinder or half thickness of plate)
r_0	Particle radius
R	First thermal shock parameter
R'	Second thermal shock parameter
R''''	Thermal shock damage resistance parameter
R_{st}	Thermal stress crack stability parameter
t	Time after exposure to ΔT
t_p	Thickness of double cantilever beam specimen
t_w	Thickness of web of double cantilever beam specimen
T	Temperature
T_x	Temperature at radius x
ΔT	Temperature differential
ΔT_c	Critical temperature differential
$\Delta T_c'$	Second critical temperature differential
u	Crack opening
u^*	Crack opening at failure of bridging particle
v	Volume fraction of porosity
v_m	Volume fraction of matrix
v_p	Volume fraction of particles
W_s	Weight of specimen
W_t	Total energy per unit volume of a body
ΔW_s	Weight differential before and after immersion
x	Distance
Y	Crack/specimen geometry parameter
α	Coefficient of thermal expansion
$\Delta\alpha$	Coefficient of thermal expansion differential
β	Biot modulus
γ	Fracture surface energy
γ_{ic}	Energy required to initiate crack
γ_{WOF}	Energy required to propagate crack
ϵ	Strain
θ	Normalised time after exposure to ΔT
κ	Normalised thermal shock generated stress intensity factor
λ	$k/\rho C$
υ	Poisson's ratio
υ_m	Poisson's ratio of matrix

υ_p Poisson's ratio of particle

ρ Density

ρ_s Density of specimen

ρ_w Density of water

σ Stress

σ_0 Normalising characteristic stress

$\sigma_{bending}$ Three point flexure fracture stress

σ_f Uniaxial tensile fracture stress

σ_r Radial thermal stress

σ_t Radial tensile stress

σ_u Stress below which $P_s=1$ (usually taken as 0)

σ_θ Tangential thermal stress

$\omega(\epsilon)$ Function of ϵ

Ψ Thermal stress reduction factor

Ω Normalised thermal stress

CHAPTER ONE

INTRODUCTION

1.1 BACKGROUND

The widespread use and acceptance of ceramics as engineering materials is severely limited by their intrinsic brittleness and lack of reliability. Recent research in the field has concentrated on increasing the fracture strength, therefore increasing the probability of survival in a given environment, whilst retaining the many attractive properties of ceramics such as their high stiffness and hardness, low density, and resistance to oxidation, corrosion, wear and elevated temperature degradation.

The uniaxial tensile fracture strength, σ_f, of a brittle material is given by the well known relationship as

$$\sigma_f = \frac{YK_{Ic}}{\sqrt{a_0}} \qquad 1.1$$

where Y is a well documented crack/specimen geometry parameter, K_{Ic} is the mode I critical stress intensity factor, which is commonly equated with the fracture toughness, and a_0 is the flaw size.

Equation 1.1 shows that the strength and hence reliability of ceramics may be improved in two ways. Firstly, by optimising the processing procedure, the flaw size may be decreased. This method does not alter the mode of fracture in any

way, hence the material would still suffer catastrophic failure (i.e. unstable propagation of the dominant flaw). Furthermore, post-processing damage may still occur, possibly increasing the flaw size. Secondly, the fracture toughness may be increased, making the material less susceptible to post-processing damage, and possibly avoiding a catastrophic mode of failure. Small increases in fracture toughness may be achieved by manipulation of the microstructure (porosity, grain size and shape). Significantly greater increases are offered by the introduction of a second phase, thereby producing a ceramic matrix composite (CMC).

Various CMC materials have been produced, allowing the understanding and exploitation of several different toughening mechanisms. Table 1.1 outlines the major mechanisms of toughening in various CMC materials and gives approximate upper bound fracture toughness values which may be expected for each mechanism. Several processing methods have been devised for the fabrication of CMCs, including modified conventional ceramic processing techniques, direct metal oxidation, molten metal infiltration of porous oxide ceramic networks, and adapted polymer matrix composite methods. It is well known that the toughest CMCs are those incorporating fibres as the second phase. Such composites, however, tend to show undesirable anisotropic properties. The problem of anisotropy may be overcome by the use of inert ceramic particles as the reinforcing phase, although these composites do not show appreciable toughening capabilities. The incorporation of a particulate ductile metal reinforcing phase within a ceramic matrix offers the potential of producing tougher composites than a brittle/brittle system, providing the ductility of the metallic phase can be exploited.

The incorporation of a ductile metal second phase material into a ceramic matrix may increase the resistance to crack propagation in a number of ways, the most effective being ductile particle crack bridging. The major toughening mechanism(s) in operation will depend on several factors, including the size, shape and distribution of the reinforcing particles, their mechanical properties, and also

the nature of the chemical or mechanical bonding at the interface between the particle and matrix. In addition, the microstructural features of the matrix (e.g. porosity, grain size and shape, purity) have a significant effect on the bulk fracture toughness of the composite.

Ceramics have long been used in applications requiring thermal and chemical stability at elevated temperatures, e.g. furnace linings, crucibles, tool tips, turbine blades, high performance engine parts, etc. These conditions often result in the ceramic component being subjected to rapid changes in temperature. Due to the brittleness of ceramic materials and their catastrophic manner of failure, it is essential to be able to evaluate the probability of survival of the part under a given set of conditions. The theory concerning the thermal shock behaviour of monolithic ceramic materials is well established. However, the evolution of ceramic matrix composites intended for applications in severe thermal environments has presented a problem. The theories developed for monolithic ceramics cannot be applied directly to CMCs as the thermal shock induced crack behaviour is expected to be different for this class of materials. Much of the recent work regarding the thermal shock behaviour of CMCs has been concentrated on the modification of the existing theories in order to increase knowledge and understanding in this field.

A previous study of a hot pressed Al_2O_3-Fe CMC has shown the composite to have an increased toughness compared to the matrix material (Trusty, 1994). It was anticipated that the increase in fracture toughness observed for such a ductile particle reinforced CMC may offer improved mechanical performance in thermal shock, wear and impact applications. Previous studies of the thermal shock resistance of ductile particle reinforced CMCs have been of a qualitative nature only, and the actual influence of the second phase and consequent increase in K_{Ic} on the thermal shock behaviour of the material has not been established. The present study, therefore, was concerned with the thermal shock behaviour of an Al_2O_3-Fe CMC. The primary aim of the current work was to determine whether

or not the incorporation of the ductile phase leads to an improved thermal shock resistance compared to monolithic matrix alumina; in particular whether the increase in fracture toughness alone results in superior performance. In order to study and quantify this particular property, the evaluation of the mechanical properties and fracture behaviour of the material was necessary. The project also involved a study of the processing of the composite, since it was envisaged that a large quantity of material would be required in order to study thermal shock behaviour, hence the method of hot pressing was not the most practical. Therefore, in addition to working with the hot pressed composite, the sintering behaviour of the composite was studied, resulting microstructure/property relationships were evaluated, and comparisons were made with the hot pressed material throughout the project.

1.2 OUTLINE OF THESIS

Following the introductory chapter, the literature relevant to the project is reviewed in Chapter 2. This begins with background theoretical considerations concerning ductile particle reinforced CMCs, and the toughening mechanisms observed in practice. Processing methods of such composites are discussed, as well as the influence and importance of matrix/particle interfaces. The final section of the literature review covers thermal shock theory and its application to CMCs. Chapter 3 explains the experimental techniques utilised throughout the study, and includes relevant literature. Chapter 4 is concerned with the characterisation of the materials used in this study, in terms of density and microstructure. The results and discussion of all mechanical testing of the composites are given in Chapter 5. This chapter includes fracture toughness testing, flexural strength testing and data analysis, and a comparison of all data with monolithic alumina. The thermal shock behaviour of the composites is dealt with in Chapter 6, from high temperature behaviour and retained strength through to damage observation and semi-quantitative analysis. Chapter 7 presents the conclusions from the current project and proposals for further work concerning

ductile particle reinforced CMCs.

Table 1.1 A Comparison of Various Toughened Ceramics (after Evans 1990).

Mechanism	Max. Toughness (MPa $m^{½}$)	Exemplary Materials	Limitation
Metal Dispersion	≈ 25	Al_2O_3 / Al Al_2O_3 / Ni WC / Co	T ≤ 1300 K Oxidation
Whiskers/Platelets	≈ 15	Si_3N_4 / SiC Si_3N_4 / Si_3N_4 Al_2O_3 / SiC	Oxidation T ≤ 1500 K
Fibres	≥ 30	Al_2O_3 / Al_2O_3 SiC / SiC SiC / C	Processing Coatings Fibres
Microcracking	≈ 10	Al_2O_3 / ZrO_2 SiC / TiB_2 Si_3N_4 / SiC	T ≤ 1300 K Strength
Transformation	≈ 25	ZrO_2 (MgO) HfO_2	T ≤ 900 K

CHAPTER TWO

REVIEW OF THE LITERATURE

2.1 INTRODUCTION

This chapter presents a review of the literature relevant to the current study. Firstly, the theoretical considerations regarding toughening in ductile particle reinforced CMCs are introduced, along with further factors influencing the exploitation of the ductility of the second phase. The importance of the ceramic/metal interface and its influence on the properties of the composite is then explained. This is followed by a description of actual ductile particle reinforced materials, their properties, and various processing methods currently employed in their fabrication. Finally, a review of the literature concerning the thermal shock behaviour of monolithic ceramics and CMCs is presented, outlining the background theory and quantification of thermal shock resistance for these materials.

2.2 DUCTILE PARTICLE TOUGHENED CERAMIC MATRIX COMPOSITES

2.2.1 Introduction

Several ductile particle reinforced CMC systems have been studied over recent years. The majority of ductile metal reinforced CMCs have shown significant

increases in fracture toughness compared with the monolithic matrix material. The most successful composites of this type are those exhibiting a high degree of ductile particle bridging across the parting crack faces behind the crack tip. Although ductile particle bridging is the most effective of toughening mechanisms, unfortunately it is not always observed in composites of this type. Other toughening mechanisms frequently occur which, although still beneficial, do not exploit the full toughening potential of the ductile phase.

2.2.2 Theoretical Considerations

2.2.2.1 Quantification of Toughening Increment

Several attempts have been made to quantify the toughening increment attributed to the crack bridging process, with the objective of relating the nominal stress $\sigma(u)$, carried by the stretching particle for a given crack opening u, to the uniaxial plastic flow properties of the ductile material.

Following Ashby *et al.* (1989),

$$\sigma(u) = \frac{F(u)}{\pi r_0^2} \qquad 2.1$$

where F is the force and r_0 the initial radius of the particle.

The nominal stress function $\sigma(u)$, once derived, can be related to the enhanced toughness of the composite (Sigl *et al.* 1988, Ashby *et al.* 1989, Flinn *et al.* 1989),

$$\Delta G_{Ic} = f \int_0^{u^*} \sigma(u)\, du \qquad 2.2$$

where f is the area fraction of ductile material intercepted by the crack and u* is the crack opening when the ductile particle fails. Scaling the nominal stress with the yield stress, σ_y, and u with a characteristic dimension of the second phase, r_0,

gives

$$\Delta G_{Ic} = \chi f \sigma_y r_0 \qquad 2.3$$

in which χ is a "work of rupture" parameter, given by

$$\chi = \int_0^{\frac{u^*}{r_0}} \frac{\sigma(u)}{\sigma_y} d\frac{u}{r_0} \qquad 2.4$$

χ depends upon the ductility of the reinforcement, the work hardening coefficient, and the extent of interfacial debonding.

This analysis is based on the assumption that each individual ductile particle intercepted by the crack is plastically stretched until it necks to a point prior to failure. Also, additions to the total closure forces exerted across a propagating crack from intact particles elsewhere in the process zone have been neglected. Studies performed on systems involving ductile particle failure by necking have shown acceptable agreement between theory and experiment.

Although it has been stressed that a strong interface is required in such composite systems, a partially debonded interface is beneficial to toughening. Strong matrix/particle interfacial bonding implies that the maximum gauge length of the ductile reinforcement is equal to the small initial crack opening, hence only a small volume of ductile material may contribute to toughening. A degree of debonding generates a greater gauge length and hence a larger volume of material able to contribute to the desired toughening mechanism (Ashby *et al.* 1989, Shercliff *et al.* 1992). This is shown schematically in figure 2.1. However, since it is difficult to control the degree of debonding of a ceramic/metal interface in a particulate system, a strong rather than weak bond is more desirable.

2.2.2.2 Influence of Matrix/Particle Property Mismatch

For a particulate composite consisting of two phases with differing coefficients of thermal expansion, internal stresses are generated within and around particles as the composite cools from the processing temperature. The matrix/particle interface is subjected to a radial tensile stress when the coefficient of thermal expansion of the particle is greater than that of the matrix. The linear elastic solution for the tensile stress, σ_t, can be calculated using the relationship proposed by Selsing (1961),

$$\sigma_t = \frac{\Delta\alpha\Delta T}{[(1+\nu_m)/2E_m]+[(1-2\nu_p)/E_p]} \qquad 2.5$$

where $\Delta\alpha$ is the difference in the two coefficients of thermal expansion, ΔT is the cooling range over which the internal stress is no longer relaxed by the system, E is the Young's modulus and υ is the Poisson's ratio. Subscripts m and p represent the matrix and particle respectively. From equation 2.5, the magnitude of the stress developed is independent of particle size. It has however been shown experimentally (e.g. Davidge & Green, 1968) that for a specific system, cracking occurs around particles greater than a critical size. Particles having a diameter above the critical size are expected to show either failure of the ceramic/metal interface when either cooling from the processing temperature (or when subjected to an external stress), or cracks propagating radially from the particles. The former occurs when $\alpha_p > \alpha_m$, and the latter, which is more detrimental to the strength of the material, occurs when $\alpha_p < \alpha_m$. The critical particle size, d_c, may be calculated from the relationship proposed by Davidge & Green,

$$d_c = \frac{8K_{Ic}^2}{(\sigma_t)^2(1-\nu_m)+2(E_m/E_p)(1-2\nu_p)} \qquad 2.6$$

Davidge & Green stated that in the design of composite materials for high strength, the particle and matrix expansion coefficients should be matched, and that the particle size should be as small as possible.

Krstic *et al.* (1981) concluded that low residual stress levels are essential for effective crack/particle interaction in a composite of metallic particles in a brittle matrix in order to utilise the inherent ductility of the second phase. Although, in systems where the mismatch in thermal expansion coefficient between the metallic reinforcement and the ceramic matrix induces residual stresses in the matrix as the composite cools from the processing temperature, it has been found that this can cause microcracking, and can have a significant effect on toughening (Wang *et al.* 1991). Toughening due to microcracking is known to occur in several two phase CMCs, e.g. zirconia toughened alumina (ZTA) (Rühle & Evans, 1989) and magnesia-partially-stabilised-zirconia (MgPSZ) (Marshall & Swain, 1988). The mechanism involves the formation of microcracks within regions of local residual tension caused by a mismatch in coefficients of thermal expansion. The passage of a macrocrack then activates any microcracks formed, causing further dissipation of energy away from the propagating macrocrack, hence an increase in toughness. However, this contribution is partially counteracted by a degradation of the material ahead of the microcrack. The full extent of the degradation is presently unknown (Evans, 1990).

It is well known that a significant mismatch in Young's modulus between the matrix and the reinforcing particles can have a substantial effect on the direction of crack propagation (e.g. Krstic *et al.* 1981, Baran *et al.* 1990). A propagating crack is attracted towards a ductile metal inclusion of lower modulus than the matrix (Krstic *et al.* 1981, Vekinis, 1992). The metal/ceramic interfacial bond strength then determines whether crack propagation occurs via the interface or through the particle. Crack deflection occurs when the ceramic/metal interfacial bond strength is considerably lower than the yield stress of the reinforcing particle (Moore & Kunz, 1987), resulting in crack propagation along the interface and subsequent debonding. Therefore no toughening increase due to plastic deformation is gained from the ductile particle. However, a lesser degree of toughening is still observed due to the increased tortuosity of the crack path and any frictional forces that must be overcome to extract the particle from its original

socket, i.e. "pull-out" (Moore & Kunz, 1987, Krstic *et al* 1990, Baran *et al.* 1990, Sun *et al.* 1991, Ashby & Beaumont, 1992, Vekinis, 1992, Sun, 1993, Wang *et al.* 1993, Thompson & Raj, 1994, Trusty, 1994, Zhang, 1995).

2.2.2.3 Importance of Ceramic/Metal Interface

In addition to the effects of inclusion particle size, a mismatch in Young's modulus and a mismatch in the coefficient of thermal expansion, the chemistry of the ceramic/metal interface in metal reinforced CMCs is also of great importance. Factors responsible for determining the nature of the interfacial bonding between two phases include the thermodynamics of any interfacial reaction, crystallographic relationships and atomic structure at the interface. It is commonly thought that strong interfacial bonding is necessary in particulate ductile phase toughened ceramic matrix composites, in order to prevent particle pull-out and hence achieve the maximum possible toughening potential offered by the ductile particles (as explained previously). Much work has therefore concentrated on the understanding and control of the structure and properties of such ceramic/metal interfaces.

Ceramics such as alumina are not readily wetted by liquid metals (i.e. the contact angle $> 90^{o}$). It is often assumed that such non-wetted interfaces will be weak, although this is not always true. In fact, some contradictory evidence has been found.

The wettability of an oxide by a metal and adhesion in such a system increases with growing affinity of the liquid phase metal for oxygen. This was demonstrated during a study of the wettability of sapphire by liquid copper-oxygen alloys by Chaklader *et al.* (1968). In this study, the addition of copper oxide to copper metal in amounts of from 1 to 72 % of the metal weight caused a progressive decrease in contact angle. It was therefore concluded that the degree of wetting of the solid by the liquid was dependent on the amount of oxygen in the system.

The lowering of interfacial energy was thought to be the consequence of a chemical reaction at the interface, resulting in the formation of $CuAlO_2$.

Sun (1993) investigated the Al_2O_3/Ni interfacial characteristics in a Ni particle toughened alumina, and successfully attempted to improve the degree of interfacial bonding by control of the oxygen partial pressure within the fabrication environment. It was found experimentally and theoretically that although an increased oxygen partial pressure aided wetting of the alumina by the nickel during processing, it also resulted in the formation of $NiAl_2O_4$ spinel at the Al_2O_3/Ni interface, which was shown to be detrimental to the fracture properties of the composite. Critical oxygen partial pressures for both the wetting of α-Al_2O_3 by liquid Ni and the formation of nickel aluminate spinel were calculated, and it was found that the critical oxygen partial pressure for wetting was greater than that for spinel formation at the proposed processing temperature. Hence wetting was always accompanied by spinel formation. However, by the use of a two step pre-consolidation heat treatment and a suitable hot pressing process in order to gain control over the oxygen partial pressure during processing, wetting was achieved, thus producing a mechanically and chemically improved ceramic/metal interface, whilst the formation of excessive spinel was avoided. The fracture toughness of the composite produced in such a way was found to be higher than those produced without the pre-consolidation heat treatment, and exhibited a more desirable K_R curve behaviour.

The thermochemical aspects of the alumina/iron system have been studied extensively; this is mainly due to its importance in iron and steel making. The only stable intermediate oxide in the pseudobinary system FeO-Al_2O_3 is $FeAl_2O_4$ which has a spinel structure, and is formed in suitable conditions by the reaction

$$\gamma\text{-}Fe(s) + \tfrac{1}{2}O_2(g) + \alpha\text{-}Al_2O_3(s) \rightarrow FeAl_2O_4(s)$$

Trumble (1992) used thermochemical data to calculate the oxygen activity

dependence of aluminate formation at solid Fe/α-Al_2O_3 interfaces. Equilibrium interfacial aluminate formation ($FeAl_2O_4$) requires a critical activity of oxygen dissolved in the metal. The calculated threshold oxygen levels for aluminate formation increase with increasing temperature. The minimum oxygen concentration in γ-Fe necessary for spinel formation at γ-Fe/α-Al_2O_3 interfaces increases from approximately 1 at. ppm at 1224 K to 20 at. ppm at 1623 K. The oxygen concentration in γ-Fe as a function of temperature for the equilibrium {γ-Fe(ss), $FeAl_2O_4$, Al_2O_3} is shown in figure 2.2.

2.2.2.4 K_R Curve Behaviour

The increase in steady-state toughness due to the incorporation of ductile particles capable of crack bridging is shown in equation 2.3. In toughened ceramics, however, steady-state toughness is always preceded by resistance curve (K_R curve) behaviour and the corresponding development of a finite process zone. In a material showing K_R curve behaviour, the ease of crack propagation is significantly affected by events occurring in the wake of the crack. It should be remembered, however, that K_R curve behaviour is not a material property, but is specimen dependent. Even so, the determination of K_R curves for various materials can be a useful comparative method. Events such as ductile particle bridging and particle pull-out occurring in the so-called "process zone" behind the advancing crack tip cause the critical stress intensity factor to increase until a plateau value is reached (figures 2.3 and 2.4). This indicates that the process zone has reached a critical maximum length. The optimum material would possess a very steep K_R curve, reaching a high plateau toughness almost immediately. A simple analysis has shown that the slope of the curve for a ductile particle reinforced CMC diminishes as the extent of debonding increases (Ashby *et al.* 1989, Rühle & Evans, 1989).

Plastic straining of ductile particles within the process zone results in a toughening process known as crack shielding. In contrast to the bridging mechanism, crack shielding processes tend to be enhanced by incorporating ductile particles of small

size and low yield strength into the matrix (Sigl *et al.* 1988). As a consequence of ductile straining of the particles, energy is dissipated in the surrounding process zone, again contributing to the overall increase in toughness. Energy is also dissipated by crack blunting, which involves the deformation of ductile inclusions intercepted by an advancing crack, effectively blunting the crack (Vekinis, 1992).

Several monolithic non-transforming polycrystalline ceramics also exhibit K_R curve behaviour, due to grain-localised crack bridging in which intact bridging grains exert closure forces along the crack faces in the wake of an advancing crack tip. The closure forces result from frictional pull-out of the bridging grains from the matrix. Thus K_R curve behaviour in monolithic ceramics is generally associated with coarse microstructures and/or high grain aspect ratios (e.g. Li *et al.* 1995, Fett *et al.* 1995, Xu *et al.* 1995).

2.2.3 Practical Composite Systems

2.2.3.1 Processing Methods

It is known that the sinterability of a matrix is decreased significantly with increasing inclusion volume fraction (Bordia & Raj, 1986, Tuan & Chen, 1995), and that this is due to the following two factors; a) interactions between the randomly distributed inclusions that constrain the matrix and b) the packing of the matrix phase, especially in regions immediately surrounding the inclusions (Fan & Rahaman, 1992). Fan & Rahaman studied the effect of inclusion size on the sinterability of a ZnO-ZrO_2 composite, and concluded that as the inclusion size was decreased, for a given volume fraction, the relative density of the sintered body also decreased. This was thought to be due to two factors. Firstly, porosity in the matrix was partitioned within two distinct regions, i.e. immediately surrounding the inclusions and within the bulk of the matrix. The porosity surrounding the inclusions was thought to be a form of sintering damage caused by packing inhomogeneities of the local matrix phase. Secondly, clustering of the

inclusions would be expected to become increasingly severe with smaller inclusion size, which may lead to a greater degree of localised inclusion networks and result in a greater constraint on the matrix.

One of the problems typically encountered with this fabrication technique for ductile particle CMCs is low final density caused by poor wetting of the ceramic by the metallic melt during pressureless liquid phase sintering (Tuan & Brook, 1992). For the Al_2O_3-Ni system, fully dense composites can be prepared for a nickel content of up to 13 volume %. Above this threshold value, the relative density achieved after sintering decreases to around 97 % for a composite containing 20 volume % nickel (Tuan *et al.* 1995). Another common consequence of poor wettability is a weak particle/matrix interface, preventing the exploitation of the full toughening potential of the ductile phase.

Wang *et al.* (1993) sintered composites consisting of silver inclusions within an alumina matrix. They discovered that a significant weight loss occurred within the 1200 °C to 1500 °C range, and that a silver-free alumina surface layer formed during sintering. Further investigation revealed that, as a consequence of the poor wetting behaviour of molten silver on alumina, silver was rejected from the alumina surface layer at around 1000 °C to 1200 °C. As the temperature was increased further, evaporation of the silver resulted in a significant loss of weight and the formation of the silver-free surface layer (which then prohibited further loss of silver from the bulk microstructure). It was also concluded that the presence of molten silver at grain boundaries during the sintering process prevents excessive grain growth, therefore refining the matrix microstructure.

Many previous studies of CMCs have favoured hot pressing as the method of fabrication (e.g. Hing & Groves, 1972, Krstic *et al.* 1981, Moore & Kunz, 1987, Jessen & Lewis, 1990, Sun *et al.* 1991, Bannister *et al.* 1992, Sun, 1993, Trusty, 1994). The main advantages over conventional sintering offered by hot pressing are higher achievable densities (up to 100 % theoretical density) and restricted

grain growth, resulting in superior mechanical properties. Hot pressing requirements for powders are less stringent than for sintering because of the additional energy source available for densification. Relatively coarse powders may be successfully pressed, although the optimum average particle size is between 0.5 μm and 1.5 μm. However, due to the fact that hot pressing involves the application of a uniaxial pressure, the possibility of sacrificing material isotropy must be realised. A second disadvantage with this process, compared to conventional sintering, is the limitation of component shape and complexity. The high cost and processing difficulties associated with hot pressing mean that commercial manufacturers are often reluctant to utilise the technique.

Powder processing routes offer the potential to tailor the final microstructure of the composite. This could involve pretreatment of the metallic powder prior to blending; this may be an oxidative heat treatment to enhance the wettability of the ceramic by the metal (Moore & Kunz, 1987, Sun, 1993), or an acidic treatment of the raw metallic phase in an attempt to maximise the degree of mechanical interlocking at the ceramic/metal interface (Moore & Kunz, 1987). Alternatively, the milling procedure may be altered to produce a discrete distribution of metallic particles in the final composite or a continuous network of reinforcing metallic phase (Sun, 1993, Trusty, 1994). However, a disadvantage of a conventional powder processing method for ductile particle reinforced CMCs is that high internal stresses caused by the mismatch in thermal expansion coefficients between the ductile particles and the matrix material may be induced during cooling from the processing temperature (Tuan & Brook, 1992). This has led to the development of various alternative methods of fabrication.

An alternative CMC fabrication procedure used by Aghajanian *et al.* 1989, Salas *et al.* 1991, Tuan & Brook, 1992, is the DIMOX (Direct Metal Oxidation) method. In this process, a ceramic preform (particulate or fibrous) is infiltrated by a molten metal alloy which undergoes an oxidation reaction with the surrounding atmosphere. The reaction product (e.g. Al_2O_3 in Al-Al_2O_3

composites) is formed as a continuous phase; the unreacted reactant (e.g. Al) is found in channels within the reaction layers. The growth of the oxide occurs continuously away from the initial molten alloy/ceramic preform interface while fresh alloy is supplied to the gas/metal reaction interface via fine microscopic channels through the oxide product.

Whereas the DIMOX method involves infiltrating a porous ceramic preform with molten metal, composites of Al_2O_3-Al have recently been produced using dense ceramic preforms (Loehman *et al.* 1996). The ceramic preforms used typically had densities greater than 90 % of theoretical with no open porosity; the formation of the ceramic-metal composite was driven by the strongly negative Gibbs energy for reaction. In the Al-mullite system, the reactive metal penetration produces a fine grained alumina skeleton with an interspersed metallic phase according to the general reaction

$$(x+2)Al + (3/y)MO_y \rightarrow Al_2O_3 + Al_xM_{3/y}$$

The ceramic-metal composites produced in this way have improved fracture properties whilst retaining similar hardness and Young's modulus values to that of monolithic alumina.

A further method investigated by Ritland & Readey (1994) is the vapour phase sintering of a porous Al_2O_3 substrate in a gaseous HCl atmosphere, and subsequent infiltration by molten Cu containing dissolved Cu_2O for improved wettability of the porous Al_2O_3. This resulted in a three dimensional interpenetrating networked composite of Al_2O_3 and Cu. Sintering the Al_2O_3 in HCl allows the control of grain growth and therefore influences the interfacial properties.

2.2.3.2 Toughening and Fracture Behaviour

The vast majority of studies concerning ductile particle toughened CMCs have shown an increase in fracture toughness when compared with the monolithic matrix values. For example, increases of up to 250 % of the matrix toughness were reported for DIMOX Al_2O_3-Al composite materials, the increase being attributed to the high degree of plastic deformation of the continuous ductile phase (Aghajanian *et al.* 1989).

Following a study of a magnesium aluminate spinel matrix reinforced with platinum particles by Thompson & Raj (1994), it was confirmed that a particle size dependent debonding phenomenon existed, where small platinum particles (1 μm) remained well bonded to the matrix and failed in a relatively ductile manner with up to 85 % strain to failure, whereas larger particles (4 μm to 10 μm) experienced catastrophic debonding after small amounts of plastic deformation. This behaviour was observed despite similar initial spinel/platinum interfacial strengths. Further, Thompson & Raj (1994) also found that smaller particles (≈1 μm) experienced large strains to failure with a corresponding ultimate tensile strength (UTS) of 550 MPa, whereas larger particles (≈12 μm) failed at less than 25 % strain, and also had a lower UTS. This difference in ductility was explained by the authors in terms of debonding at the ceramic/metal interface. It was suggested that debonding depends on the length of the dislocation pile up at the interface, and therefore, on the particle size.

Tuan & Brook (1992) fabricated a series of Al_2O_3-Ni composites with inclusion sizes ranging from ≈1 μm to 4 μm, and found that the increase in fracture toughness was at a maximum for an inclusion size of around 2.5 μm. However, after calculating the residual interfacial radial tensile stress caused by the mismatch in the coefficient of thermal expansion, and applying the energy balance concept (§ 2.2.2.2), a critical particle size of 4.5 μm was predicted. It was proposed that the difference between the theoretical and experimental results may

be due to the fact that the composites were not fully dense.

Tuan *et al.* (1995) also studied the effect of varying the nickel content (in the Al_2O_3-Ni system) on the microstructure, toughness and flexural strength. It was found that the distribution of Ni particles was discrete up to a Ni content of 13 volume %, whereas for a composite containing 20 volume % Ni, an interpenetrating network was thought to exist. The flexure strength and fracture toughness increased with Ni content up to 13 volume % Ni. This was attributed to matrix grain refinement and crack bridging respectively. The 20 volume % Ni composite showed a decreased toughness and strength; this was thought to be due to the fact that the size of the Ni reinforcement was found to be greater than the critical size.

The interfacial bonding between a reinforcing metallic particle and a ceramic matrix was found to be highly dependent on the mismatch in the coefficients of thermal expansion and Young's moduli between the two materials (Krstic *et al.* 1981). The study involved two glass matrix composites, one reinforced with partially oxidised Ni particles, the other with partially oxidised Al particles. It was concluded that a large mismatch in the coefficient of thermal expansion led to bypassing of the particles by a propagating crack (as in the Ni reinforced glass), whereas a reduction in the thermal and elastic stresses promoted satisfactory interfacial bonding resulting in a composite showing a 60 fold increase in toughness compared to the monolith. Interfacial debonding accompanied by energy dissipation due to plastic deformation has been observed in several systems including Al_2O_3-Ag (Wang *et al.* 1993), Al_2O_3-Ni (Sun *et al.* 1991, Tuan & Brook, 1992, Sun, 1993, Shercliff *et al.* 1994), Al_2O_3-Pt (Thompson & Raj, 1994), and Al_2O_3-Fe (Trusty, 1994). Often leading to the increase in fracture resistance with crack extension (K_R curve behaviour), the process involves the nucleation of debonds at the interface ahead of the crack. Growth of the debonds by combined debonding of the interface and plastic deformation of the metal eventually causes crack extension. This process occurs at a fracture resistance substantially lower

than that expected for ductile fracture by plastic void growth.

Many metallic materials have been investigated as potential toughening phases. Baran *et al.* (1990) studied the fracture toughness and fracture behaviour of a glass reinforced with spherical particles of two gold-based alloys, and found that the softer, more ductile alloy was a more effective toughening additive than the harder alloy. It can therefore be concluded that for the mechanism of crack bridging by plastic deformation of the ductile phase to occur in preference to crack deflection by interfacial failure, the yield stress of the constrained metallic particle must be lower than the fracture stress of the ceramic/metal interface.

Shercliff *et al.* (1994) produced a composite comprising an alumina matrix reinforced with short nickel fibres. The K_R curve behaviour of this material was evaluated using the double torsion technique. However, the K_R curve for the composite was found to be less steep, with a lower plateau toughness, than that obtained for the monolithic matrix alumina. This was attributed to the low proportion of ductile failures observed.

Studies of the K_R curve behaviour of other ductile particle reinforced CMCs have shown promising results. Sun (1993) showed that a microstructure consisting of a network of metallic inclusions showed an improved K_R curve behaviour than a discrete dispersion for an Al_2O_3-20 volume % Ni composite system, due to the former having a greater resistance to pullout (maximum toughness values reached were 13 MPa $m^{½}$ and 5.6 MPa $m^{½}$ respectively). However, the microstructure having a discrete particle dispersion showed a shorter process zone length., i.e. a steeper K_R curve. Trusty (1994) observed a relatively small increase in toughness for a particulate Al_2O_3-20 volume % Fe composite, reaching a plateau value of 6.2 MPa $m^{½}$ with a partially developed process zone length of 5.4 mm (measured using the double cantilever beam (DCB) technique). The increase in toughness was attributed mainly to crack deflection. A networked Al_2O_3-20 volume % Fe composite showed a higher degree of crack bridging by plastically

deformed ductile particles, and an improved K_R curve, reaching a plateau toughness of 9.6 MPa $m^{½}$ with a crack length of 4.5 mm. Trusty isolated the observed toughening mechanisms for each composite, and evaluated the independent contributions to the increased fracture toughness observed during DCB testing. The numerical values assigned to each mechanism were found to be in the correct proportions when compared with each other. However, a discrepancy existed between the experimentally derived values and theoretically derived values for the energy dissipated when a ductile particle necks to the point of failure. This was attributed to the simplified nature of the modelling, in that additional toughening mechanisms of crack branching and residual stress effects had been neglected. Additionally, Trusty concluded that optimum short-crack toughening was shown by the composite containing a discrete dispersion of iron particles, whereas the networked microstructure exhibited favourable long-crack toughening properties. A composite containing both networked *and* discrete dispersions was then fabricated, and was found to show an improved K_R curve behaviour, with a plateau toughness of 10.3 MPa $m^{½}$ for a crack length of 6.5 mm.

2.3 THERMAL SHOCK BEHAVIOUR

2.3.1 Introduction

The following section presents a review of the literature relevant to the thermal shock behaviour of ceramic materials, beginning with an account of the practical and theoretical considerations regarding monolithic ceramics, followed by a discussion regarding the validity of the application of the established theory to CMCs. This is then followed by a review of the progress made concerning the evaluation and prediction of the thermal shock behaviour of various particulate reinforced CMCs.

2.3.2 Theoretical Considerations Regarding Monoliths

Early studies regarding the quantitative analysis of the thermal shock behaviour of monolithic ceramics were conducted following two different approaches. The first of these considered a ceramic body subjected to a sudden change in temperature, ΔT (Buessem, 1956). During quenching, the thermal stresses generated result in a tensile stress at the surface of the component. At a critical temperature differential ΔT_c, the tensile stress is equal to the tensile fracture stress of the material, σ_f, therefore causing the initiation of cracks. No attempt was made at this stage to consider the retained strength of the component following thermal shock, i.e. the initiation of fracture was regarded as the point of failure. This condition is given by

$$\sigma_f = \frac{\alpha E \Delta T_c}{1-\nu} \qquad 2.8$$

where α is the coefficient of thermal expansion, E the Young's modulus and υ the Poisson's ratio of the material. Rearranging equation 2.8 to give a critical temperature differential for the onset of cracking for an infinitely fast quench gives what is known as the first thermal shock parameter, R

$$R = \Delta T_c = \frac{\sigma_f (1-\nu)}{\alpha E} \qquad 2.9$$

At this stage, however, an infinitely fast quench is assumed, which in practice is impossible to achieve. Therefore, the stress reduction factor Ψ is introduced to take into account the finite time required for heat transfer to occur. Ψ is a number between 0 and 1 and is a function of the Biot modulus, β ,

$$\beta = \frac{rh}{k} \qquad 2.10$$

where r is a characteristic dimension (half radius or half width of the specimen),

h is the heat transfer coefficient, and k is the thermal conductivity. The variation of Ψ with non-dimensional time, θ (as defined later in equation 2.22), for several values of β is shown in figure 2.5.

Equation 2.8 is modified to be

$$\sigma_f = \frac{\Psi \alpha E \Delta T_c}{1-\nu} \qquad 2.11$$

Rearranging equation 2.11 gives a critical temperature differential, below which no cracking is observed

$$\Delta T_c = \frac{1}{\Psi} \cdot \frac{\sigma_f (1-\nu)}{\alpha E} \qquad 2.12$$

The second thermal shock resistance parameter R' introduces k, therefore taking into consideration the finite time for heat transfer to occur

$$R' = Rk = \frac{\sigma_f (1-\nu) k}{\alpha E} \qquad 2.13$$

The use of R parameters to predict the critical temperature differential at which thermal fracture initiates has given fair agreement with experimental data (e.g. Davidge & Tappin, 1967, Hasselman, 1969).

However, for some applications the severity of damage sustained from thermal shock is more important than the initiation of fracture, e.g. refractory ceramics. Therefore, an alternative approach to the analysis of thermal shock behaviour was adopted by Hasselman (1969). The so-called damage resistance approach disregarded the question of fracture initiation, concentrating instead on the extent of crack propagation and the subsequent changes in material properties.

For situations where the extent of crack propagation is more important than the initiation of fracture, Hasselman introduced a thermal shock damage resistance parameter

$$R'''' = \frac{K_{Ic}^{\ 2}}{\sigma_f^2(1-\nu)} = \frac{2E\gamma}{\sigma_f^2(1-\nu)} \qquad \textbf{2.14}$$

where γ is the fracture surface energy.

Since the thermal shock resistance parameters R and R' are proportional to σ_f, but R'''' is proportional to the square of the inverse of σ_f, resistance to the initiation of thermal fracture demands materials of high strength, whereas resistance to crack propagation and damage accumulation requires low strength. A similar but opposite requirement prevails regarding the Young's modulus. Accurate calculation of these thermal shock resistance parameters is complicated by the fact that the properties involved are temperature dependent. Thus, R parameters are generally only used as a method of ranking ceramics in terms of their thermal shock resistance, and not for design purposes.

In 1969, Hasselman also developed a unified theory of thermal shock for brittle ceramics in terms of both fracture initiation and crack propagation. It was proposed by Hasselman that the driving force for crack propagation is derived from the elastic energy stored in the body at the instant of fracture. Hasselman said that the total energy (W_t) per unit volume of a body is the sum of the elastic energy plus the fracture energy of the cracks, i.e.

$$W_t = \frac{3(\alpha\Delta T)^2 E}{2(1-2\nu)}\left\{1+\frac{16(1-\nu^2)Na^3}{9(1-2\nu)}\right\}^{-1} + 2\pi Na^2\gamma \qquad \textbf{2.15}$$

where E is the Young's modulus of the crack-free material, a is the crack length and N is the number of cracks. Following the general Griffith approach, cracks are unstable between those limits for which

$$dW_t/da = 0 \qquad \textbf{2.16}$$

Substitution of equation 2.15 into equation 2.16 results in a critical temperature

differential required for crack instability

$$\Delta T_c = \left\{\frac{\pi\gamma(1-2\nu)^2}{2E\alpha^2(1-\nu^2)}\right\}^{1/2}\left\{1+\frac{16(1-\nu^2)Na^3}{9(1-2\nu)}\right\}[a]^{-1/2} \qquad \textbf{2.17}$$

Equation 2.17 is illustrated in figure 2.6. The variation in critical temperature differential with increasing crack length passes through a minimum with the region of crack instability bound by two values of crack length. The effect of crack density is also shown. For initially short cracks, after the initiation of fracture, the elastic energy release rate exceeds the fracture surface energy. This excess energy is transformed into kinetic energy of the propagating crack, which will continue to propagate until the energy released is equal to the total surface fracture energy at a final crack length a_f, i.e.

$$\frac{3(\alpha\Delta T_c)^2E}{2(1-2\nu)}\left\{\left\{1+\frac{16(1-\nu^2)Na_0^3}{9(1-2\nu)}\right\}^{-1}-\left\{1+\frac{16(1-\nu^2)Na_f^3}{9(1-2\nu)}\right\}^{-1}\right\}$$

$$=2\pi N\gamma(a_f^2-a_0^2) \qquad \textbf{2.18}$$

where a_0 is the initial crack length (see figure 2.6). For short initial cracks with $a_f >> a_0$, the final crack length can be written as

$$a_f=\left\{\frac{3(1-2\nu)}{8(1-\nu^2)a_0N}\right\}^{1/2} \qquad \textbf{2.19}$$

This implies that, apart from the dependence on Poisson's ratio, the extent of crack propagation for a short initial crack is independent of material properties and is inversely proportional to crack density and initial crack size. Based on this theoretical approach, the expected change in crack length and corresponding changes in strength with temperature differential are shown in figure 2.7. For brittle materials with a short initial crack length a_0, the strength and crack length remain unchanged until ΔT_c is reached. At this critical temperature differential, cracks will begin to propagate to a final length a_f, with a corresponding sharp

decrease in strength. Further increases in ΔT result in a plateau of strength and crack length, while new cracks propagate to length a_f. Only at a further critical temperature differential, $\Delta T_c'$, will crack growth occur quasi-statically, causing a gradual decrease in strength. This prediction of thermal shock behaviour has been verified for various brittle materials (e.g. Davidge & Tappin, 1967, Hasselman, 1970, Gupta, 1972).

For materials having long initial cracks, propagation will occur quasi-statically, resulting in a more gradual decrease in strength (also shown in figure 2.7). The quasi-static crack propagation and corresponding strength degradation may be minimised by reducing the thermal stress crack stability parameter, R_{st}, introduced by Hasselman for materials having long initial crack length such as refractory brick, where

$$R_{st} = [\gamma/\alpha^2 E]^{1/2} \qquad \textbf{2.20}$$

Although the theories regarding the onset and arrest conditions for fracture developed by Hasselman enabled predictions of thermal fracture for small inherent flaws, this condition is often exceeded. It was therefore necessary to consider the propagation and arrest behaviour in the macrocrack regime, hence there was a need for a fracture mechanical approach. Evans & Charles (1977) adopted a generalised parametric approach concerning the stress intensity factor at a crack tip.

This complex problem can generally only be solved for a given specimen geometry, using numerical techniques. For convective heat transfer conditions, the thermal stresses generated in a body can be described by the normalised parameters

$$\Omega = \frac{\sigma(1-\nu)}{E\alpha\Delta T} \qquad \textbf{2.21}$$

$$\theta = \frac{kt}{C\rho r^2} \qquad 2.22$$

$$\beta = \frac{rh}{k} \qquad 2.23$$

where t is the time after exposure to ΔT, ρ is density and C is specific heat. Using these parameters, Evans & Charles generalised the relation between time and surface stress and the corresponding stress distribution within a body (as illustrated in figure 2.8). The behaviour of a crack in a thermal stress field can be deduced from the dependence of the crack length on the stress intensity factor. The stress intensity factor for a small crack ($a/r \leq 0.25$, where a is the crack length) propagating in this stress field is given by

$$K = 2\sqrt{a/\pi}\int_0^a \frac{\sigma(x)[1+F(x/a)]}{\sqrt{a^2-x^2}}dx \qquad 2.24$$

where F(x/a) is a weight function given by

$$F(x/a) = (1-x/a)[0.2945 - 0.3912(x/a)^2 + 0.7685(x/a)^4$$

$$-0.9942(x/a)^6 + 0.5094(x/a)^8] \qquad 2.25$$

Equation 2.24 can then be normalised by substituting the expressions given in equations 2.21, 2.22 and 2.23 to give the normalised stress intensity factor, κ, as

$$\kappa = \frac{K(1-\nu)}{E\alpha\Delta T\sqrt{r}} = \frac{2}{\sqrt{\pi}}\sqrt{a/r}\int_0^1 \frac{\Omega(x/r)[1+F(x/a)]d(x/a)}{\sqrt{1-(x/a)^2}} \qquad 2.26$$

The analysis is quoted as being valid for small cracks ($a/r \leq 0.25$), although finite element analysis suggests reasonable agreement to $a/r \leq 0.5$, providing the number of cracks present is small. Such a numerical analysis requires data for the term Ω (x/r). When the cracks are sufficiently small such that the component

compliance is unaffected by the cracks, it is possible to use the stress that exists in the absence of a crack to obtain κ. Jaeger developed formulae for the radial and tangential thermal stresses in an uncracked solid cylinder for small values of time (Jaeger, 1945). The case of the tangential thermal stress, σ_θ, only will be considered, since firstly the extent of the tensile stress generated at the surface of a component is of prime importance when considering the conditions of fracture initiation, and secondly $\sigma_\theta > \sigma_r$. For a solid cylinder ($0 \le x \le r$), where T_x is the temperature at radius x, the result is known to be

$$\sigma_\theta = \frac{E\alpha}{1-\nu}\left\{\frac{1}{r^2}\int_0^r xT_x dx + \frac{1}{x^2}\int_0^x xT_x dx - T_x\right\} \qquad 2.27$$

Now if k, ρ, C are the thermal conductivity, density and specific heat of the material of the cylinder respectively, and $\lambda = k/\rho C$, introducing the formulae for the temperature differential ΔT, we obtain

$$\frac{(1-\nu)\sigma_\theta}{E\alpha\Delta T} = 2\sum_{s=1}^{\infty}\frac{e^{-\lambda B_s^2 t/r^2}}{B_s^2 J_1(B_s)}\left\{J_1(B_s) + \frac{r}{x}J_1\left\{x\frac{B_s}{r}\right\} - B_s J_0\left\{x\frac{B_s}{r}\right\}\right\} \qquad 2.28$$

where $\pm B_s$, s=1, 2,... are the roots of

$$J_0(B) = 0 \qquad 2.29$$

Table 2.1 shows values of $(1-\upsilon)\sigma_\theta/E\alpha\Delta T$ calculated using this formula for various values of the parameters (x/r) and ($\lambda t/r^2$).

Introduction of the heat transfer coefficient, h, gives the temperature T as

$$T = 2rh\Delta T\sum_{s=1}^{\infty}\exp^{-\lambda B_s^2 t/x^2}\frac{J_0(xB_s/r)}{(r^2h^2 + B_s^2)J_0(B_s)} \qquad 2.30$$

where the B_s are the roots of

$$BJ_1(B) - rhJ_0(B) = 0 \qquad 2.31$$

Following Jaeger and using this result in equation 2.27 (correcting for a typographic error in the original work), the thermal stress may be written as

$$\frac{(1-\nu)\,\sigma_\theta}{E\alpha\Delta T} = \qquad \textbf{2.32}$$

$$\sum_{s=1}^{\infty} \frac{2rh\exp^{-\lambda B_s^2 q r^2}}{B_s(r^2h^2+B_s^2)J_0(B_s)}\left\{J_1(B_s)+\frac{r}{x}J_1\left\{\frac{xB_s}{r}\right\}-B_sJ_0\left\{\frac{xB_s}{r}\right\}\right\}$$

Figure 2.9 shows the crack length dependence of κ for several values of normalised time, θ, and two Biot moduli, as determined analytically in the short crack regime (after Evans & Charles, 1977). Using this approach it is possible to construct plots showing the envelope of K curves against crack length for a body of known dimensions and a specific ΔT, as shown schematically in figure 2.10. The behaviour of a material of known dimensions and critical stress intensity factor (K_{Ic}), subjected to conditions of severe thermal shock may now be predicted in terms of crack initiation, propagation and arrest. A crack will propagate when the thermal shock generated stress intensity factor at the crack tip exceeds the fracture toughness of the material. The crack may propagate either in a stable or unstable manner, depending on the initial crack length. For short initial cracks ($a_i < a_m$, where a_m is the crack length at maximum K), propagation will be unstable as the stress intensity factor increases with increasing crack length up to a_m, and propagation will stop when the stress intensity factor falls below K_{Ic} (assuming the elastic energy released by the propagating crack is immediately dissipated elsewhere; this is not usually the case, and a degree of over-run is expected). A further increase in thermal shock generated stress intensity factor is then required to cause further crack growth. Alternatively, for long initial cracks ($a_i > a_m$), propagation will be stable, and crack arrest will occur when K falls below K_{Ic}.

Pompe (1993) and Bahr *et al.* (1993) have extended this work and considered the propagation of multiple cracks. For multiple crack propagation it is essential that

K still increases after the largest initial crack has begun to grow such that smaller initial cracks reach K_c slightly later in time and will also start to propagate. Smaller cracks may be activated even if they have been partly unloaded as a consequence of previous crack propagation (providing the crack spacing is large enough). Computer simulated crack patterns have been generated, and show similarities to experimentally observed patterns. Additionally, it has been shown that a transient state is reached in which all activated small cracks have approximately equal lengths and spacings. Following this condition, only a few cracks propagate deep (relative to the microstructural features of the material) into the sample. It is the relative depth of the largest crack which will therefore determine the retained strength.

2.3.3 Theoretical Considerations Regarding Ceramic Matrix Composites

The work of Evans & Charles was extended by Swain (1990), who explored the influence of K_R curve behaviour on the thermal shock resistance of duplex ceramics and CMCs. He found that materials exhibiting a pronounced K_R curve showed an improved resistance to severe thermal shock. The non-linear stress-strain behaviour of such materials was found to reduce the magnitude of thermal stress due to the reduction in Young's modulus as a function of strain ϵ, such that

$$E(\epsilon) = E_0[1-\omega(\epsilon)] \qquad 2.33$$

where $\omega(\epsilon)$ is an increasing function of strain. Also, as a consequence of the reduction in thermal stress, the thermal shock generated stress intensity factor as estimated by the fracture mechanics approach is also greatly reduced. The equation for the normalised thermal stress is then given by

$$\Omega = \frac{\sigma(1-\nu)}{E(1-\omega)\alpha\Delta T} \qquad 2.34$$

with a similar modification for κ in equation 2.26.

Two criteria must be satisfied for unstable crack growth in materials that exhibit K_R curve behaviour (Marshall & Swain, 1988), i.e.

$$K_A > K_R \qquad 2.35$$

and

$$dK_A/da \geq dK_R/da \qquad 2.36$$

where K_A is the applied stress intensity factor and K_R is the crack growth resistance (K_R curve). Crack arrest will occur when $K_R > K_A$. Therefore, the combined effect of non-linear stress-strain behaviour and K_R curve behaviour governs the thermal shock behaviour of the material. This is shown in figure 2.11 for a zirconia toughened alumina (after Swain, 1990). The effect of the reduced Young's modulus on the calculated thermal shock generated stress intensity factor is also shown for $\Delta T = 500\ ^{\circ}C$. Crack arrest will occur at the intersection of the reduced stress intensity factor curve and the superimposed K_R curve.

The nature of crack growth (i.e. stable or unstable) may be understood qualitatively from the schematic plot shown in figure 2.12. Crack propagation is initially stable, as can be seen from the motion of the point of intersection of the expanding K curve with the sloping K_R curve. This is different from the situation in figure 2.10, where crack propagation was initially unstable for the material having a constant fracture toughness. The nature of crack propagation changes from stable to unstable where the K_R curve touches the envelope of the K curves. Crack arrest is assumed to occur when the K curve falls below the K_R curve. This final crack length then determines the severity of strength degradation. Therefore, materials having a strong K_R curve behaviour are probably the most suitable for thermal shock applications, as the final crack length for both stable and unstable crack propagation is decreased. For ceramics with very steep K_R curves, the

situation could arise that the stress intensity factor increases more slowly than the K_R curve, hence even for short cracks unstable crack propagation would be impossible (Schneider, 1991).

2.3.4 Practical Studies of the Thermal Shock Behaviour of Particulate CMCs

Lutz & Swain (1991) looked at the effect of an increasing fracture toughness on the thermal shock behaviour of duplex and composite ceramic materials, concentrating on the interrelation between flaw tolerance, K_R curve behaviour and thermal shock strength degradation in ceramics. The analytical approach developed by Evans & Charles was utilised, with Ω (x/r) being calculated from stress/strain measurements evaluated using strain gauges mounted on the tensile and compressive sides of a flexure specimen. It was anticipated that similar behaviour would be observed under thermal shock-induced stress gradients. It was found that the incorporation of pressure zones in yttria tetragonal zirconia leads to a slightly increased flaw tolerance, steeper K_R curve and a higher retained strength following thermal shock.

Also studied by Swain (1990) was the effect of specimen size on the thermal shock strength degradation of a CMC. Thermal stress curves were produced for various values of r for a given temperature differential. The predicted depths of arrested cracks (relative to the specimen thickness) were subsequently found to be greater than for smaller samples, and consequently has a greater effect on the retained strength. The predicted strength degradation was found to be in reasonable agreement with experimental data.

The thermal shock response of cobalt reinforced tungsten carbide was investigated by Han & Mecholsky (1990). As a consequence of the oxidation of the material at high temperatures, the fracture toughness was found to decrease as the temperature differential was increased. It was therefore suggested that the

prediction based on Hasselman's model for ΔT_c should be reconsidered, as it does not take into account a change in fracture toughness after thermal shock, even though the relation of strength behaviour versus ΔT_c qualitatively follows the theory.

Janssen *et al.* (1993) investigated the thermal shock behaviour of a metal infiltrated ceramic, and found that the composites showed a continuous degradation in retained flexural strength at temperature differentials between 200 °C and 300 °C rather than the sudden loss of strength associated with monoliths. The increased damage resistance was attributed to the increasing toughness with crack extension caused by the bridging of cracks by ductile ligaments.

Mignard *et al.* (1996) studied the thermal shock behaviour of a coarse grain porous alumina. Experimental work showed that the material behaved in a similar manner to a refractory ceramic, i.e. exhibiting a high proportion of the original strength following thermal shock from $\Delta T > \Delta T_c$. The alumina was also found to exhibit a shallow K_R curve behaviour due to its coarse microstructure, rising from an initial K_{Ic} of 2.7 MPa $m^{½}$ to 3.6 MPa $m^{½}$ for a crack extension of 0.7 mm. However, quantitative theoretical analysis showed that the increase in toughness observed was not strongly significant in the determination of conditions for crack arrest.

The effect of porosity and metallic particle additions on the thermal shock resistance of sintered ceramics was studied both theoretically and experimentally by Arnold *et al.* (1996). It was found that thermal shock resistance (considered as the second thermal shock resistance parameter) had a maximum at a certain porosity, and that above certain porosities, the presence of pores has a detrimental effect on thermal shock resistance. The authors then suggested that if porous materials are considered as a special case of composite materials, then relations valid for porous materials can be transferred to composite materials and

vice-versa. Subsequently, this theory was investigated using the examples of borosilicate sintered glass with incorporated antimony particles, and eutectic calcium titanate ceramic with incorporated paladium particles. In the case of the glass-antimony composite, improvements in thermal shock resistance of about 15 % (relative to the non-porous matrix) with 10 volume % antimony were calculated and confirmed experimentally, while for calcium titanate-paladium composites, a 15 % (relative to the non-porous matrix) improvement in thermal shock resistance was achieved with only 5 volume % metallic phase.

2.4 CONCLUDING REMARKS

The first section of this chapter presented a review of the literature available concerning ductile particle reinforced CMCs. The major theoretical considerations regarding ductile particle toughening of brittle matrices have been discussed. Several mechanisms responsible for toughening have been introduced, in addition to the microstructural properties which determine the extent of toughening observed for several systems. It appears that many mechanisms may contribute to the overall fracture resistance of a given composite, with the most effective being that of ductile particle bridging; the extent to which this occurs for a given system being highly dependent on the strength of the ceramic/metal interface. A *moderately* strong interface is known to be the optimum in terms of maximising the potential for ductile particle bridging to occur. Various processing methods have been addressed, highlighting their advantages and disadvantages with respect to the resulting properties of the composite. Several new technologies are currently in the development stages, although the hot pressing technique is the most common for the CMCs in question, primarily because of the relative ease of producing a dense, reproducible microstructure. However, the need to be able to sinter the materials is also recognised. In the second section of the chapter, the theory regarding the thermal shock behaviour of monolithic ceramics and CMCs has been explained, followed by an account of the theoretical attempts at quantification of the thermal shock behaviour of dual phase CMCs

with particular relevance to ductile particle reinforced CMCs. Various works regarding the thermal shock behaviour of several CMC materials have been reviewed, with particular attention being given to the fracture mechanics approach and the influence of K_R curve behaviour on the thermal shock behaviour of a CMC. Generally, it appears that particulate CMCs do not show the classic catastrophic loss of strength at a critical temperature differential, as proposed by Hasselman and verified for the majority of monoliths. Instead, a more gradual decrease in retained strength over a range of temperature differentials is observed.

Table 2.1 Calculated normalised tangential thermal stress in circular cylinders for infinite Biot modulus (after Jaeger, 1945).

	x/r									
Theta	0.005	0.01	0.015	0.02	0.05	0.1	0.15	0.2	0.5	1.0
0	.8455	.7845	.7390	.7014	.5479	.3942	.2919	.2179	.0384	.0021
0.1	.2384	.3534	.3972	.4153	.3960	.3065	.2313	.1735	.0306	.0017
0.2	-.0286	.0549	.1194	.1628	.2404	.2125	.1654	.1252	.0222	.0012
0.3	-.0742	-.0700	-.0402	-.0077	.0992	.1184	..0978	.0752	.0134	.0007
0.4	-.0772	-.1021	-.1059	-.0971	-.0158	.0300	.0319	.0259	.0047	.0003
0.5	-.0773	-.1072	-.1255	-.1337	-.1002	-.0481	-.0292	-.0203	-.0035	.000
0.6	-.0773	-.1077	-.1298	-.1455	-.1562	-.1132	-.0827	-.0614	-.0108	.000
0.7	-.0773	-.1077	-.1304	-.1486	-.1900	-.1636	-.1263	-.0954	-.0169	-.001
0.8	-.0773	-.1077	-.1305	-.1492	-.2084	-.1991	-.1586	-.1208	-.0215	-.001
0.9	-.0773	-.1077	-.1305	-.1493	-.2171	-.2202	-.1783	-.1365	-.0243	-.001
1.0	-.0773	-.1077	-.1305	-.1493	-.2196	-.2271	-.1850	-.1418	-.0253	-.001

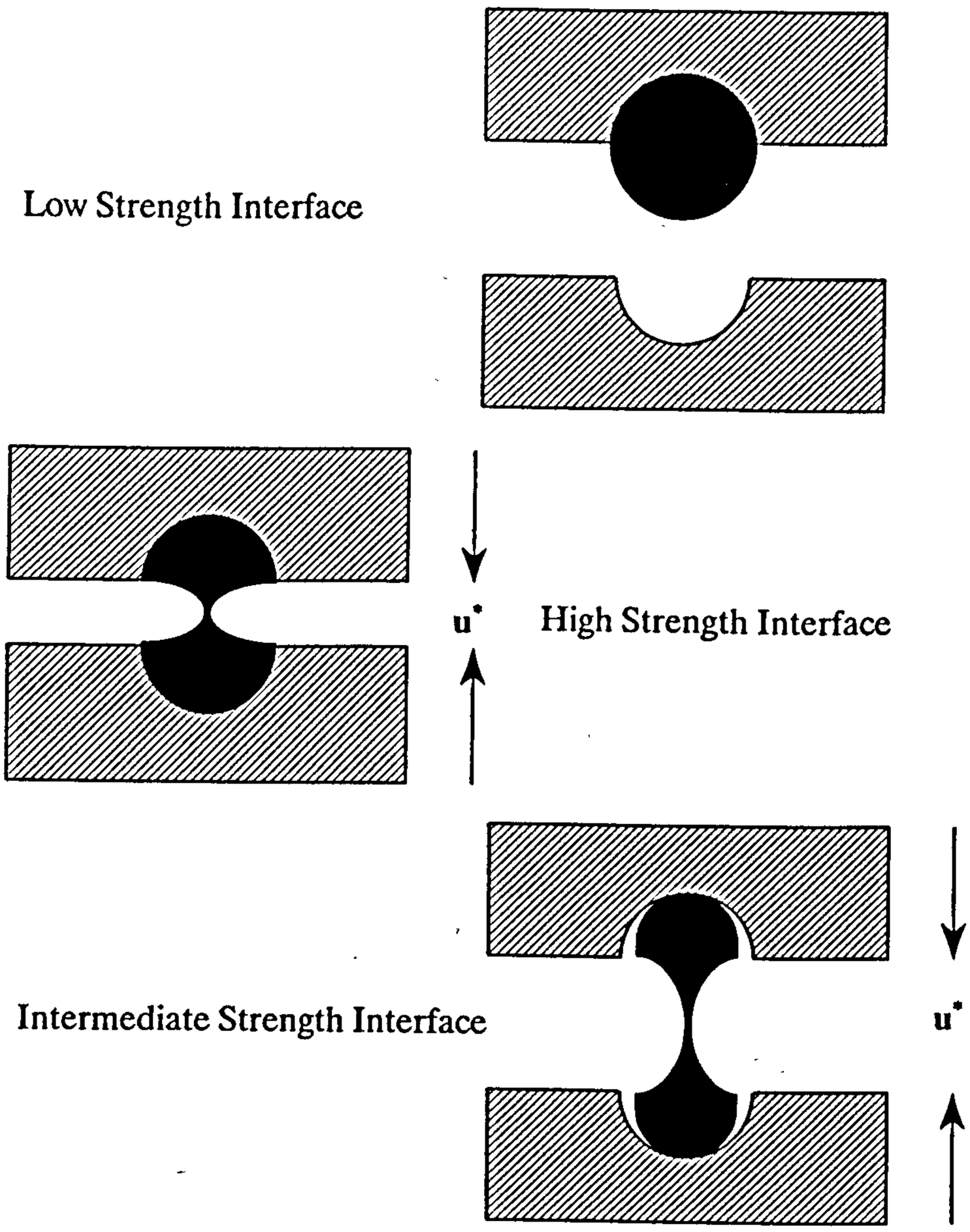

Figure 2.1 Schematic illustration showing the effect of matrix/particle interfacial bond strength on the volume of ductile material able to dissipate energy due to plastic deformation.

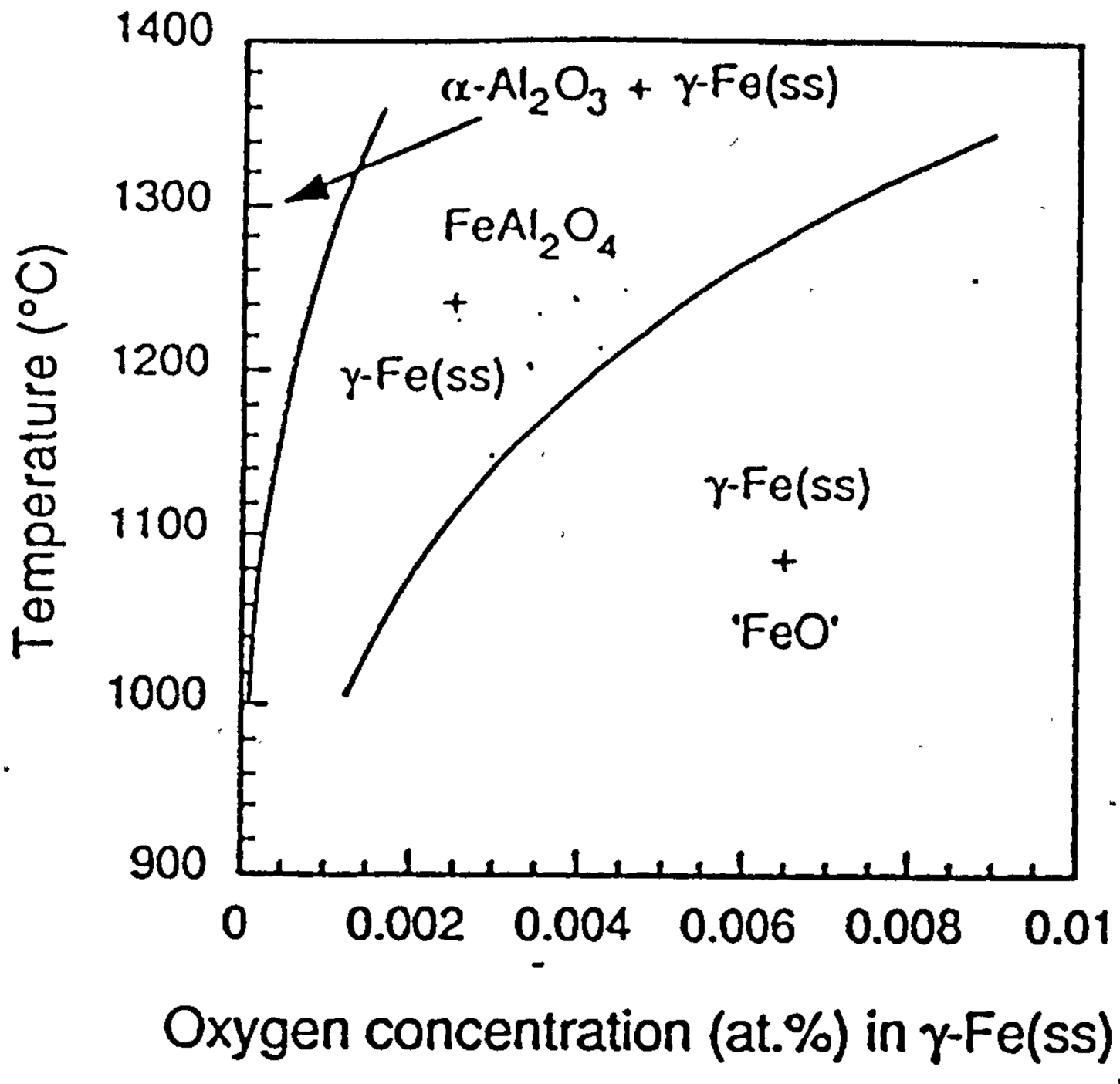

Figure 2.2 Oxygen concentration in γ-Fe as a function of temperature for the equilibrium {γ-Fe(ss), $FeAl_2O_4$, Al_2O_3} (after Trumble, 1992).

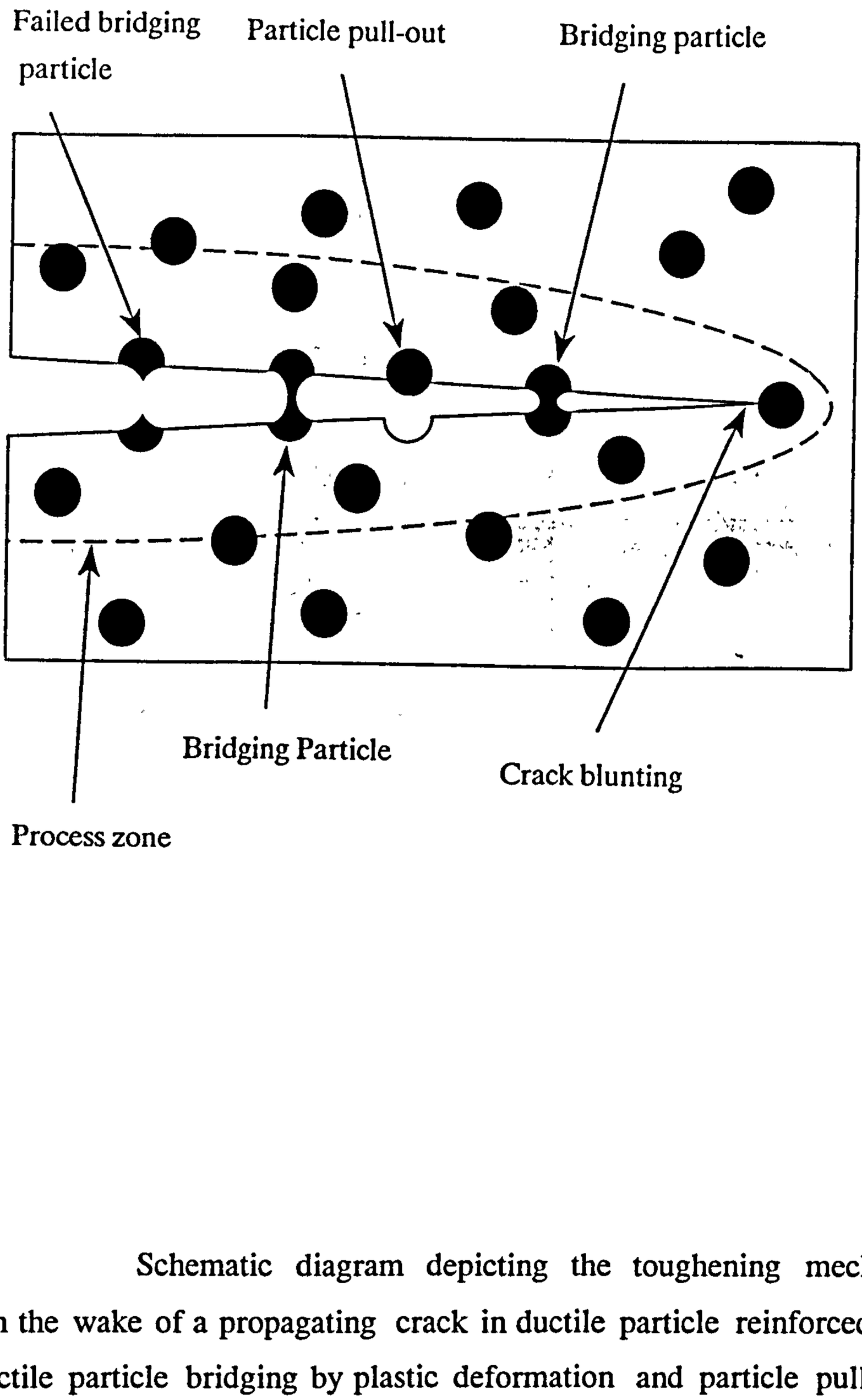

Figure 2.3 Schematic diagram depicting the toughening mechanisms occurring in the wake of a propagating crack in ductile particle reinforced CMC, showing ductile particle bridging by plastic deformation and particle pull-out.

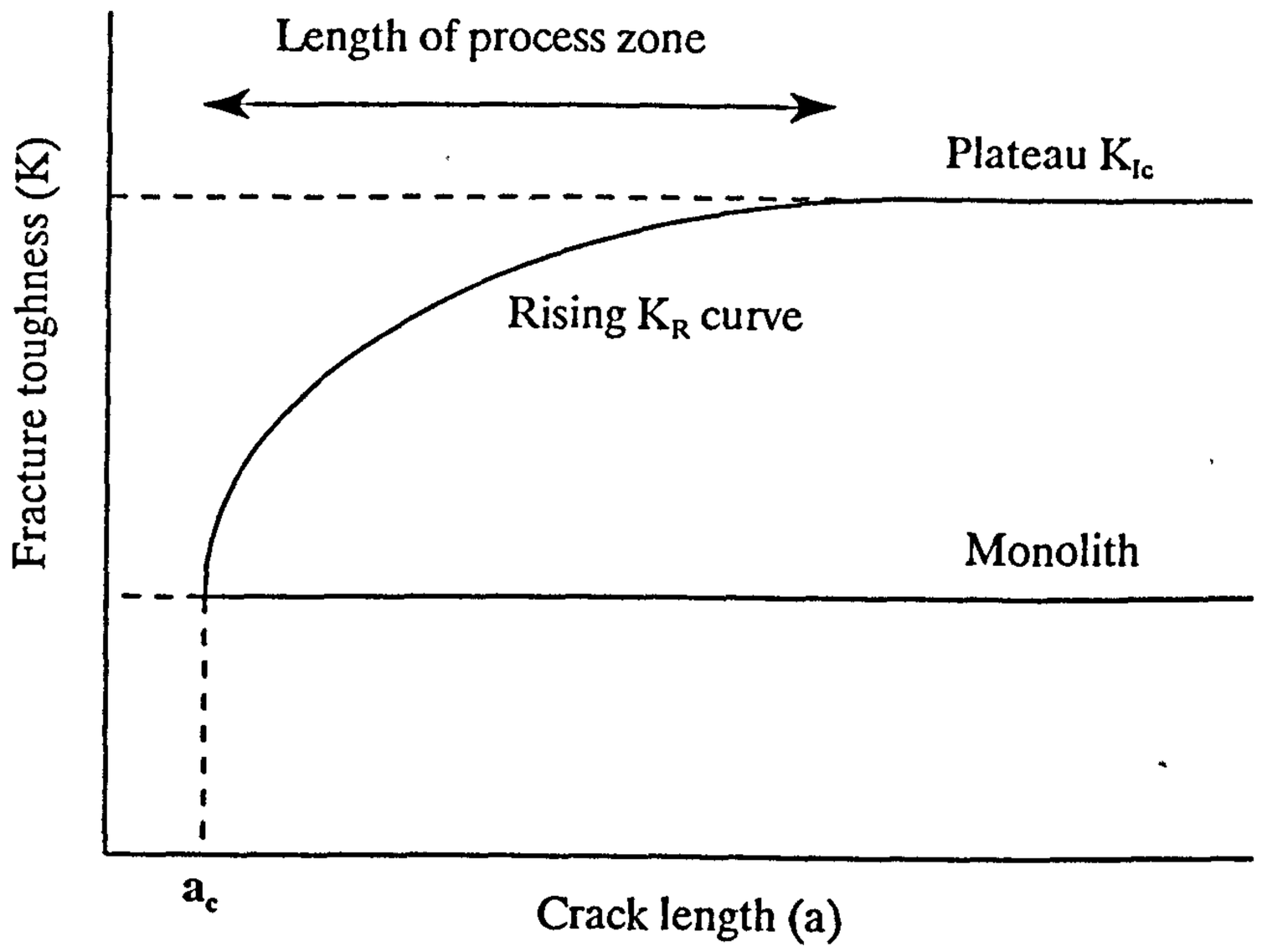

Figure 2.4 Schematic diagram showing the increase in fracture toughness with increasing crack length, known as K_R curve behaviour, where a_c is the critical flaw size.

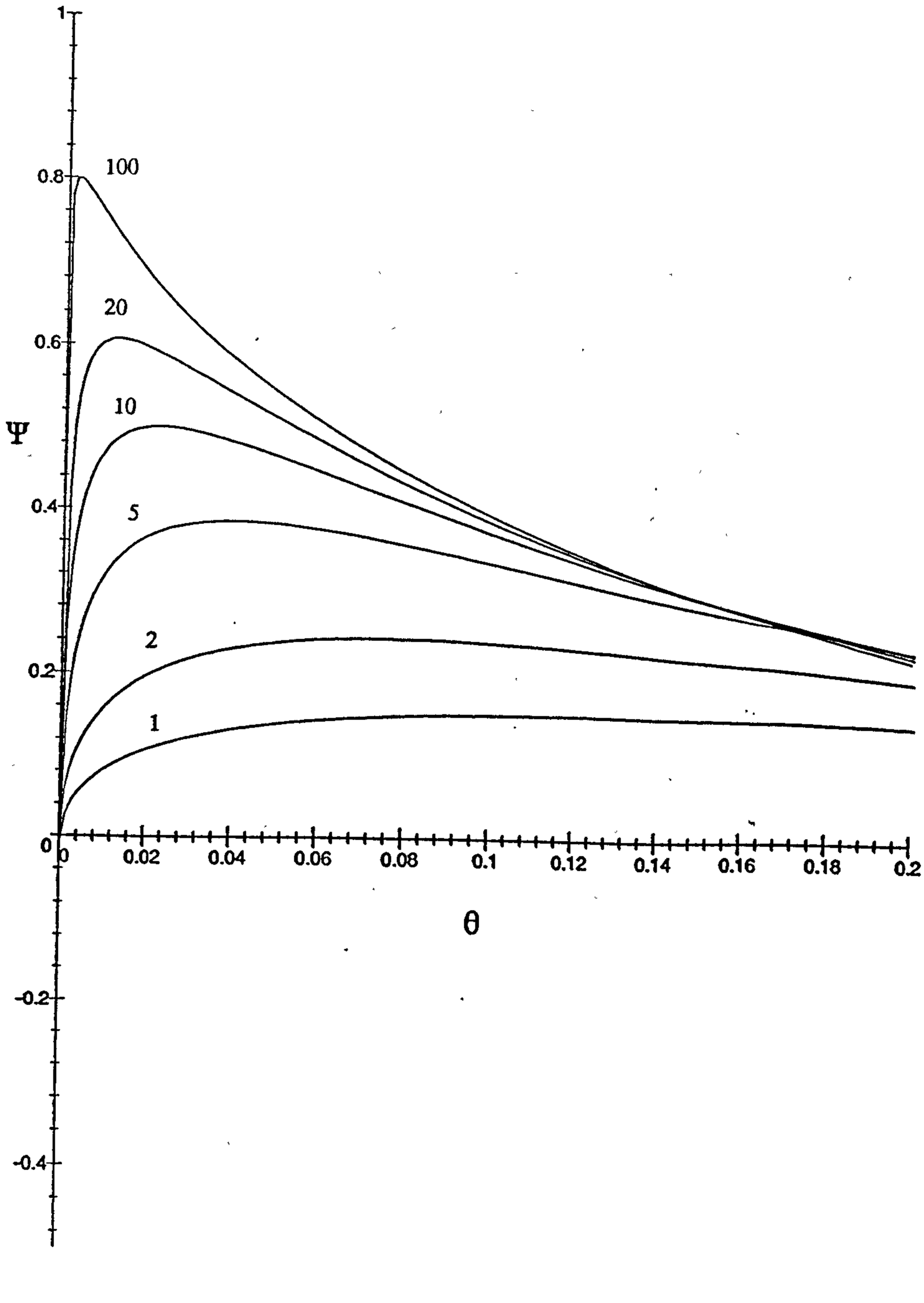

Figure 2.5 Variation of stress reduction factor with non-dimensional time for several values of Biot modulus.

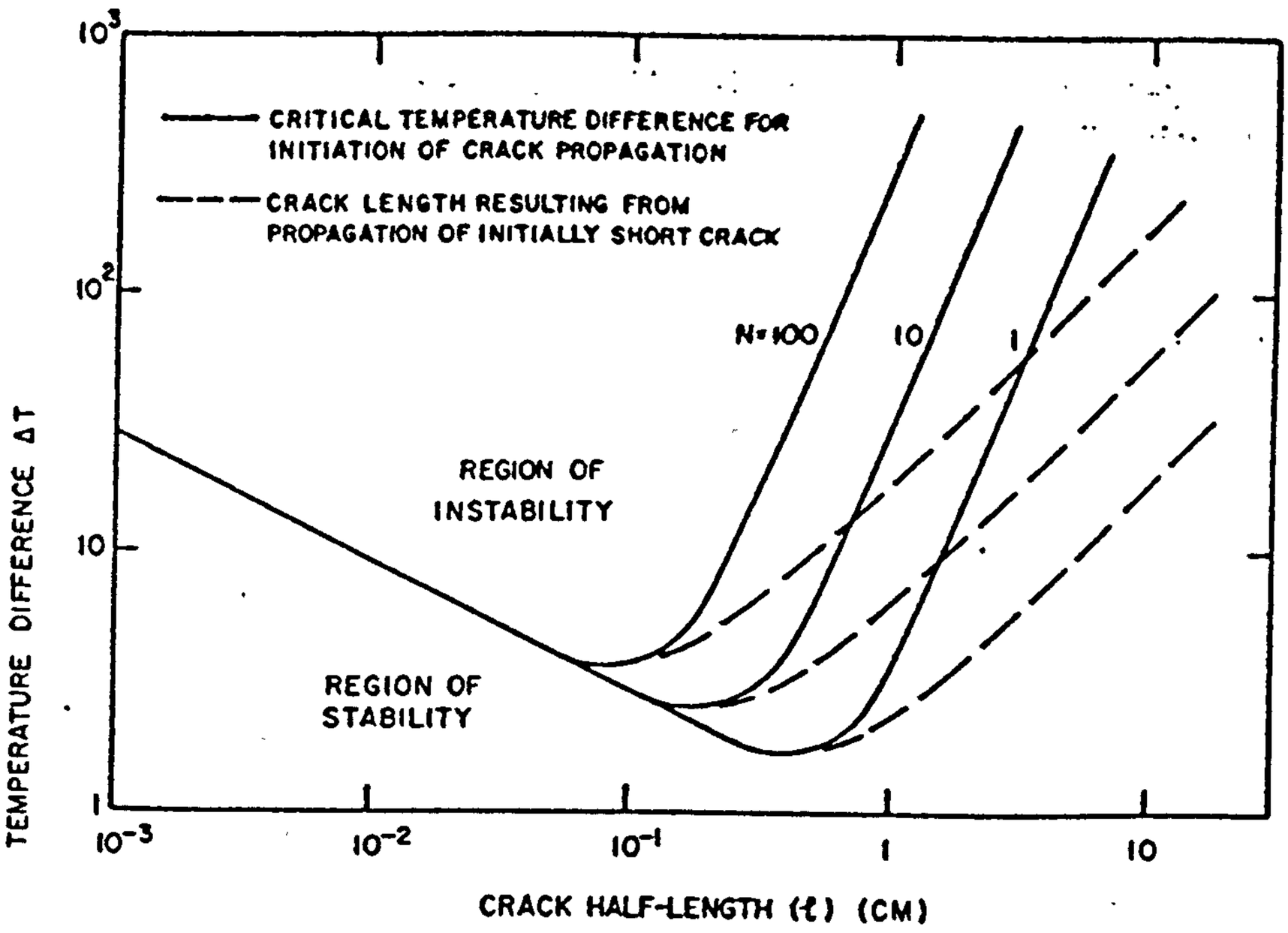

Figure 2.6 Temperature differential required to initiate crack propagation as a function of crack length and crack density N (Poisson's ratio=0.25) (after Hasselman, 1969).

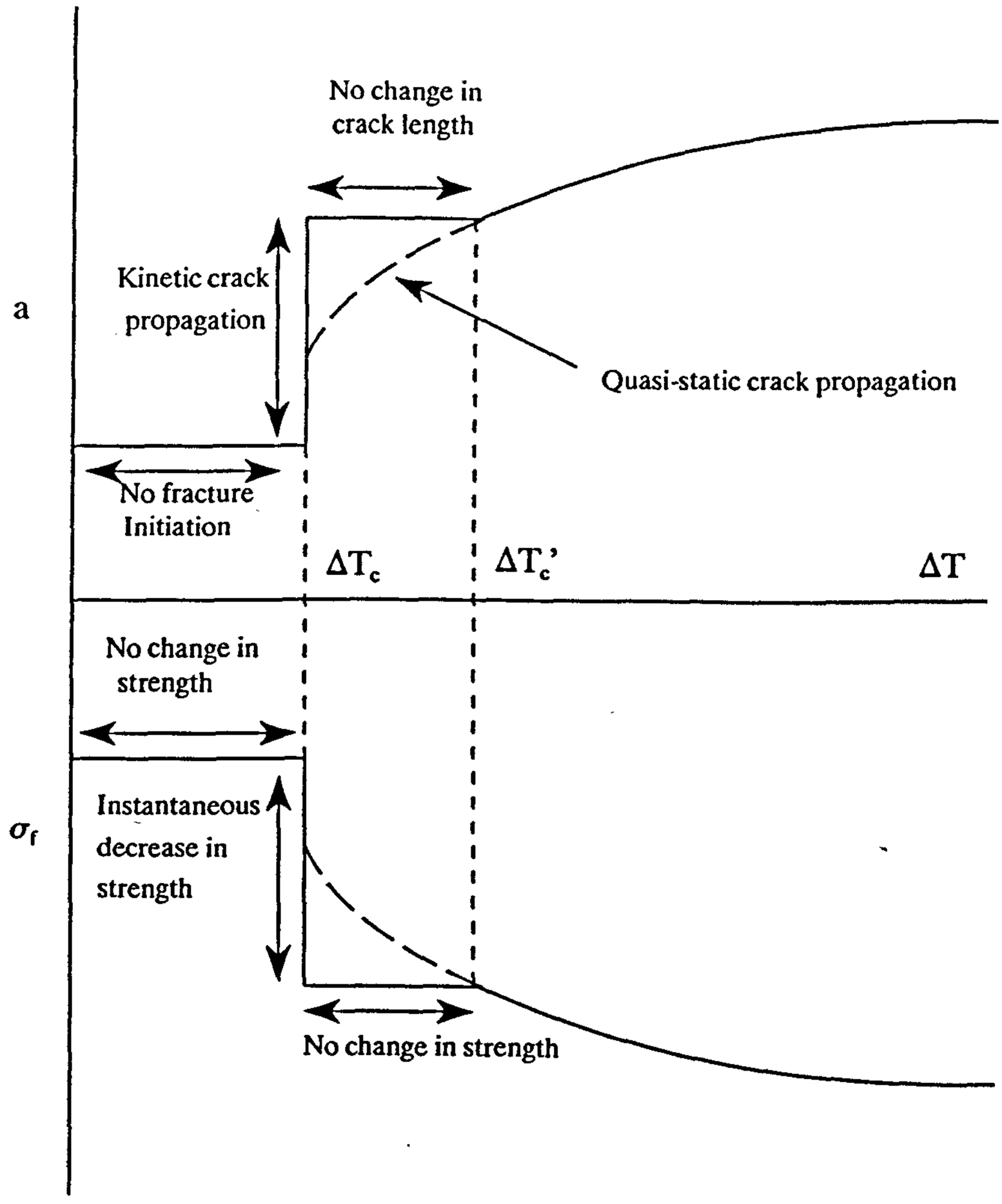

Figure 2.7 Crack length and strength as a function of thermal history (after Hasselman, 1969).

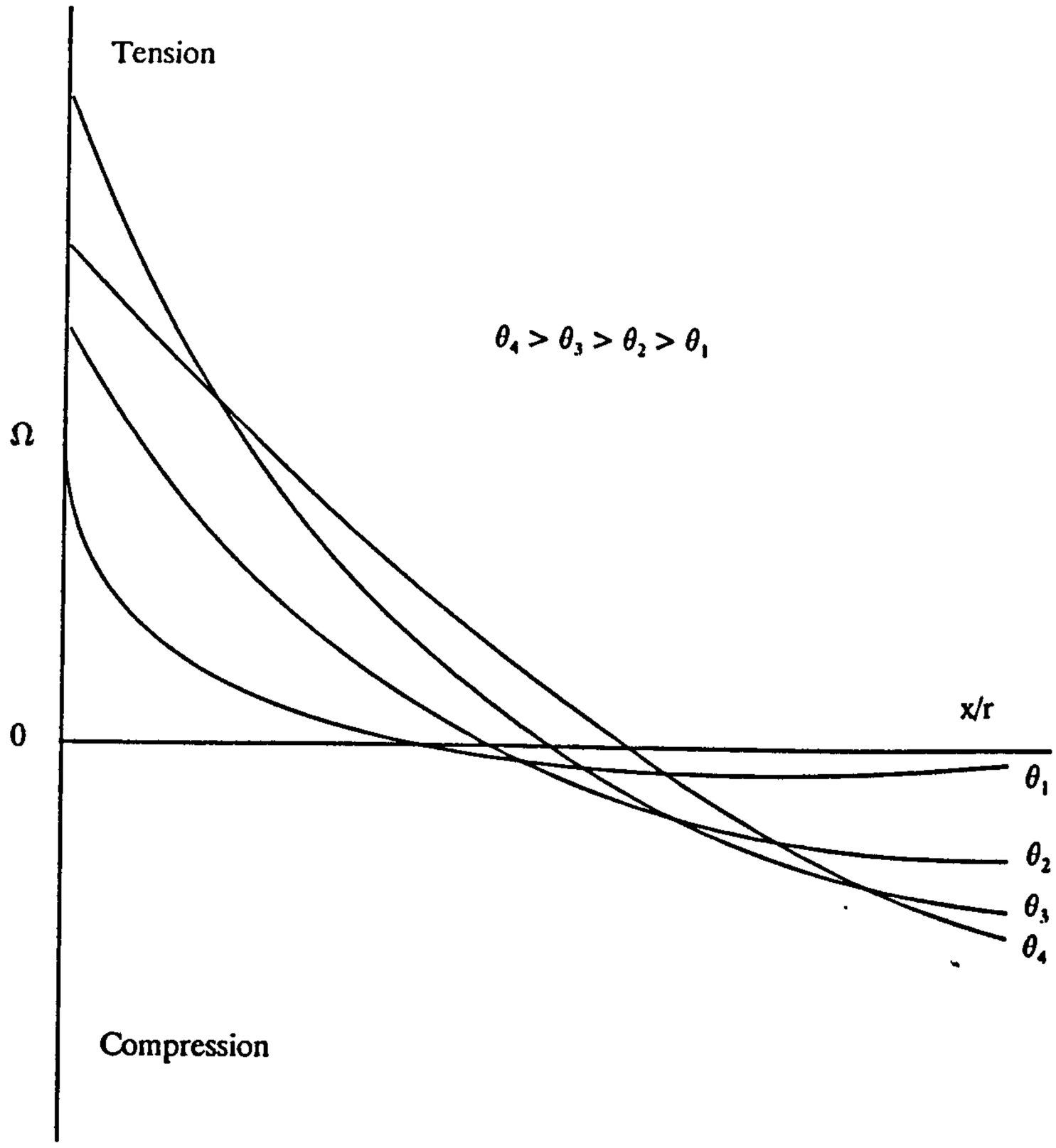

Figure 2.8 Schematic representation of stress gradient, i.e. normalised stress (Ω), versus normalised position (x/r), in a transient thermal field under convective heat-transfer conditions for various values of normalised time (θ).

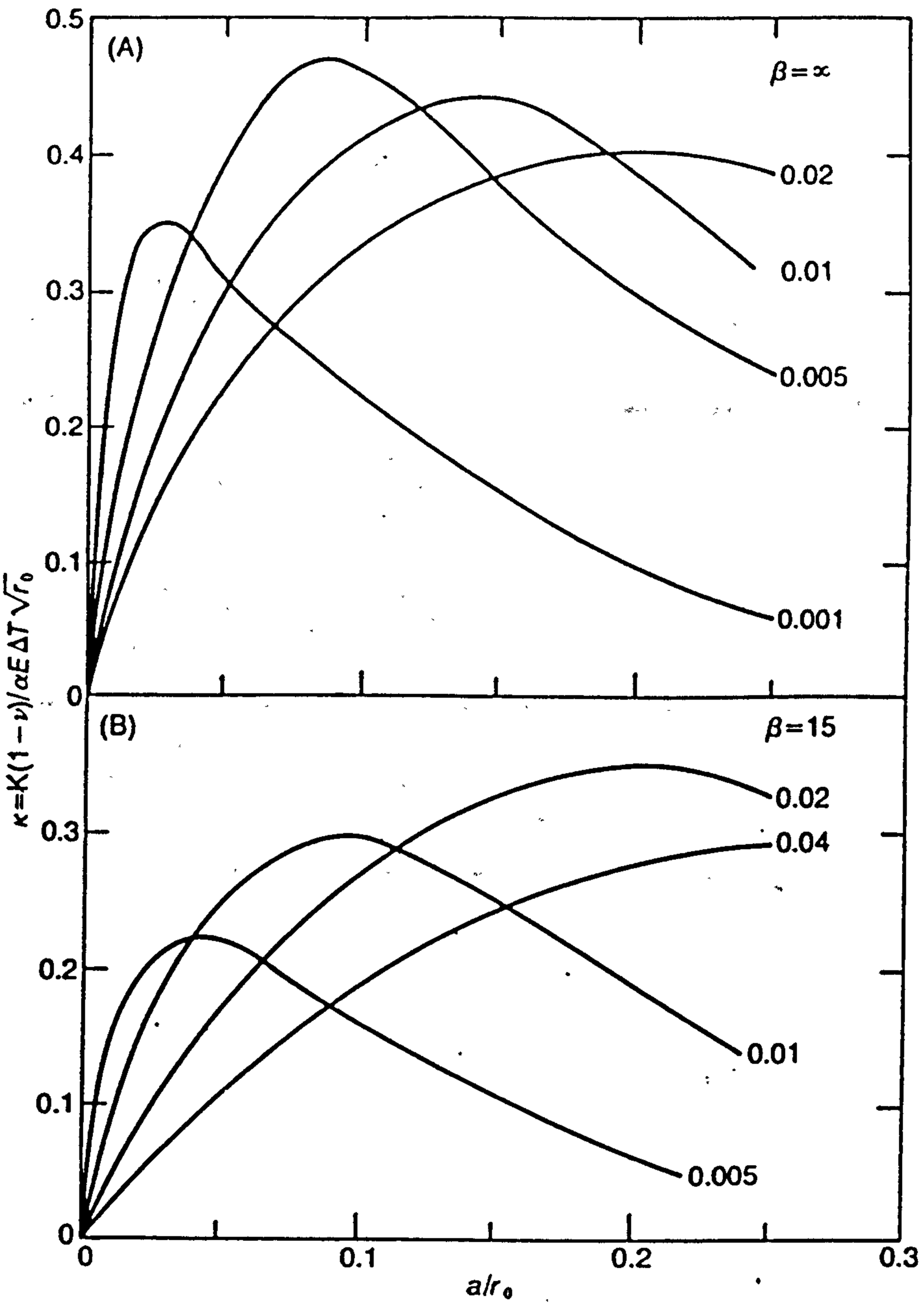

Figure 2.9 Crack length dependence of normalised thermal shock generated stress intensity factor, κ, for several values of normalised time, θ (indicated opposite each curve), for two values of Biot moduli, as determined analytically in the "short" crack extreme (after Evans & Charles, 1977).

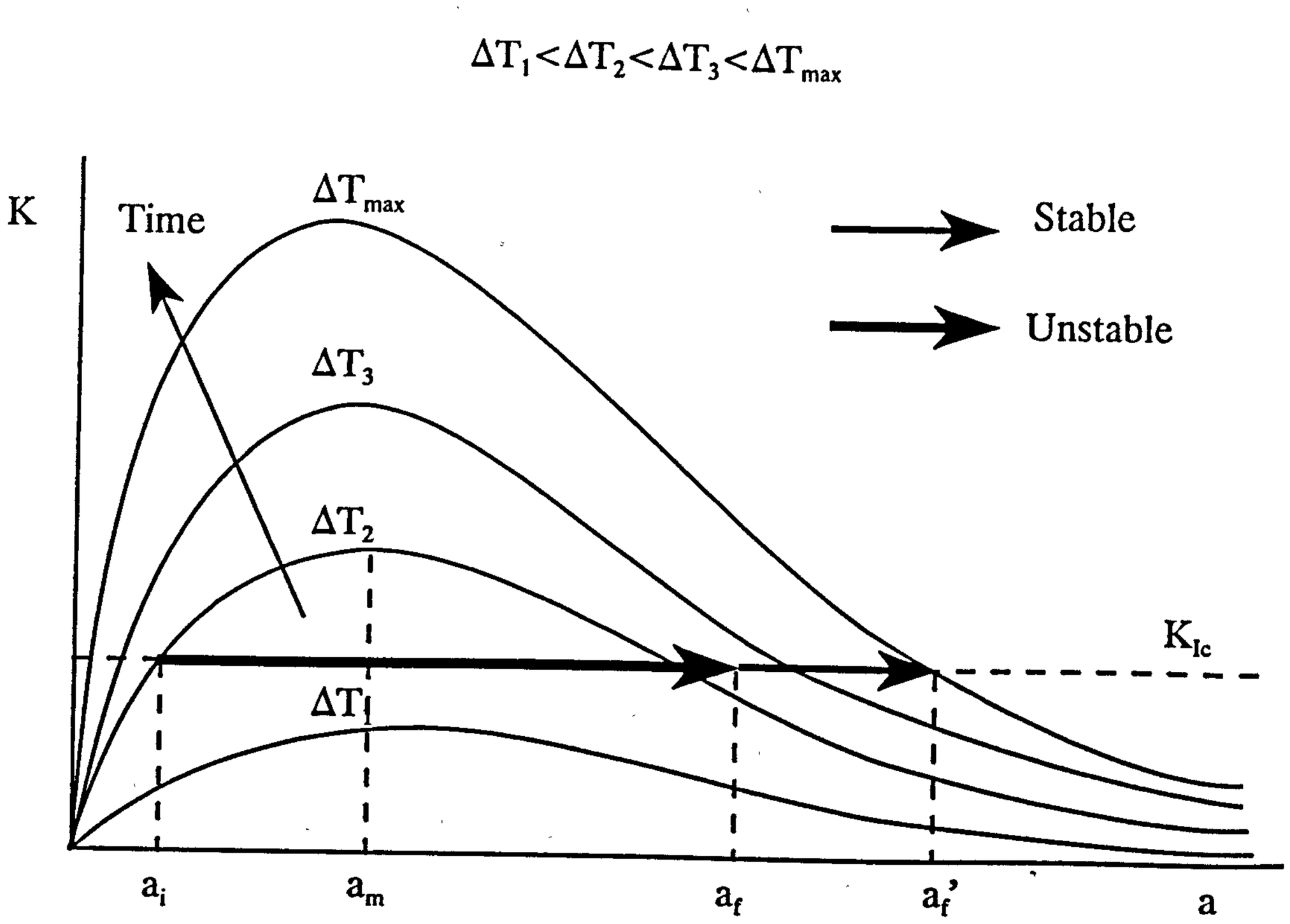

Figure 2.10 Schematic diagram showing dependence of the thermal shock generated stress intensity factor on the critical temperature differential and time. Shown is the initiation of unstable crack propagation for a crack with length a_i, the crack arrest at a_f, and the following stable crack growth from a_f to a_f' at increased temperature differentials (after Schneider, 1991).

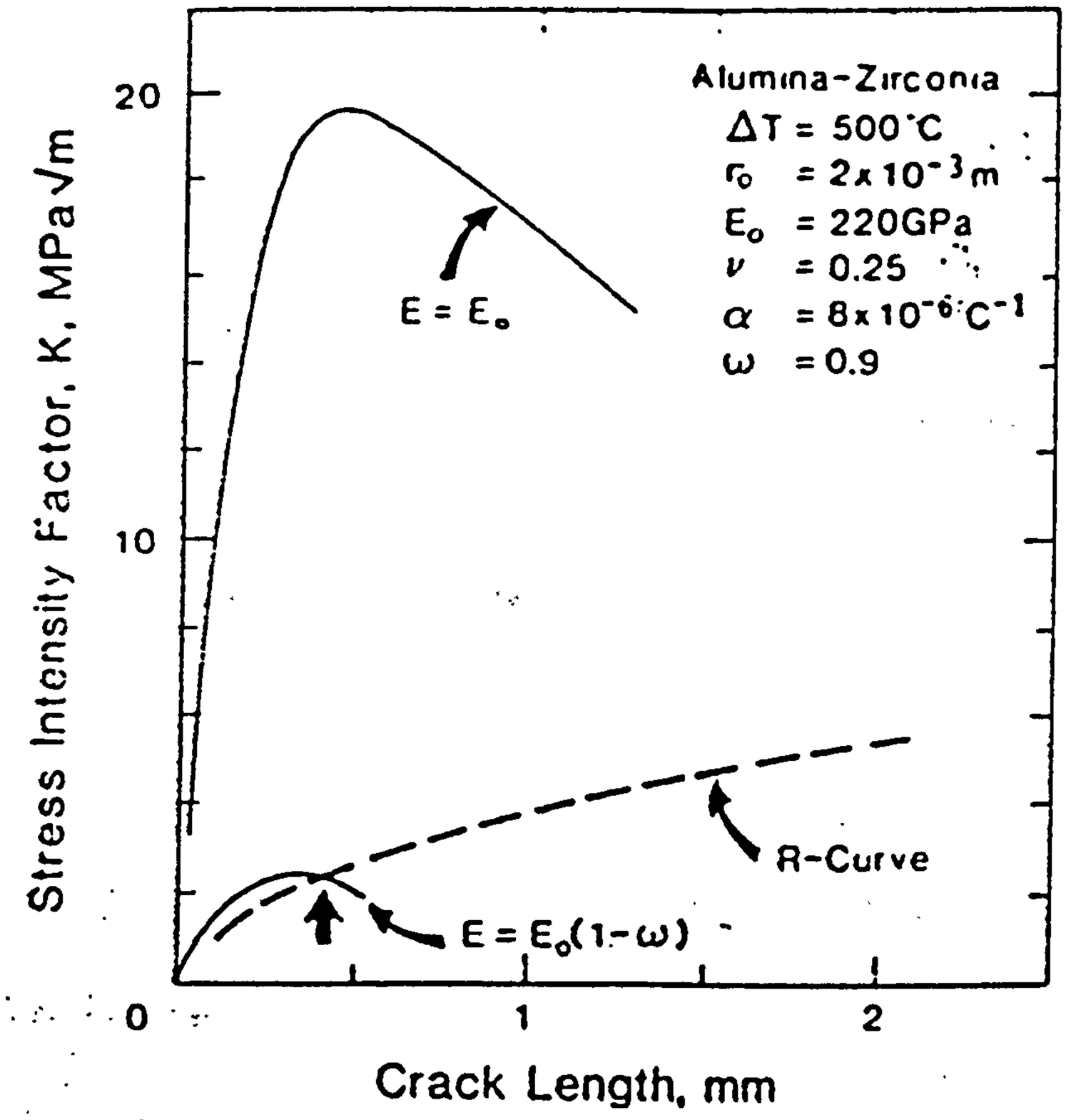

Figure 2.11 Calculated values of the thermal shock generated stress intensity factor for 2 mm radius bars of alumina-zirconia subjected to a temperature differential of 500 °C. The two curves are calculated on the basis of the original Young's modulus and the reduced Young's modulus (reduced according to $E_0(1-\omega)$), for a Biot modulus of 15. The K_R curve of this material is also superimposed on the plots (after Swain, 1990).

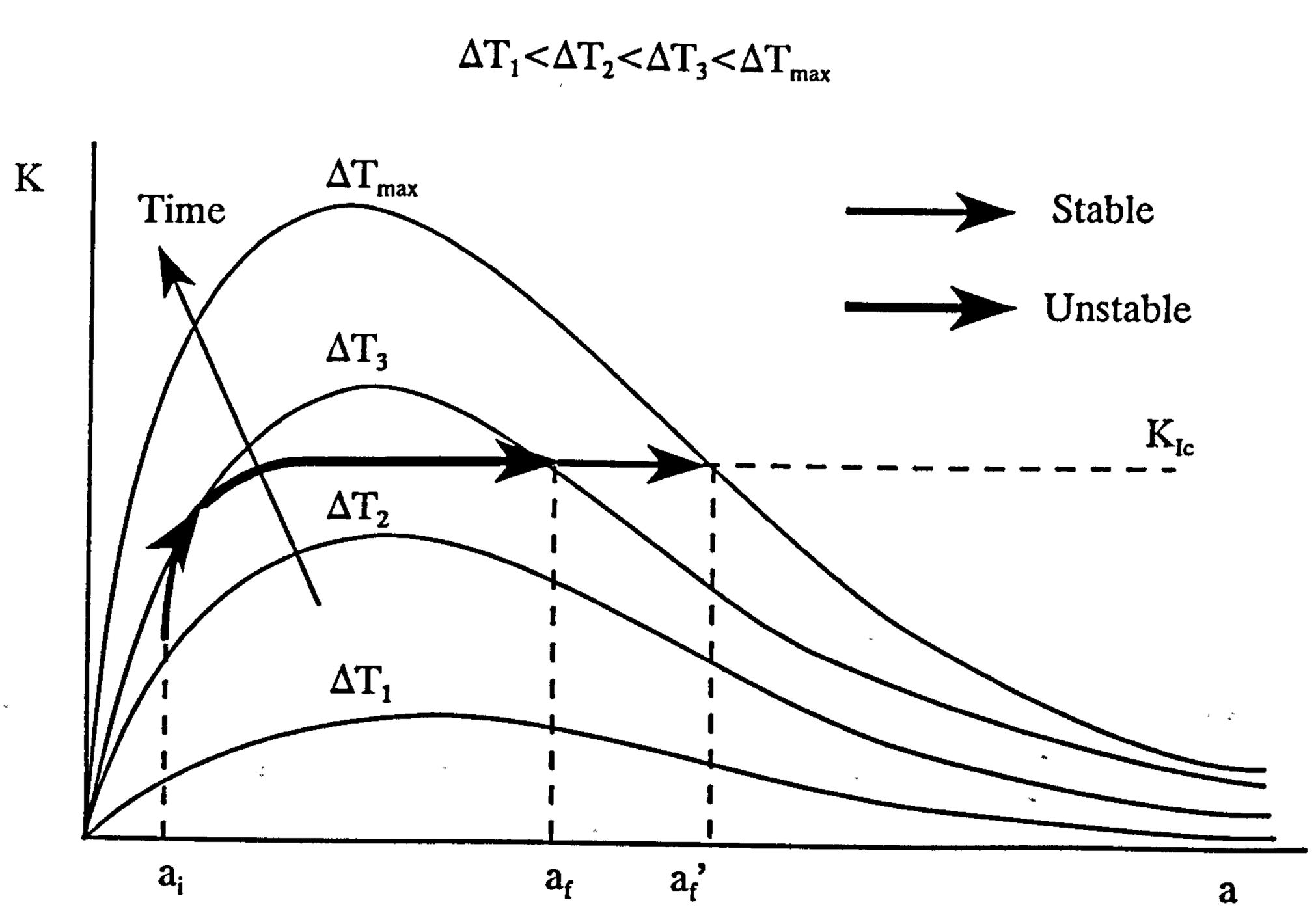

Figure 2.12 Schematic plot representing conditions of stable and unstable crack growth for material showing K_R curve behaviour (after Pompe, 1993).

CHAPTER THREE

MATERIALS AND EXPERIMENTAL TECHNIQUES

3.1 INTRODUCTION

This chapter begins with an introduction to the starting materials used in the present study, and presents a detailed account of the composite processing methods employed. This is followed by explanations of the various techniques and equipment used throughout the work, including material characterisation, mechanical testing and thermal shock studies. Relevant literature concerning the experimental aspects of the work is included.

3.2 FABRICATION OF MATERIALS

3.2.1 Introduction

The composite material of interest is an alumina matrix reinforced with 20 volume % discrete iron particles. Two different matrix alumina powders were used, depending on the proposed method of processing. Throughout the study, composite A refers to the powder blend produced using alumina powder A; similarly composite B refers to the powder blend produced using alumina powder B. Details of the composition and production of each blend are given in the following section.

3.2.2 Raw Materials

Alumina powder "A", used to produce hot pressed composites, was AKP-30 α-Al_2O_3 supplied by Sumitomo Chemical Co. Ltd., Tokyo, Japan. The particle size was specified as being in the region of 0.4 μm, and the purity > 99.99 %. Alumina powder "B", used to produce all sintered composites, was 995/234 α-Al_2O_3 supplied by Morgan Matroc Ltd., Rugby, England, and contained approximately 3 % of a polymeric binder (consisting of 1 part acrylic and 1 part polyethyleneglycol). The iron powder used was common to all composites produced, having a specified particle size range of 6-9 μm and purity of > 99.99 %, supplied by H. C. Starck, Dusseldorf, Germany. Figure 3.1 is a series of photomicrographs showing the morphology of the raw alumina and iron powders. Monolithic alumina (hot pressed AKP-30) was used for comparative purposes throughout the study, and a commercial zirconia toughened alumina (supplied by Morgan Matroc Ltd.) was also used as a comparative material regarding the evaluation of thermal shock behaviour.

3.2.3 Powder Preparation

The two distinct powder blends were produced in an identical manner. Correct proportions of each powder were weighed to give a blend containing 20 volume % iron (taking the densities of pure iron and high purity alumina to be 7860 kg m^{-3} and 3980 kg m^{-3} respectively (Nuffield Book of Data, 1984)). Isopropanol was added to the powder mixture to produce a slurry. Several alumina pebbles were also added in order to facilitate the mixing process and to break up large agglomerates which may have been present in the alumina powder. The slurry was then milled for 6 hours in a polypropylene bottle. Following the milling process, the slurry was placed into a low temperature oven (50 °C) for 12 hours to evaporate the alcohol, leaving a dry, composite powder blend. This method has been shown to produce a homogeneous, discrete particle distribution with this particular composite system (Trusty, 1994).

3.2.4 Powder Densification

3.2.4.1 Introduction

Two methods of powder densification were utilised to produce a dense CMC. The first of these was hot pressing in a graphite die. The second method involved cold uniaxial pressing to produce a "green" powder compact, which was subsequently sintered in a high temperature tube furnace. The need to be able to produce the composite via the conventional sintering route rather than hot pressing arises from the limitations imposed by the hot pressing technique, i.e. the high cost per billet, the restrictions on the complexity of shape produced and the excessive amount of cutting and grinding required to produce samples of the required geometry. Monolithic alumina was processed in an identical way to the hot pressed Al_2O_3-Fe composite.

3.2.4.2 Hot Pressing

Powder blend A was used throughout the study for the production of all hot pressed Al_2O_3-Fe composites. The cylindrical graphite die (diameter 25 mm) was loaded with approximately 30 g of powder and inserted into a Clark Scientific Hot Press (illustrated schematically in figure 3.2). The graphite resistance heating element was heated at a ramp rate of 20 °C min^{-1} to a temperature of 1400 °C and held for 30 minutes, whilst a uniaxial pressure of 30 MPa was applied. The pressure was then released, and the apparatus allowed to cool naturally to room temperature. The graphite die and heating element were protected from oxidation throughout the procedure by continually flushing the apparatus with argon gas. Following hot pressing, it was usually necessary to extract the billet from the die using an Instron 1195 tensile testing machine with a cross-head speed of 1 mm min^{-1}.

3.2.4.3 Greenbody Production and Conventional Sintering

Greenbodies were produced prior to sintering by cold uniaxial pressing in a hardened steel die. Boron nitride powder was lightly brushed over the internal surfaces of the die to aid greenbody extraction, prevent sticking and reduce friction (consequently minimising the development of internal residual stress). Batches of 10-15 g of composite powder blend (both A and B) were pressed at pressures ranging from 5 to 60 MPa using an Instron 1195 tensile testing machine with a cross-head speed of 1 mm min^{-1} to produce a greenbody of approximate dimensions 10 mm in height and 25 mm in diameter. A further batch of powder compacts was pressed at 93 MPa (courtesy of Dr. J. Kirk, Morgan Matroc Ltd.) Fracture surfaces of greenbodies pressed at various pressures were observed using a Cambridge Instruments 250 scanning electron microscope (SEM) in order to determine the extent of any plastic deformation of the iron particles. The surfaces were sputter coated with gold prior to observation to prevent charging in the microscope.

Thermal gravimetric analysis (TGA) was conducted on a small sample of a blend B greenbody to determine the temperature range over which the polymeric binder was likely to be removed during sintering. The instrument used was a Marlin Scientific thermal analyser, which allowed any change in mass of the sample with increasing temperature to be monitored accurately. A sample of approximately 30-50 mg was analysed, and the atmosphere in the heating chamber was air.

The melting point of pure iron is 1535 °C (Nuffield Book of Data, 1984). Sintering schedules were therefore carried out using maximum temperatures ranging from 1550 °C to 1800 °C, so that the metallic phase was likely to be molten at the sintering temperature, thereby increasing the wettability of the alumina matrix by the iron. Initial sintering trials were conducted in a tube furnace. The alumina tube was continually flushed with high purity argon

throughout the sintering process to prevent oxidation of the iron phase. Greenbodies were placed either on a graphite plate or in a graphite powder bed. Heating ramp rates were set at either 5 °C min^{-1} or 20 °C min^{-1}, and the dwell time at maximum temperature set at either 1 or 2 hours. After holding at the maximum temperature for the required duration, the furnace was allowed to cool naturally to room temperature, after which the sample was then removed.

3.3 CHARACTERISATION OF MATERIALS

3.3.1 Introduction

Characterisation of the composites and monolithic alumina produced was performed using conventional techniques for density measurement, microstructural examination, fractography and thermal gravimetric analysis.

3.3.2 Density Measurement

The densities of the composites produced throughout the study were measured using Archimedes' immersion principle. Prior to measurement, both sintered and hot pressed specimens were lightly abraded to remove any outer skin (for hot pressed specimens) or globules of iron (caused by sweating during the sintering process) which may have formed, which were unlikely to be representative of the bulk composite. The samples were firstly weighed in air, then in water. The following equation was used to calculate the density

$$\rho_s = \frac{W_s \rho_w}{\Delta W_s} \qquad 3.1$$

where ρ_s is the density of the specimen, W_s is the weight of the specimen, ρ_w is the density of water and ΔW_s is the difference in weight of the specimen before and after immersion in water. The density calculated may also be expressed as a percentage of the theoretical density of the composite (% T.D.). The

theoretical density was calculated using a simple rule of mixtures, taking the densities of alumina and iron to be 3970 kg m^{-3} and 7860 kg m^{-3} respectively (Nuffield Book of Data, 1984), and found to be 4748 kg m^{-3}. The density of the hot pressed monolithic Al_2O_3 was also measured and compared with that reported in the literature.

As the above method could not be used for porous materials, an approximate density value for the green powder compacts was calculated by dividing the mass of the compact by the volume (estimated using a micrometer).

3.3.3 Microstructural Examination of Polished Surfaces

Composite samples were sectioned using a small bench-top cut-off machine equipped with a diamond cut-off wheel. The samples were then mounted in bakelite. Grinding and polishing was performed using an automatic polishing machine (Struers, Planopol-2). The samples were ground successively using diamond impregnated wheels (Struers) of 125 μm, 40 μm, 20 μm and 10 μm, using water as the lubricant, and cleaning the sample in an ultrasonic bath between each stage. Polishing was carried out using fine cloths (Struers, DUR) with an alcohol based lubricant and 6 μm, 3 μm and 1 μm diamond sprays.

A Hitachi S3200N scanning electron microscope was used for microstructural examination, typically in secondary electron mode with a 5-10 keV electron beam. Prior to examination, polished samples were sputter coated with gold (Edwards S150B coating unit with a current of 20 mA and potential of 1 kV for 1.5-2 minutes) to prevent charging within the microscope. The average second phase particle size and area fraction were estimated using a linear approximation technique.

3.3.4 Microstructural Examination of Fracture Surfaces

The surfaces of fractured flexure samples (including hot pressed and sintered composites and monolithic alumina) were examined using a Hitachi S3200N scanning electron microscope in secondary electron mode with a 5-10 keV electron beam. Fracture surfaces were sputter coated with gold prior to examination (as for microstructural analysis). The average grain size of the alumina matrix was measured using the linear intercept method where the average grain size D is given by

$$D = 1.56 \frac{C_1}{MN_1} \qquad 3.2$$

where C_l is the total length of the test line, N_i is the number of intercepts, M is the magnification and the proportionality constant 1.56 is a correction factor for random slices through a model system (Wurst & Nelson, 1972).

3.4 MECHANICAL PROPERTIES

3.4.1 Introduction

The major mechanical properties of interest in this study were fracture toughness and strength. The following section outlines the techniques employed in determining each of these properties, along with a short discussion concerning the applicability of a Weibull type analysis for flexure test data of ductile particle reinforced CMCs. Hot pressed monolithic alumina was also studied enabling a comparison of results.

3.4.2 Fracture Toughness

3.4.2.1 Background

Several established techniques for measuring the fracture toughness of a ceramic material exist, including indentation, controlled flaw flexure testing, single edge notched beam (SENB), double torsion (DT) and double cantilever beam (DCB) methods.

One of the most common of these is the indentation method, which has the advantages of being quick and easy to perform, and requiring only a relatively small sample of material. The test involves indenting a polished surface with a "sharp" indenter, which, providing the load exceeds a critical value, leaves a residual impression on the surface. If the load is sufficiently high, one or more crack systems may result. Depending on the nature of the cracking, the fracture toughness of the material may be calculated from the length of the surface cracks initiated at the apices of the indentation and the diagonals of the indentation. Evans & Charles (1976) studied the relationship between the indentation fracture behaviour of various ceramics and the fracture toughness values obtained using the double torsion technique, and consequently developed an empirical fracture toughness equation. Since then, many authors have developed equations relating fracture toughness to crack length and indentation size; most of these may be found in a review by Ponton & Rawlings (1989). The existence of so many equations in the literature highlights the fact that the fracture toughness results obtained using this method are equation dependent. Also, the equations quoted are valid only for materials showing the development of specific crack systems on indenting, i.e. the median-radial system. Sun (1993) attempted to determine the K_R curve behaviour of an Al_2O_3-Ni composite material using the indentation method, and concluded that the technique was unsuitable for such composites. He showed that, for a composite with a microstructure consisting of discrete nickel particles in an alumina matrix, an over-estimation of fracture toughness is

obtained due to regions of deformation and unusual cracking being prominent around an indentation impression. Energy dissipated in this manner is not accounted for in the existing indentation toughness equations. Similarly, Trusty (1994) studied the indentation behaviour of an Al_2O_3-20 volume % Fe composite, and also concluded that the use of the established indentation method as a measurement of fracture toughness was not suitable for this particular material. Indentation fracture toughness values obtained were shown to be gross overestimates due to the fact that the classic median-radial crack system did not develop.

Controlled flaw flexure testing is another technique for determining the fracture toughness of ceramics. This has been successfully employed for several monolithic and composite ceramic materials (e.g. Govila, 1980, Bhattacharya & Petrovic, 1992, Braun *et al.* 1992, Li & Watanabe, 1995, Xu *et al.* 1995, Kovar & Readey, 1996, Stech & Rödel, 1996). The method typically involves indenting a highly polished surface, followed by four point flexure testing of the sample. The surface crack length resulting from the indentation and also the fracture strength of the sample (typically in four point bending) are measured. This procedure may then be repeated for a range of indentation loads enabling the generation of a plot of fracture strength versus flaw size, and the fracture toughness may then be calculated using equations proposed by Govila (1980). However, due to the development of non-ideal cracking in alumina-iron composites as explained above, it is questionable as to whether this method would yield accurate fracture toughness data for the composite system of interest.

The single edge notched beam (SENB) method, used by Zhang *et al.* 1995, Fett *et al.* 1995, Hsueh & Becher, 1995, Nishida & Hanaki, 1995, requires the machining of a notch on the tensile face of a flexure specimen using a thin diamond impregnated cut-off wheel. During subsequent flexure testing, the notch tip acts as a pre-crack, giving rise to stable crack growth which may be monitored in-situ. Additionally, machining of the notch can be followed by sharpening of the

notch tip using a sharp razor blade in conjunction with a diamond paste. This technique was successfully utilised by Nishida & Hanaki to determine the K_R curve behaviour of a toughened monolithic silicon nitride. The SENB technique was attempted in the present study. A diamond cut-off wheel was used to machine a notch in one long face of a three point flexure test specimen, of approximate dimensions 40 mm x 5 mm x 4 mm. The sample was then subjected to a standard flexure test (details are given in Appendix 1), with the notched edge being placed under a tensile stress. Crack propagation was monitored using a travelling microscope.

A more reliable technique for determining the fracture toughness of ceramic materials is the well established double torsion (DT) technique (Hodkinson & Nadeau, 1975, Govila, 1980, Sun *et al.* 1991, Shercliff *et al.* 1994, Trusty, 1994). The important feature of this test is that the stress intensity factor is independent of crack length, therefore a crack should propagate stably under constant load. A typical DT specimen consists of a plate which is partially cracked along the centre to form two beams. The beams are then loaded in torsion via four point bending at the cracked ends. At a sufficiently high load, a crack will propagate from the crack tip. The mathematical analysis for this technique assumes that all displacements are related to the torsional displacements of the two beams, neglecting the possibility of either shear strains in the individual beams or flexure of the uncracked portion of the specimen. Advantages of this technique over other fracture toughness testing techniques include the fact that the compliance of a DT specimen is linearly proportional to the crack length, i.e. the critical forces required for crack propagation are independent of crack length. Also, the sample has a relatively simple geometry and small size, even for long crack lengths, hence only relatively low forces are required. One of the problems associated with this technique, however, is that the propagating crack may deviate from the machined groove (Hodkinson & Nadeau, 1975), thereby introducing error into the measurement of crack length. Additionally, it has been shown that the crack front profile is not straight through the specimen thickness, but extends

further along the side of the plate under tension, forming a curved crack front. This is thought to be the cause of disagreement between workers concerning final K_{Ic} values. The DT technique is, however, regarded as being a suitable method for measuring the fracture toughness and K_R curve behaviour of a ductile particle reinforced CMC (Aghajanian *et al.* 1989, Sun *et al.* 1991, Trusty, 1994), although some difficulty in avoiding unstable crack propagation has been reported (Shercliff *et al.* 1994).

3.4.2.2 Double Cantilever Beam Method

The double cantilever beam (DCB) method has been proposed as a valid way of measuring the fracture toughness and K_R curve behaviour of several ductile reinforced CMCs (Trusty, 1994, Sun, 1993). This method was chosen as the most suitable for evaluation of the $K_R$curve behaviour of the Al_2O_3-Fe composite in this study since it has been successfully used in a previous study concerning the toughening mechanisms operating in this specific system (Trusty, 1994). The specimen configuration is shown in figure 3.3. The approximate DCB test specimen dimensions were l_p=18 mm, $2h_p$=9 mm, t_p=2 mm, t_w=1 mm. A groove approximately 0.5 mm deep and 2 mm wide was machined along the longitudinal centre line of each side of the specimen. This was intended to act as a crack guide during testing, preventing deviation of the propagating crack from the centre line. The groove was polished to aid crack observation using successive grades of SiC paper, followed by 20 μm and 3 μm diamond pastes. A notch approximately 3-4 mm long was machined at one end of the sample to facilitate crack initiation at the start of the DCB test. Brass end tags were then attached using a two part epoxy adhesive (D.P. 490, supplied by 3M, Reading). The finished specimens were then sputter coated with gold. The specimens were tested using a straining stage situated within the chamber of a Cambridge Instruments S100 SEM, allowing in-situ monitoring of crack growth and crack/particle interactions. The loading rate used for each test was 0.01 mm min^{-1}. A photograph of the straining stage and testing set up within the SEM is shown

in figure 3.4.

The fracture resistance of the specimen was calculated using the following modified DCB formula (after Trusty, 1994)

$$K_{Ic} = \sqrt{\frac{P^2 b_c^2}{t_w I'} \cdot \left\{1 + 0.7 \frac{h_p}{b_c}\right\}} \qquad 3.3$$

where b_c is the distance from the crack tip to the loading axis, I' is the second moment of area of the cross-section shown in figure 3.3, and P is the load. It has been shown by Trusty (1994), in a study of the compliance of monolithic alumina subjected to DCB testing, that any bending moment developed in the brass end tags has a negligible effect on the data obtained from subsequent testing of CMC materials.

3.4.3 Flexure Strength

3.4.3.1 Flexure Testing

The strength of engineering ceramics is generally determined using the flexure strength test method, due to the difficulty and high cost involved in conducting direct tensile tests on such materials. However, a review of the flexure test by Quinn & Morrell (1991) has expressed concern regarding the reproducibility of flexure data, as it is typically specific to a particular batch of material, and properties are very much dependent on the precise fabrication and preparation procedures. A beam specimen of rectangular cross section is placed in either a three or four point loading fixture (shown schematically in figure 3.5), and loaded to failure. The four point configuration is often preferred as a greater volume of material is placed under maximum stress, although the simplicity of the three point configuration is often favoured for research and development purposes. Several standard test methods exist. Although the standards have many

similarities, several differences in sample preparation and testing apparatus must be taken into consideration.

Throughout this project, three point flexure testing of all materials has been performed adhering to the ASTM standard guidelines as closely as possible; a summary of conditions is given in Appendix 1. Fractured samples were retained for fracture surface examination.

3.4.3.2 Statistical Analysis

Fracture of monolithic engineering ceramics occurs by the catastrophic propagation of a critical defect when subjected to a sufficiently high stress. Strength limiting defects in this class of ceramic materials are generally in the order of 5-200 μm in size, and are typically either microstructural features introduced during processing (for example, porosity, foreign bodies, abnormally large grains) or the result of machining/preparation damage. The magnitude of the strength limiting defect will vary from sample to sample, consequently a significant scatter in the strengths of nominally identical specimens is to be expected. The most common method of characterising the spread of strength values makes use of statistical methods proposed by Weibull. The probability of survival of the specimen, P_s, is given as

$$P_s = \exp -\left\{\frac{\sigma - \sigma_u}{\sigma_0}\right\}^m \qquad 3.4$$

where σ is the point stress, σ_u is the stress below which fracture is assumed to have zero probability (usually taken as zero), σ_0 is the characteristic strength and m is the Weibull modulus which characterises the width of the distribution. For the purpose of plotting data, it is typical to take natural logarithms of equation 3.4 twice and rearrange, thus

$$\ln\ln(1/P_s) = m\ln(\sigma - \sigma_u) - m\ln\sigma_0 \qquad 3.5$$

A plot of lnln $(1/P_s)$ as ordinate versus ln σ as abscissa typically results in a straight line of gradient m.

The Weibull approach has become accepted as a standard method of expressing the statistical nature of the variation in strength of ceramic materials. However, concern has been expressed as to the validity of such an analysis to ductile particle reinforced CMCs. Shercliff *et al.* (1994) suggested that a Weibull analysis would be inappropriate for a composite consisting of an alumina matrix reinforced with chopped nickel wires, as the metal inclusions act as nucleation sites for flaws, and the wires are considerably larger than the matrix grain size. Hence the distribution of flaws is related to the size and aspect ratio of the wires, which will not fit the assumed Weibull distribution. Additionally, it was concluded that the introduction of surface flaws during specimen preparation would dominate the failure process.

The statistical variation in strength for flexure test results in this study was analysed and presented using the Weibull approach, however, since it appears to be accepted by the majority of workers studying toughened ceramics (e.g. Kendall *et al.* 1986, Li & Watanabe, 1995). Duan & Mai (1995) also used a Weibull type analysis to study the effect of K_R curve behaviour on the strength and reliability of toughened ceramic materials, although a modified analysis was proposed which was able to predict the non-linearity observed in the ln ln $(1/P_s)$ versus ln σ strength distribution curve.

3.5 THERMAL SHOCK BEHAVIOUR

3.5.1 Introduction

The following section concentrates on the experimental procedures and analytical techniques involved in the evaluation of the thermal shock behaviour of the Al_2O_3-Fe composite materials. Firstly, a short review of thermal shock experimental procedures is given, followed by an account of the techniques utilised during this study.

3.5.2 Thermal Shock Experiments

Several experimental techniques for inducing controlled thermal stresses in ceramics have been developed. A quench experiment is the most common and established technique for determining the thermal shock behaviour of a ceramic. A typical quench experiment involves slowly heating a specimen in a furnace, allowing sufficient time for thermal equilibrium to be reached. A sudden decrease in temperature can then be imposed by transferring the sample to the quenching medium. Various quenching media have been used, including boiling water, oil and liquid metal alloy, although the most widely used is water at room temperature. The residual strength of the samples is then measured (typically by flexure testing), and correlated to the temperature differential experienced. This method is an effective way of comparing the thermal shock resistance of various materials according to their critical temperature differential, ΔT_c. Other quench media such as oil produce higher values of ΔT_c due to the reduction in the rate of heat transfer.

Results obtained using this method generally correlate well with the ranking order predicted by the thermal shock resistance parameters, as water produces severe thermal shocks with high values of Biot modulus. However, actual values of ΔT_c calculated using R parameters generally differ from those obtained experimentally,

as the actual thermal stresses a specimen experiences during a quench test are different from those assumed in an ideal condition. Therefore the calculation of thermal stresses arising from quenching is difficult. According to Pompe *et al.* (1993), this fact alone renders quenching experiments suitable only for comparing the thermal shock behaviour of materials. The heat transfer coefficient, h, is often a difficult parameter to assess, especially when water is used as the quench medium, since h is affected by different boiling phenomena. Figure 3.6 shows that h is not a constant for a certain quenching medium; it varies with sample temperature and is also influenced by the surface finish of the specimen. Singh *et al.* (1981) identified three boiling regimes. In region (a), heat is transferred by convection. In the nucleate boiling region (b), the heat transfer coefficient increases rapidly with increasing temperature as bubbles nucleate and grow on the heated surface. As the bubbles leave the surface, cooler liquid rushes to fill the voids. Region (c) occurs at a higher temperature differentials, and results in a decreasing value of h, as a poorly conducting vapour film surrounds the entire specimen surface. Thompson & Rawlings (1988) showed that if room temperature water is replaced with boiling water as the quenching medium, the conditions at the specimen surface are changed from nucleate boiling to film formation, resulting in a lower heat transfer coefficient.

The variation of heat transfer coefficient combined with the difficulty in quantifying the thermal stress fields produced during quenching has led to the development of new thermal shock tests, e.g. the disc irradiation method. This method appears to be growing in popularity, particularly for work involving quantitative thermal stress analysis. The following additional requirements are met by this method (Schneider, 1991):

i) Quantitative evaluation of the temperature and thermal stress field.

ii) Thermal shocks also possible at temperatures above 1000 °C.

iii) Short cycling periods to permit thermal cycling with more than 1000 cycles.

During the test, the centre of a ceramic disk is subjected to a fast heating rate by irradiation with halogen lamps (Schneider, 1991) or an electron beam in a vacuum (Pompe *et al.* 1993). The induced higher thermal expansion at the centre of the disk is constrained by the cooler outer rim, causing tensile hoop stresses at the edge and tangential and radial compressive stresses in the centre, as shown schematically in figure 3.7. If the thermal stresses generated are expected to be below the fracture strength of the material, a radial notch is cut into the edge of the disk to act as a stress amplifier. Crack propagation will occur when the critical stress intensity factor at the crack tip is exceeded. The thermal stresses and stress intensity factor may then be calculated. The failure time is measured by acoustic emission and the critical thermal shock generated stress intensity factor calculated.

Becher *et al.* (1979) studied the effect of specimen size on the critical temperature differential of various ceramics, using the quench method. It was found that the thermal shock resistance of ceramics is generally strongly influenced by the specimen size, and thus the Biot modulus, even under severe cooling and heating conditions. Critical specimen dimensions required for a transition to a ΔT_c that is independent of size will be a function of both h and k, and are estimated at approximately 3 mm for a glass-ceramic, > 5 mm for Si_3N_4, and apparently > 6 mm for Al_2O_3. The ΔT_c values for Al_2O_3 bars having a square cross-section and semi-dimensions of 0.75 and 1.5 mm were found to be 260 °C and 210 °C respectively, after conventional quenching into water at room temperature.

A further important point is that demonstrated by Davidge & Tappin (1967), regarding the effect of specimen size on the measurement of the retained flexural strength. It was found that there was a factor of 1.5 difference between the flexural strengths of large (1 cm^2, 10 cm span) and small (5 mm^2, 1 cm span) alumina bars. It was pointed out that such variations can be explained in terms of Weibull analyses, where the greater the volume of material under maximum stress, the higher the probability of encountering a larger flaw, hence the lower

the strength.

A recent modification to the traditional quench test was proposed by Andersson & Rowcliffe (1996). The indentation-quench method defines the critical temperature differential to induce significant thermal shock damage (ΔT_c) based on a criterion which involves a minimum amount of crack growth and a minimum fraction of growing cracks. Advantages of this technique over standard quench techniques include the fact that subsequent mechanical testing is not required, and a comparatively small number of test pieces are necessary. The test can also be performed on any geometry, hence it is applicable to actual components. The test has shown good agreement with the literature for three ceramic matrix composite materials (Al_2O_3-TiC-TiN, Al_2O_3-ZrO_2 and Al_2O_3-SiC).

3.5.3 Water Quenching

Test bars of material were prepared using the same procedure as for flexure test samples, as detailed in section 3.4.2.1. Small bars of approximately 20 mm x 4 mm x 2 mm were produced due to the size limitations imposed by the dimensions of the hot pressed composite billets. All other materials investigated were tested on a similar scale to enable a direct comparison of results. Each test bar was polished to a 1 μm finish on one large face using the procedure detailed in section 3.3.3. Samples were placed into a preheated furnace at the required temperature and allowed 15 minutes to reach thermal equilibrium. The samples were then removed from the furnace and immediately immersed in cold water (room temperature water, of approximately 20 °C). Finally, the samples were dried thoroughly. Generally, four similar samples were tested for each material at a given value of ΔT. Materials tested included both hot pressed and conventionally sintered Al_2O_3-Fe composites, hot pressed monolithic alumina and a commercial zirconia toughened alumina (ZTA).

3.5.4 Measurement of Retained Strength

The flexure strength following thermal shock treatment was determined using the three point flexure test as outlined in section 3.4.3.1. Following water quenching, no further surface preparation was carried out, i.e. any oxide which may have formed at higher temperatures was not removed. Care was taken to ensure that the sample face polished to a 3 μm finish became the face exposed to a tensile stress during flexure testing.

3.5.5 Damage Observation

Any cracking incurred during thermal shock treatment was studied using both SEM and confocal scanning laser microscope (CSLM) techniques.

A low magnification photo-montage of a shocked specimen could be constructed using the CSLM in fluorescence mode. Following the thermal shock treatment, the initially highly polished surfaces of specimens were very lightly abraded using a 0.5 μm cloth wheel (Struers) to remove any iron oxide which may have formed during exposure to high temperatures. The samples were then soaked in a water based fluorescent dye (Britemore 446, Castrol, supplied by Morgan Matroc Ltd.). Immersion in an ultrasonic bath accelerated dye penetration. Finally, the specimens were removed from the dye and any surplus dye wiped off. The dye fluoresces when exposed to ultraviolet light of wavelength ≈ 446 nm.

Additionally, smaller specimens (2.5 mm x 2.5 mm x 2.5 mm) were prepared as above to allow the examination of crack patterns resulting from thermal shock treatments covering a range of temperature differentials.

SEM was also used to examine damage caused by thermal shock. A Cambridge Instruments S250 SEM was used for secondary electron mode imaging of gold sputter coated samples, paying particular attention to fracture origins and

crack/ductile particle interactions.

3.5.6 High Temperature Behaviour in the Absence of Thermal Shock

Samples of both Al_2O_3-Fe composites were subjected to various heat treatments not involving any thermal shock. This was done in order to establish whether or not the heat treatment alone caused any cracking and subsequent strength degradation, or chemical change of the composite phases.

A set of similarly prepared and heat treated samples were left in an un-shocked condition. The flexure strength of these samples was measured in order to ensure that any strength degradation observed in the shocked samples was due only to the actual thermal shock and not wholly or partly due simply to exposure to an elevated temperature.

Thermal gravimetric analysis (TGA) was conducted using a Marlin Scientific thermal analyser instrument. A 30-50 mg sample of hot pressed Al_2O_3-Fe composite material was subjected to a heating cycle in an atmosphere of air involving a ramp rate of 50 °C min^{-1}, reaching a maximum temperature of 1200 °C. During this period, any changes in mass were recorded.

In addition to TGA, both hot pressed and conventionally sintered Al_2O_3-Fe composites were examined using SEM after polishing samples to a 1 μm surface finish, followed by heat treating the samples in a muffle furnace over a range of temperatures for various durations. The prepared surfaces were then gold coated and observed using SEM (secondary imaging).

3.6 CONCLUDING REMARKS

The chapter has presented accounts of the materials and experimental techniques used throughout the study. The raw materials used in the fabrication of the Al_2O_3-Fe composites have been introduced, along with materials used for comparative purposes. The processing methods utilised have been explained. Finally, characterisation techniques have been discussed.

a)

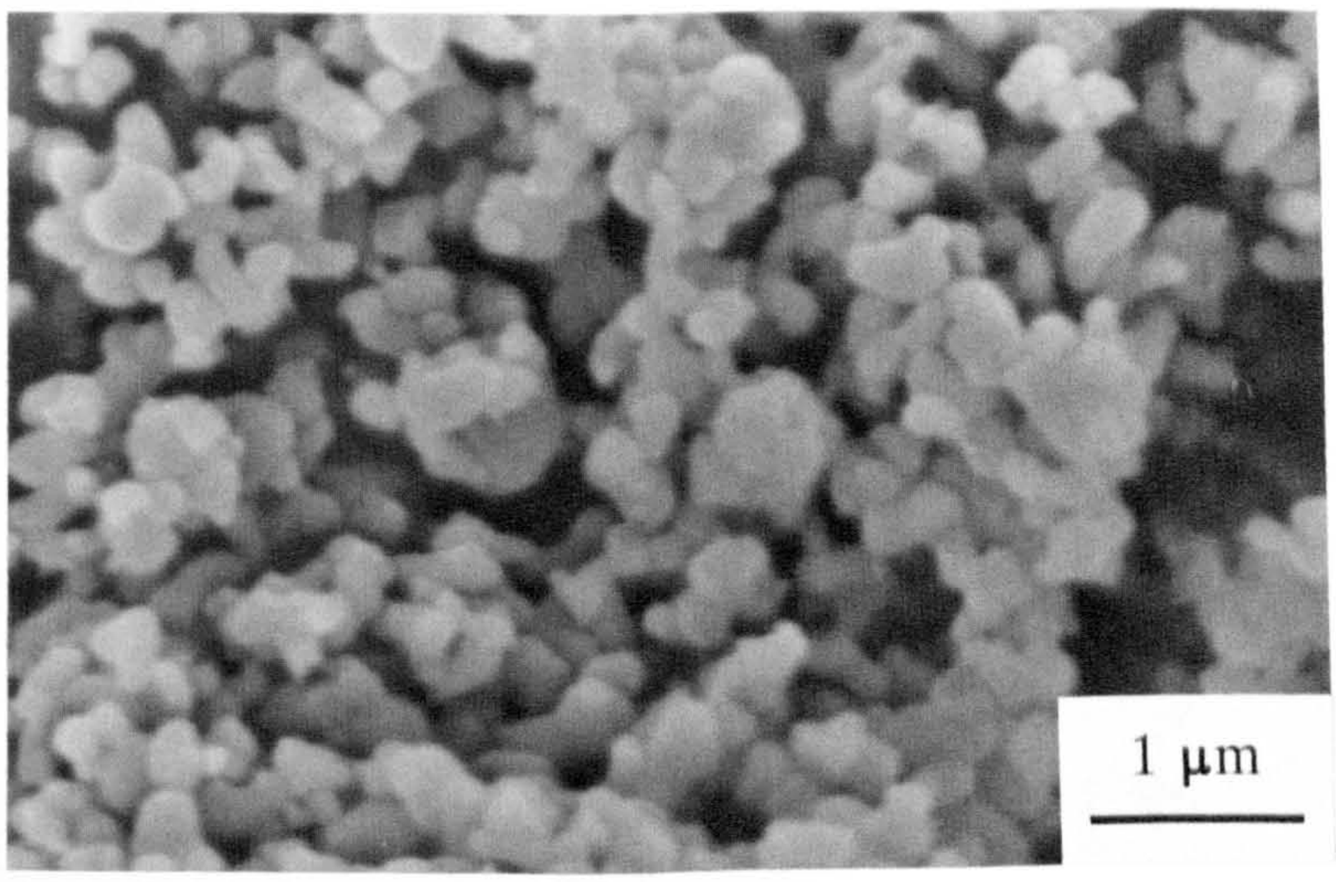

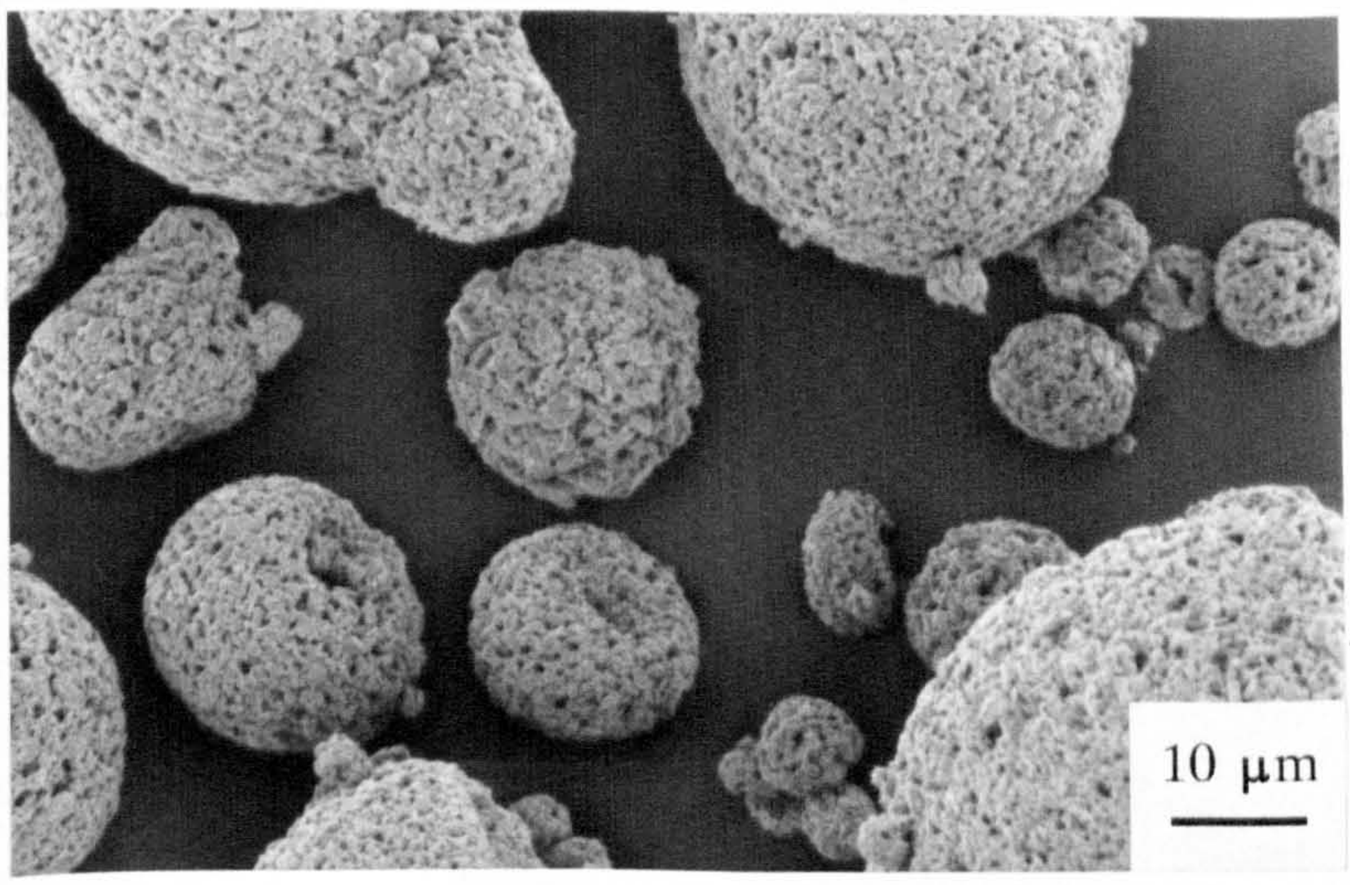

b)

c)

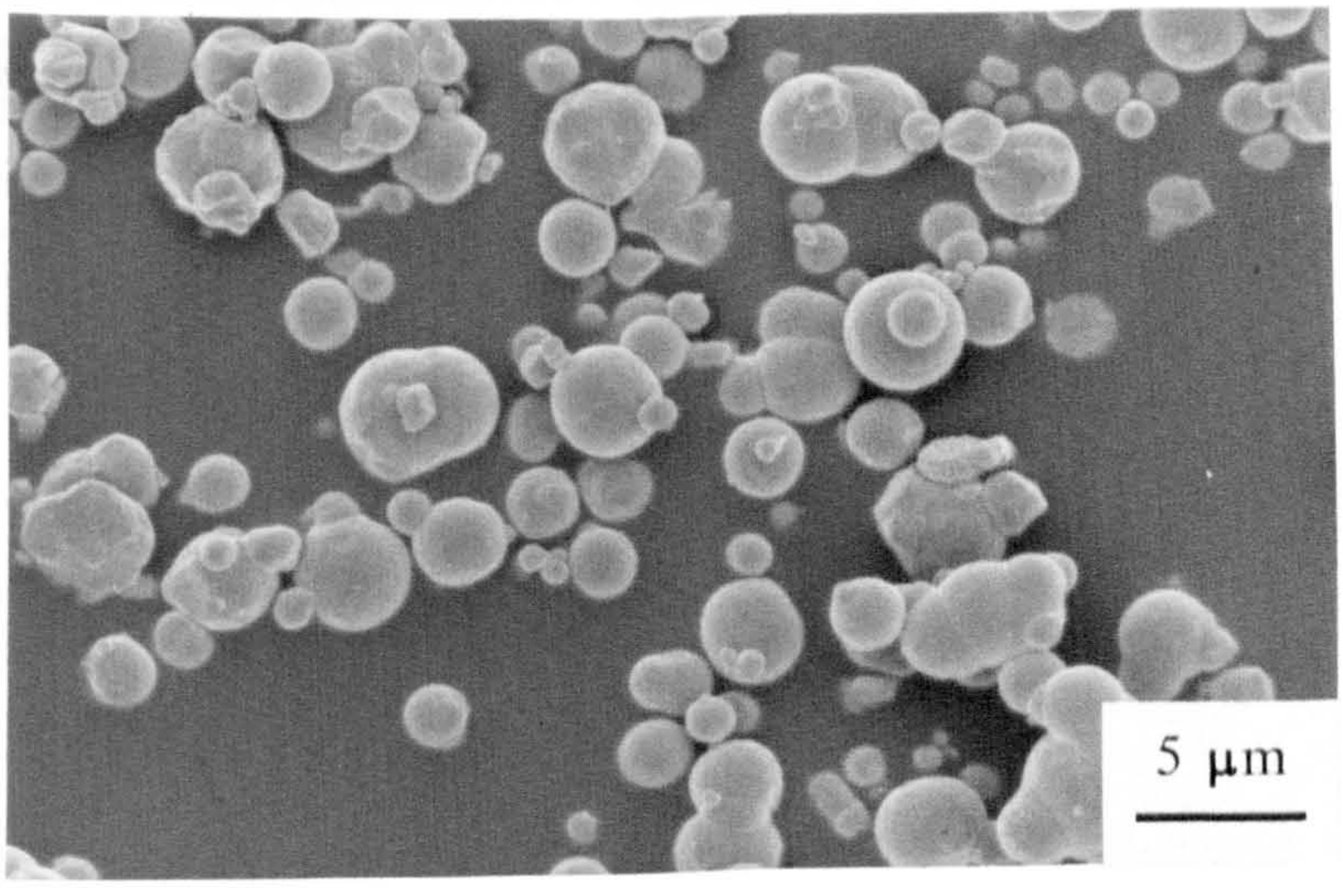

Figure 3.1 Photomicrographs (secondary electron images) of as received **a)** alumina powder 'A', **b)** alumina powder 'B' and **c)** iron powder.

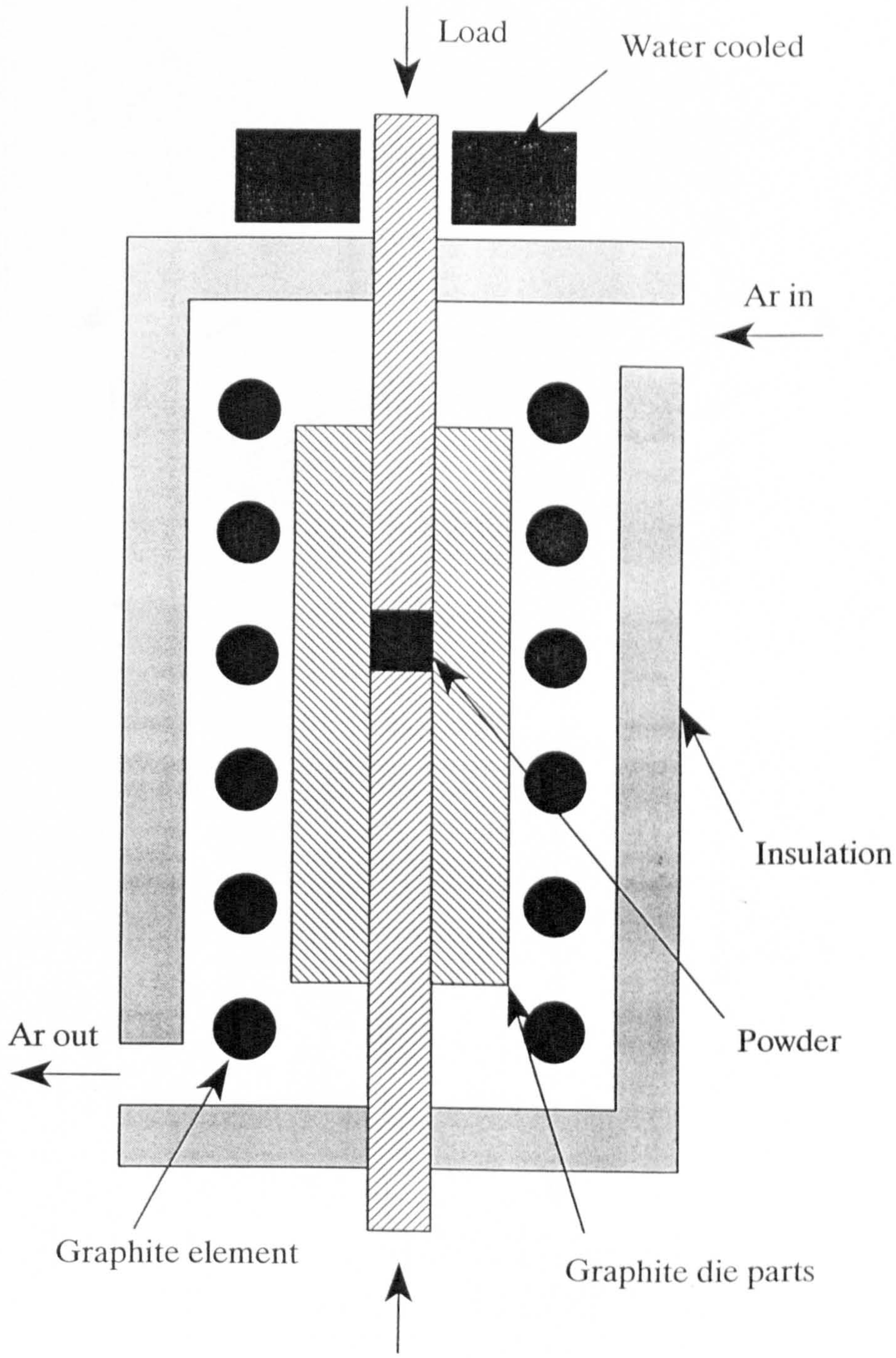

Figure 3.2 Schematic diagram showing hot press equipment and arrangement of graphite die parts.

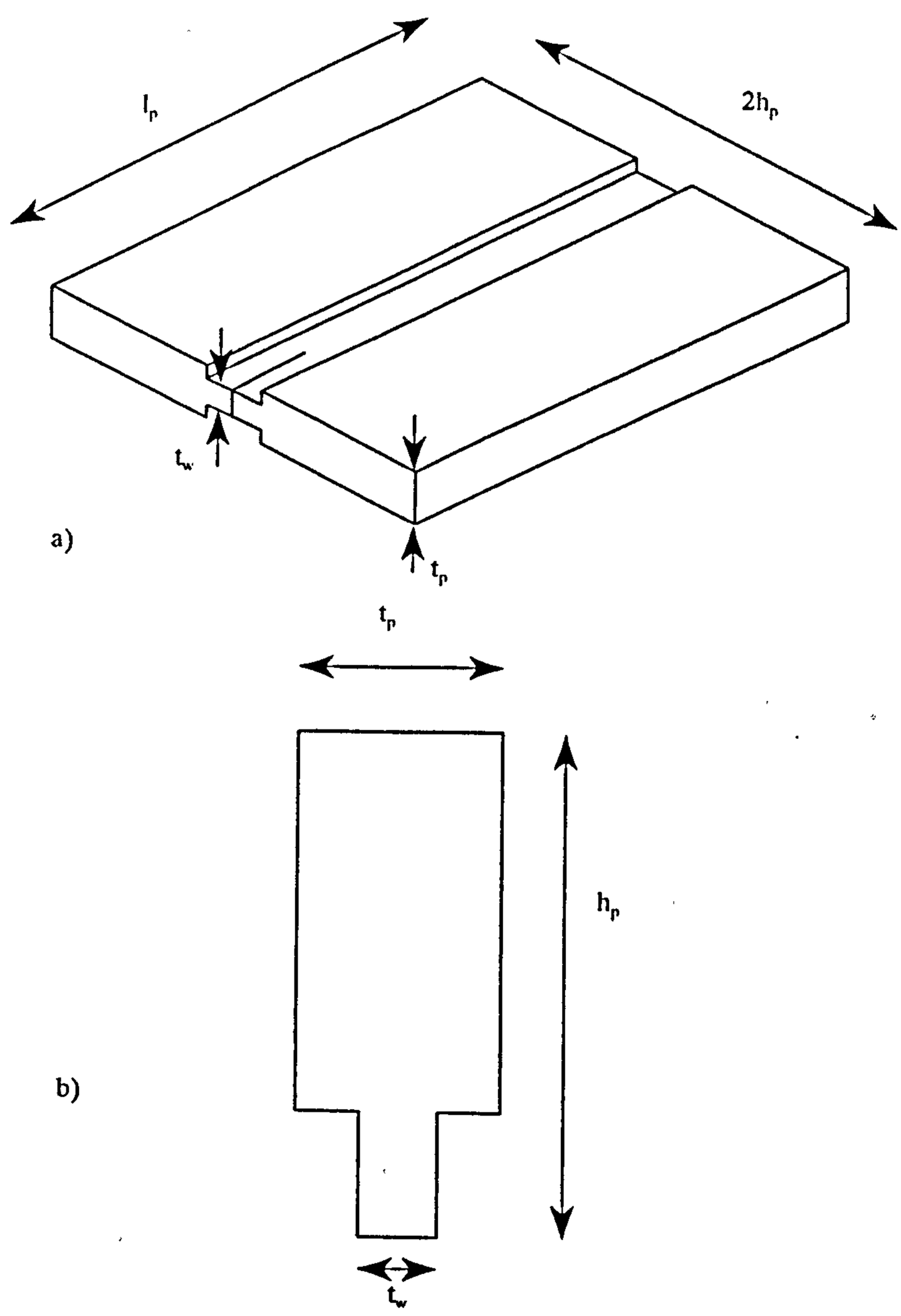

Figure 3.3 Schematic illustrations of DCB specimen; **a)** sample configuration and **b)** cross-section of half of the specimen.

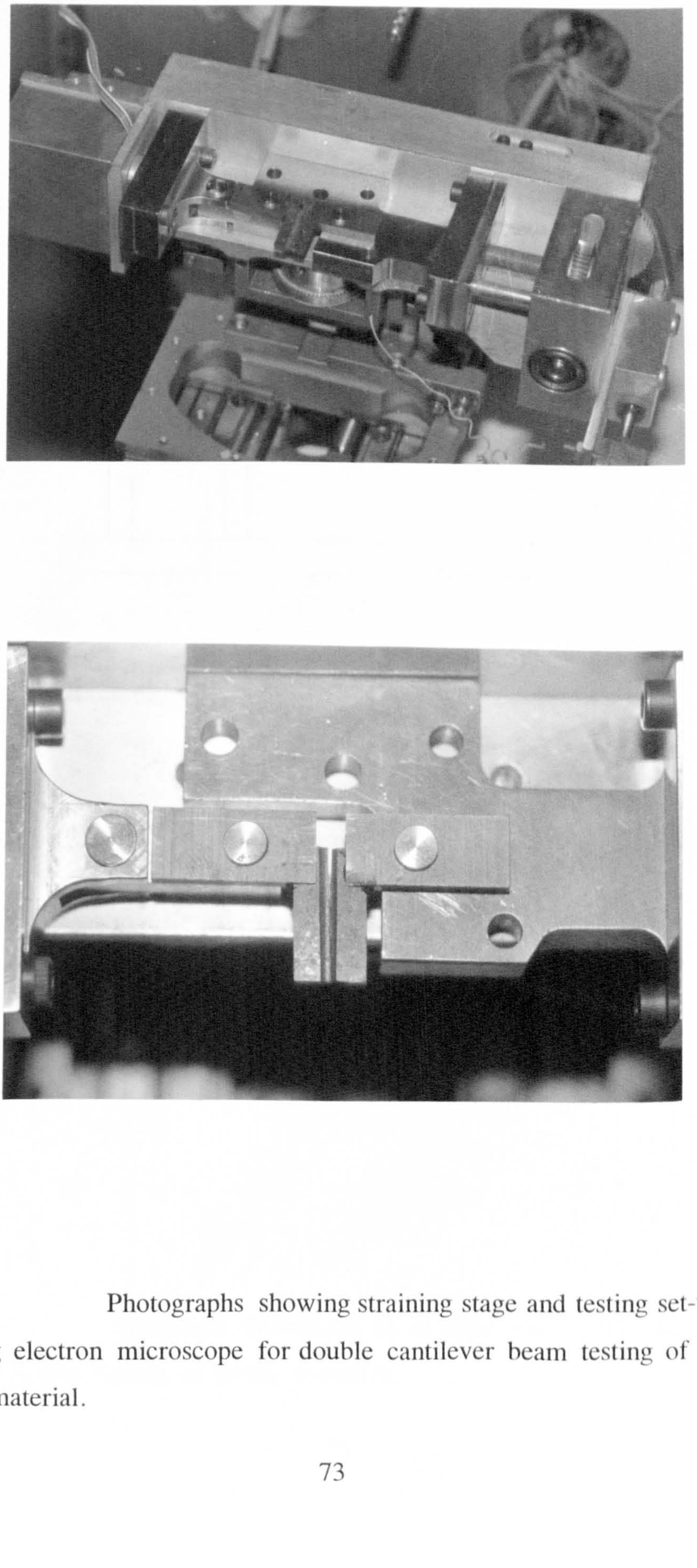

Figure 3.4 Photographs showing straining stage and testing set-up within the scanning electron microscope for double cantilever beam testing of Al_2O_3-Fe composite material.

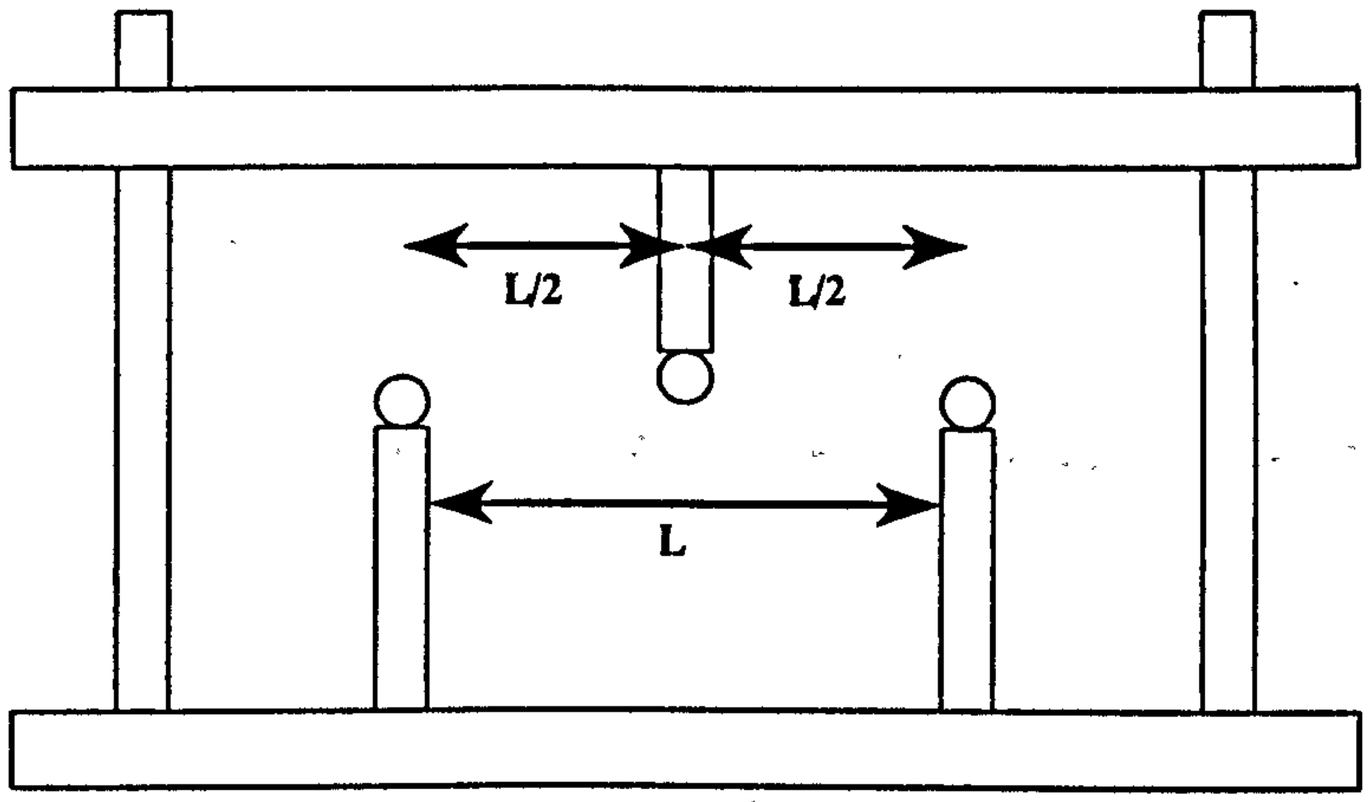

Figure 3.5 Schematic illustration of **a)** three and **b)** four point loading fixtures for flexure testing of brittle materials.

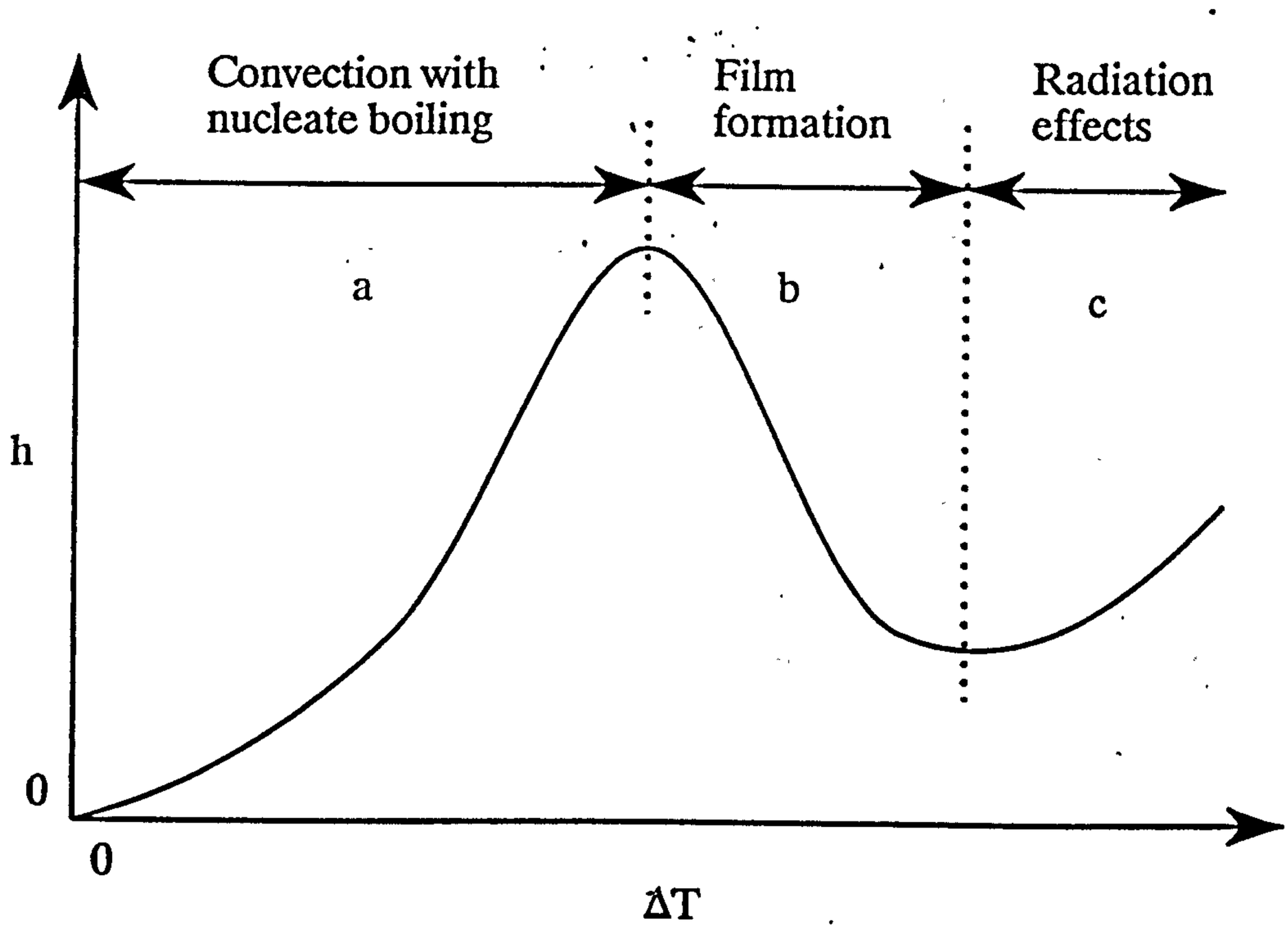

Figure 3.6 Schematic diagram showing the variation of h with temperature (after Davidge & Tappin, 1967).

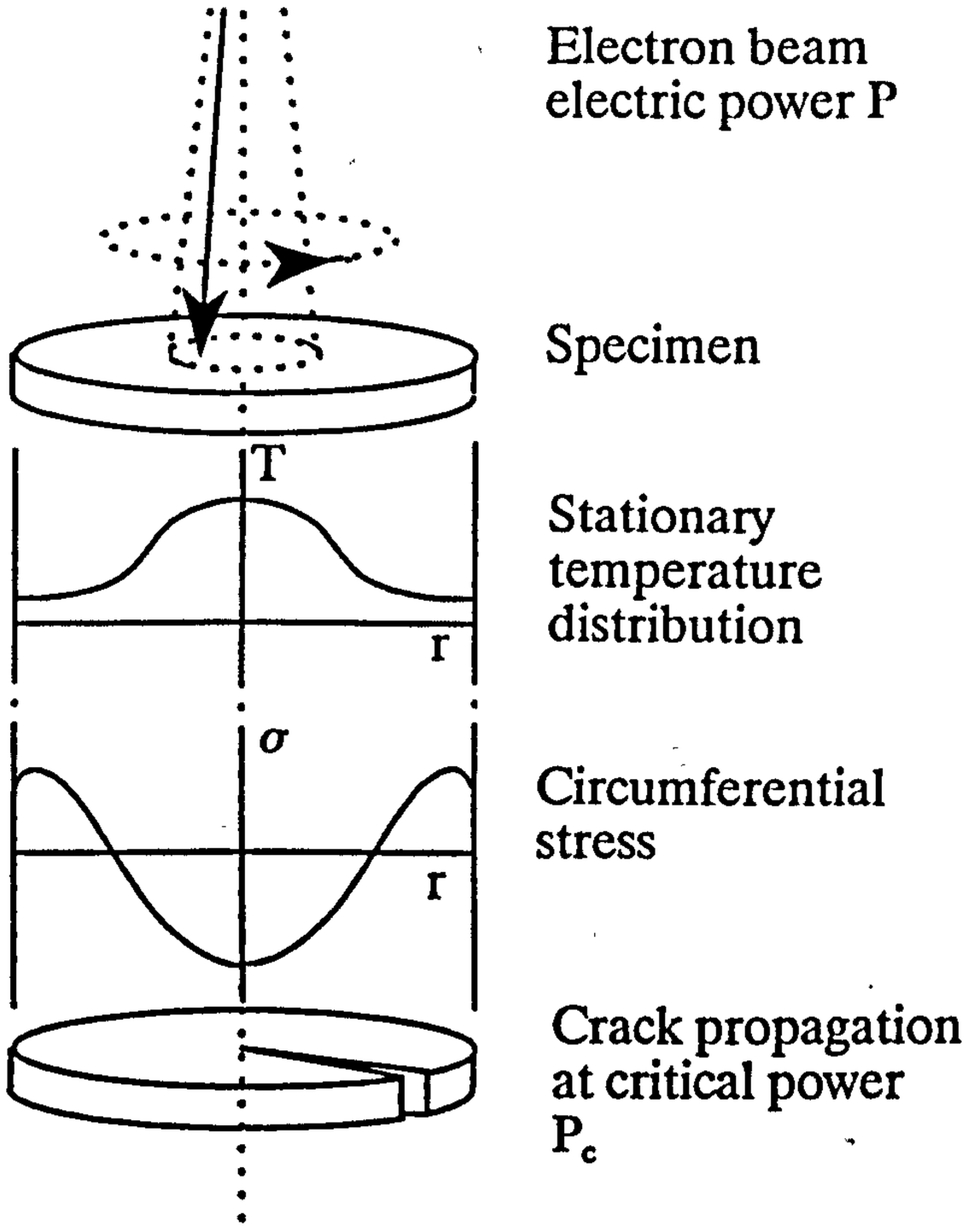

Figure 3.7 Schematic of disc radiation experiment, showing temperature distribution and distribution of circumferential thermal stress (after Pompe *et al.* 1993).

CHAPTER FOUR

CHARACTERISATION OF MATERIALS

4.1 INTRODUCTION

The following chapter presents the results obtained and the observations made concerning the characterisation of the hot pressed monolithic Al_2O_3, and both the hot pressed and sintered Al_2O_3-Fe composite materials. The density and microstructure of the composites are discussed in terms of processing/microstructure relationships.

4.2 DENSITY MEASUREMENT

4.2.1 Hot Pressed Materials

The density of all composites was measured using Archimedes' principle, and generally quoted as a percentage of the maximum possible theoretical density (% T.D.), estimated using a simple rule of mixtures calculation. The hot pressed samples were lightly abraded prior to density measurement to remove the outer metallic skin, which was unlikely to be representative of the bulk material. Al_2O_3-20 volume % Fe composites fabricated via the hot pressing route had little porosity, having densities measuring > 99 % T.D. This result was reproducible and consistent with the literature. Hot pressing has been favoured for the

processing of alumina-metal composite materials by many authors, due to the high densities obtainable (e.g. Hing & Groves, 1972, Krstic *et al.* 1981, Moore & Kunz, 1987, Sun *et al.* 1991, Bannister *et al.* 1992, Trusty, 1994). The density of the hot pressed monolithic Al_2O_3 was measured to be 3968 kg m^{-3}, which compares well with the literature (3970 kg m^{-3}).

4.2.2 Greenbodies and Sintered Composites

4.2.2.1 Greenbodies

The effect of increasing uniaxial pressure on the green density of the powder compacts produced prior to sintering was investigated. This procedure is a typical precursor to any sintering trials, allowing the determination of the optimum compaction pressure for greenbody production. The most suitable uniaxial pressure will be one which produces a greenbody having a relatively high green density and sufficient green strength to allow general handling. However, a compromise must inevitably be reached as too high a compaction pressure is likely to result in excessive sticking between the die and the powder compact (making extraction from the die difficult), along with "springback", i.e. the release of internal elastic stress following the removal of the uniaxial pressure, causing fracture of the greenbody (e.g. Sun, 1993, Shercliff *et al.* 1994).

Initial trials regarding the production of Al_2O_3-Fe greenbodies involved the uniaxial pressing of batches of powder blend A in a hardened steel die using a range of compaction pressures. However, regardless of the uniaxial pressure used, the greenbodies produced tended to disintegrate upon extraction from the die due to their extremely poor green strength. Powder blend B was then utilised. The binder present in blend B improved the green strength of the compacts, enabling successful extraction from the steel die and subsequent handling. Figure 4.1 is a photograph showing several greenbodies after extraction from the steel die. The consequence of the low green strength of powder blend A compacts is clearly

demonstrated. Figure 4.2 shows a plot of greenbody density against applied uniaxial pressure for blend B compacts. An increased pressure results in a higher green density, although the curve reaches a plateau value of approximately 60 % theoretical density with a pressure of approximately 40 MPa. It therefore appears that increasing the pressure further would not benefit green density. Since the use of higher pressures would also result in the generation of greater internal stresses (which can result in fracture during sintering) and a higher degree of sticking, making extraction from the die difficult, it was decided to produce greenbodies at a uniaxial pressure of 20 MPa, having a relative green density of approximately 59 %.

A further batch of composite blend B powder was uniaxially pressed into bars at 93 MPa (courtesy of Dr. J. Kirk, Morgan Matroc Ltd.). No problems regarding excessive sticking or springback were reported. The green density of the bars was estimated to be approximately 62 % T.D. It was envisaged that the increased green density would lead to improvements in the final density of the sintered composites.

Several authors have reported similar trends regarding green density versus compaction pressure for alumina-metal powder compacts. However, uniaxial pressures reported are generally considerably greater than that found to be sufficient in this study, e.g. up to 300 MPa for uniaxially pressed Al_2O_3-Al (Vekinis, 1992), 30-130 MPa for uniaxially pressed Al_2O_3-Ni (Sun, 1993), 120 MPa for uniaxially pressed Al_2O_3-Ag (Wang *et al.* 1993), up to 500 MPa for uniaxially pressed Al_2O_3-Ni (Shercliff *et al.* 1994), 44 MPa for uniaxially pressed Al_2O_3-ZrO_2-Ag (Tuan & Chen, 1995). Despite the higher pressures used in these cases, maximum relative green densities of around 55-60 % are reported.

4.2.2.2 Sintered Composites

Composite greenbodies were sintered in a tube furnace which was continually

flushed with argon, using a range of sintering schedules. Prior to density measurement, all sintered composite samples were lightly abraded to remove any globules of pure iron which may have formed on the surfaces due to sweating. Initial trials and density measurements showed that sintering the bars on a graphite slab resulted in considerably higher final density values than sintering the bars in a graphite powder bed (resulting in relative densities of 95 % T.D. and 87 % T.D. respectively for a maximum temperature of 1700 °C for 1 hour). This was thought to be due to the greater exposed surface area of carbon in powder form producing a more reducing sintering atmosphere, therefore further decreasing the partial pressure of oxygen in the system, hence reducing the ability of the molten iron to wet alumina. The reduction in wettability resulted in a greater degree of sweating for the composite sintered in the graphite powder bed. Sun (1993) studied the control of the sintering atmosphere using powder beds containing differing proportions of alumina and graphite powders. It was found that the Al_2O_3-Ni composite sintered in a 100 % graphite powder bed sweated considerably, due to the highly reducing atmosphere preventing wetting of the ceramic by the molten metal. A 50 % graphite + 50 % Al_2O_3 powder bed was found to produce a less reducing atmosphere, consequently decreasing sweating, resulting in a relatively dense composite material. It is thought that the sintering of Al_2O_3-Fe greenbodies on a graphite slab results in a similar sintering atmosphere to the alumina/graphite powder bed used by Sun. Further trials were therefore carried out using a graphite slab only. Figure 4.3 shows the influence of the sintering temperature on the final density of the sintered composites. The most dense composites were produced using higher sintering temperatures, giving a maximum of 95 % T.D. at a temperature of 1700 °C. A further increase in temperature to 1800 °C resulted in a minimal increase in density. The degree of sweating increased with increasing sintering temperature. Increasing the dwell time at maximum temperature from 1 hour to 2 hours resulted in an increase in relative density of only 1 %.

4.3 MICROSTRUCTURAL EXAMINATION OF POLISHED SURFACES

4.3.1 Hot Pressed Composite

Figure 4.4 is a photomicrograph showing the microstructure of a polished section through the hot pressed Al_2O_3-Fe composite (section taken parallel to pressing direction). The microstructure consists of a random, homogeneous distribution of irregularly shaped iron particles dispersed within the alumina matrix. Any porosity (< 1 %) is fine and evenly dispersed. Sun (1993) reported a degree of directionality (perpendicular to the direction of pressing) for hot pressed Al_2O_3-Ni composites; this was not observed for the Al_2O_3-Fe composite produced in this study.

4.3.2 Sintered Composites

Figure 4.5 shows the effect of sintering the composite greenbodies a) on a graphite slab, and b) in a graphite powder bed. From the photomicrographs, it can be seen that the specimen sintered in a powder bed has an area devoid of iron particles. This would explain the low density of 87 % T.D., and is due to the highly reducing sintering atmosphere as explained in § 4.2.2.2. This resulted in a high degree of sweating of the near-surface iron. Figures 4.6 to 4.10 are photomicrographs showing the microstructure of polished sections through the range of composites sintered on a graphite slab. The alumina matrix of the samples sintered at 1550 °C and 1625 °C for 1 hour is only partially sintered. This can be seen from the large areas of open porosity which show a more powder-like than grain-like texture. At higher sintering temperatures of 1700 °C and above, the matrix appears to be more adequately sintered, with the degree of porosity decreasing with increasing sintering temperature. This is in agreement with the density results presented in § 4.2.2.2. As with the hot pressed composite, the microstructure consists of an apparently random, homogeneous distribution of iron

particles within the alumina matrix, although the individual particles do not show the same degree of morphological irregularity as in the hot pressed material; this is probably due to the fact that the sintering process did not involve the application of pressure. It is suspected that the uniaxial pressure of 30 MPa used at maximum temperature during the hot pressing procedure induces plastic flow of the softened iron, resulting in the further elimination of intergranular porosity and the production of a partially mechanically interlocked matrix/particle interface, thus partially overcoming the poor wetting behaviour of the metal. Further examination of the microstructures shows that the particle size increases as the sintering temperature is increased. Concomitantly, there is a larger matrix grain size and a reduced number of second phase inclusion sites (triple points). Table 4.1 summarises the microstructural features, in terms of particle size and area fraction, of both the hot pressed and sintered composites.

4.4 MICROSTRUCTURAL EXAMINATION OF FRACTURE SURFACES

4.4.1 Hot Pressed Materials

Fracture surfaces of hot pressed composite flexure test samples were studied using the SEM, in order to further examine microstructural features of the composite materials. Typical examples are shown in figure 4.11. It can be seen that the alumina matrix has a consistently small grain size, with little intergranular porosity. Also examined was the fracture surface of monolithic alumina (see figure 4.12), which had been processed in an identical way to the hot pressed composite. The matrix grain size measurements of both hot pressed materials are shown in table 4.1. The grain size of the monolithic alumina was found to be 50 % greater than that measured for the composite, despite identical processing (2.1 μm and 1.4 μm respectively). It was concluded that the iron incorporated in the composite had probably inhibited grain growth during processing, although it is acknowledged that the optimum hot pressing schedule for the composite is not necessarily the

optimum for the monolith.

4.4.2 Greenbodies and Sintered Composites

4.4.2.1 Greenbodies

Fracture surfaces of powder compacts were examined using the SEM in order to determine the extent of plastic deformation of the iron particles which may have occurred during cold uniaxial pressing. It was anticipated that the use of higher pressures would cause a degree of plastic deformation, thus increasing the chances of forming irregularly shaped iron inclusions in the sintered composite. Figures 4.13 and 4.14 are photomicrographs of the fracture surfaces of greenbodies pressed at pressures of 20 MPa and 93 MPa. It can be seen that even at the higher pressure, the lighter coloured iron particles remain smooth and approximately spherical, suggesting that little or no plastic deformation has occurred during pressing.

4.4.2.2 Sintered Composites

Examination of the fracture surfaces of all conventionally sintered composites revealed the trends in grain size as shown in figure 4.15. Also shown in figure 4.15 is the influence of the sintering temperature on second phase particle size (taken from polished surfaces) and final density. Photomicrographs of the fracture surfaces are shown in figures 4.16 to 4.20. The grain size of the two composites sintered at 1550 °C and 1625 °C could not be calculated due to incomplete sintering of the matrix. At temperatures of 1700 °C and above, increasing the maximum sintering temperature led to an increase in the alumina matrix grain size and a corresponding increase in the iron particle size. The grain size of all sintered composites was significantly greater than that of the hot pressed composite, due to longer exposures at higher temperatures causing grain growth.

Five major requirements must be considered when deciding on the optimum sintering schedule for the Al_2O_3-Fe composite system. These are:

i) Maximum achievable density.

ii) Minimal sweating of iron.

iii) Optimum degree of ceramic/metal interfacial bonding.

iv) Minimum possible matrix grain size.

v) Particle size close to theoretical critical size for maximum toughness and bridging potential.

The critical particle size for both composites was calculated using the method of Davidge & Green (see section 2.2.2.2),taking the following data from the Nuffield Book of Data (1984) and the Handbook of Properties of Technical & Engineering Ceramics Part 1 (Morrell, 1985); $\alpha_p = 11.7 \times 10^{-6}\ K^{-1}$, $\alpha_m = 7.7 \times 10^{-6}\ K^{-1}$, $\upsilon_p = 0.29$, $\upsilon_m = 0.22$, $E_p = 211$ GPa, $E_m = 380$ GPa. The values for ΔT were taken to be 1380 °C and 1680 °C for the hot pressed composite and sintered composites respectively (i.e. maximum processing temperature - room temperature). The stress generated was calculated to be 1.54 GPa for the hot pressed material and 1.87 GPa for the sintered. The critical particle sizes d_c were found to be 12 μm and 8 μm respectively, taking the fracture toughness for monolithic alumina as 3.1 MPa $m^{½}$ in both cases (Trusty, 1994). The effect of the particle size on the fracture behaviour of both composites will be addressed in chapter 5.

Since contradictory processing variables are necessary in order to satisfy each of these requirements (i.e. high processing temperatures are required for increased density and flow of iron, whereas lower temperatures are favoured to reduce grain growth and second phase particle size), a compromise of 1700 °C for a dwell time of 1 hour was decided upon and used for all further processing of conventionally sintered composites. This gives a composite of 95 % theoretical density, with matrix grain size and iron particle size of 4.5 μm and 6.7 μm respectively. Thus the particle size in both the hot pressed composite and the sintered composite is lower than the critical particle size calculated, particularly in the case of the hot pressed composite.

4.5 CONCLUSIONS

Al_2O_3-Fe composites consisting of 20 volume % Fe have been successfully fabricated using the techniques of hot pressing and conventional pressureless sintering. The hot pressing procedure allowed the production of dense (> 99 % T.D.),reproducible composites, having a desirable microstructure (small grain size, complex second phase particle morphology). The conventional sintering route has yet to be optimised. The optimum uniaxial pressure for the production of Al_2O_3-Fe (+ 3 % PEG binder) greenbodies appears to be around 20 MPa, giving a relative density of approximately 59 %. Using a sintering temperature of 1700 °C with a dwell time of 1 hour in an inert atmosphere produces a composite having a density of only 95 % T.D., with an acceptable microstructure. It is envisaged that further work on the sintering behaviour of the composites may lead to an improved microstructure, having a smaller matrix grain size and higher density, the aim being to reproduce as closely as possible the microstructure achieved by the hot pressing technique.

Table 4.1 Summary of microstructural features of alumina-iron composites and monolithic alumina.

Sample	Average grain size (μm)	Area fraction of particles	Average particle size (μm)
H.P.* Al_2O_3	2.1	N/A	N/A
H.P.* Al_2O_3-Fe	1.4	0.39	3.9
Sintered Al_2O_3-Fe 1550 °C x 1h	Sintering incomplete	0.28	5.2
Sintered Al_2O_3-Fe 1625 °C x 1h	Sintering incomplete	0.40	5.6
Sintered Al_2O_3-Fe 1700 °C x 1h	4.5	0.39	6.7
Sintered Al_2O_3-Fe 1800 °C x 1h	6.5	0.33	9.2
Sintered Al_2O_3-Fe 1700 °C x 2h	6.2	0.39	7.7

* H.P. → Hot pressed.

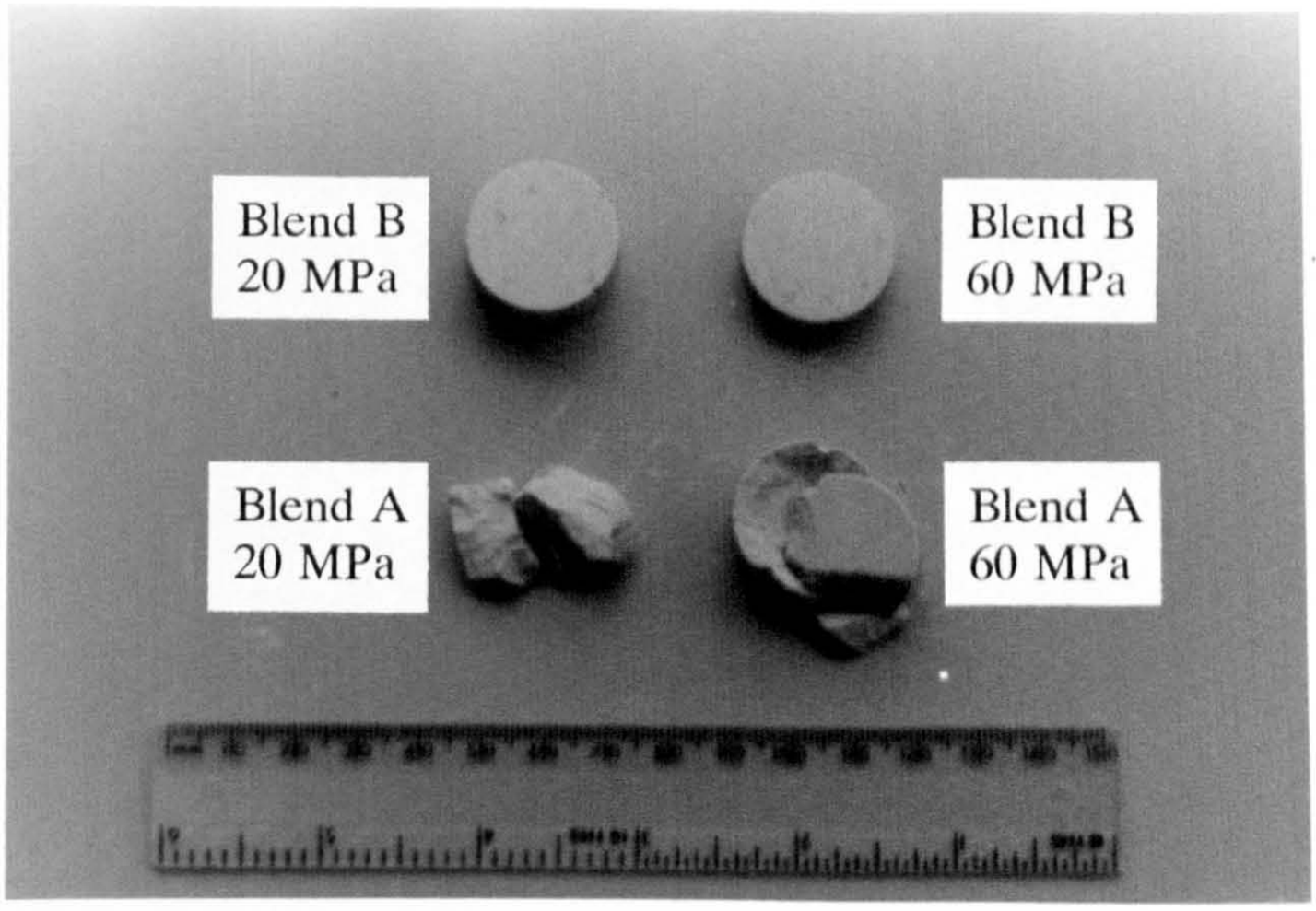

Figure 4.1 Photograph showing composite greenbodies uniaxially pressed at 20 MPa and 60 MPa, of both blends A and B, after extraction from the steel die. Note the improved green strength of the compact containing the polymeric binder.

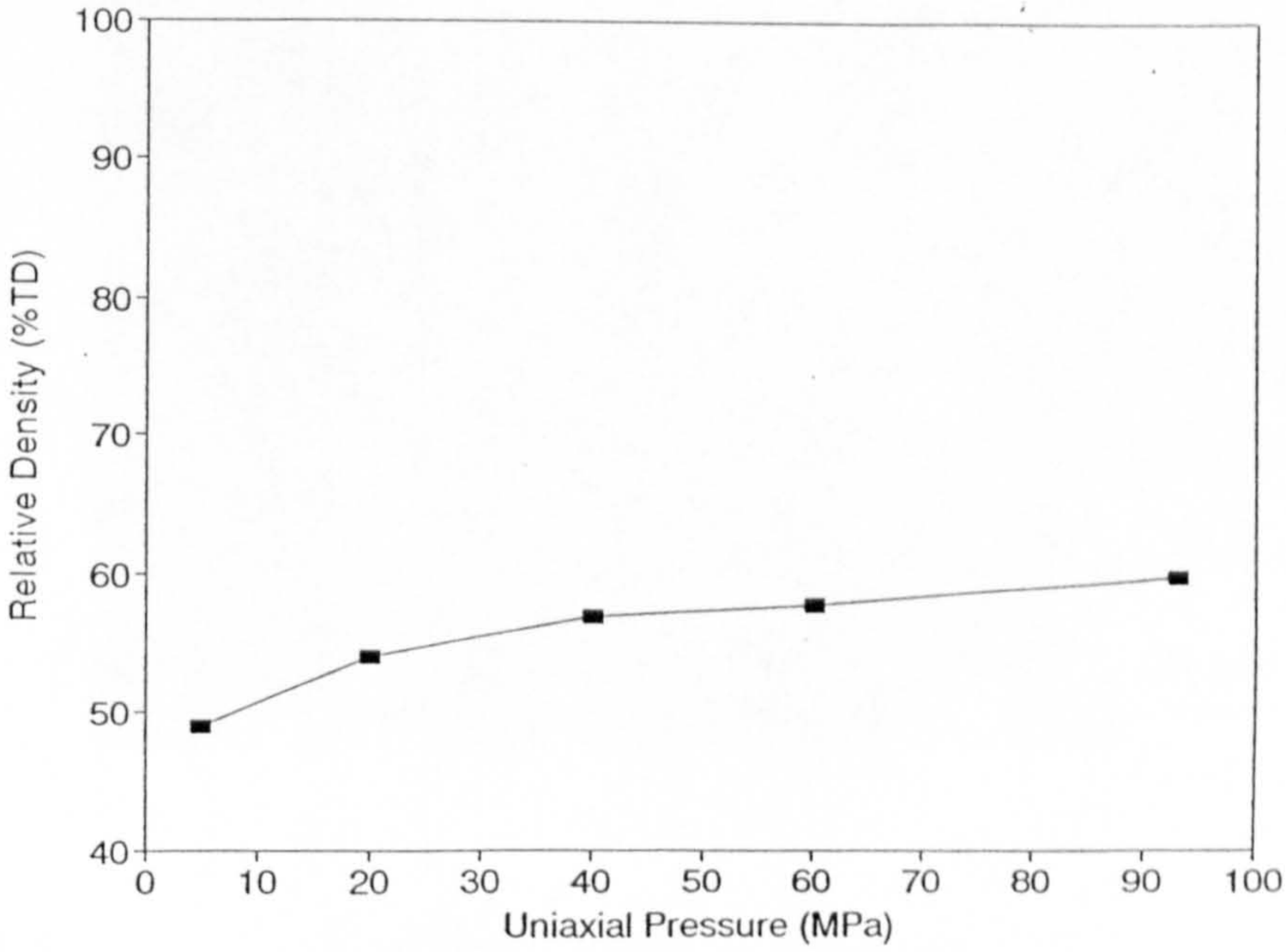

Figure 4.2 Plot of relative green density versus uniaxial compaction pressure for composite powder blend B compacts.

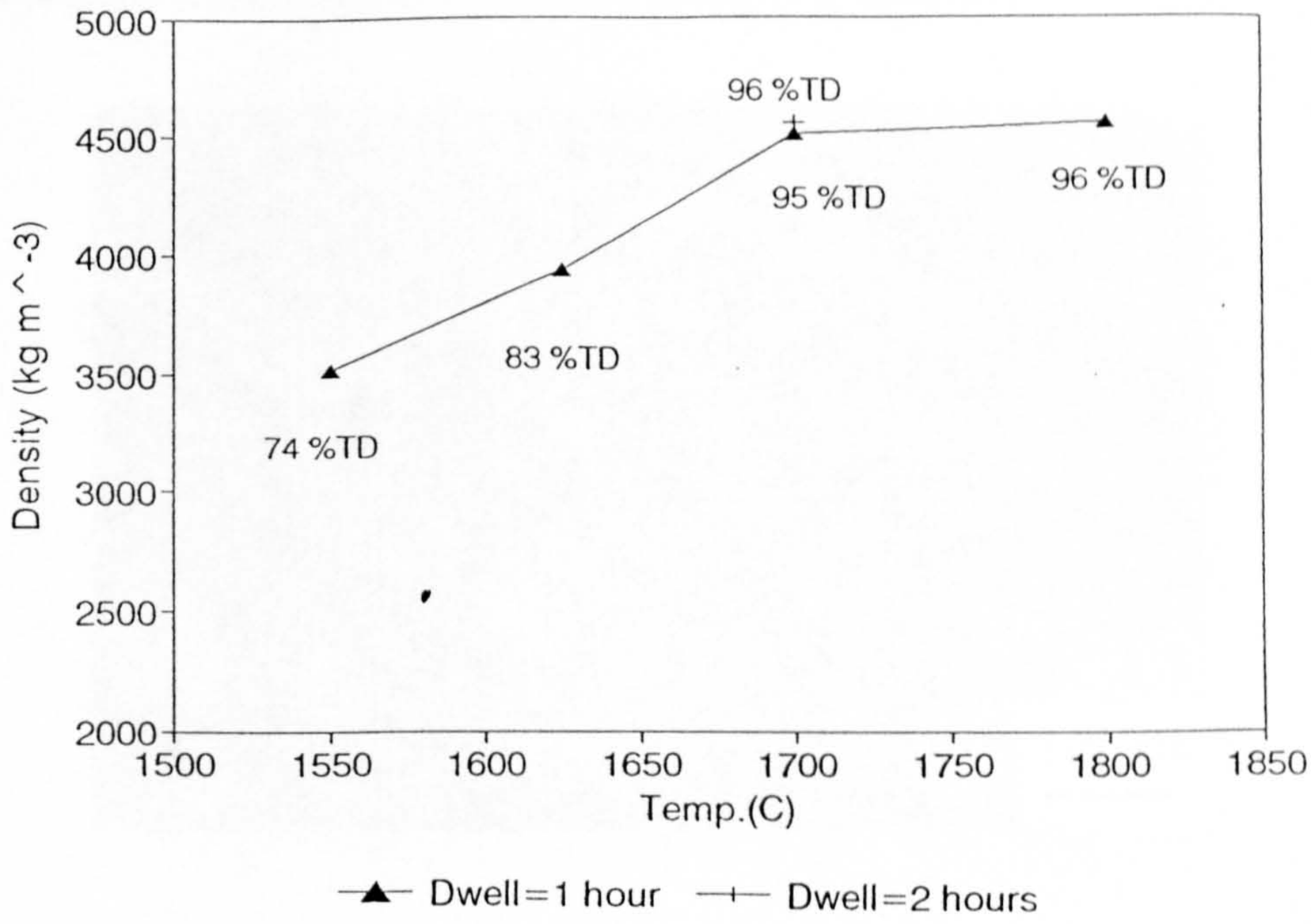

Figure 4.3 Plot showing the influence of the sintering temperature on the final density of powder blend B composites.

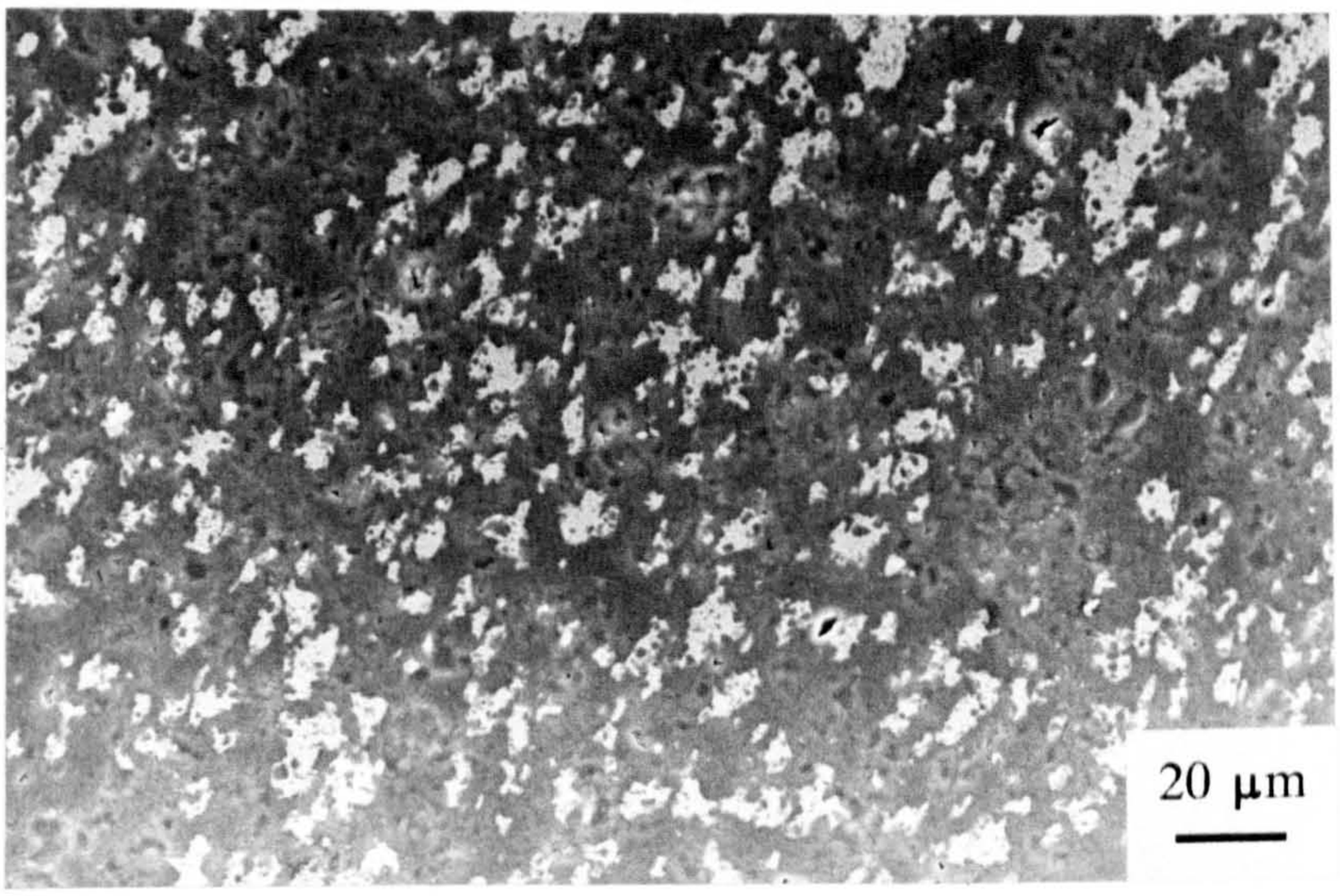

Figure 4.4 SEM photomicrograph (secondary electron image) of the microstructure of the hot pressed Al_2O_3-Fe composite. Note the irregularity of the lighter coloured Fe particles and the dense matrix.

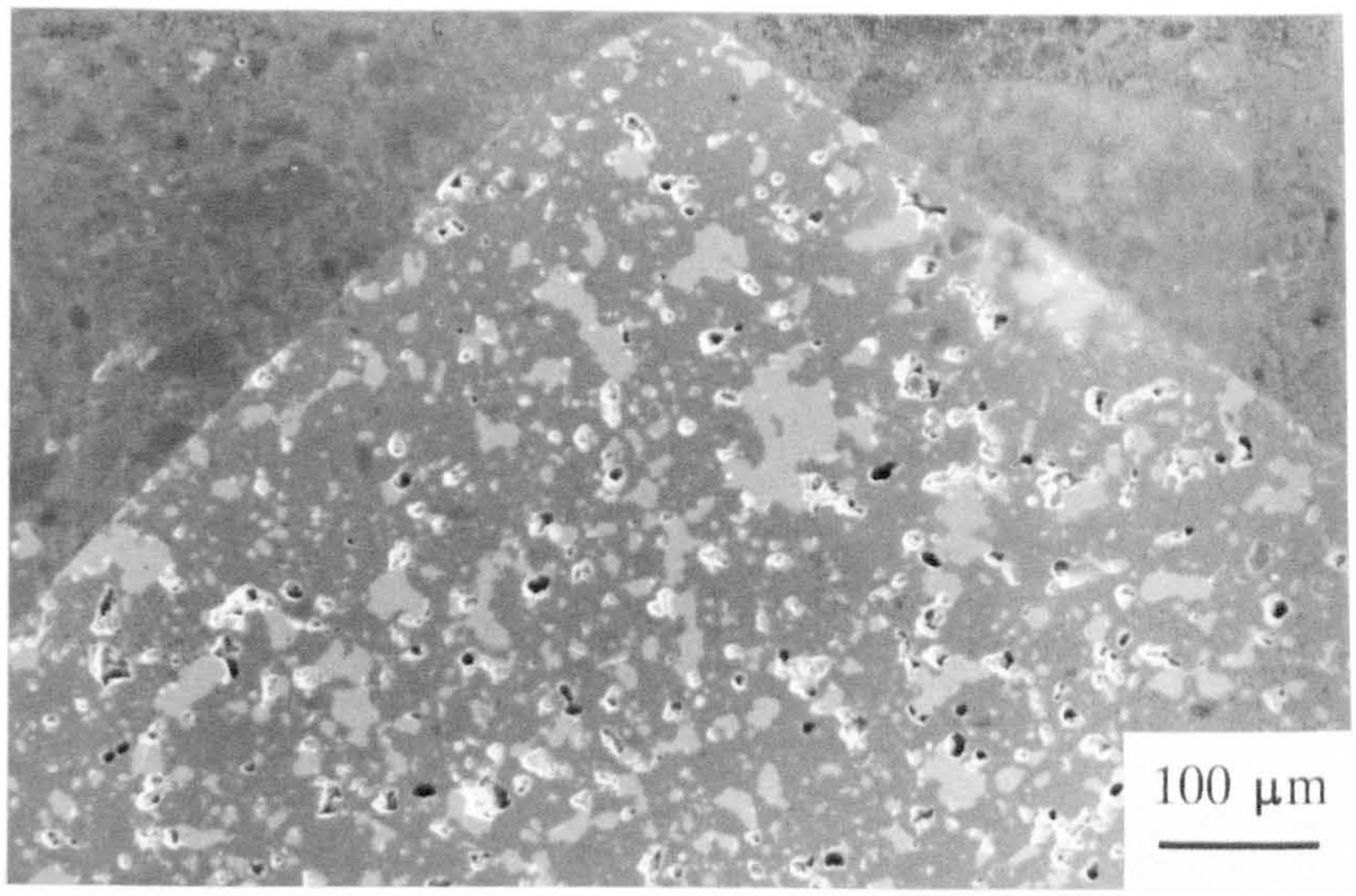

Figure 4.5 SEM photomicrographs (secondary electron images) of the edge of two Al_2O_3-Fe composites sintered at 1700 °C for 1 hour, **a)** on a graphite slab and **b)** immersed in a graphite powder bed. Note the higher degree of near-surface microstructural porosity in a).

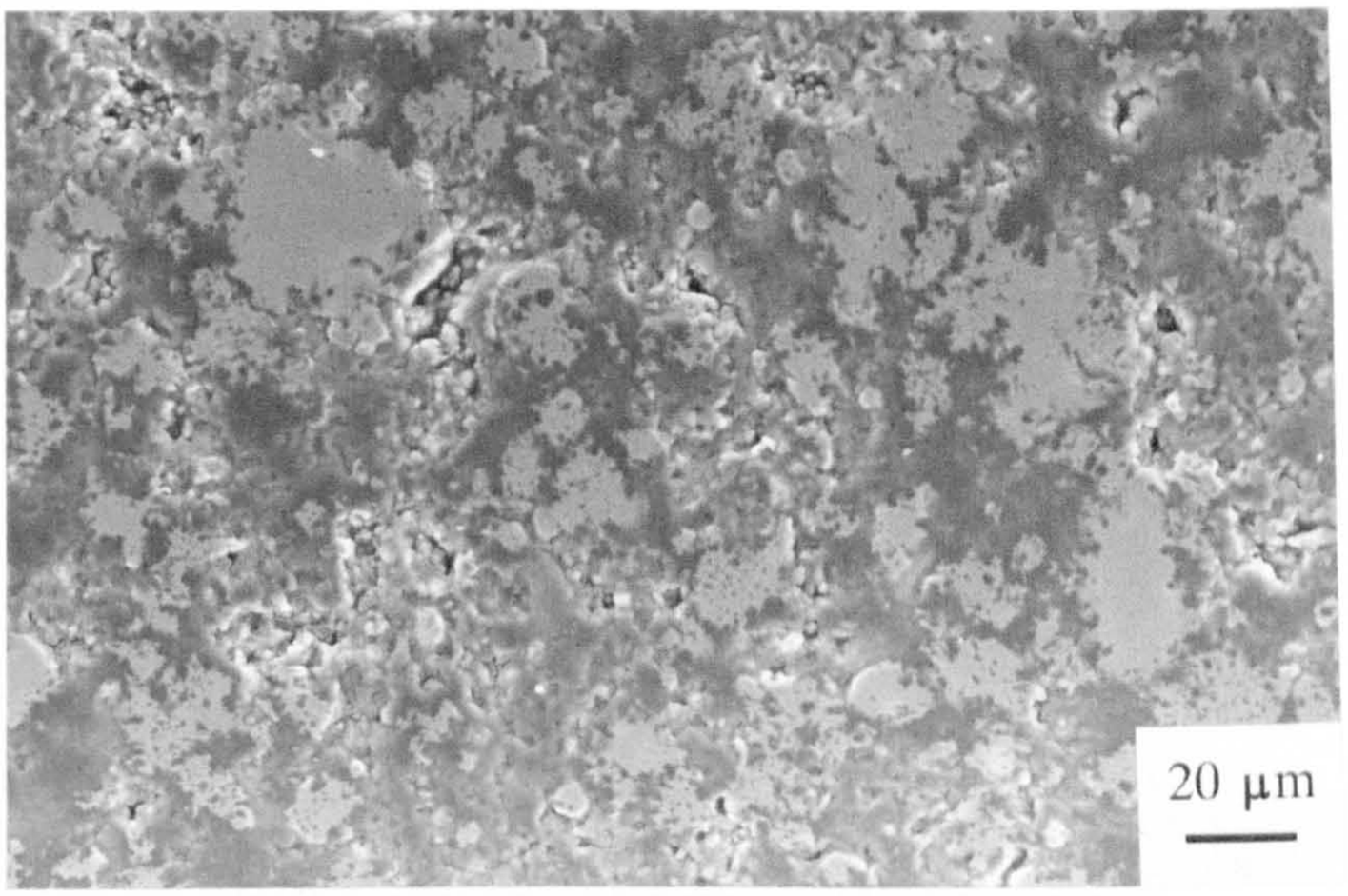

Figure 4.6 SEM photomicrograph (secondary electron image) of the microstructure of an Al_2O_3-Fe composite sintered at 1550 °C for 1 hour. Note the incomplete sintering of the alumina matrix.

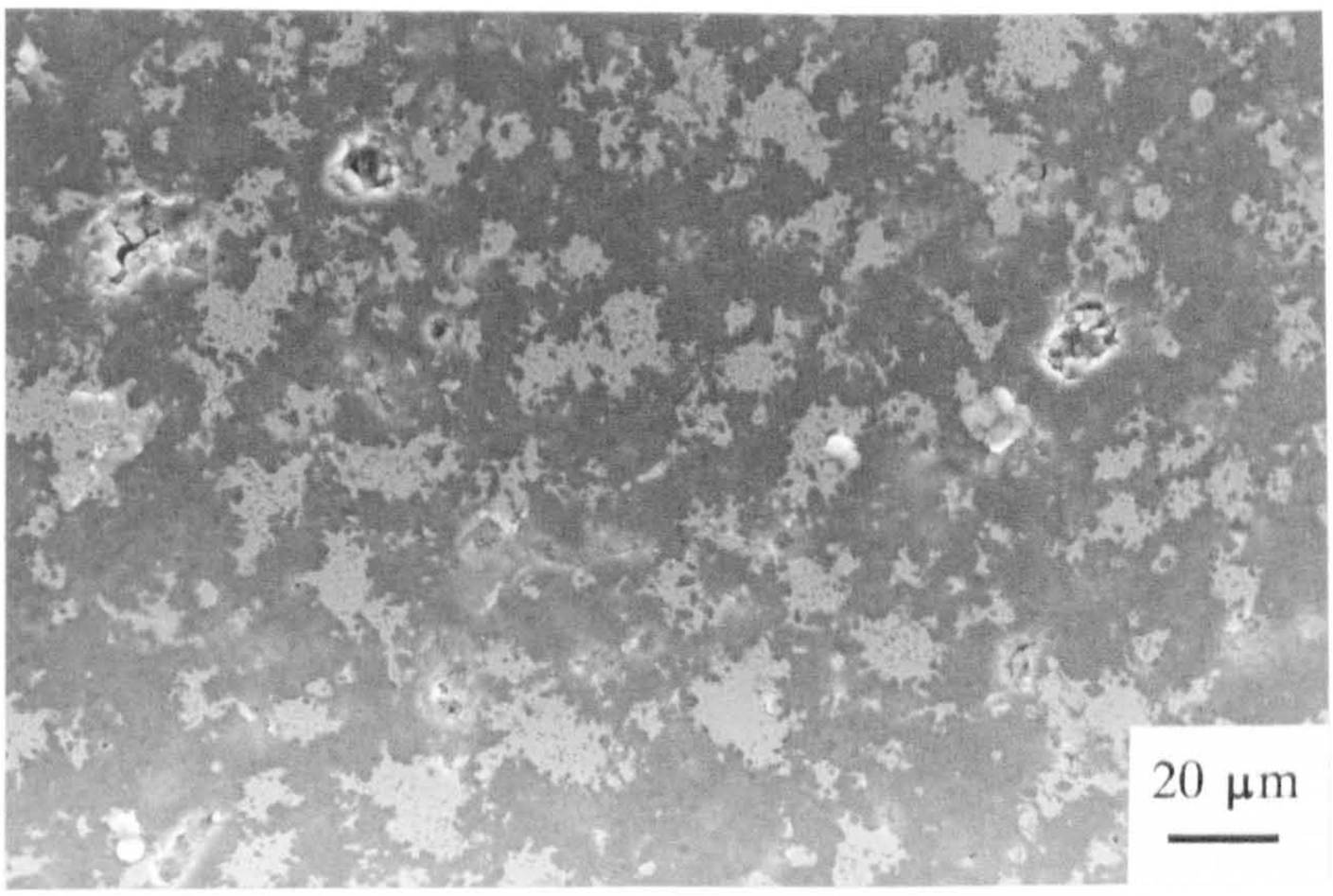

Figure 4.7 SEM photomicrograph (secondary electron image) of the microstructure of an Al_2O_3-Fe composite sintered at 1625 °C for 1 hour. Although an improvement on the microstructure shown in figure 4.6, the alumina matrix remains only partially sintered.

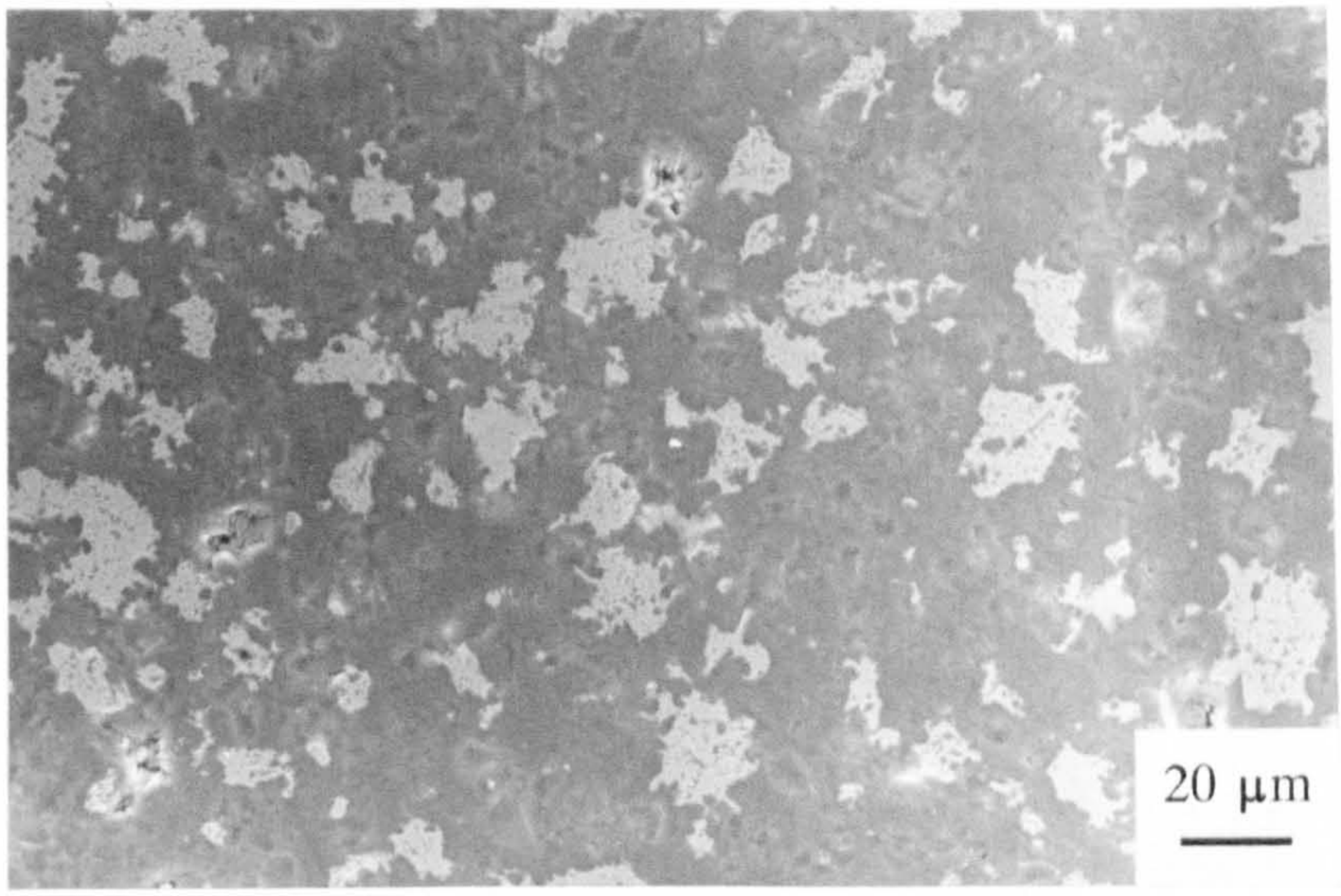

Figure 4.8 SEM photomicrograph (secondary electron image) showing the microstructure of an Al_2O_3-Fe composite sintered at 1700 °C for 1 hour. The alumina matrix appears to be sufficiently sintered, with little porosity.

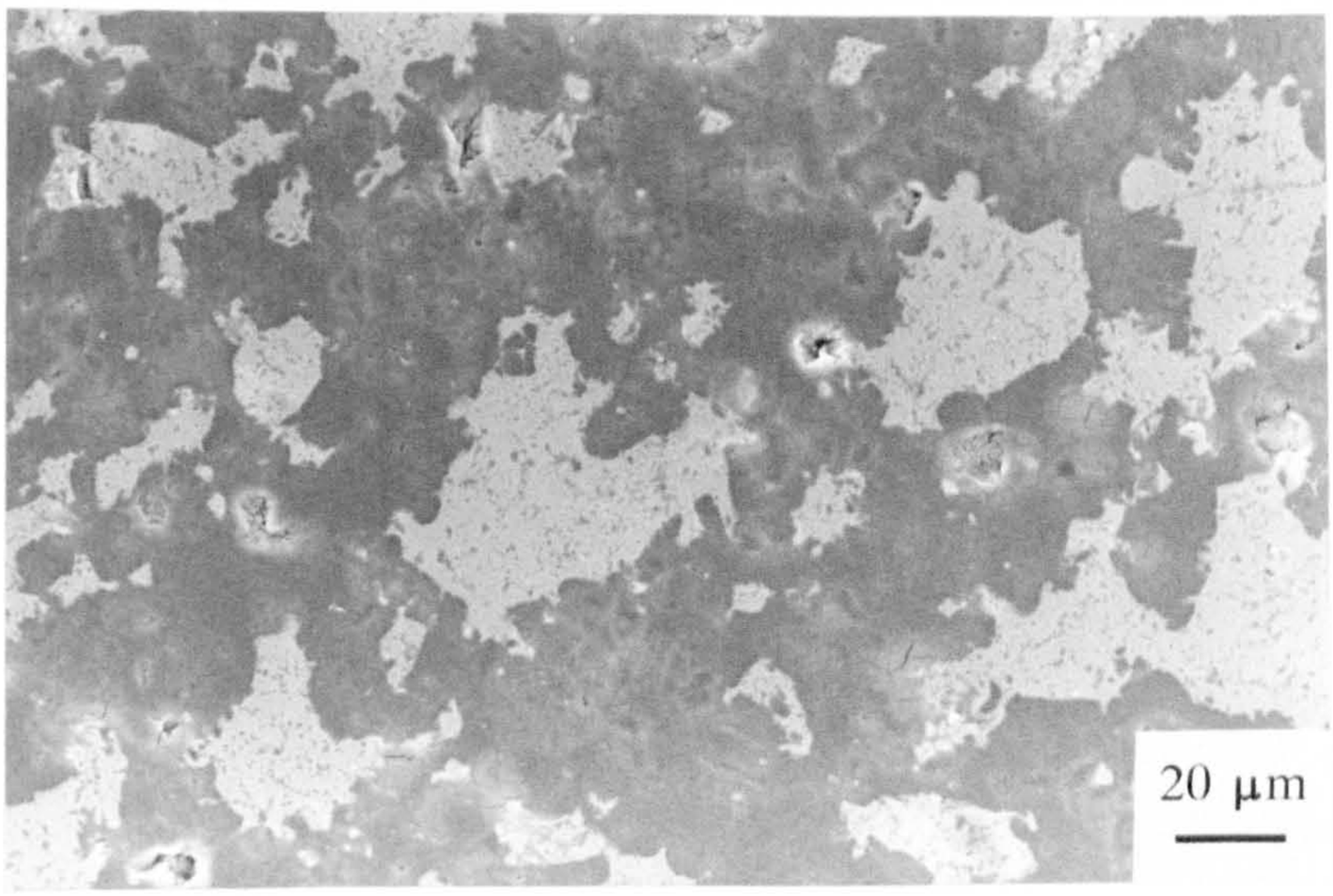

Figure 4.9 SEM photomicrograph (secondary electron image) showing the microstructure of an Al_2O_3-Fe composite sintered at 1800 °C for 1 hour.

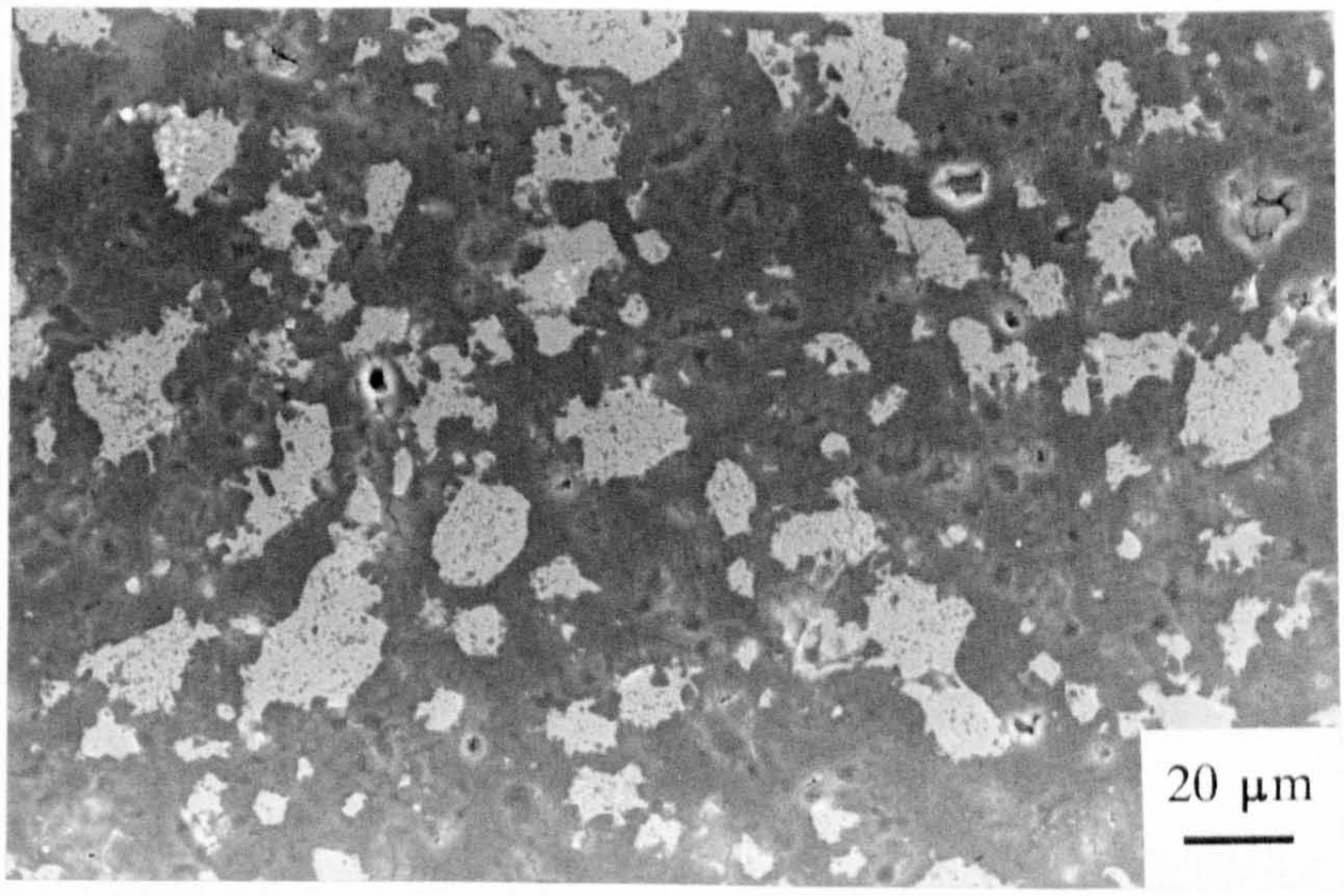

Figure 4.10 SEM photomicrograph (secondary electron image) showing the microstructure of an Al_2O_3-Fe composite sintered at 1700 °C for 2 hours. The increased dwell time at maximum temperature appears to have had little effect on the resulting microstructure (cf. figure 4.8).

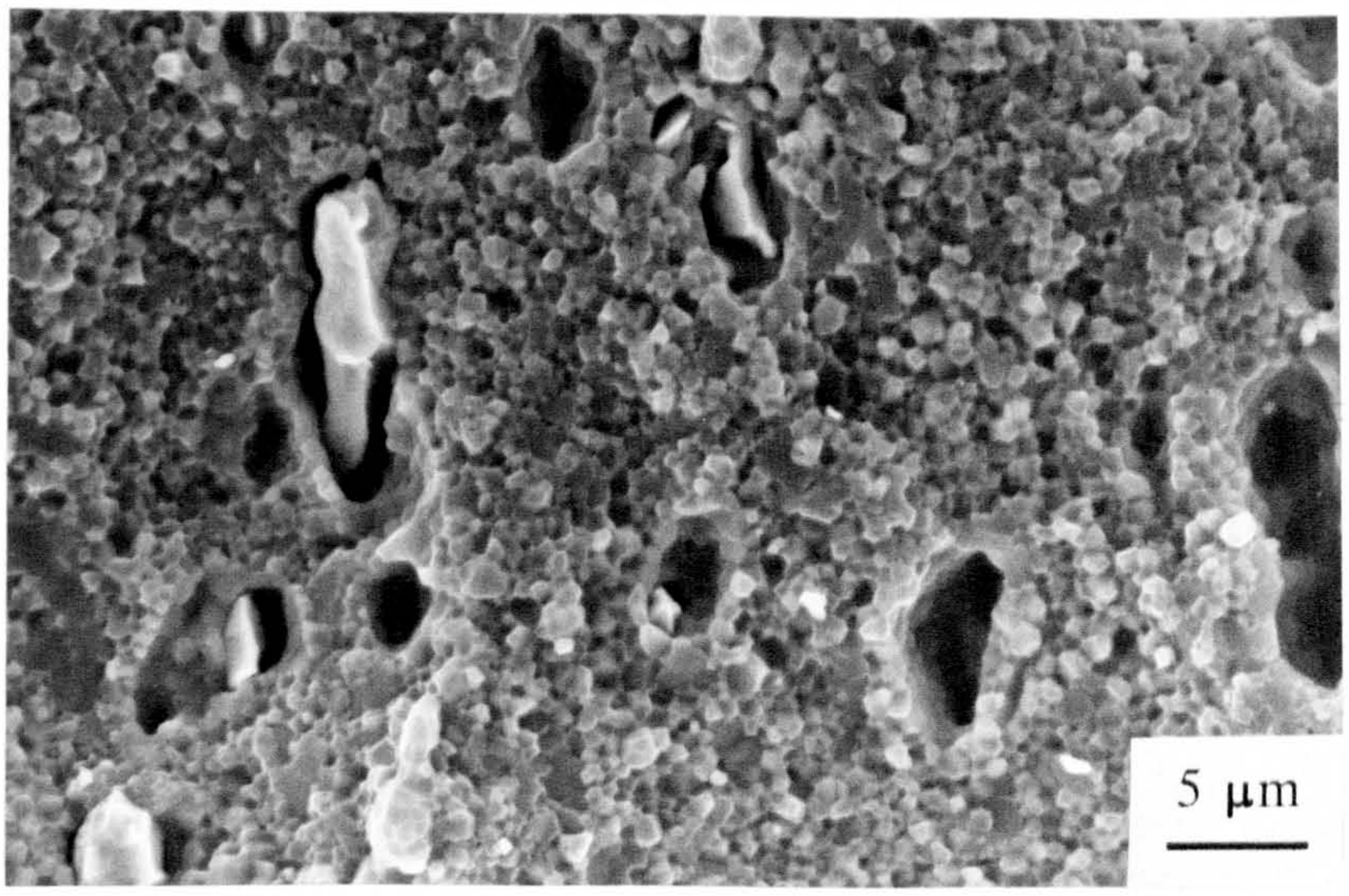

Figure 4.11 SEM photomicrograph (secondary electron image) showing the fracture surface of the hot pressed Al_2O_3-Fe composite. Note the small matrix grain size of approximately 1.4 μm.

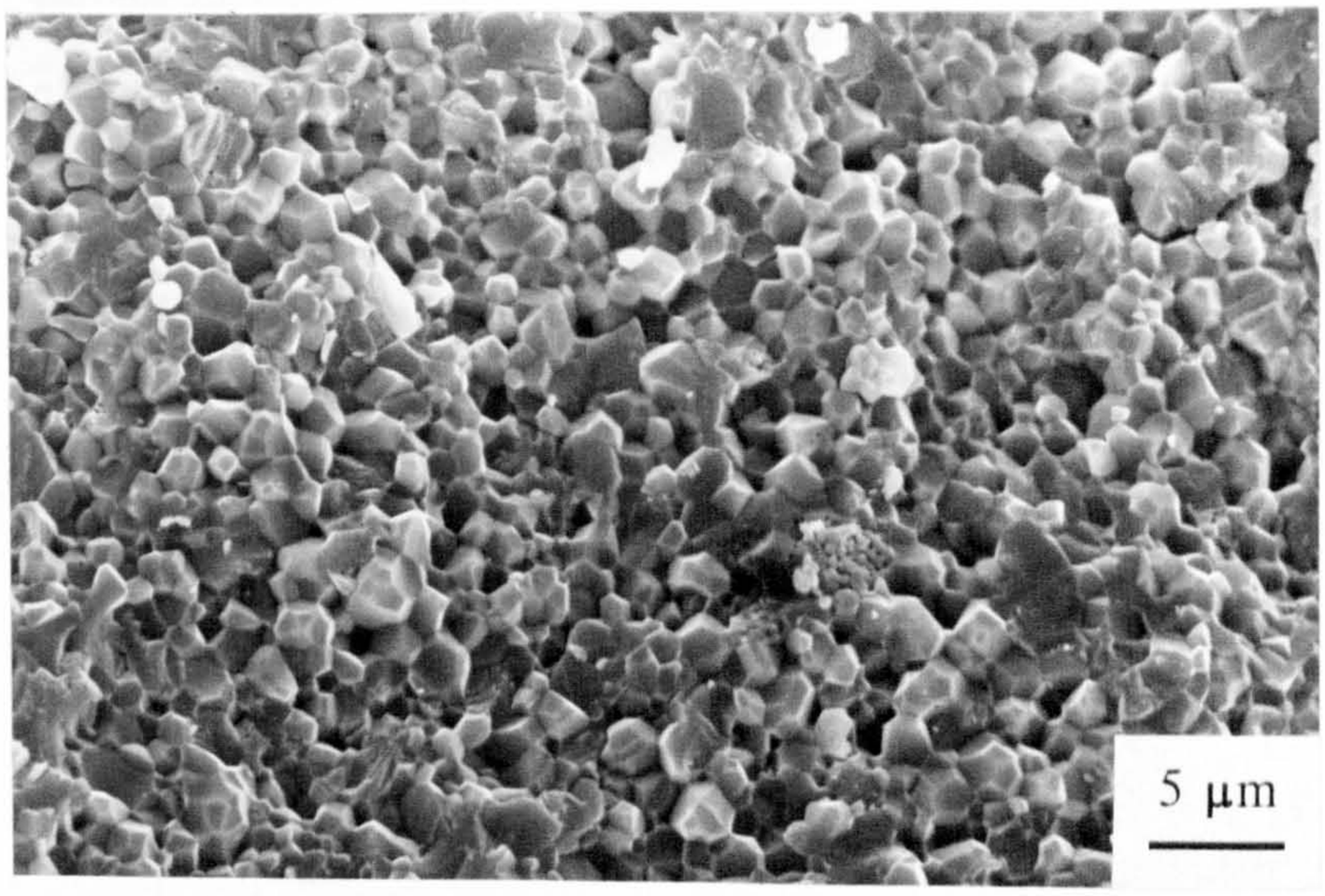

Figure 4.12 SEM photomicrograph (secondary electron image) showing the fracture surface of the hot pressed monolithic Al_2O_3. Note that the grain size of approximately 2 μm is larger than that of the hot pressed Al_2O_3-Fe composite.

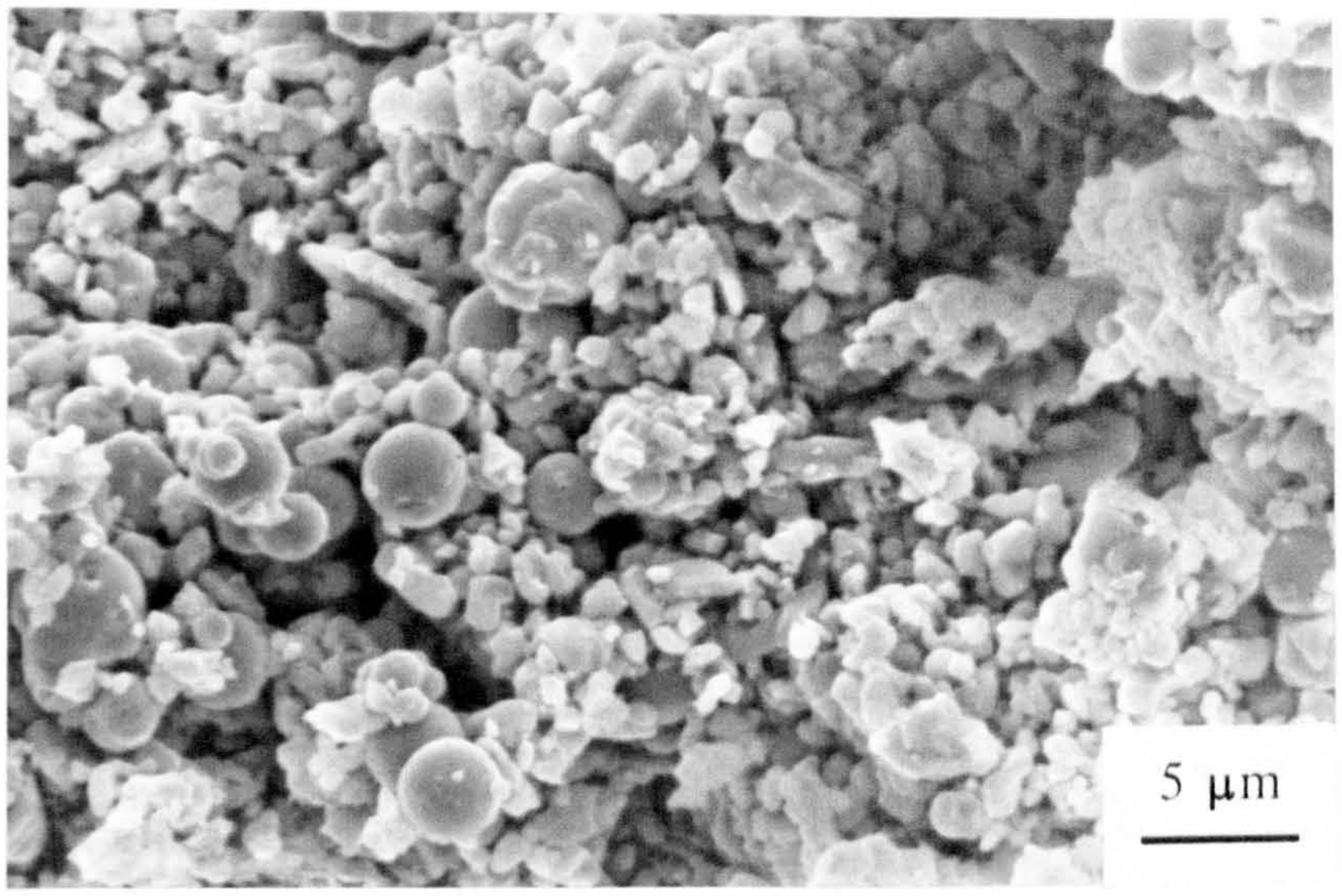

Figure 4.13 SEM photomicrograph (secondary electron image) of the fracture surface of a composite powder blend B greenbody which has been uniaxially pressed at 20 MPa, showing the lack of plastic deformation of the iron particles during pressing.

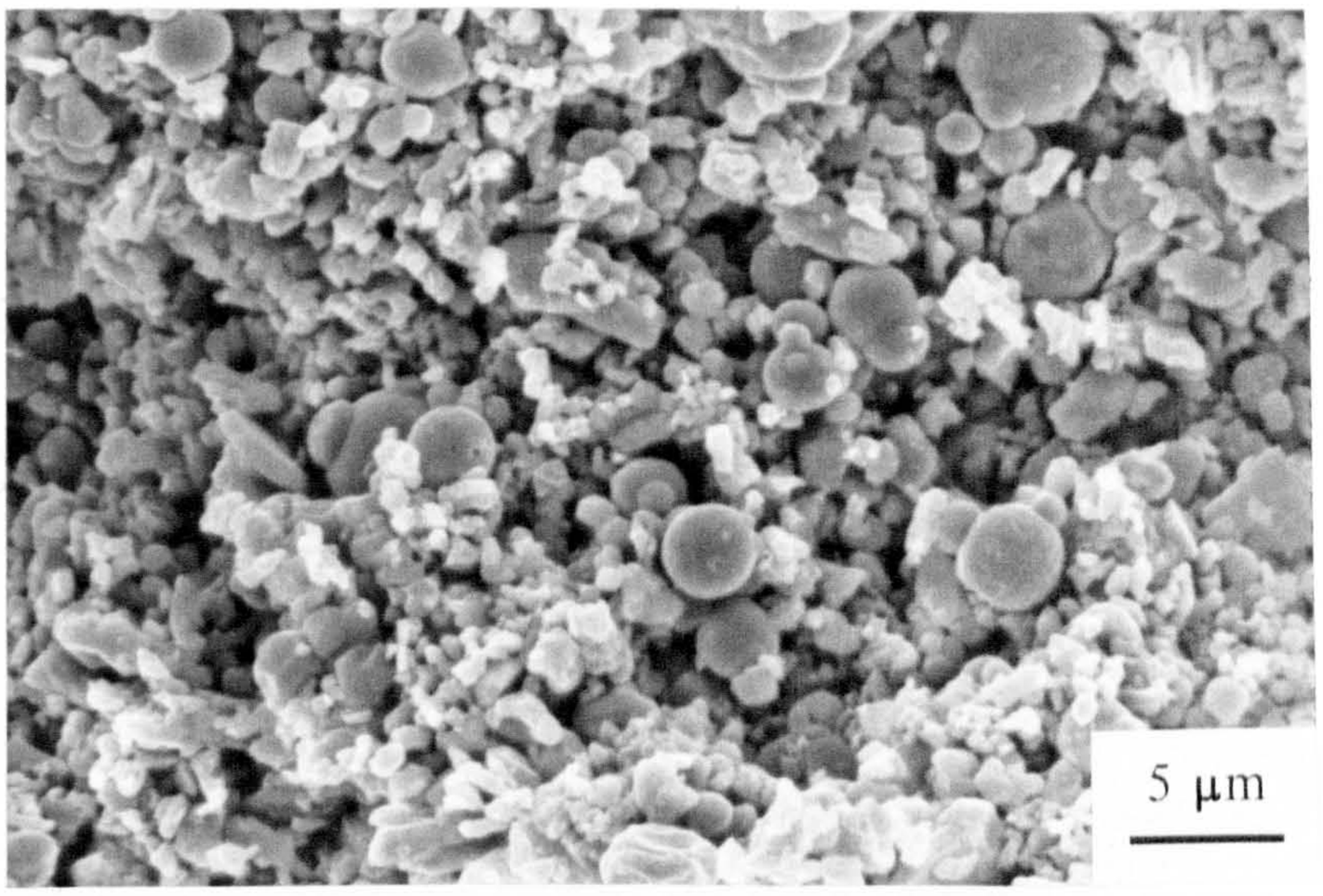

Figure 4.14 SEM photomicrograph (secondary electron image) showing the fracture surface of a composite powder blend B greenbody which has been uniaxially pressed at 93 MPa, showing the absence of deformation of the iron particles even at the higher uniaxial pressure.

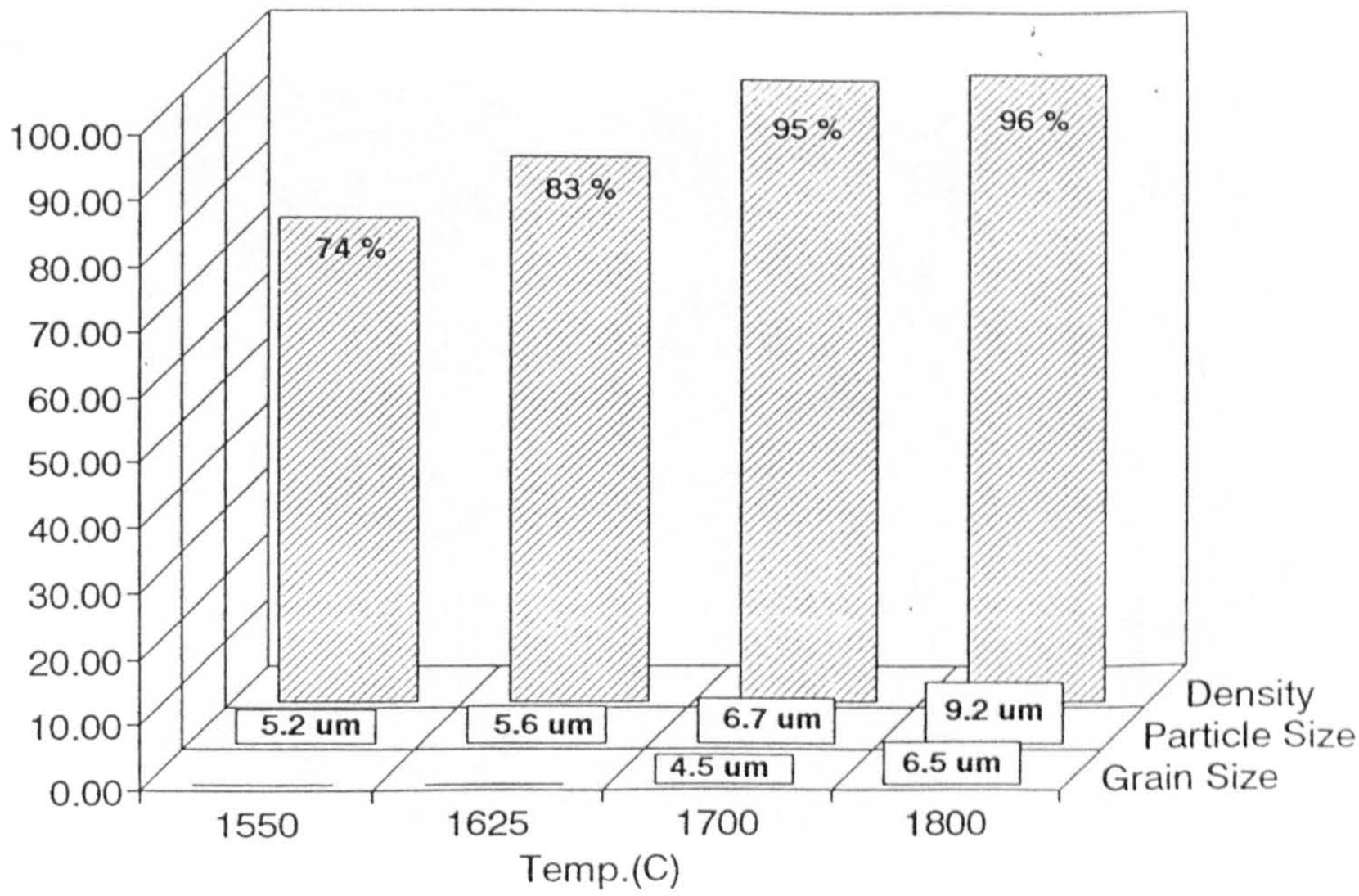

Figure 4.15 Bar chart summarising the densities and microstructural features of the sintered Al_2O_3-Fe composites.

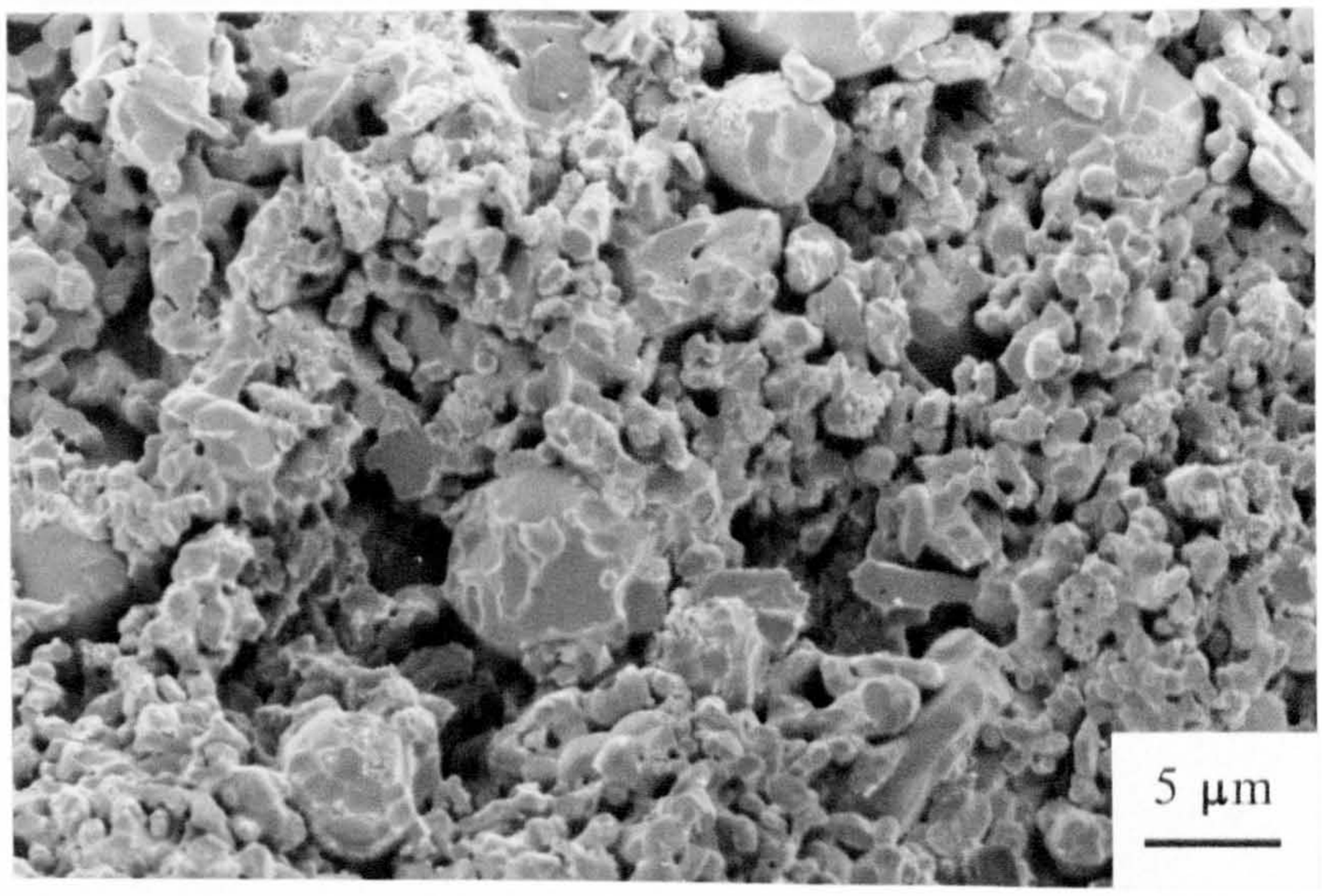

Figure 4.16 SEM photomicrograph (secondary electron image) of the fracture surface of an Al_2O_3-Fe composite sintered at 1550 °C for 1 hour, showing gross porosity due to incomplete sintering of the matrix.

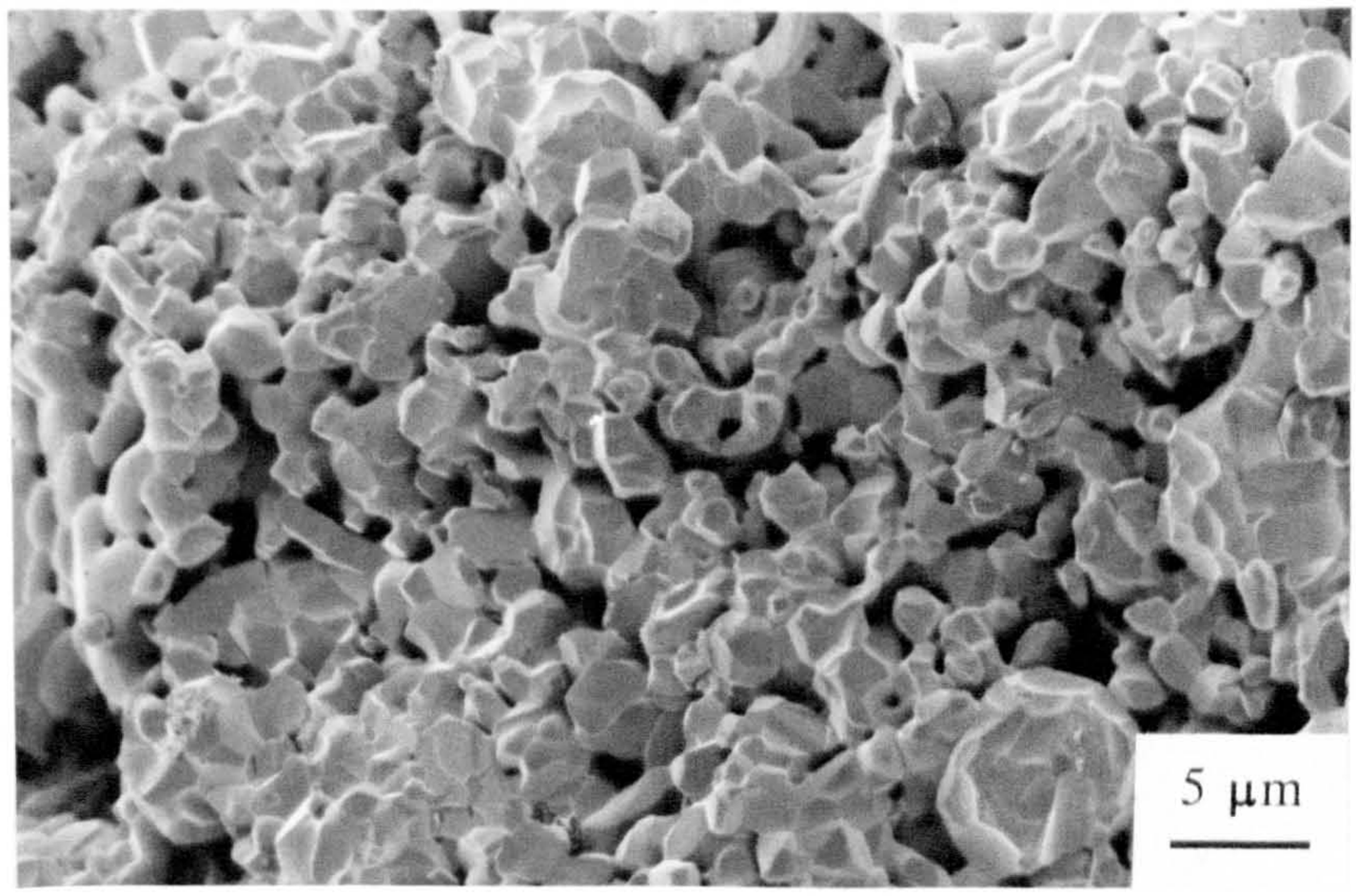

Figure 4.17 SEM photomicrograph (secondary electron image) of the fracture surface of an Al_2O_3-Fe composite sintered at 1625 °C for 1 hour.

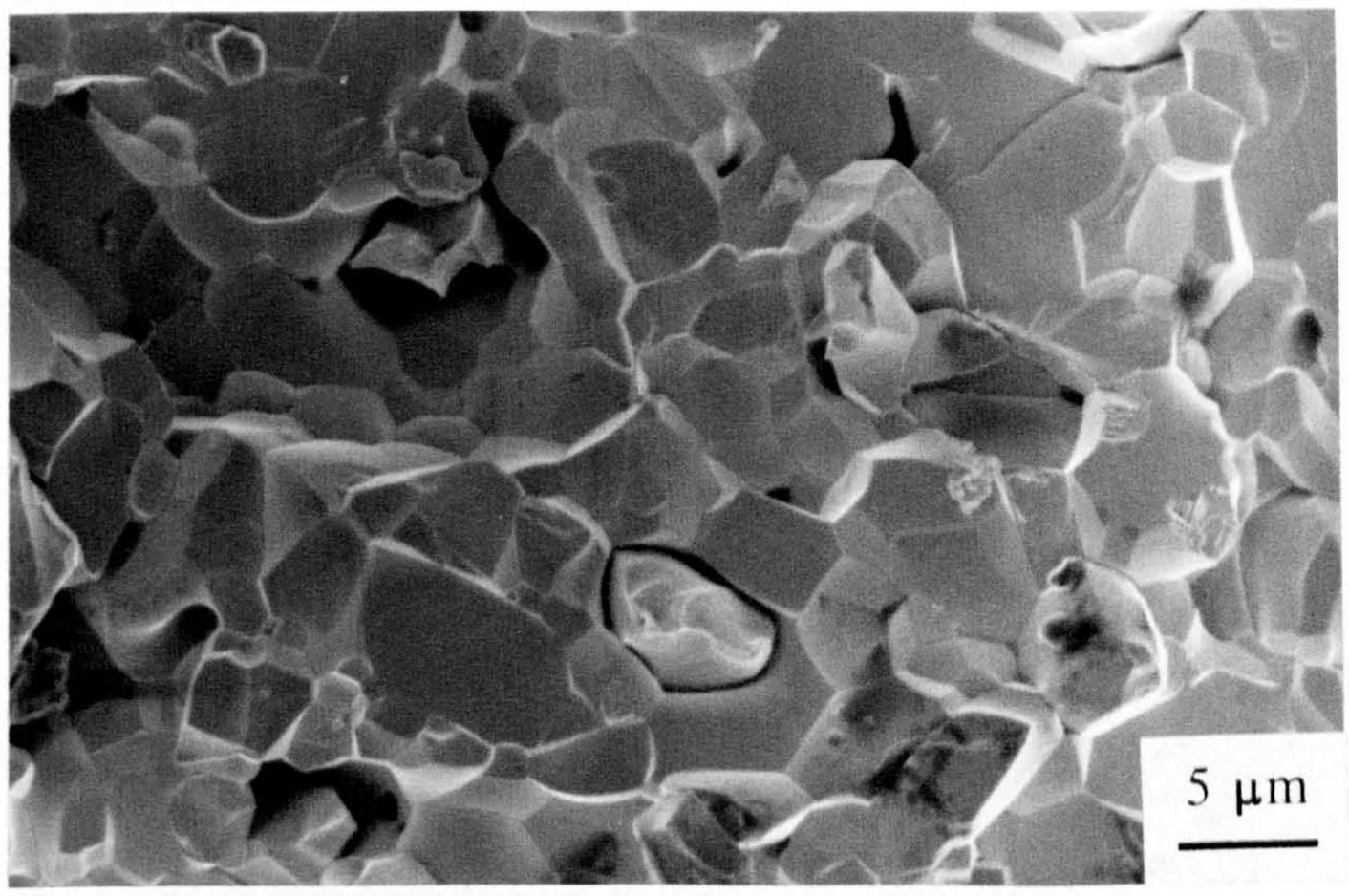

Figure 4.18 SEM photomicrograph (secondary electron image) of the fracture surface of an Al_2O_3-Fe composite sintered at 1700 °C for 1 hour, showing improved matrix sintering.

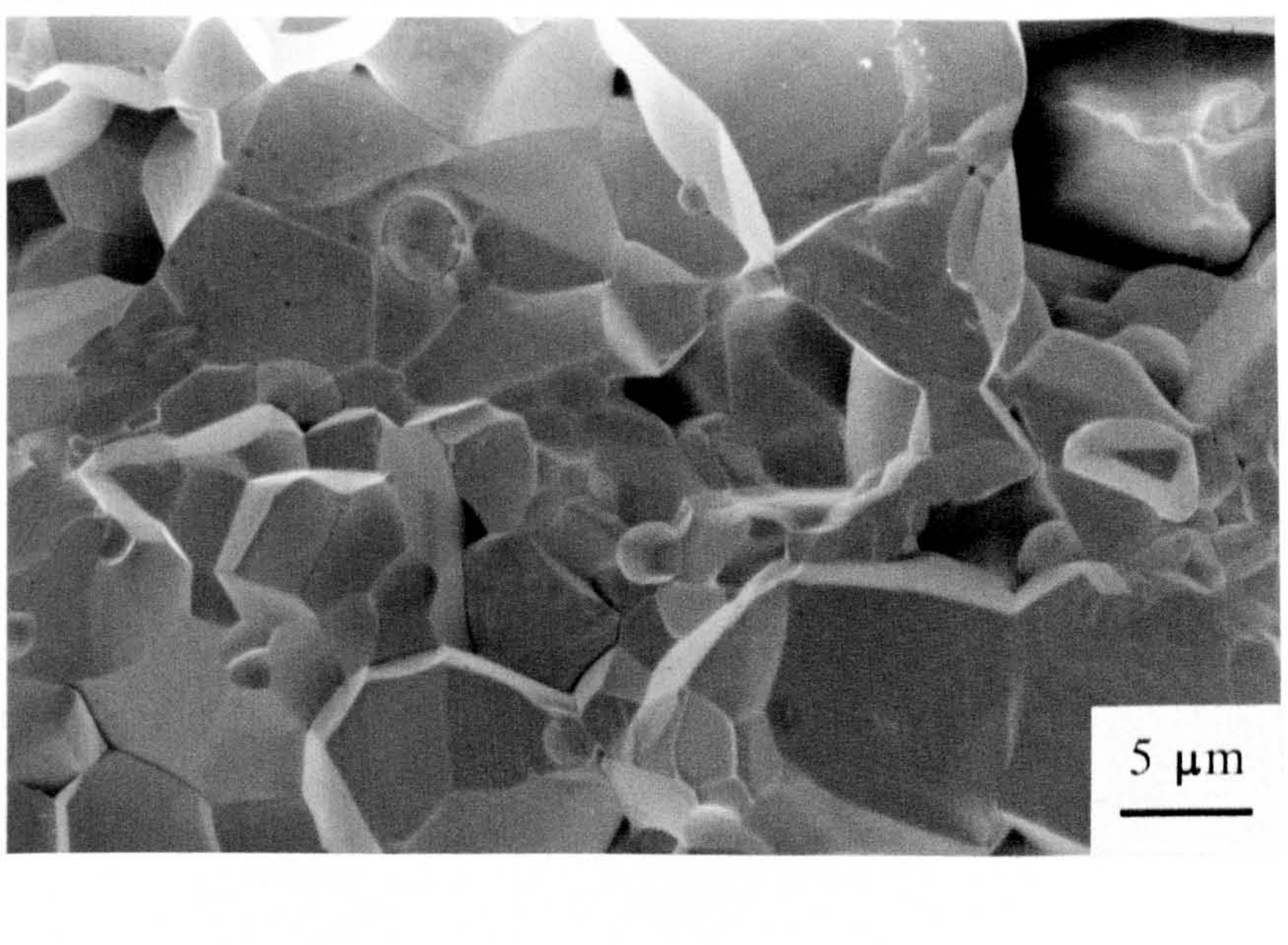

Figure 4.19 SEM photomicrograph (secondary electron image) of the fracture surface of an Al_2O_3-Fe composite sintered at 1800 °C for 1 hour. Note the gradual increase in matrix grain size as the sintering temperature is increased (figures 4.16 to 4.19).

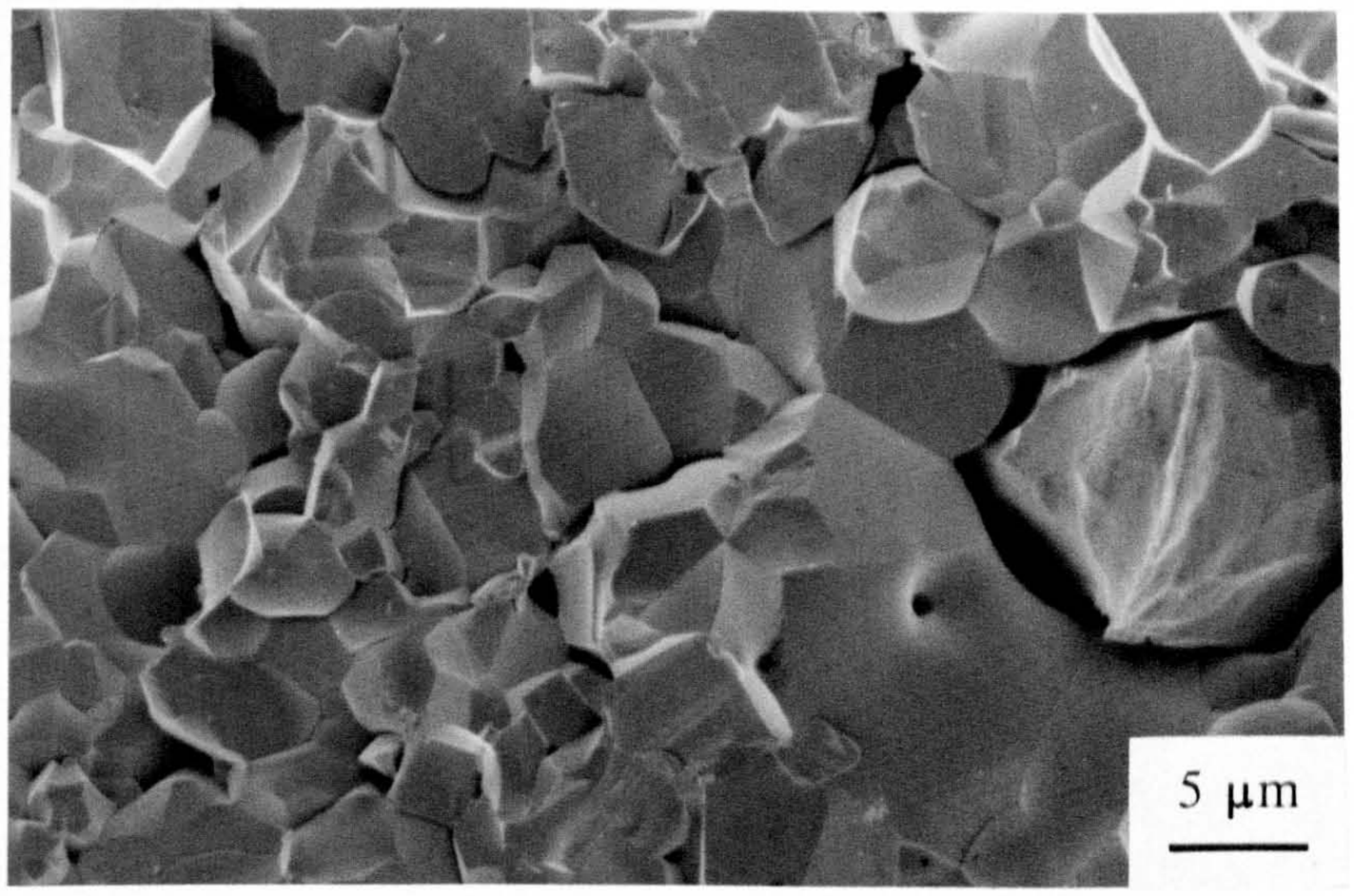

Figure 4.20 SEM photomicrograph (secondary electron image) of the fracture surface of an Al_2O_3-Fe composite sintered at 1700 °C for 2 hours, showing the increase in matrix grain size with increasing dwell time at the sintering temperature (cf. figure 4.18).

CHAPTER FIVE

EVALUATION OF MECHANICAL PROPERTIES

5.1 INTRODUCTION

Chapter 5 presents the results of the mechanical testing of both the hot pressed and sintered Al_2O_3-Fe composite materials. The first section concentrates on the fracture toughness and fracture behaviour of the composites, whereas the second section is concerned with the flexural strengths of the composites, which are compared with the hot pressed monolithic matrix alumina. The influence of the composite microstructure and composite fabrication process is discussed in relation to both the fracture behaviour and the flexural strength.

5.2 FRACTURE TOUGHNESS AND K_R CURVE BEHAVIOUR

5.2.1 Single Edge Notched Beam Method

Initial attempts to measure the fracture toughness and K_R curve behaviour of the sintered Al_2O_3-Fe composite material were made using the single edge notched beam (SENB) method. Several test bars of the sintered composite were prepared as explained in chapter 3. Despite using a slow cross-head speed of 0.5 mm min^{-1}, stable crack propagation proved impossible to achieve using this method. Attention was therefore focused on the alternative double cantilever beam

technique, which allowed the use of more controlled force application and in-situ monitoring of crack propagation.

5.2.2 Double Cantilever Beam Method

Stable crack growth was obtained using the DCB method. Table 5.1 shows the resulting crack length and load data for the sintered Al_2O_3-Fe composite material. The corresponding fracture toughness values were calculated using equation 3.3, and hence the K_R curve was constructed, as shown in figure 5.1. The sintered composite exhibits a rather pronounced K_R curve, with the fracture toughness rising linearly from around 3 MPa $m^{½}$ to approximately 8.3 MPa $m^{½}$ for a crack length of 5 mm. The value of K_{Ic} for small crack lengths is in good agreement with that obtained for monolithic alumina using the DCB technique (Trusty, 1994). Since the curve does not show an obvious plateau region (i.e. constant K_{Ic} once a certain crack length has been reached), it is expected that the process zone is not fully developed, and that the maximum fracture toughness may increase further with increasing crack length. Similar K_R curve behaviour was observed following DCB testing of a hot pressed Al_2O_3-20 volume % Fe composite (Trusty, 1994), with the fracture toughness again rising linearly with increasing crack length, reaching a maximum of 6.9 MPa $m^{½}$ for a crack length of 5.4 mm (maximum fracture toughness value modified according to correction by Trusty).

5.2.3 Crack/Ductile Particle Interactions

Figure 5.2 shows photomicrographs taken during a DCB test within the scanning electron microscope. The figure demonstrates a typical route of crack propagation, with the ceramic/metal interface being the favourable path. This indicates that the interface is weak, preventing the exploitation of the ductility of the reinforcing phase. However, the crack path remains relatively tortuous as a consequence of the fact that the metal particles are considerably larger than the grain size of the matrix, hence a contribution to the K_R curve of the sintered

composite is made through the toughening mechanism of crack deflection.

Examination of the fracture surfaces of DCB samples confirms that the increasing toughness is only partly a consequence of plastic deformation of the metallic particles leading to crack bridging. Figure 5.3 shows examples of photomicrographs of the fracture surfaces. In the vast majority of cases, particles visible on a fracture surface have not been plastically deformed by an intercepting crack, but merely have been pulled from their original sockets as a crack has been deflected around the particle and along the ceramic/metal interface. This is shown in figure 5.3 a, and is characterised by the existence of angular impressions of matrix alumina grains on the surfaces of the iron particles, with little or no evidence of plastic deformation or Poisson's contraction. It is apparent that only in a minority of cases is the ductility of the second phase exploited. This occurrence leads to necking of the particle prior to fracture, usually to a point or knife-edge, accompanied by a corresponding Poisson's contraction of the particle, as clearly demonstrated in figure 5.3 b. It may therefore be concluded that only a fraction of the observed increase in toughness is due to plastic deformation of the metallic phase and the corresponding crack bridging mechanism, and that the majority of the improvement in fracture toughness is a result of crack blunting and deflection mechanisms, leading to failure of the ceramic/metal interface and subsequent particle pull-out. This behaviour is indicative of a weak ceramic/metal interfacial bond, and is a common occurrence in several ductile particle reinforced CMC systems due to the poor wettability of ceramic materials by metals (e.g. Moore & Kunz, 1987, Krstic *et al.* 1990, Baran *et al.* 1990, Sun *et al.* 1991, Ashby *et al.* 1992, Vekinis, 1992, Wang *et al.* 1993, Sun, 1993, Shercliff *et al.* 1994, Thompson & Raj, 1994, Trusty, 1994, Zhang, 1995).

5.2.4 Influence of Microstructure

In addition to being strongly dependent on the matrix/particle interfacial strength and the subsequent amount of plastic deformation of the metallic phase, the

fracture behaviour of the composite is also dependent on many other microstructural factors. Firstly, it has been shown that many monolithic ceramics exhibit K_R curve behaviour (cf. § 2.2.3). It is therefore important to consider whether the observed K_R curve behaviour of the Al_2O_3-Fe composite in this particular study can be attributed solely to the influence of the metallic inclusions, or whether a contribution is made by the matrix to the observed increasing fracture toughness with increasing crack length. The fracture surfaces of the composite shown in figure 5.3 reveal an equiaxed grain structure, of relatively fine grain size. Since K_R curve behaviour in some monoliths is due to crack bridging by grains of high aspect ratio and the corresponding frictional forces between individual grains which must be overcome to allow further crack propagation, it is envisaged that no significant contribution to the fracture resistance of the composite is made by the matrix alumina. Furthermore, examination of in-situ crack propagation during DCB tests reveals no evidence of crack wake grain bridging. DCB testing of monolithic matrix alumina of similar grain structure was performed by Trusty (1994), and showed that unstable crack propagation was unavoidable, and a single value fracture toughness of 3.1 MPa $m^{½}$ was calculated. It is this result for the matrix fracture toughness which will be used throughout the remainder of this study.

A further microstructural feature influencing the fracture behaviour and degree of ductile particle crack bridging is the size and morphology of the second phase particles. The theoretical critical particle size required for maximum crack bridging potential may be calculated using the method proposed by Davidge & Green (1968) (see § 2.2.2). As discussed in chapter 4, the critical particle size for this particular composite system is approximately 12 μm for the hot pressed material and 8 μm for the sintered material, the difference arising from the increased thermal residual stress induced during cooling from a higher processing temperature in the case of the sintered composite. As can be seen from table 4.1, the actual mean particle sizes for the hot pressed and sintered composites are 3.9 μm and 6.7 μm respectively. Although both actual values are lower than the

calculated values for optimum bridging potential, the actual and theoretical particle sizes of the sintered material are relatively close. It is therefore reasonable to expect a higher degree of ductile particle bridging for the sintered material on the grounds of particle size alone. The shape of the inclusions is also a critical factor in determining the degree of ductile particle bridging, especially since the ceramic/metal interfacial strength is low. A particle having an irregular shape and re-entrant cavities is more likely to deform plastically due to its degree of mechanical interlocking with the matrix, and its bridging potential is likely to be less dependent on the strength of the interface. Conversely, a regular, near spherical shaped particle is reliant upon the strength of the ceramic/metal interface to successfully bridge a propagating crack. For the Al_2O_3-Fe composites, the hot pressed material appears to show slightly greater irregularity in the shape of the iron particles than the sintered material. It is therefore expected that the hot pressed composite may show a greater degree of ductile particle bridging than the sintered material on consideration of particle shape alone. Given the considerations and requirements regarding the influence of the composite microstructure on the fracture behaviour, it is debatable as to which processing technique would, in theory, lead to the tougher composite.

Figure 5.4 shows a plot of the stress intensity curves with increasing crack length for both the sintered and hot pressed Al_2O_3-Fe composite materials and also hot pressed monolithic alumina (data for hot pressed composite and monolithic alumina after Trusty, 1994). It can be seen that DCB testing of the composites has not shown one composite to exhibit a significantly higher degree of ductile particle bridging than the other. Neither of the composites appears to be able to exploit the full potential of the ductile phase, regardless of particle shape, size and differences in internal thermally induced stress, due to the weak Al_2O_3/Fe interface. The observed difference in K_R curve behaviour between the hot pressed and the sintered composites is thought to be due to the increased levels of porosity present in the sintered material leading to a higher degree of crack blunting. Indeed during in-situ observation of crack propagation, a propagating

crack tip often became "lost" within areas of closed porosity. It has however, been shown that both composites exhibit K_R curve behaviour, resulting in a substantial increase in fracture toughness with respect to the parent matrix material.

5.3 FLEXURAL STRENGTH

5.3.1 Hot Pressed Monolithic Alumina

Table 5.2 presents the results of the 3 point flexure tests performed on hot pressed monolithic alumina. A statistical analysis of monolithic alumina was not performed due to limitations concerning the amount of material available. The mean room temperature flexural strength of 464 MPa is in good agreement with the literature for a fine grained, hot pressed alumina (Morrell, 1985).

5.3.2 Hot Pressed Composite

Table 5.2 also presents the results of the 3 point flexure tests performed on the hot pressed Al_2O_3-Fe composite. The room temperature flexural strength was found to be 641 MPa (at P_s=0.5). The increase in flexure strength of almost 40 % over the monolithic Al_2O_3 appears to be in agreement with the trends observed by Tuan & Chen (1995), who concluded that increasing the inclusions content increased the flexural strength of an Al_2O_3-Ag composite (up to 15 %), and that the greater inclusion content caused refinement of the microstructure. The matrix grain sizes for the hot pressed Al_2O_3-Fe and hot pressed monolithic Al_2O_3 were 1.4 μm and 2.1 μm respectively. Similarly, Wang *et al.* (1993) suggested that during the sintering of an Al_2O_3-Ag composite, the presence of molten silver inclusions at grain boundaries prevents grain growth, thereby refining the microstructure of the alumina matrix. Since the Al_2O_3-Fe composite material is hot pressed (therefore preventing excessive grain growth) and the iron is likely to be almost molten at the processing temperature, the phenomenon of grain refinement is thought to be the cause of the significant increase in flexure strength

observed in this study for the hot pressed composite.

All failures involved unstable crack propagation. Fracture surfaces of a selection of fractured hot pressed specimens were gold coated and examined using the SEM. No difference in the failure mechanism between stronger or weaker samples was established; this was due partly to the difficulty encountered in determining the precise origin of failure for the majority of samples. However, figure 5.5 shows two photomicrographs revealing the origin of failure in a hot pressed Al_2O_3-Fe flexure sample. The flaw responsible for failure in this case appears to be a near-surface large agglomeration of iron particles, present on the face subjected to a tensile stress during flexure testing.

5.3.3 Sintered Composite

Also shown in table 5.2 are the results of the 3 point flexure testing performed on the conventionally sintered Al_2O_3-Fe composite (sintered at 1700 °C for 1 hour). The room temperature strength was found to be 148 MPa (at P_s=0.5). All fractures were catastrophic, and fractured pieces were again retained for examination. The low strength of the sintered composite represents a significant reduction compared to the monolithic matrix alumina, and a dramatic reduction compared to the composite produced by hot pressing. Shercliff *et al.* (1991) found that the incorporation of chopped nickel wires in an alumina matrix resulted in a severe loss in room temperature strength from 400 MPa for the monolithic matrix alumina to 135 MPa for the composite. Such a decrease in strength was attributed to the presence of large flaws acting as sites for crack initiation. Similarly, Zhang (1995) found that sintered composites of Al_2O_3-Ni showed a decrease in flexural strength compared to the monolithic matrix material for inclusion volume fractions of > 12 % Ni, and for sintered Al_2O_3-Ni-Ti composites, a severe decrease in strength was observed in all cases. Zhang concluded that the inclusion of metal particles leads to porosity, agglomerates or other large complex defects which are responsible for the low strength. Also, composites containing

relatively large metal particles suffer a further reduction in strength, as such particles act as large defects.

Clearly, in the hot pressed composite, the metallic particles are beneficial to the flexure strength. However, this is not the case for the sintered composite. It may be concluded that the difference arises from the difficulty of producing dense, fine-grained composites by pressureless sintering.

5.3.4 Statistical Analysis

Weibull plots of (ln ln $(1/P_s)$) against (ln σ_f) are shown in figures 5.6 and 5.7 for the hot pressed and conventionally sintered Al_2O_3-Fe composites respectively. The gradient of the best fit line is equal to the Weibull modulus, m. The Weibull modulus for the two composites was calculated to be approximately equal to 9. The values obtained are comparable with those reported in the literature for particulate CMCs (e.g. 8.4 and 12.2 for Al_2O_3-ZrO_2 (Duan *et al.* 1995)). The plot for the hot pressed composite appears to show a degree of bimodality. For the purposes of calculating the gradient of the best fit line, all 30 data points were taken into account. However, the majority of the set lie on a line of increased Weibull modulus ($m \approx 16$). It is suggested that the lower strength values may be a consequence of surface damage (possibly iron particle pull-out, caused during the grinding and polishing of the flexure samples), whereas the higher strength and higher Weibull modulus group probably failed from internal microstructural defects, although there is no fractography evidence to support this suggestion. The data for the sintered composite, although a slightly smaller set, appear to lie on a line of single modulus.

Any increase in Weibull modulus observed for a CMC is due to the narrowing of the flaw size distribution, rather than a consequence of the higher toughness. Kendall *et al.* followed this by showing that an increase in toughness alone had no effect on the Weibull modulus. However, it was shown that materials displaying

K_R curve behaviour did give an increase in Weibull modulus and hence reliability. This increase was attributed to the fact that the material (ZTA) deviated from ideal Griffith type behaviour. Since the hot pressed Al_2O_3-Fe composite studied in the present work exhibits K_R curve behaviour, and cannot be expected to behave in a purely brittle manner, the theory proposed by Kendall *et al.* could explain the possible increase in Weibull modulus for the composite over that typically calculated for the monolithic matrix Al_2O_3 (e.g. 9.5 for 95 % Al_2O_3, Morrell, 1985).

5.3.5 Influence of Microstructure

The fracture toughness and fracture behaviour of both the sintered and hot pressed Al_2O_3-Fe composites are similar. It is therefore concluded that the large difference in flexural strength between the two composites is due to a difference in the critical flaw size. The critical flaw size a_c may be calculated for each material using equation 1.1. Rearranging the relation to give a_c as the subject (and incorporating a factor of 1.12 to account for the fact that the strength determining critical flaw is likely to be a surface defect) gives

$$a_c = \left\{ \frac{K_{Ic}}{1.12\sigma_f} \right\}^2 / \pi \qquad 5.1$$

Here, σ_f represents the uniaxial tensile fracture stress, calculated from the three point flexural strength using the following standard equation

$$\sigma_f = \frac{\sigma_{bending}}{[2(m+1)^2]^{1/m}} \qquad 5.2$$

where m is the Weibull modulus.

For hot pressed Al_2O_3-Fe and sintered Al_2O_3-Fe, σ_f were 356 MPa and 82 MPa respectively (taking $\sigma_{bending}$ values corresponding to P_s=0.5),resulting in a_c=19 μm and 363 μm respectively. For the hot pressed monolithic Al_2O_3, σ_f was calculated

using equation 5.2 for a range of Weibull moduli between 5 and 12, and found to be between 197 MPa and 286 MPa. Consequently a_c was calculated to be in the range of 29 μm to 63 μm.

The major microstructural features linked to flaw size (and hence fracture stress) for the monolith are grain size and porosity, and for the composites the size of the second phase particles is an additional factor. Density measurements and fractographic studies have revealed the degree of porosity present and the matrix grain size for the three materials (see § 4.2 and 4.4 respectively). Figures 5.8 and 5.9 show typical examples of fracture surfaces of flexure test specimens for the hot pressed and sintered composites.

The relatively low porosity, small grain size and small metallic particle size of the hot pressed Al_2O_3-Fe composite lead to a low critical flaw size (comparable in magnitude to intrinsic microstructural features) and corresponding high flexural strength. The slightly larger grain size of the hot pressed monolithic alumina is thought to increase the critical flaw size, decreasing the flexural strength compared with the hot pressed composite. Microstructural examination of fractured surfaces of the sintered composite has revealed that areas of only partially sintered (therefore porous) matrix material exist in the sintered composite, the magnitude of which corresponds with the calculated critical flaw size.

A further influencing factor is the strength of the Al_2O_3/Fe interface. As the degree of interfacial bonding has been shown to be minimal, it is suspected that the majority of the second phase iron particles are effectively acting as pores, particularly in the sintered composite where the degree of irregularity of the shape of the particles in minimal, thus reducing the potential for mechanical interlocking upon interaction with a propagating crack. It may therefore be concluded that the sintered Al_2O_3-Fe composite tends to behave in flexure as an alumina containing up to 25 % porosity. The fact that the flexural strength of the hot pressed composite is substantially greater than that of the sintered material also suggests

that the degree of matrix/particle interfacial bonding is increased in the former, possibly as a consequence of the forced contact between the ceramic and the metal during hot pressing. An additional possibility is that the mean second phase particle size is smaller, therefore resulting in the generation of a lower thermal stress during cooling from the processing temperature. Furthermore, the processing temperature was 300 °C greater for the sintered material, also resulting in a higher thermal stress on cooling from the processing temperature (see § 4.4.2.2).

5.4 CONCLUSIONS

This chapter has presented the results obtained from experimental evaluation of the fracture toughness and flexure strength of both the hot pressed and the sintered Al_2O_3-Fe composite materials. The properties of hot pressed monolithic Al_2O_3 are also given to enable a direct comparison between the composites and the parent matrix material in terms of their mechanical properties. The fracture toughness and fracture behaviour of the sintered composite material has been evaluated using the DCB method. It has been found that the composite exhibits K_R curve behaviour, and that the increase in fracture toughness observed is a consequence of the second phase particles. However, the full toughening potential of the ductile metal particles is not exploited, due to a weak ceramic/metal interface. The K_R curve behaviour is therefore attributed only partly to the mechanism of ductile particle bridging; the remainder of the toughening increment being due to crack deflection and subsequent particle pull-out, and crack blunting in areas of increased porosity. The behaviour is similar to that found previously for the hot pressed composite. Both composites are substantially tougher than the monolithic matrix material.

The flexure strength of the composites has been evaluated using a standard three point flexure test. It has been shown that the strength of the hot pressed composite is significantly greater than the parent monolithic matrix material, and

this has been attributed to the more refined grain structure of the matrix. However, the strength of the sintered composite was found to be significantly lower than that of the matrix material, due to relatively high degrees of porosity and the poor bonding between the matrix and the second phase particles, resulting in an order of magnitude increase in the critical flaw size.

Table 5.1 Results of DCB testing of sintered Al_2O_3-Fe composites.

a) Sample DCB#1

P (N)	a (mm)	b_c (mm)	t_w (mm)	t_p (mm)	h_p (mm)	K_{Ic} (MPa $m^{1/2}$)
54.0	0.71	5.64	0.89	2.21	4.96	4.06
55.0	0.85	5.78	0.89	2.21	4.96	4.20
56.0	1.28	6.21	0.89	2.21	4.96	4.48
56.0	1.50	6.43	0.89	2.21	4.96	4.58
58.0	1.52	6.45	0.89	2.21	4.96	4.75
60.0	1.99	6.92	0.89	2.21	4.96	5.15
61.0	2.81	7.74	0.89	2.21	4.96	5.65
61.0	3.02	7.95	0.89	2.21	4.96	5.75
64.0	3.36	8.29	0.89	2.21	4.96	6.22

b) Sample DCB#2

P (N)	a (mm)	b_c (mm)	t_w (mm)	t_p (mm)	h_p (mm)	K_{Ic} (MPa $m^{1/2}$)
67.0	2.46	5.76	0.75	2.20	4.69	6.34
67.5	4.37	7.67	0.75	2.20	4.69	7.74
68.0	5.05	8.35	0.75	2.20	4.69	8.28

Table 5.2 Summary of results of three point flexure testing for monolithic Al_2O_3, hot pressed Al_2O_3-Fe composite and sintered Al_2O_3-Fe composite.

	Hot pressed Al_2O_3	Hot pressed Al_2O_3-Fe	Sintered Al_2O_3-Fe
No. of samples	5	30	20
Weibull modulus	-	8.8	8.9
Flexure strength (MPa)	464 Mean	641 at P_s=0.5	148 at P_s=0.5

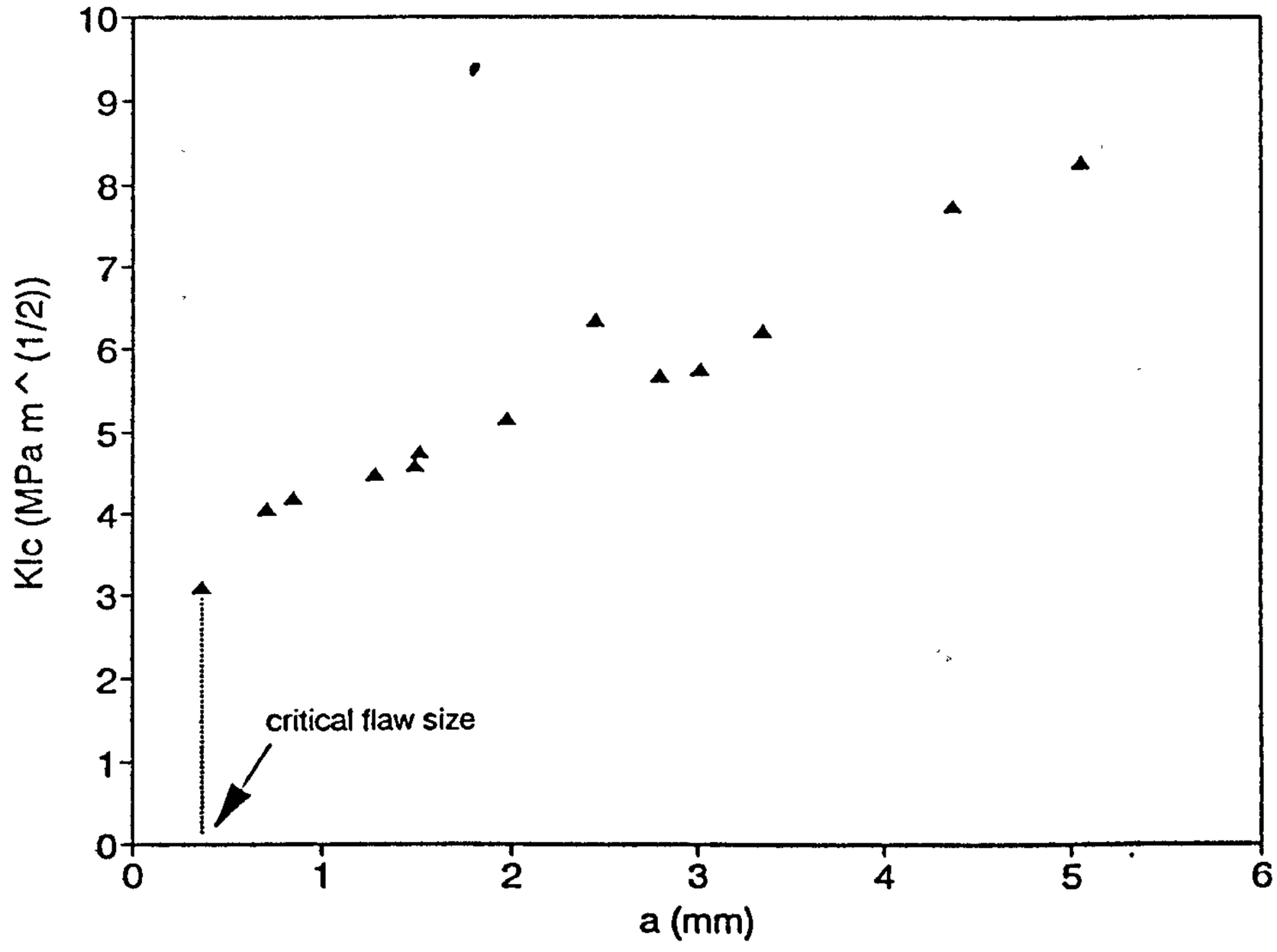

Figure 5.1 Plot showing critical stress intensity factor as a function of crack length (K_R curve behaviour) for sintered Al_2O_3-Fe composite material (determined by DCB technique). Data are taken from two DCB specimens.

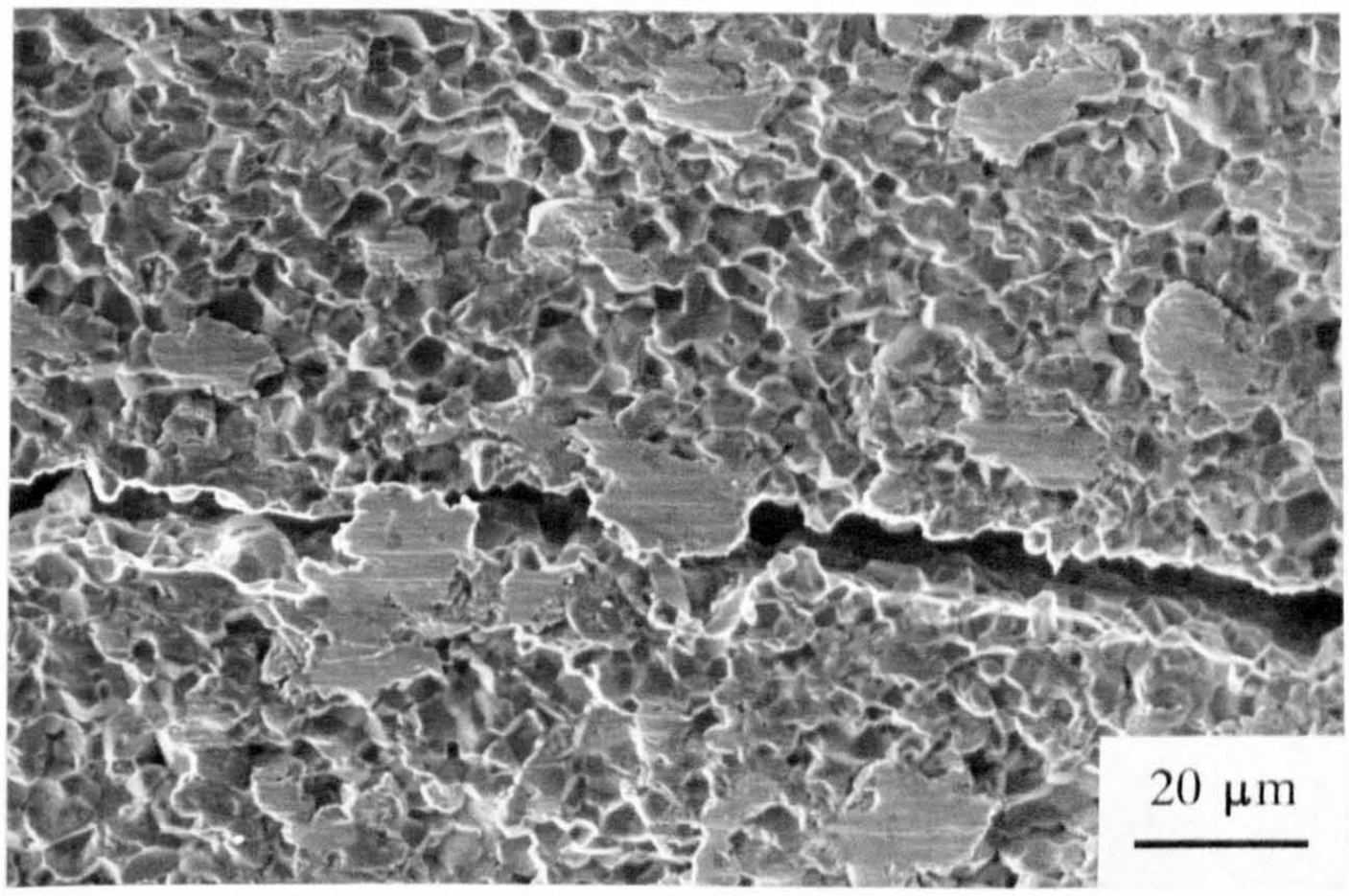

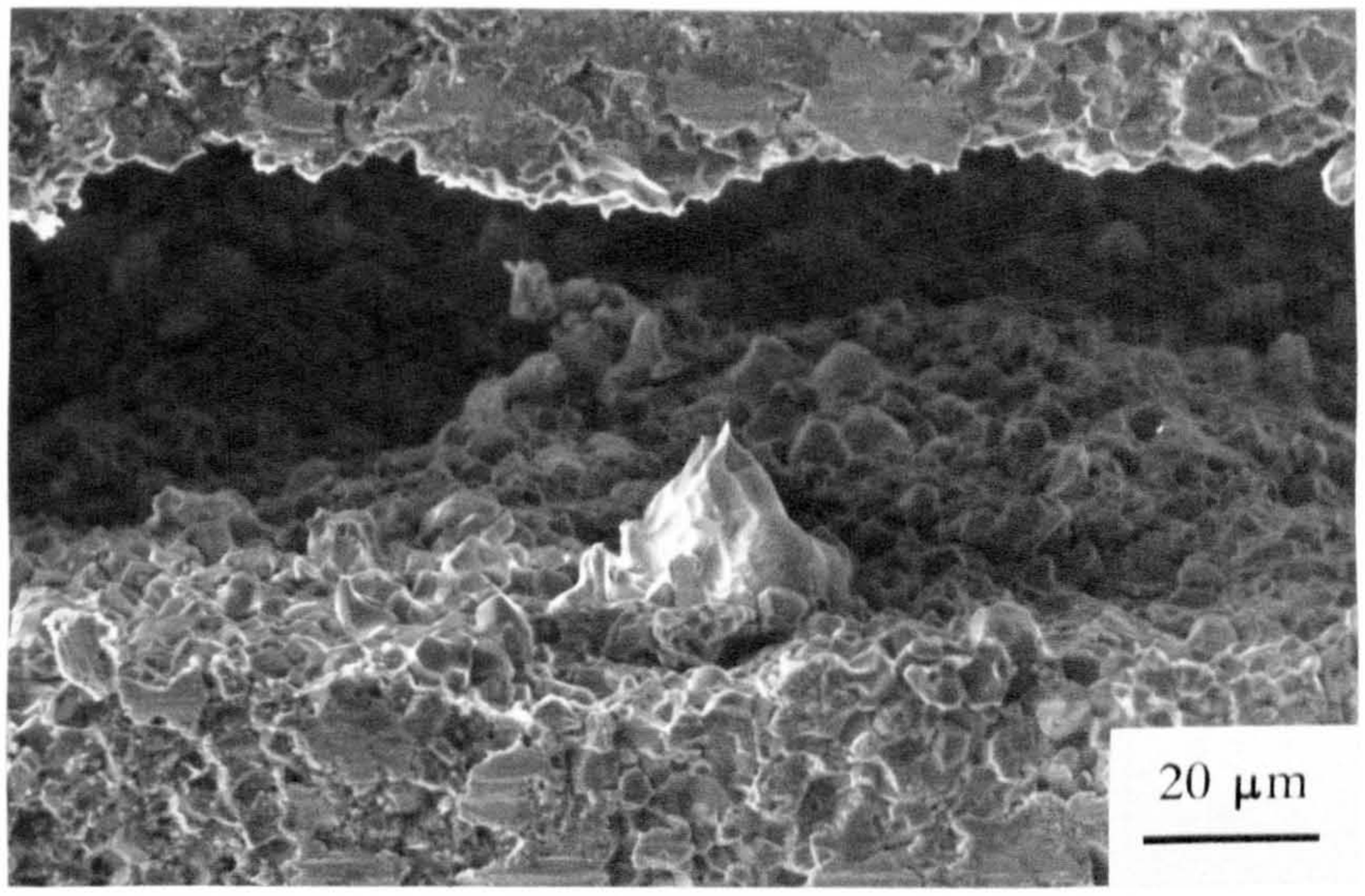

Figure 5.2 SEM photomicrographs (secondary electron images) of sintered Al_2O_3-Fe composite during DCB testing. The direction of crack propagation is from right to left. Note that ceramic/metal interfacial failure occurs in preference to plastic deformation and bridging behaviour.

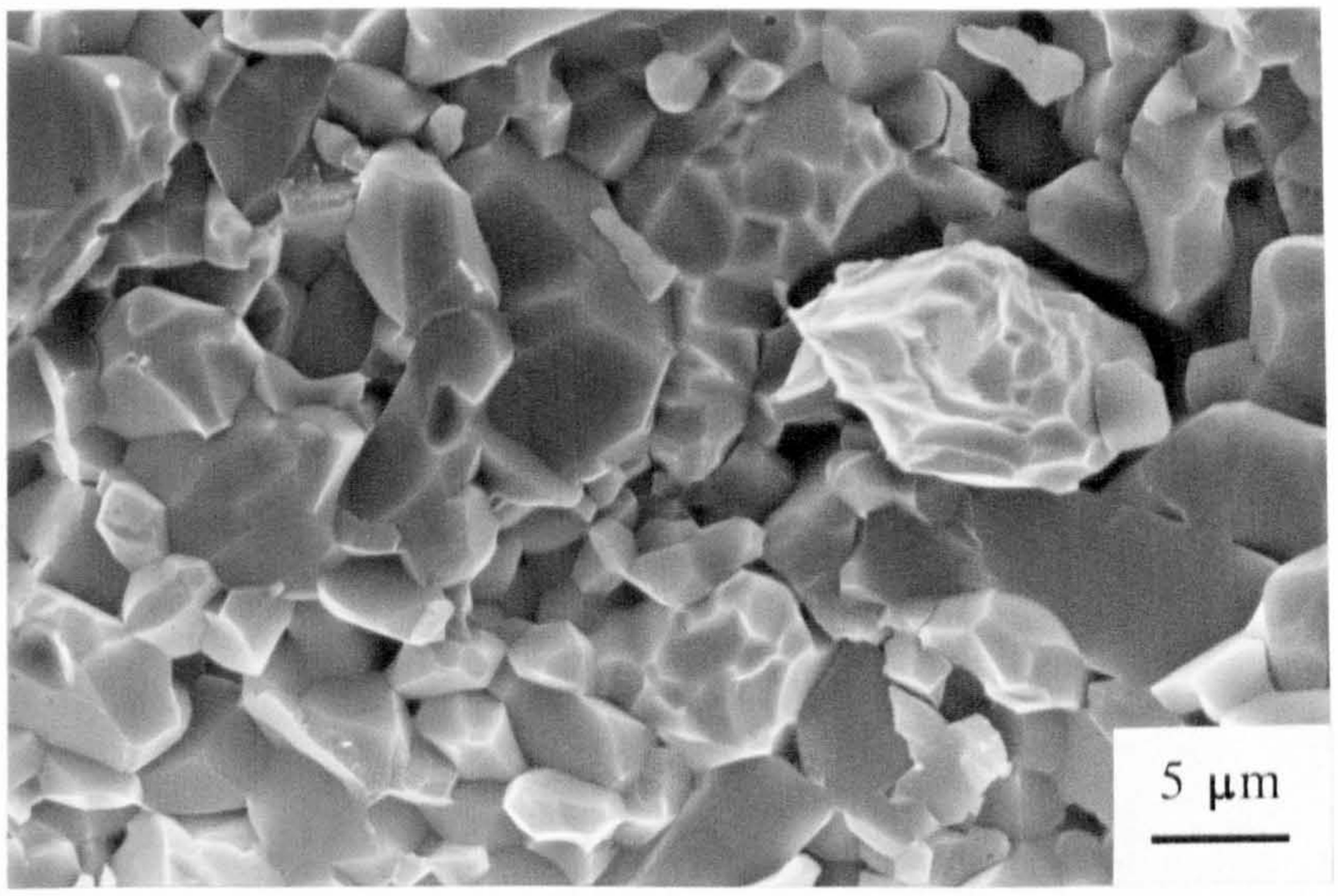

a)

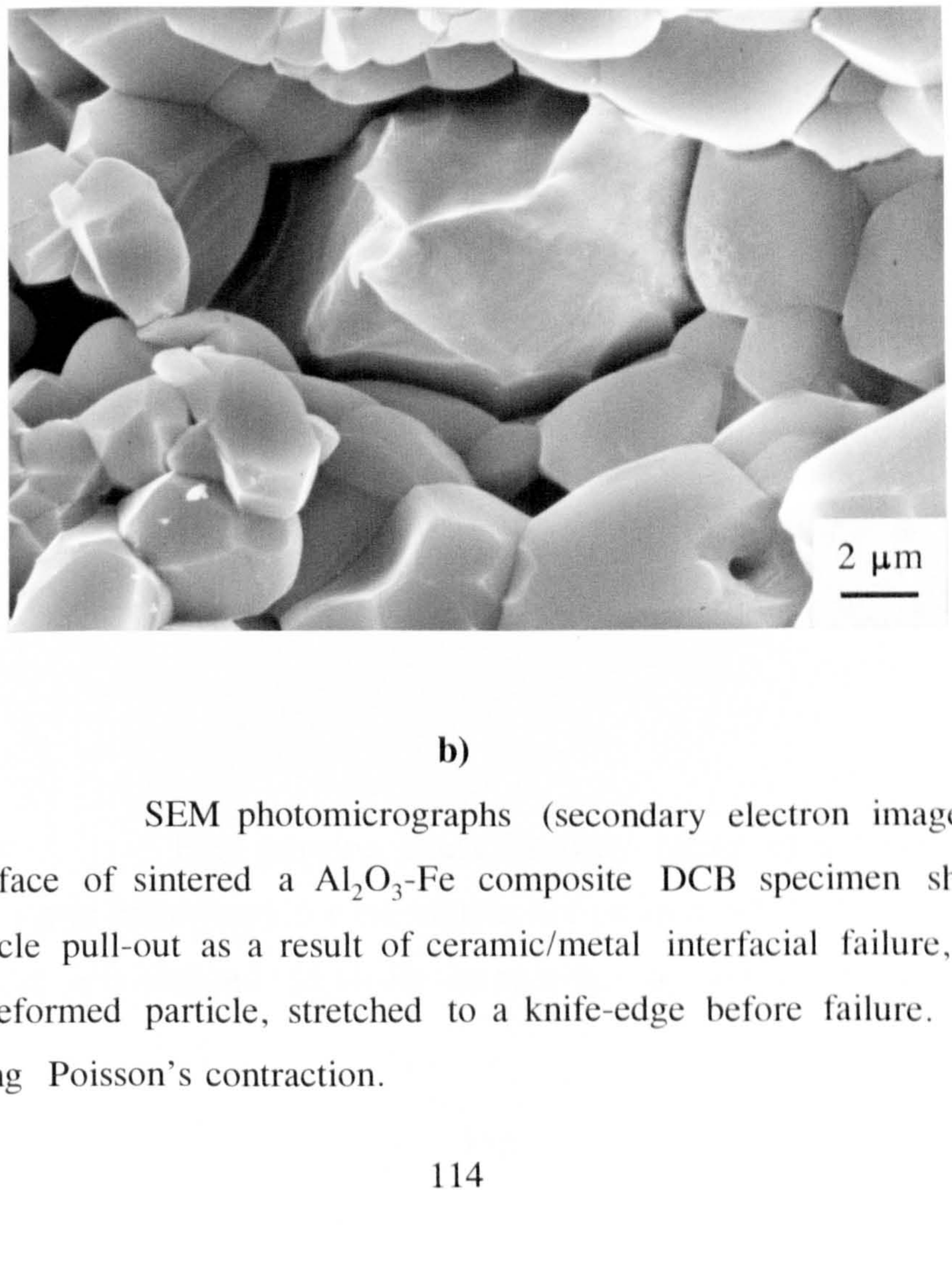

b)

Figure 5.3 SEM photomicrographs (secondary electron images) of the fracture surface of sintered a Al_2O_3-Fe composite DCB specimen showing **a)** ductile particle pull-out as a result of ceramic/metal interfacial failure, and **b)** a plastically deformed particle, stretched to a knife-edge before failure. Note the corresponding Poisson's contraction.

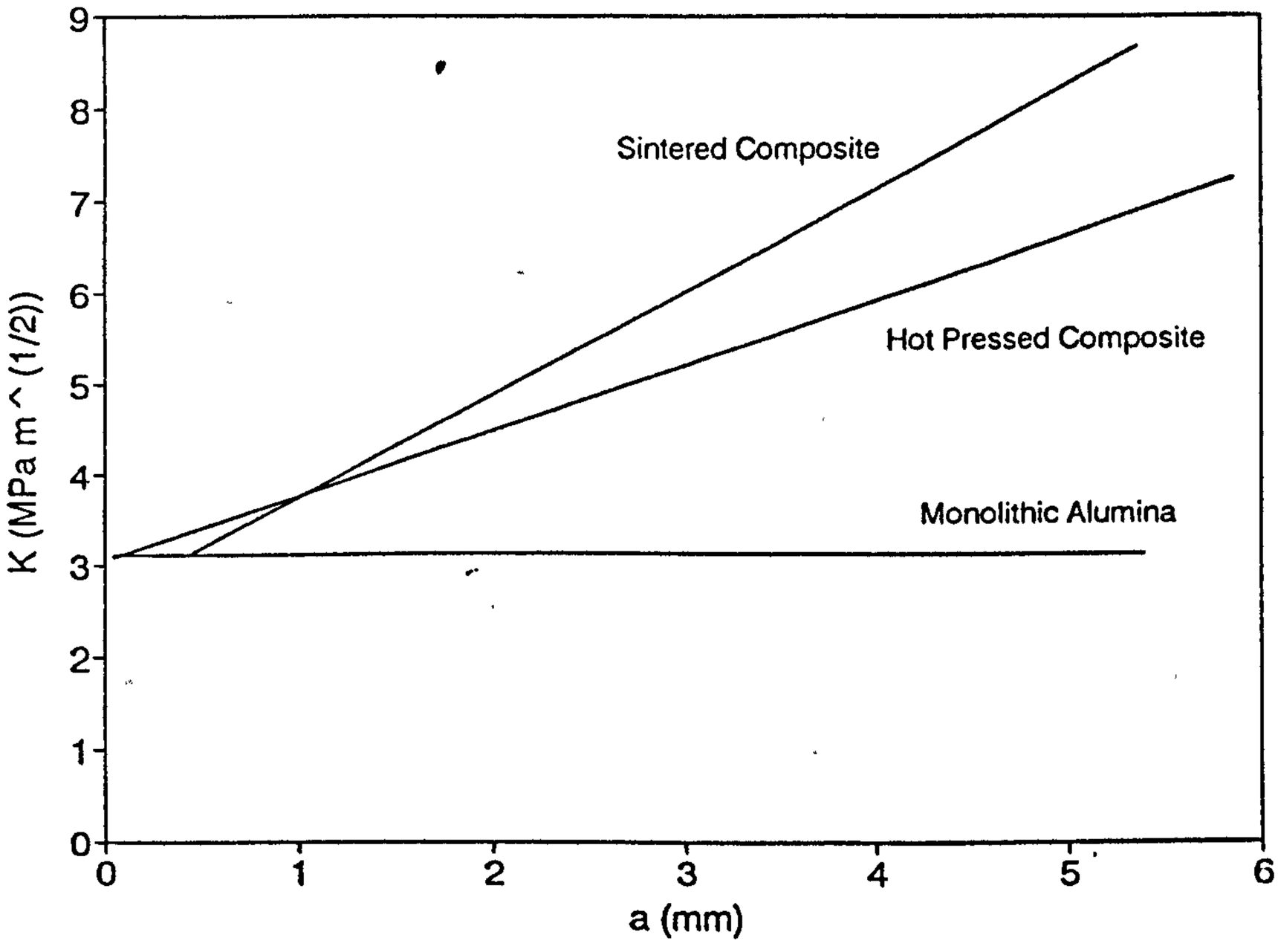

Figure 5.4 Plot showing stress intensity factor as a function of crack length (K_R curve behaviour) for monolithic hot pressed Al_2O_3, hot pressed Al_2O_3-Fe composite and sintered Al_2O_3-Fe composite. Individual data points omitted for clarity.

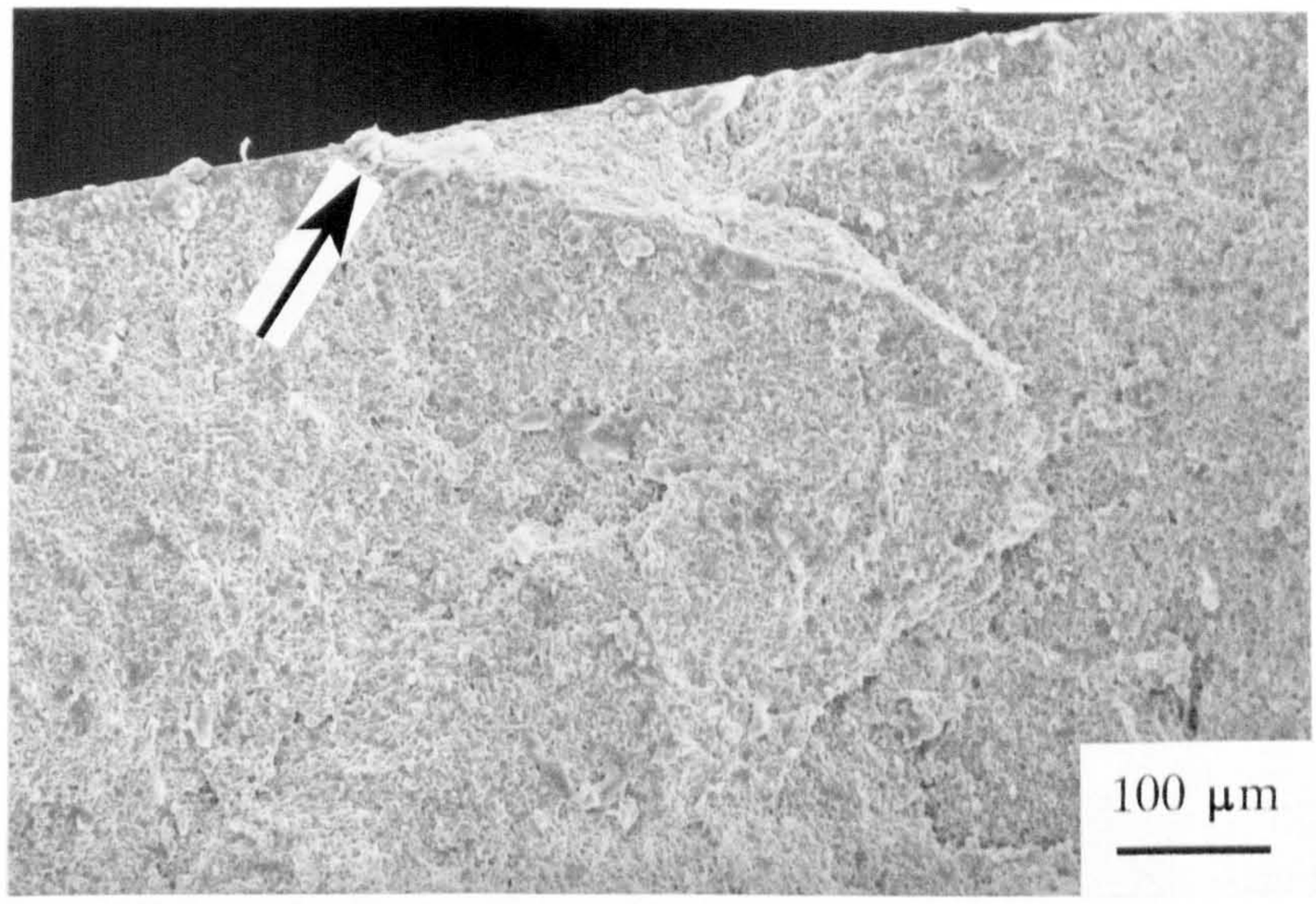

a)

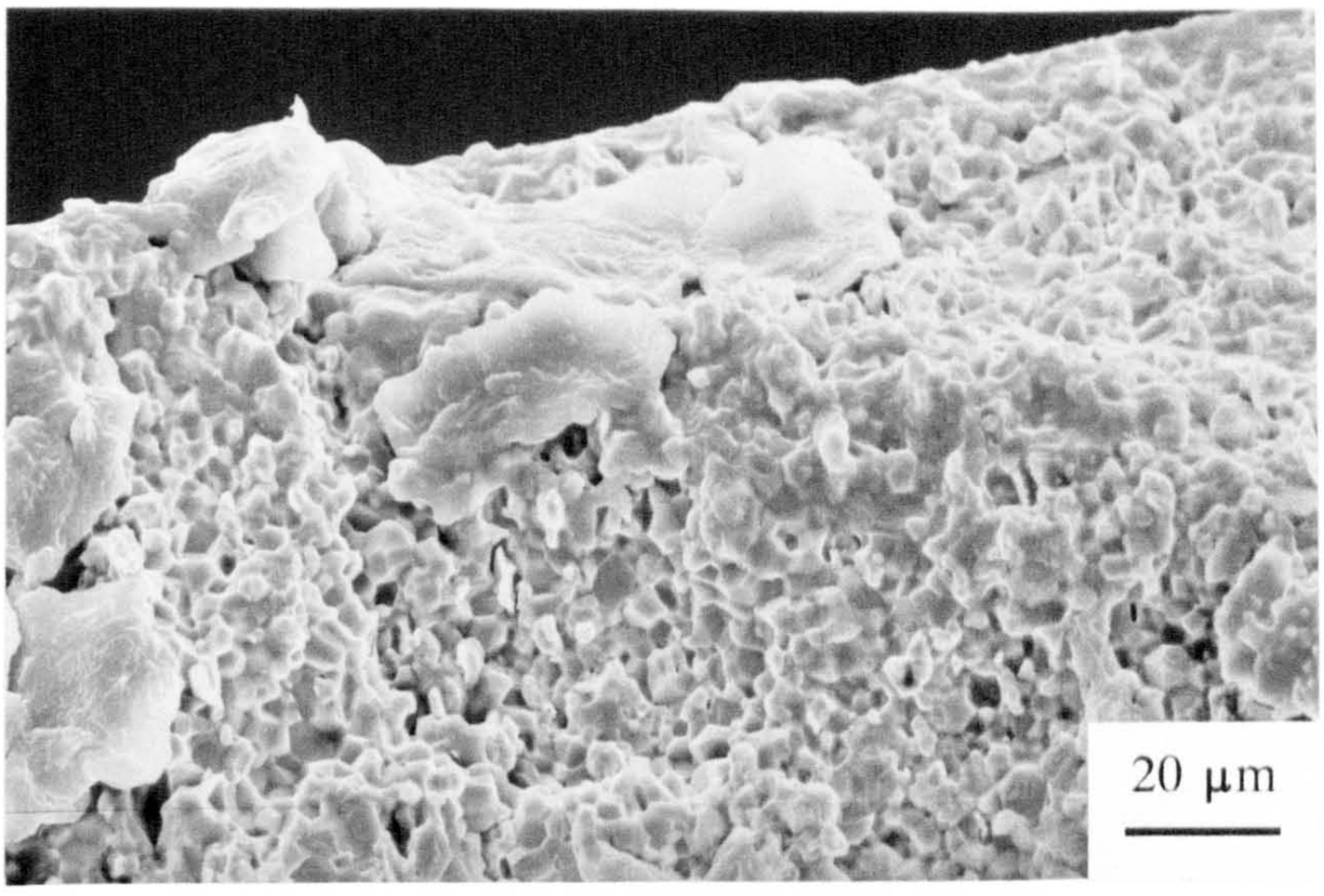

b)

Figure 5.5 SEM photomicrographs (secondary electron images) showing the fracture surface of a hot pressed Al_2O_3-Fe composite flexure specimen. The suspected failure origin is a large agglomeration of Fe particles near to the tensile free surface (arrowed in **a)**, magnified in **b)**).

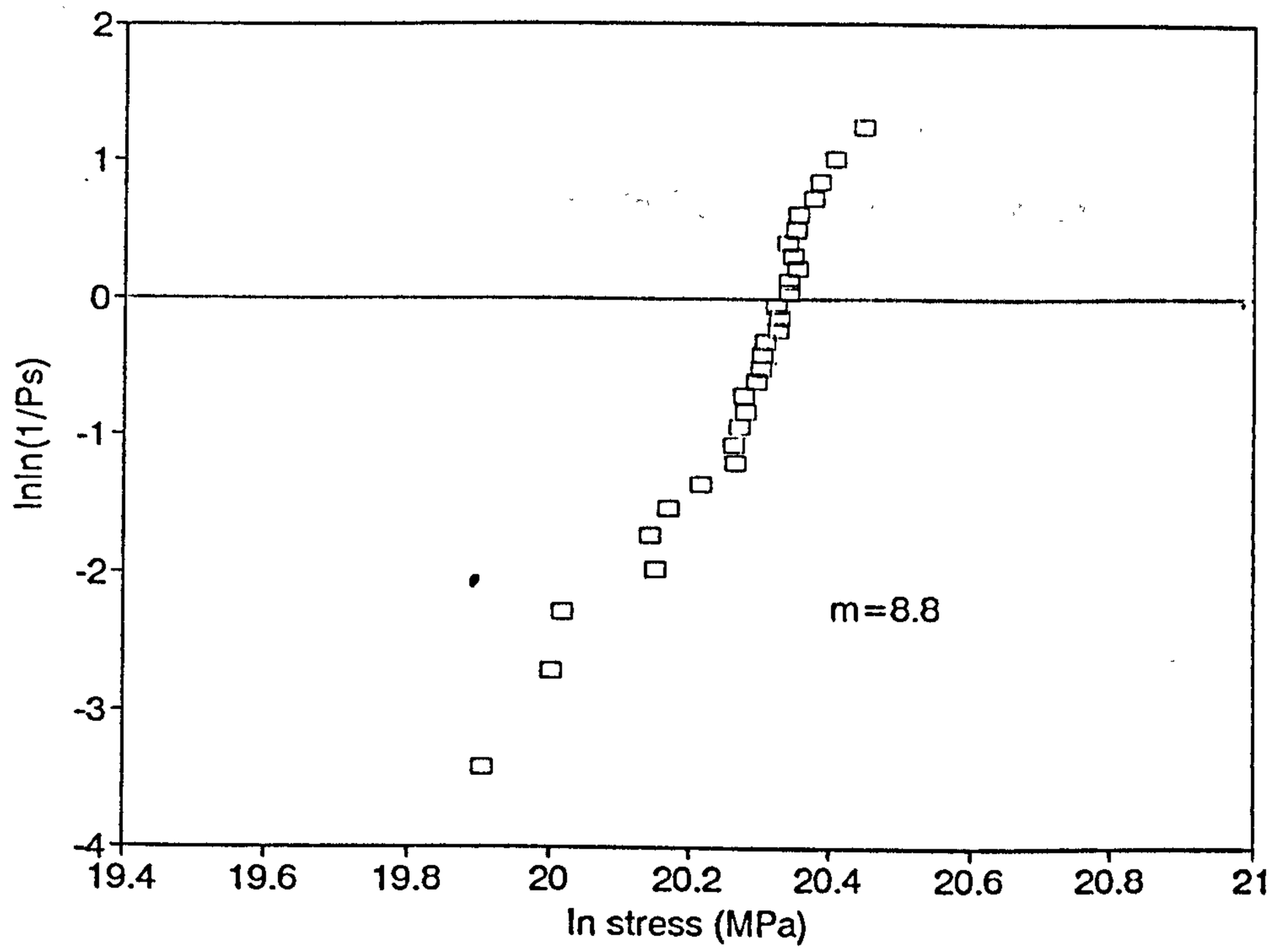

Figure 5.6 Weibull plot for the hot pressed Al_2O_3-Fe composite material. Note the possible bimodality.

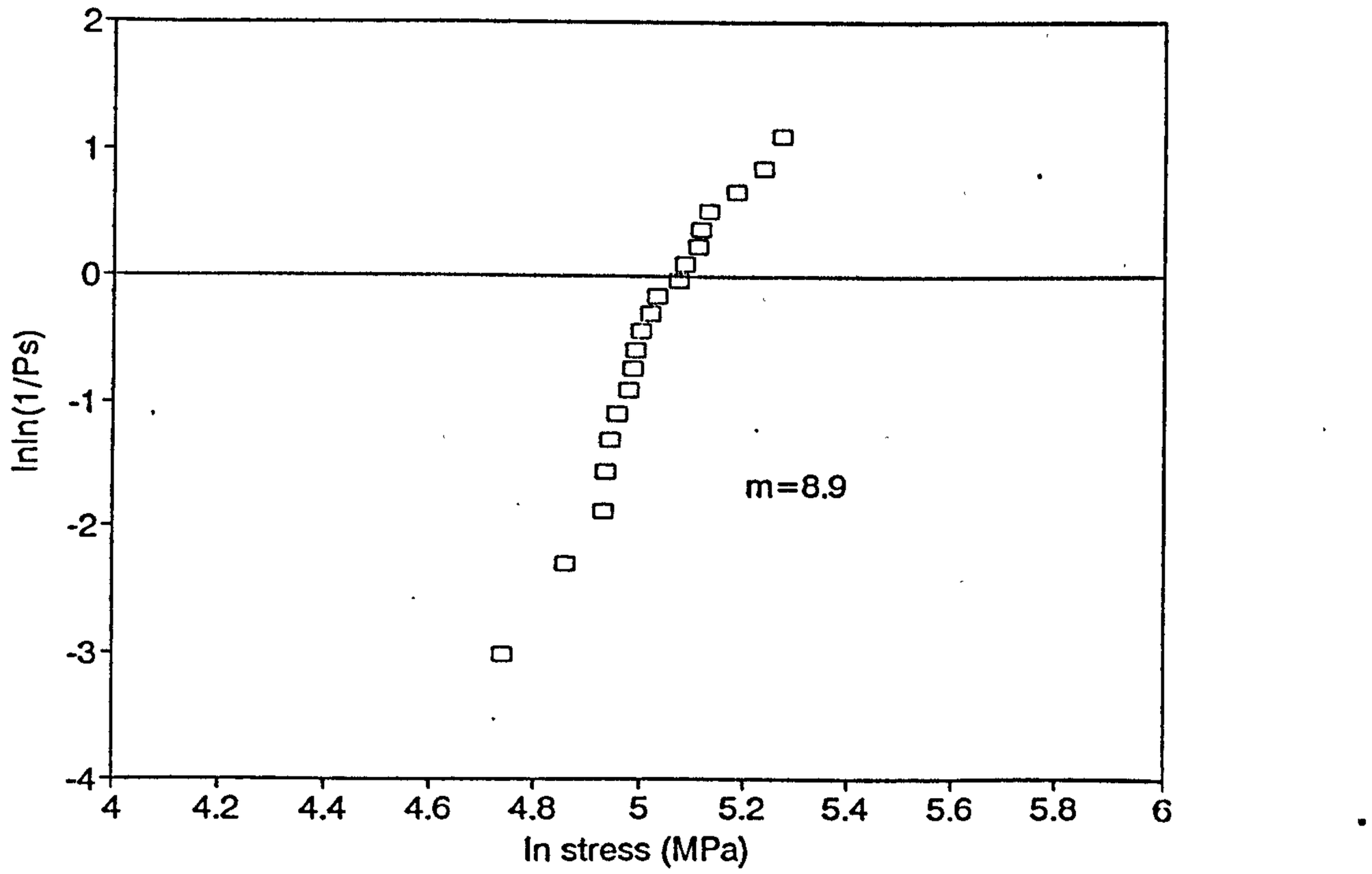

Figure 5.7 Weibull plot for the sintered Al_2O_3-Fe composite material, showing the data to lie on a line of single gradient.

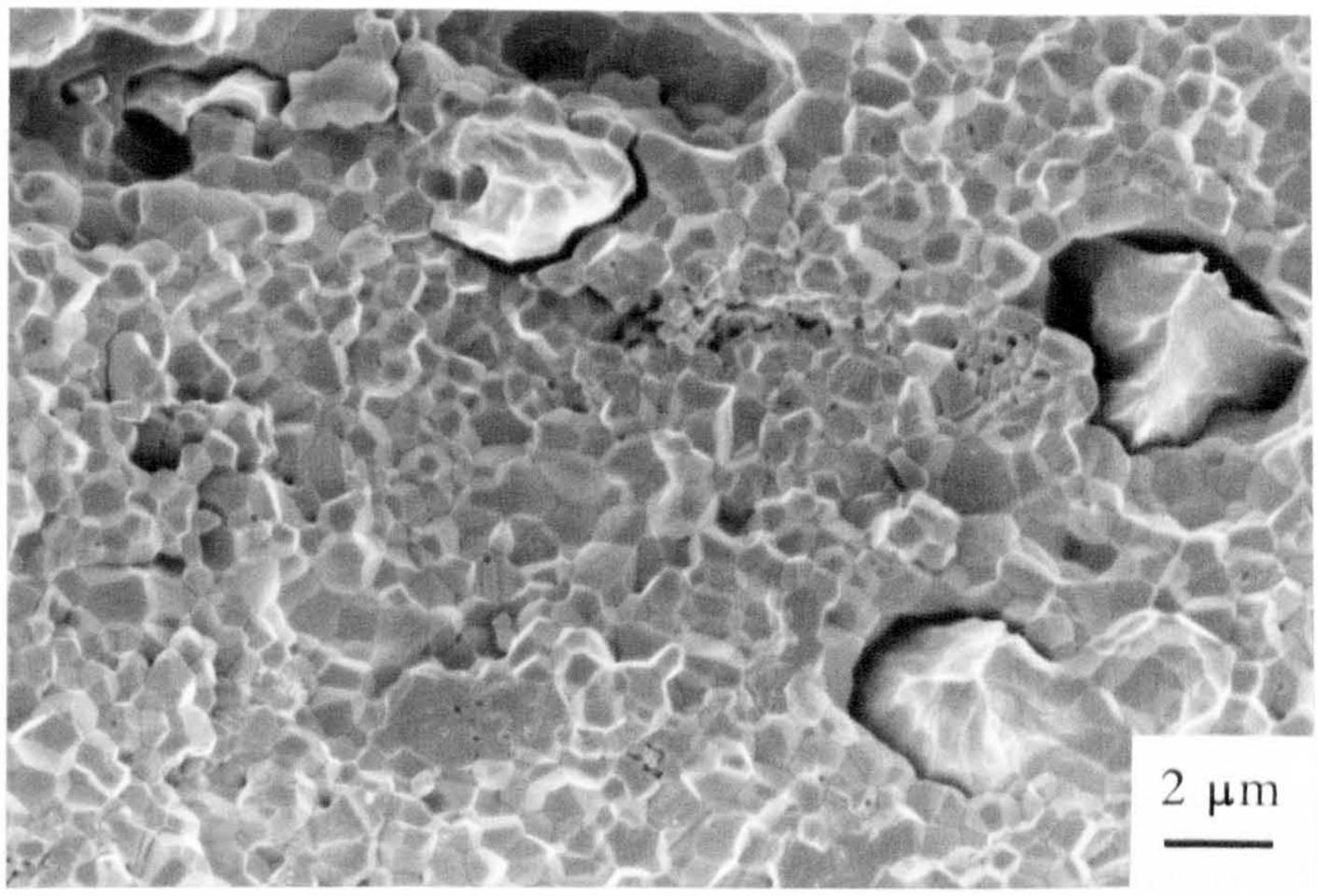

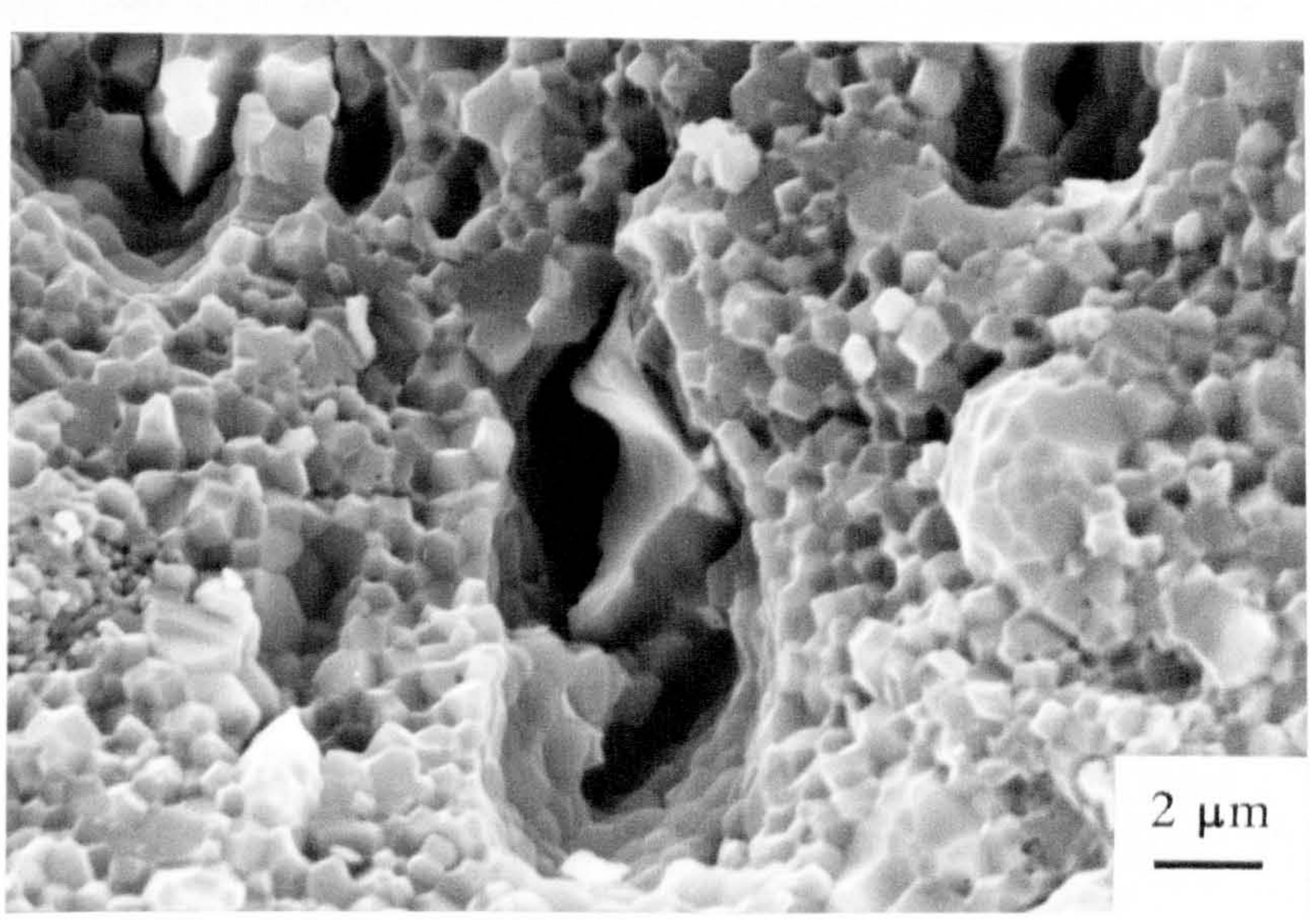

Figure 5.8 SEM photomicrographs (secondary electron images) showing typical fracture surfaces of hot pressed Al_2O_3-Fe composite flexure specimens.

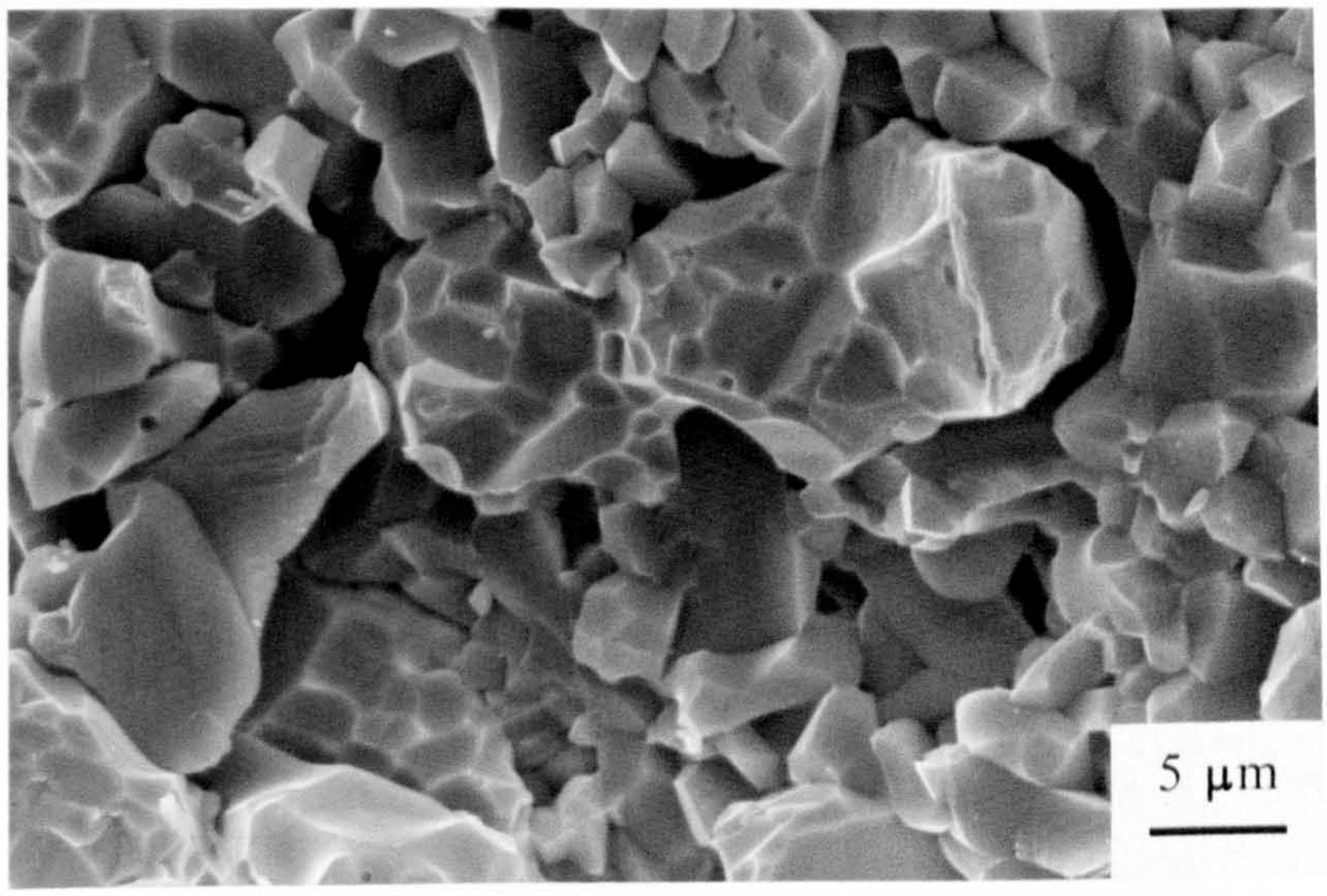

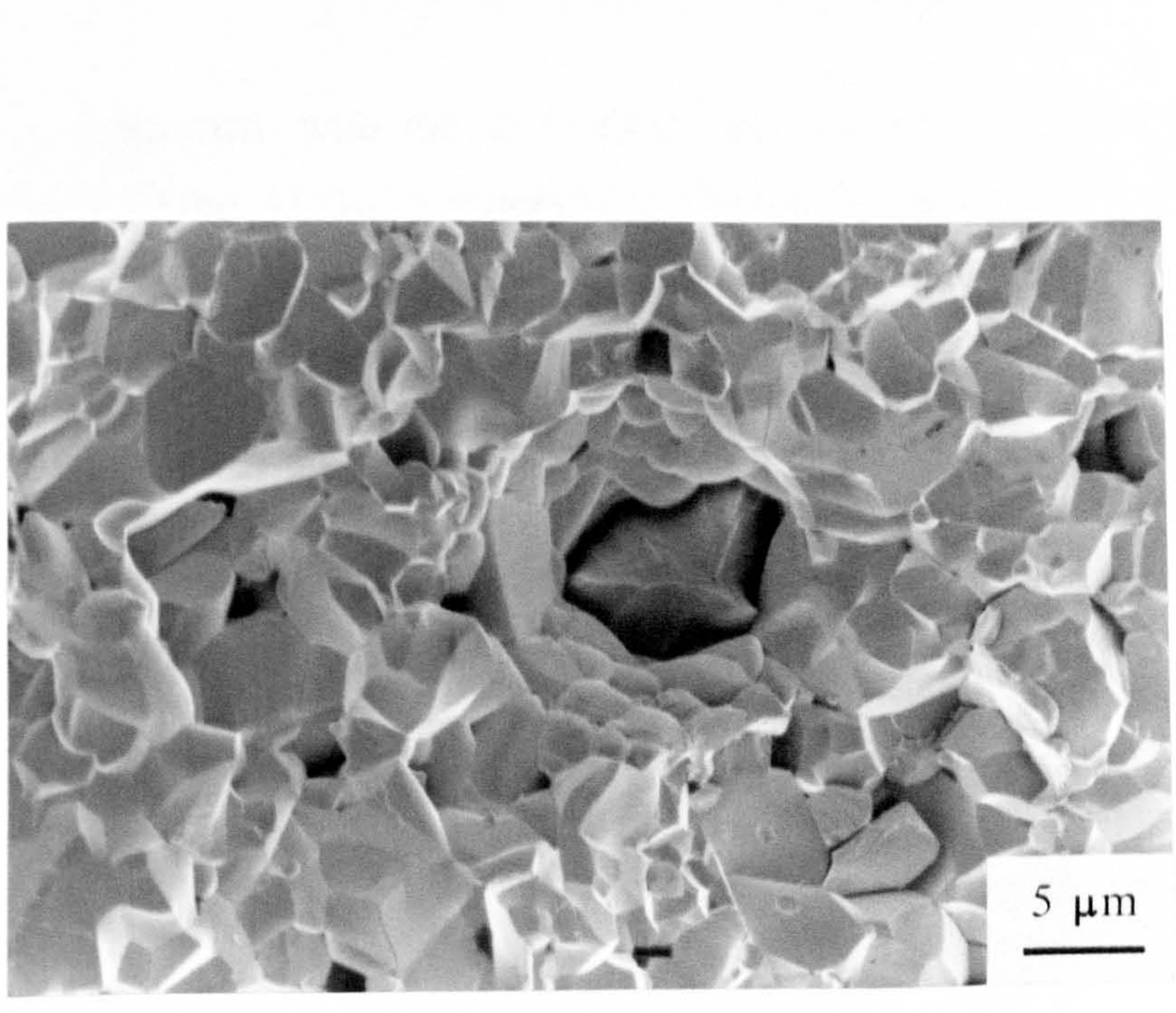

Figure 5.9 SEM photomicrographs (secondary electron images) showing typical fracture surfaces of sintered Al_2O_3-Fe composite flexure specimens. Note the increased porosity and fewer plastically deformed particles compared to figure 5.8.

CHAPTER SIX

THERMAL SHOCK BEHAVIOUR AND THEORETICAL ANALYSIS

6.1 INTRODUCTION

Chapter 6 is concerned with the evaluation and understanding of the thermal shock behaviour of the Al_2O_3-Fe composites produced in this study. The problem has been approached in several ways. Firstly, experiments were conducted to ascertain that any degradation in strength observed following thermal shock treatment was a direct consequence of the rapid change in external temperature imposed on a sample, and not due to a breakdown of the composite at elevated temperature. The influence on the composites of exposure to elevated temperatures was observed using thermal gravimetric analysis and scanning electron microscopy techniques. Experimental work was then carried out in order to determine the critical temperature differential, ΔT_c, at which thermal shock induced cracking is observed, and also the degree of the degradation of retained strength following thermal shock treatments for $\Delta T > T_c$. To enable a direct comparison of results, the thermal shock resistance and retained strength of hot pressed monolithic alumina and a commercially available zirconia toughened alumina composite were also studied. Observation of thermal shock induced damage was made possible by the use of scanning electron microscopy (revealing the nature of crack/ductile particle interactions) and confocal scanning laser microscopy (used for fluorescence work to reveal crack patterns and densities).

Finally, a semi-quantitative analysis of the thermal shock behaviour of the composites has been attempted, combining aspects of the generalised approach proposed by Evans & Charles (1977) with the influence of K_R curve behaviour.

6.2 HIGH TEMPERATURE BEHAVIOUR

Several hot pressed and sintered Al_2O_3-Fe composite specimens were inserted into a furnace at 520 °C. After a dwell time of 15 minutes (to allow equilibrium to be reached), power to the furnace was cut and the samples left to cool to room temperature inside the furnace. Subsequent flexure testing showed that the flexure strength of the samples had not been affected by the heat treatment. Hence it may be concluded that any degradation in strength observed during thermal shock testing is a consequence only of the rapid change in thermal environment imposed by the quench procedure, and not in any way due to exposure to elevated temperatures.

Thermal gravimetric analysis (TGA) was performed on a small (approximately 30 mg) sample of hot pressed Al_2O_3-Fe composite material. The sample was heated in air to 1200 °C at a constant ramp rate of 50 °C min^{-1}. Any change in mass occurring during this cycle was monitored. Figure 6.1 shows the read-out obtained from the TGA experiment, presented as a plot of mass versus temperature. The mass can be seen to increase initially as the temperature is increased from room temperature to around 200 °C, where a plateau is reached. From approximately 200 °C to 700 °C, the mass appears to increase slowly and linearly. Above 700 °C, the mass appears to increase in an exponential form. The behaviour observed suggests that the iron exposed at the surface of the composite is oxidising as the temperature is increased, as one would expect in air. The initial mass gain appears to be parabolic, coinciding with the formation of a passive iron oxide layer preventing further oxidation of the iron. As the temperature is further increased beyond 700 °C, the rate of gain of mass increases exponentially, due possibly to the breakdown or cracking of the protective iron

oxide layer, thus continually exposing reactive iron to the high temperature atmosphere.

The conclusions reached as a result of TGA were confirmed by examination of polished surfaces of samples of hot pressed Al_2O_3-Fe composite. Specimens were polished to a 1 μm finish before being inserted into furnaces at temperatures of 300 °C, 500 °C and 800 °C and held for periods of 15 minutes and 60 minutes. After this time, the samples were removed and allowed to cool to room temperature, then sputter coated with gold to prevent charging in the scanning electron microscope. Heat treatment at 300 °C for both 15 minutes and 60 minutes had no effect on the appearance of the polished section. Figures 6.2 to 6.5 show the resulting microstructure and surface appearance of the initially polished surfaces of the specimens treated at 500 °C and 800 °C. Treatment at 500 °C resulted in the growth of an acicular phase (thought to be iron oxide) on the exposed surfaces of the iron particles. Increasing the ageing time from 15 minutes to 60 minutes had little effect at this intermediate temperature. However, treatment at 800 °C resulted in a similar needle-like growth after ageing of the sample for 15 minutes, and a dramatic increase of growth after ageing for 60 minutes. Observation of the latter case showed that the iron particles appear to be raised above the polished matrix surface, with extensive growth of acicular iron oxide obscuring the matrix/particle boundaries.

Having ensured that exposure of the Al_2O_3-Fe composite materials to elevated temperatures alone does not contribute to the degradation of strength during any subsequent thermal shock experiments, the formation and influence of the iron oxide was not studied further.

6.3 RETAINED STRENGTH

6.3.1 Hot Pressed Monolithic Alumina

The retained flexural strength of hot pressed monolithic alumina following thermal shock treatments over a range of temperature differentials is shown in figure 6.6. The measured retained flexural strength corresponds favourably with the reported experimental data in the literature for a fine grained monolithic alumina (e.g. Davidge & Tappin, 1967, Hasselman, 1970, Gupta, 1975) and the theoretical predictions proposed by Hasselman (1969) concerning the mechanism of thermal shock induced strength degradation for monolithic ceramics (as discussed in § 2.3.2). The characteristic retained strength versus temperature differential curve shows no strength degradation for temperature differentials of $\Delta T < 200\,^{\circ}C$. The critical temperature differential (ΔT_c) at which strength degradation and therefore cracking is evident occurs at approximately 200 °C. At this point, the retained strength drops dramatically to around 130 MPa. Further increasing ΔT above ΔT_c results in a more gradual degradation of strength. Although only a small number of specimens were tested for each value of ΔT, it can be seen that the degree of scatter in each set of results decreases as $\Delta T > \Delta T_c$. This is consistent with theory in that for $\Delta T < \Delta T_c$, the flexural strength of a specimen is dependent upon the size of the largest flaw (a_c), which may vary considerably within a batch of material, as a_c will depend upon microstructural defects or inhomogeneities introduced during processing and/or machining damage. The scatter in retained flexural strength is reduced for $\Delta T > \Delta T_c$ as the thermal shock induced crack is then the larger strength determining flaw.

6.3.2 Hot Pressed Composite

Figure 6.7 shows the retained flexural strength against temperature differential curve for the hot pressed Al_2O_3-Fe composite. Immediately obvious is the substantially higher retained strength of the composite compared to hot pressed

monolithic alumina over the entire range of ΔT values from 0 °C to 800 °C. Further, the retained strength as a fraction of the initial strength for the hot pressed composite was greater than for monolithic alumina for any given value of ΔT. The critical temperature differential was found to be approximately 300 °C. Another prominent feature of figure 6.7 is the retention of ≈50 % of the original strength at ΔT_c, compared to the monolith showing a decrease of around 70 % at ΔT_c, i.e. the severity of cracking at the critical temperature differential was substantially greater for the monolith. Further, for $\Delta T_c < \Delta T < 500$ °C, the hot pressed composite retains a flexural strength of > 200 MPa. Indeed for treatments of $\Delta T > 500$ °C, it appears that a plateau in retained strength is reached (at around 200 MPa), with minimal additional strength degradation observed for further increases in ΔT.

The effect on ΔT_c of introducing a second phase thereby producing a dual phase or composite ceramic is a controversial matter. Lutz *et al.* (1991) concluded that the ΔT_c for a duplex ceramic is not, or is only slightly reduced compared to the parent monolithic material, and the retained strength is significantly improved. Conversely, Aghajanian *et al.* showed that both the ΔT_c and the retained strength following thermal shock was greater for Lanxide Al_2O_3-Al composites than for monolithic alumina. The hot pressed Al_2O_3-Fe composite of interest in this study shows an improved ΔT_c in addition to an increased retained strength. Hence it may be concluded that the thermal shock resistance of the hot pressed Al_2O_3-Fe composite material is greater in terms both ΔT_c and retained strength than hot pressed monolithic alumina.

6.3.3 Sintered Composite

The retained flexural strength versus temperature differential curve for the sintered Al_2O_3-Fe composite is shown in figure 6.8. The shallow curve shows that no definite ΔT_c value can be defined, although a degree of strength degradation appears to occur for $\Delta T \approx 200$ °C to 300 °C. It is also evident that any strength

degradation is minimal, even for the most severe of thermal shock treatments (i.e. $\Delta T=800\,^{\circ}C$). The most striking difference, however, between the retained strength curves of the hot pressed and sintered composites is the low initial strength of around 150 MPa for the sintered material compared to around 600 MPa for the hot pressed (as discussed in § 5.3). The absolute retained flexural strength of the sintered composite for $\Delta T > 200\,^{\circ}C$ was greater than that observed for monolithic alumina, although lower than for the hot pressed composite. The thermal shock behaviour observed for the sintered Al_2O_3-Fe composite material is similar to that expected for a typical alumina refractory, having a low initial strength and a gradual decrease in retained strength following thermal shock (e.g. Larsen *et al.* 1974, Morrell, 1985). It is apparent, therefore, that the thermal shock resistance of the sintered Al_2O_3-Fe composite is significantly lower than that of the hot pressed composite in terms of the absolute strength exhibited following thermal shock treatment from any given ΔT. However, the relative degree of strength degradation with increasing severity of thermal shock is lower for the sintered material (i.e. the ratio retained strength/initial strength is greater for the sintered material).

6.3.4 Zirconia Toughened Alumina

To enable a comparison between the thermal shock behaviour of the ductile particle toughened alumina composites with the behaviour of a commercially available toughened alumina, a zirconia toughened alumina (ZTA) was subject to retained strength measurements following thermal shock treatment. The resulting retained strength versus ΔT curve is shown in figure 6.9. The ZTA can be seen to behave in a similar fashion to a traditional monolithic engineering ceramic in terms of possessing a definite ΔT_c, accompanied by a sudden loss of strength, followed by a more gradual degradation as ΔT is increased further. In fact the curve is very similar to that shown in figure 6.6 for monolithic alumina. The initial flexural strengths of the two materials were similar. The strength of the ZTA was maintained at this level until $\Delta T=\Delta T_c \approx 250\,^{\circ}C$. Temperature differentials $> \Delta T_c$

resulted in a sudden decrease in retained strength, although the retained strength remains greater for ZTA than for monolithic alumina at all $\Delta T > \Delta T_c$. A similar result concerning the retained strength of ZTA was reported by Thompson & Rawlings (1991). Therefore, the thermal shock resistance of the ZTA is greater than that of the monolithic alumina, both in terms of the critical temperature differential for the onset of strength degradation and the absolute and relative retained strength, although the retained strength as a percentage of the initial strength is substantially lower than for the alumina-iron composite materials.

6.3.5 Discussion

Figure 6.10 shows the curves of retained strength versus temperature differential for all four materials (individual data points have been omitted for clarity). There are several important differences in thermal shock behaviour between the four materials, the most prominent of which is the refractory-like strength degradation exhibited by the sintered alumina-iron composite, compared to the more traditional high strength engineering ceramic behaviour shown by monolithic alumina and ZTA. The hot pressed Al_2O_3-Fe material acts as a high strength engineering ceramic, but also shows high strength retention properties for $\Delta T > \Delta T_c$.

The refractory-like behaviour is typical of several particulate ceramic matrix composite systems (Aghajanian *et al.* 1989, Lutz & Swain, 1991, Lutz *et al.* 1991, Swain, 1991, Janssen *et al.* 1993). Aghajanian *et al.* produced a series of Al_2O_3-Al composites, each having different microstructures as a direct consequence of the various processing methods employed. The mechanical properties and thermal shock behaviour of the composites were studied. It was found that the composite containing the highest levels of porosity exhibited a gradual decrease in retained strength following thermal shock treatment. The same composite was also found to show the lowest flexural strength. It was concluded that the gradual decrease in retained strength, typical of a weaker ceramic, was due to the fact that only a

limited amount of elastic energy is available in the quenched body when crack initiation occurs. This was said to result in stable crack propagation that was a monotonically increasing function of ΔT, which consequently caused the residual strength to decrease monotonically with increasing ΔT.

Swain (1990) showed that the thermal shock strength degradation can be related to the ratio of energy required to propagate a crack (γ_{WOF}), to the energy required to initiate a crack (γ_{ic}). Swain concluded, and demonstrated experimentally for various magnesia-partially stabilised zirconia ceramics (Mg-PSZ), that materials with a flat K_R curve should suffer a severe strength degradation upon thermal shock treatment from ΔT_c, due to the γ_{WOF}/γ_{ic} ratio being approximately equal to 1. Further, that ceramics with a pronounced K_R curve behaviour were thought to be more resistant to thermal shock damage because of a higher γ_{WOF}/γ_{ic} value.

Janssen *et al.* identified metal infiltrated ceramics as attractive materials for applications requiring both high strength *and* thermal shock resistance, after showing that the retained strength following thermal shock for an Al_2O_3-Al composite was substantial even after water quenching from 520 °C, and that catastrophic strength degradation did not occur. Additionally it was found that the composites containing the larger Al ligaments (0.9 μm diameter compared to 0.2 μm diameter) showed virtually no strength degradation for ΔT of up to approximately 500 °C. The improved thermal shock behaviour over the monolithic matrix material was thought to be due to the fact that only stable crack growth had occurred (as the composite was expected to exhibit a pronounced K_R curve), and that the ductile ligaments provided structural integrity following thermal shock treatments of $\Delta T > \Delta T_c$, despite a heavily cracked matrix.

A further interesting feature of figure 6.10 is the maximum temperature differential which can be withstood prior to thermal stress induced cracking and corresponding strength degradation. This situation occurs at approximately

ΔT=200 °C for both the hot pressed monolithic Al_2O_3 and the ZTA as discussed previously, which agrees well with the reported data for these materials. ΔT_c is increased to around 300 °C for the hot pressed Al_2O_3-Fe material. However, although there appears to be no definitive ΔT_c for the sintered Al_2O_3-Fe composite, it is evident that strength degradation does not occur until $\Delta T \geq$ 200-300 °C. Materials are often ranked in terms of their thermal shock resistance parameters (R parameters), thus enabling the comparison of various materials in terms of both their resistance to crack initiation and subsequent crack propagation. The two R parameters of interest are R' and R''''. R' represents the resistance to crack initiation during rapid quenching, and R''''indicates the resistance to crack propagation and corresponding strength degradation for $\Delta T > \Delta T_c$ (see § 2.3.2), where

$$R' = \frac{k\sigma_f(1-\nu)}{E\alpha} \qquad 6.1$$

and

$$R'''' = \frac{K_{Ic}^2}{\sigma_f^2\,(1-\nu)} \qquad 6.2$$

In order to perform the calculations for the materials of interest, several material properties had first to be measured (or estimated where measurement was not possible). The uniaxial tensile fracture strengths of the two Al_2O_3-Fe composites and hot pressed monolithic Al_2O_3 are reported in chapter 5. Also presented in chapter 5 are the results of the fracture toughness evaluation for the sintered composite material, plus the data reported in the literature regarding the fracture toughness of the hot pressed composite and monolith. It was necessary to estimate the thermal properties (k and α) of the composite materials. It is unlikely that the difference in thermal shock behaviour between the monolithic Al_2O_3 and the Al_2O_3-Fe composite is due solely to a change in k and/or α, as such a change would simply result in a shift of ΔT_c, and not a change in the manner of strength degradation as has been observed. Also, since the second phase material

is discontinuous, it was initially assumed that the thermal conductivity of the Al_2O_3-Fe composites would remain similar to that for the monolith. It was also proposed that the coefficient of thermal expansion of the Al_2O_3-Fe composites would be similar to that of monolithic Al_2O_3, since the matrix would be expected to constrain and prevent the greater expansion of the iron particles at elevated temperatures. Following a similar argument, the Poisson's ratio of the composite materials is likely to be determined by that of the monolith, especially as the ceramic/metal interfacial bond strength is known to be low (§ 5.4).

Initially, the Young's moduli of the Al_2O_3-Fe composites was estimated using the mechanics of materials approach utilised by Sun (1993) and Trusty (1994) which considers an array of cubic particles in a matrix, and gives the modulus as

$$\frac{E_c}{E_m} = \frac{E_m + (E_p - E_m)\, v_p^{2/3}}{E_m + (E_p - E_m)\, v_p^{2/3}\,(1 - v_p^{1/3})} \qquad 6.3$$

where the subscripts c, p and m refer to the composite, particle and matrix respectively, and v_p is the volume fraction of particles (E_m and E_p taken as 380 GPa and 211 GPa respectively (Morrell, 1985, Nuffield Book of Data, 1984)). Thus the Young's modulus for both the hot pressed and sintered composites was calculated to be 344 GPa.

However, for the sintered composite, the Young's modulus was expected to be reduced further as a consequence of the additional 5 % matrix porosity. To account for this, the modulus of the alumina matrix (E_m) was modified using the following expression for the case of small, closed, randomly distributed spherical pores (Wachtman, 1969, as cited by Davidge, 1979), to give the modified modulus, E_m', as

$$E_m' = E_m\,(1 - 1.9v + 0.9v^2) \qquad 6.4$$

where v is the volume fraction of porosity, taken as 0.06 (i.e. all the porosity is present in the matrix only). Thus the modified matrix modulus reduces to 336

GPa. Replacing E_m with E_m' in equation 6.3 then gives the Young's modulus for the sintered Al_2O_3-Fe composite as 310 GPa.

During the final stages of the project, the Young's moduli of the two Al_2O_3-Fe composites was measured (using a Grindosonic technique, courtesy of Prof. R. D. Rawlings, Imperial College). The experimentally determined values were found to be 341 GPa and 258 GPa for the hot pressed and sintered composite materials respectively. For the case of the hot pressed composite, there is good agreement between the mechanics of materials approach and the experimental result. For the sintered composite, the measured value is substantially lower than that predicted. It is suggested that this is due to inferior ceramic/metal interfacial bonding compared with the hot pressed composite, i.e. significant contribution to the Young's modulus of the sintered composite by the metal particles is limited due to the weak interfacial bonding.

Both the estimated and measured values compare adequately with the Young's moduli measured for similar ductile particle reinforced composite materials. A wide range of moduli have been reported. Wang (1994) measured the modulus of an Al_2O_3-18 volume % Ni composite to be approximately 275 GPa. The decrease compared to the modulus of the matrix was attributed not only to the fact that the Ni has a lower elastic modulus and hardness than the matrix, but also because porosity increased simultaneously with Ni additions. Aghajanian *et al.* (1989) measured the Young's moduli of a series of Al_2O_3-Al composite to be in the range 88-304 GPa, depending on the volume fraction of inclusions and the degree of microstructural porosity present.

Table 6.1 lists the calculated thermal shock parameters (R' and R'''')for the hot pressed monolithic Al_2O_3 and the two Al_2O_3-Fe composites. The rankings obtained broadly support the experimental data presented in figure 6.10. The hot pressed Al_2O_3-Fe composite has the greatest R', corresponding to the significantly increased ΔT_c which can be withstood before crack initiation and degradation of

strength occurs. This result is solely due to the decreased modulus and significantly increased fracture strength of the composite compared to the monolith. The low R' of the sintered composite suggests that thermal stress induced cracking occurs for $\Delta T < 200$ °C. However, this is not seen from the retained strength versus temperature differential curve. It is expected that cracking does occur for relatively low shock treatments, but that the effect on the retained strength of the sintered composite is insignificant in comparison with the large critical flaw size. The R''''values confirm that the monolithic Al_2O_3 is less likely than the two composites to resist crack propagation, and the large R''''value for the sintered Al_2O_3-Fe indicates a relatively high resistance to crack propagation and strength degradation, as shown in figure 6.10. It should be remembered, however, that R parameters enable only a means of ranking and comparing the thermal shock resistance of various materials. Also, it must be realised that the K_{Ic} values used in the calculation of R' and R'''' are the maximum obtained during experimentation, and therefore assume the development of a process zone approximately 5 mm long in this case. In practice, it may be argued that the size of the thermal shock specimens prevents the development of a significant process zone and corresponding increase in K_{Ic}. Thus R''''is likely to be an overestimate for the two composite materials if the maximum K_{Ic} is used, whereas R'''' would underestimate the ability of the composite to resist damage if the initial K_{Ic} value (i.e. 3.1 MPa $m^{½}$) was used.

A similar observation was made by Aghajanian *et al.*, who found that a dense, sintered monolithic Al_2O_3 showed a lower ΔT_c than a series of Al_2O_3-Al composites, as well as showing the lowest degree of retained strength (in terms of the ratio of retained strength / initial strength). The first, second and fifth thermal shock resistance parameters (R, R' and R''''respectively) were then calculated, and broad agreement was found between the theoretical rankings and experimental data. In this case also, the K_{Ic} data used for calculation of R parameters appear to be maximum values obtained experimentally, suggesting that the R''''values may have overestimated the damage resistance capabilities of the

composite materials.

6.4 DAMAGE OBSERVATION

6.4.1 Scanning Electron Microscopy

Surfaces of composite specimens which had been subjected to thermal shock treatments were sputter coated with gold and examined using a scanning electron microscope (SEM). On occasion it became difficult to locate thermal shock induced damage for specimens of $\Delta T > 500$ °C due to the formation of the acicular growth on the exposed surfaces of the iron particles (as explained in § 6.2). In the majority of cases, it was possible to observe damage caused by the thermal shock treatment and the resulting interactions between a thermal shock induced crack and the second phase metallic particles. Figures 6.11 and 6.12 show examples of such thermal shock induced fractures in the hot pressed and sintered composite materials respectively.

6.4.2 Confocal Scanning Laser Microscopy

A Zeiss confocal scanning laser microscope (CSLM) with a 488 nm argon laser was used to study surface crack patterns at low magnification. It was found that this arrangement caused fluorescence of a water soluble dye (Castrol Britemore 446, supplied courtesy of Morgan Matroc Ltd.). A 516-525 nm filter was also used to reduce background noise. Using a low magnification, it was possible to produce a montage of photomicrographs showing the surface of specimens which had been subjected to thermal shock. Figure 6.13 shows a comparison of thermal shock fracture patterns in the hot pressed Al_2O_3-Fe composite and hot pressed monolithic Al_2O_3. Both specimens had been subjected to a thermal shock treatment of ΔT=400 °C. Further fluorescence work was carried out on the two hot pressed materials for various values of ΔT. Figures 6.14 and 6.15 each show a series of schematic diagrams depicting the thermal stress induced crack patterns

observed using the CSLM for a range of ΔT, for hot pressed monolithic Al_2O_3 and hot pressed Al_2O_3-Fe respectively.

6.4.3 Discussion

The photomicrographs shown in figures 6.11 and 6.12 reveal that a thermal shock induced crack may interact with the second phase particles in a number of ways. Examination of the micrographs shows that cracks caused by thermal stresses behave in much the same manner as cracks caused by mechanically applied stresses. The majority of crack/particle interactions appear to result in failure of the ceramic/metal interface, giving rise to particle pull-out and little, if any, plastic deformation of the ductile phase. On occasion, a crack may intercept a second phase particle and cause the particle to deform plastically across the two parting crack faces, resulting in ductile particle crack bridging, as demonstrated in figure 6.11 (b). The apparent tendency of most crack/particle interactions to result in interfacial failure once again indicates that the strength of the ceramic/metal interfacial bond is low, as concluded in § 5.4, and that the full toughening potential of the ductile reinforcement phase is not being utilised.

Figure 6.13 shows two montages obtained using the CSLM fluorescence technique. Both specimens were subjected to a thermal shock treatment of ΔT=400 °C. Cracking in the monolith is significantly more extensive than in the composite. This observation is in agreement with the retained strength curves shown in figure 6.10, as the relative retained strength for the monolith is lower than for the composite at ΔT=400 °C, hence the degree of cracking is expected to be greater for the monolith. An interesting feature of the crack patterns shown in figure 6.13 is that the cracks appear to be brighter for the monolith. This would imply that either the crack openings are greater, hence a greater volume of dye is exposed to the laser, resulting in a brighter image, and/or the depth of crack propagation is greater for the monolith. Additionally, the laser may penetrate the surface of the materials, causing fluorescence of dye below the surface crack. Since the

monolithic Al_2O_3 is semi-translucent and the Al_2O_3-Fe is more opaque, this may explain the brighter appearance of damage within the monolith. The latter explanation is thought to be the more probable. Attempts to study sub-surface damage and the depth of crack propagation (by removing the surface of the specimens by grinding) were abandoned as the grinding operation was found to introduce additional damage.

The approximately constant crack spacings for the monolith appear to support the experimental work by Fischer & Bahr, 1988 (as cited by Bahr, 1993) regarding multiple crack propagation. Fischer & Bahr showed that additional cracks may be activated between growing cracks providing the latter are widely spaced. A transient state is then reached where all wide spacings have disappeared, and all cracks have approximately equal lengths and spacings. Crack spacings for the hot pressed Al_2O_3-Fe composite are much larger, and only a correspondingly small number of dominant cracks are visible.

The schematic illustrations shown in figures 6.14 and 6.15 represent the surface crack patterns observed for small 2.5 mm x 2.5 mm x 2.5 mm samples after thermal shock treatments covering a range of ΔT values. The bold lines of figure 6.14 indicate the brighter appearance of the damage for the monolith compared to that observed for the composite. For both sets of results, the amount of cracking observed increases with increasing ΔT. The monolith appears to be uncracked following a thermal shock treatment of ΔT=200 °C. This would not be predicted from the residual strength versus ΔT plot, although the smaller dimensions of the samples used for CSLM work may account for this discrepancy. Again there appears to be a degree of regularity concerning the spacing of points of crack initiation, particularly for the sample subjected to ΔT=700 °C. The crack patterns observed for the series of hot pressed composite samples were less visible than for the monolith. The degree of damage was seen to increase with increasing ΔT, although samples subjected to ΔT=200 °C *and* ΔT=300 °C remained uncracked. This supports the findings concerning the residual strength

versus ΔT plot shown in figure 6.10. The degree of regularity between crack spacings observed for the composite was less than for the monolith.

6.5 SUMMARY OF EXPERIMENTAL OBSERVATIONS OF THERMAL SHOCK BEHAVIOUR

The thermal shock behaviours of hot pressed monolithic Al_2O_3, hot pressed Al_2O_3-Fe, sintered Al_2O_3-Fe and ZTA have been evaluated using the conventional water quench/flexure strength method. Prior to quench tests, it was established that exposure of the materials to high temperature alone had no effect on the flexure strength. Following quenching and retained strength measurement, it was found that both the monolith and the ZTA behaved as typical high strength engineering ceramics, showing a severe loss of strength at ΔT_c. The hot pressed composite behaved in a similar fashion, although showing a 50 % increase in ΔT_c. The sintered composite was found to behave as a typical refractory ceramic, showing a low initial strength, no definite ΔT_c and minimal strength degradation with increasing ΔT. Microstructural observations and fluorescence microscopy support the results obtained from the quench experiments.

6.6 THEORETICAL ANALYSIS OF THERMAL SHOCK BEHAVIOUR

6.6.1 Production of K Curves

The fracture mechanics method of Evans & Charles (see § 2.3.2) was used to generate curves depicting the generation of the normalised thermal shock generated stress intensity factor, κ, during thermal shock. Expressions developed by Jaeger (see § 2.3.2) have been used to calculate normalised tangential thermal stress, Ω, and its variance with normalised depth, x/r. The expressions given for Ω by Jaeger are for uncracked cylinders. However, within the scope of this work it has been assumed that the calculations are approximately valid for rods of

square cross-section, although it is realised that the maximum thermal stresses generated are likely to be greater for square section rods than for cylinders.

It was found that the hardware available for the computation of the κ curve data was not capable of evaluating both the *exact* normalised thermal stress generated in an uncracked plate (given in equation 2.32) and the *full* integral for the normalised thermal shock generated stress intensity factor (given in equation 2.26). It was found that the generation of κ curve data was possible only for certain combinations of integral limits and numbers of Bessel function roots. Trials of several combinations of these variables led to the conclusions that, firstly, only the first few solutions to the Bessel functions have a significant effect on the values of normalised thermal stress obtained from the expressions developed by Jaeger. Accurate reproductions of the data reported in Jaeger's work have been made in this study by considering only the first ten roots. Secondly, time and hardware restrictions limit the integral evaluation to an approximation between the limits of $0 \leq (x/a) \leq 0.999$. Further increasing the considered integral limits to $0 \leq (x/a) \leq 0.9999$ resulted in an increase in κ of only 1.8 %, but imposed a time of computation increase of approximately 100 %. The time necessary to produce such additional data was considered to be too long, considering the number of repeat calculations required. Hence the initial approximation was considered valid within the restrictions placed on the current work.

The computer software used to perform the calculations was Maple V Release 3. An example of the routine used for such calculations is given in Appendix 2. The example given produces a single of κ, for a single Biot modulus, β, and a single value of normalised time, θ, corresponding to a single value of normalised crack length, a/r. Such a calculation required approximately 60 minutes to compute. For each curve of κ versus a/r, approximately 15 a/r points were considered. In order to generate the envelope of maximum κ for a given β, 5 curves were produced, each corresponding to a given θ. The process was repeated for each value of β required.

Figure 6.16 shows a plot of normalised thermal stress (Ω) against normalised time (θ) for a range of Biot moduli (β). It is evident that as the Biot modulus decreases, the maximum surface tangential thermal stress generated is also decreased. This is consistent with either an increase in thermal conductivity, k, and/or a decrease in the product of semi-dimension, r, and heat transfer coefficient, h, since $\beta = rh/k$. Also apparent is the fact that for $\beta < \infty$, a finite time is required to develop maximum thermal stress; the value of θ increasing as β decreases. Figure 6.17 shows how the thermal stress varies with depth (x/r) for various values of θ (for $\beta = 20$). It can be seen that the thermal stress is tensile and at a maximum at the surface of the specimen (i.e. at $x/r = 0$), and that this reduces to zero at a certain value x/r; the actual depth of zero thermal tangential stress being dependent on θ (for a given β). As x/r increases further, the tangential thermal stress becomes compressive, although the maximum tensile stress generated is always greater than the corresponding maximum compressive stress for all values of θ, x/r and β. The change in thermal stress with θ for a given x/r ratio is shown in figure 6.18 (for $\beta = 20$). Good agreement for the three sets of results may be seen with previously published work (e.g. Jaeger, 1945, Evans & Charles, 1977, Swain, 1991), confirming that the computer routines used in the current work are correct.

The normalised stress (Ω) data may now be used in conjunction with equation 2.26 to generate curves of normalised thermal shock generated stress intensity factor (κ) against normalised crack length (a/r), for $0 \leq (a/r) \leq 0.5$. Figure 6.19 shows a plot of κ versus a/r for various values of normalised time (θ), for $\beta = 2$. In order to calculate the maximum thermal shock generated stress intensity factor generated for a specimen subjected to thermal shock, it is necessary to produce κ curves for various values of θ, as it can be seen from the figure that the maximum near-surface stress is reached at relatively low values of θ, whereas a longer period of time is required for maximum stress to be reached as a/r increases. Hence the κ envelope containing the maximum κ for each value of a/r over a range of θ is also shown in figure 6.19.

In order to construct thermal shock generated stress intensity factor curves for a particular material system, a specific value for β must be decided upon, and the normalised thermal shock generated stress intensity factor data require "denormalising". An estimate of a representative β must be made, due to the fluctuating nature of the heat transfer coefficient, h, as explained in § 3.5.2. A range of h values, and hence β values are quoted in the literature. The range of β for an alumina ceramic of r=10 mm is 3-30 (Morrell, 1977). Since β is directly proportional to r, it is reasonable to assume a range of β values of 0.3-3 for an alumina ceramic of r≈1 mm, as is the situation throughout the present study. β values of 1, 2 and 3 were therefore considered for further quantitative analysis.

Rearranging equation 2.26 to make the thermal shock generated stress intensity factor, K, the subject gives

$$K = \frac{\kappa E \alpha \Delta T \sqrt{r}}{(1-\nu)} \qquad 6.5$$

where κ is the maximum normalised thermal shock generated stress intensity factor as defined by the envelope of κ curves. Hence the construction of K versus a curves for a given material, of specific ΔT and r, is now possible. Young's moduli values are taken as 380 GPa, 341 GPa and 258 GPa for the monolith, the hot pressed composite and the sintered composite respectively, and values for α and υ are those discussed in 6.3.5. Figures 6.20, 6.21 and 6.22 show examples of K versus a curves generated for monolithic Al_2O_3 subjected to various ΔT, for β=1, 2 and 3 respectively.

6.6.2 Prediction of Crack Initiation, Crack Propagation and Strength Degradation

By superimposing the measured K_R curve of a material onto the curves of thermal shock generated stress intensity factor versus crack length, the conditions of crack initiation and arrest become clear for a defined thermal shock situation for a

known specimen. A crack will propagate unstably when $K \geq K_R$, providing also that $dK/da \geq dK_R/da$. The propagating crack will arrest when K falls below K_R, as explained in detail in § 2.3.2 and § 2.3.3. Figure 6.23 shows the constant K_R curve of the hot pressed monolithic Al_2O_3 material superimposed on the envelope of K versus a curves for thermal shock treatments of varying severity, and $\beta=2$. Immediately apparent is the ΔT required to cause crack propagation (i.e. curve corresponding to minimum ΔT required to give intersection of K curve with K_R curve) and subsequent strength degradation. The bold arrow indicates the proposed position of crack arrest for various values of ΔT, although a degree of over-run may be expected due to the kinetic nature of the propagating crack (Pompe *et al.* 1993). The β value of 2 was considered to be the most accurate estimate for the monolithic Al_2O_3, since the maximum point of the K curve corresponding to a ΔT of 200 °C generated for $\beta=2$ intersects with the superimposed constant K_R curve. Consequently, the initiation of crack propagation would be expected for a $\Delta T \approx 200$ °C, thus supporting the experimental data. Figures 6.24 and 6.25 show the K_R curves superimposed on the envelope of K versus a curves for the hot pressed and sintered Al_2O_3-Fe composite materials respectively, for various values of ΔT and $\beta=2$. Again, the values of ΔT required for the initiation of crack propagation are readily apparent, as are the proposed positions of crack arrest. It was thought initially that β for the composite materials would be lower than for the monolith due to the incorporation of metallic particles within the microstructure possibly increasing the thermal conductivity of the composites (due to the higher k for iron than alumina). This is likely to be true for the hot pressed composite, which is fully dense and is thought to have a greater degree of chemical contact between the two phases (as discussed in § 6.3.5). In the case of the sintered composite, the porosity is likely to negate some of the increase in k, such that the k value is likely to be between that of the hot pressed composite and the monolith. However, a decrease in β for the composite materials would lead to the generation of decreased thermal stress for a specific condition of thermal shock, hence a β value of 2 for the Al_2O_3-Fe materials was considered to be a reasonable conservative

estimate.

Figures 6.23, 6.24 and 6.25 show the approximate ΔT values at which $K > K_R$ for each of the three materials, assuming a Biot modulus of 2. For any given plot of K versus a, the exact K envelope corresponding to the ΔT at which $K > K_R$ generally lies between two of the K curves shown. An estimate of the ΔT required to generate such a K envelope may be made by studying the relative position of the superimposed K_R curve to the two adjacent K curves, since K is directly proportional to ΔT (see equation 6.5). Hence the ΔT values necessary to generate sufficient thermal stress to cause the initiation of crack propagation are given as approximately 200 °C, 220 °C and 400 °C for hot pressed monolithic Al_2O_3, hot pressed Al_2O_3-Fe and sintered Al_2O_3-Fe respectively. Since the experimental data presented in figure 6.10 (pertaining to the hot pressed Al_2O_3-Fe composite) shows no evidence of cracking for $\Delta T < 300$ °C to 400 °C, it was concluded that the value of Biot modulus originally chosen for this composite was an over-estimate, and the actual value would be lower (i.e. lower than that of $\beta = 2$, as assumed for the monolith). The expected decrease in Biot modulus proposed for the composite materials relative to the monolith is consistent with an increase in the thermal conductivity. It is therefore reasonable to assume that since the thermal conductivity of iron is approximately four times that of alumina (Nuffield Book of Data, 1984) at room temperature, a simple rule of mixture expression would anticipate an increase in k of the composites of approximately 50 % relative to the monolith. Furthermore since $\beta = rh/k$, such an increase in k would imply a decrease in β of approximately 50 % relative to the monolith. Subsequently, the K_R curve of the hot pressed composite material was superimposed onto the K curves calculated for a Biot modulus of 1, as shown in figures 6.26. It can be seen that the value of ΔT now sufficient to induce crack propagation for the hot pressed composite and a Biot modulus of 1 is approximately 330 °C, which supports the experimental data regarding both the retained strength versus temperature differential curve and the observations made using fluorescence microscopy. Figure 6.27 shows the equivalent curve for the

sintered composite. For the sintered material, crack propagation would be expected for values of ΔT equal to 500 °C and above only.

For the case of the sintered Al_2O_3-Fe composite, it is debatable which value of Biot modulus (either 1 or 2) is the most appropriate. It is possible that either may be a reasonable estimate. For a Biot modulus of 2, as shown in figure 6.25, thermal stress induced cracking would be predicted for ΔT values of 350 °C and 400 °C. This would support the experimental findings of both the retained strength versus temperature differential curve and the observations made using scanning electron microscopy (since cracking was observed for ΔT=400 °C, as may be seen in figure 6.12). However, it may be expected that the Biot moduli of the two Al_2O_3-Fe composites would be similar, hence a β of 1 and the corresponding plot shown in figure 6.27 would be the most accurate, in which case a discrepancy exists between the theoretically predicted ΔT required to initiate crack propagation and the ΔT observed (using scanning electron microscopy) to initiate crack propagation.

Figure 6.27 shows that for $\Delta T < 500$ °C, the envelope of maximum thermal shock generated stress intensity factor does not intersect with the superimposed K_R curve for the sintered Al_2O_3-Fe composite, due to the large calculated critical flaw size defining the beginning of the K_R curve. This would therefore imply that crack propagation would occur only for $\Delta T \geq 500$ °C, hence no degradation in strength following thermal shock treatments of lower ΔT would be expected. Several factors may be responsible for this contradiction. Due to the relatively poor microstructure of the sintered composite, it is possible the the cracking observed for ΔT=400 °C using the SEM (see figure 6.12) occurred in regions of high density, where porosity was minimal. This would have resulted in an increase in local fracture stress (relative to the bulk material) and a corresponding decrease in the local critical flaw size. Such a decrease in a_c would have lead to a point of intersection between the K_R curve and the thermal shock generated stress intensity factor curves for $\Delta T < 500$ °C, implying a degree of crack propagation

and strength degradation. Indeed if the linear K_R curve shown in figure 6.27 is extrapolated for lower crack lengths, an intersection with the thermal shock generated stress intensity factor curve corresponding to a ΔT of 400 °C would suggest the initiation and propagation of cracks at this ΔT. Such a prediction may better support the experimental data. It appears that the Biot modulus of the sintered composite may be similar to that of the hot pressed monolithic Al_2O_3. This may possibly be explained by the fact that the increased porosity of the sintered composite compared to the hot pressed composite would be expected to lower the thermal conductivity of the bulk material, as discussed earlier in this section. Additionally, it was suggested (§ 6.3.5) that the bonding (whether chemical or physical) between the metallic phase and the ceramic matrix is weaker for the sintered composite than the hot pressed composite. Consequently, any ceramic/metallic interface may present a boundary obstructing heat flow, thus possibly causing a further decrease in k. Therefore, since $\beta = rh/k$, this would result in an increase in β. Since a Biot modulus of 2 for the sintered composite more convincingly supports the experimental data, this estimate was chosen for further work regarding the prediction of the degree of strength degradation.

The influence of the increased fracture toughness (and corresponding K_R curve behaviour) of the Al_2O_3-Fe composite materials on the determination of the ΔT value required to initiate crack propagation has been shown to be negligible. This is demonstrated in figures 6.26 and 6.27, as the maximum thermal shock generated stress intensity factor for a given ΔT is reached at relatively low crack lengths (i.e. $a < 0.3$ mm). Crack lengths of this magnitude prevent the development of a significant process zone (see figure 5.4). It is therefore concluded that the increase in fracture toughness is not responsible for the increase in resistance to the initiation of thermal shock induced damage. It is thought that the differences in Young's moduli and Biot moduli between the three materials is the cause of the increased resistance to the initiation of crack propagation of the Al_2O_3-Fe composites compared to the monolith. The significantly lower Young's moduli of the composites results in a similarly significant decrease in the magnitude of the

thermal shock generated stress intensity factor generated for a given ΔT. Thus a higher ΔT may be tolerated by the two composites, still retaining the K envelope below K_R. Following this argument, it is expected that the sintered Al_2O_3-Fe composite should be capable of withstanding a slightly higher ΔT than the hot pressed equivalent. However, this is not easily confirmed using the residual strength versus ΔT data shown in figure 6.8,as the degree of strength degradation with increasing ΔT is relatively small even for severe thermal shock conditions.

An attempt has been made to correlate the predicted crack arrest lengths (and the associated degradation of retained flexural strength) with the experimentally obtained retained strength versus ΔT data for the hot pressed monolithic Al_2O_3, hot pressed Al_2O_3-Fe composite and the sintered Al_2O_3-Fe composite. The results are tabulated in table 6.2 for the three materials, each for various values of ΔT. Crack arrest lengths were taken from the thermal shock generated stress intensity factor versus crack length curves according to the position of intersection with the superimposed K_R curve, for various values of ΔT. The tensile strengths corresponding to the predicted crack lengths obtained were then calculated using equation 5.1, after rearranging to make σ_f the subject. Since the thermal shock induced crack is an edge defect propagating inwards from a free surface under maximum tensile stress, a factor of 1.12 must be introduced to account for this condition, giving

$$\sigma_f = \frac{K_{Ic}}{1.12\sqrt{\pi a}} \qquad 6.6$$

This expression has been used only to enable a first approximation to be made regarding the retained strength of a sample subjected to a given thermal shock treatment. It is accepted that such an expression is inaccurate for crack lengths of this magnitude, since the crack length is a significant proportion of the characteristic dimension. For the case of the monolith, K_{Ic} was taken as 3.1 MPa $m^{½}$ for all values of crack length, whereas for the composite materials, it was necessary to estimate the increased K_{Ic} value corresponding to the increased

proposed crack length. Hence the variation of K_{Ic} is also given in table 6.2 (estimates taken from figure 5.4, assuming a linear relationship between K_{Ic} and crack length). Conversion of the calculated tensile strengths to the equivalent flexure strengths was made using equation 5.2, after rearranging to make $\sigma_{bending}$ the subject (taking the Weibull moduli of the hot pressed monolithic Al_2O_3, hot pressed Al_2O_3-Fe composite and sintered Al_2O_3-Fe composite as 9).

Figures 6.28, 6.29 and 6.30 show the theoretically predicted retained strengths of the three materials superimposed onto the actual experimental curves obtained from the water quench experiments. It can be seen that, generally, the theoretically predicted retained strength versus temperature differential data broadly support the experimental curves for the three materials of interest. The ability of the composites to retain a higher degree of strength than the monolith following a severe shock of is attributed to the increased toughness of the Al_2O_3-Fe composites. It is concluded that the increase *is* a direct consequence of the presence of the second phase metallic particles. However, the K_R curve behaviour and increased fracture toughness exhibited is thought to be only partly due to the proposed mechanism of ductile particle crack bridging bridging. This can be deduced from examination of both the fracture surfaces of the material (see 5.3.5) and the interactions between a thermal shock induced crack and the iron particles (see § 6.4.3). The less effective toughening mechanisms of crack deflection (by metallic particles) and crack blunting (both by particles and areas of porosity) are thought to be major contributing factors leading to the increased toughness of the composites and the corresponding improved damage tolerance.

Due to the semi-quantitative nature of the analysis and the estimations of certain material properties (in particular the thermal properties of the Al_2O_3-Fe composite materials), the validity of the above analysis may be debated. However, it is clear that the preliminary thermal shock analysis broadly supports the results obtained experimentally, and the prominent features of the results of the analytical work are in particularly good agreement with experimental data. It is

envisaged that further work concerning the measurement of the heat transfer coefficient (h) and the thermal conductivity (k) of the three materials, particularly of the composites, would lead to the justification or amendment of the estimates made for the purposes of this study. Extended work regarding the application of the analysis to more accurately predict conditions of crack arrest, and the consequent strength degradation for a given thermal shock, would then be possible.

6.7 CONCLUSIONS

The evaluation of the thermal shock behaviour of a hot pressed Al_2O_3-Fe composite and a sintered Al_2O_3-Fe composite has been approached using several methods. Where relevant, the thermal shock behaviour of a hot pressed monolithic Al_2O_3 and a commercially available ZTA has also been studied, enabling a direct comparison of results. It was first established that any strength degradation observed following water quenching of the Al_2O_3-Fe composites from elevated temperatures was due solely to the rapid change in temperature imposed by quenching, and not due to high temperature exposure. The thermal shock resistance of the Al_2O_3-Fe composites has been shown to be greater than for ZTA and the monolith, both in terms of the onset of crack propagation and damage resistance. A more gradual decrease in retained strength with increasing ΔT is observed for the sintered composite. Crack patterns produced for $\Delta T > \Delta T_c$ have been examined using a fluorescent dye penetration technique. The minimum values of ΔT found to cause crack propagation for the monolithic Al_2O_3 and the hot pressed Al_2O_3-Fe composite support the results obtained from the retained strength versus ΔT experiments. Cracking has been shown to be more severe for the monolith than for the Al_2O_3-Fe composite for a given ΔT. Studies of interactions between the metallic phase and a thermal shock induced crack have revealed little evidence of crack bridging due to plastic deformation of the ductile particles. Ceramic/metal interfacial failure is observed in the majority of cases.

A semi-quantitative analysis of the thermal shock behaviour of monolithic Al_2O_3 and the two Al_2O_3-Fe composites has been attempted, based on the fracture mechanical approach developed by Evans & Charles. Estimation of the Biot moduli for the three materials was necessary. Values of $\beta=2$, $\beta=1$ and $\beta=2$ have been found to give the optimum correlation between the theoretical analysis and experimental results in terms of the critical temperature differential for the monolith, hot pressed composite and sintered composite respectively. Knowledge of the K_R curve for each material has enabled predictions to be made concerning the conditions required for the onset of crack propagation, and also the degree of strength degradation with increasing ΔT. Initial predictions of retained strength of the monolith, hot pressed composite and sintered composite show reasonably good agreement with experimental data. Further experimental work regarding the measurement of thermal properties is required to support the estimates made. It has been shown that the K_R curve behaviour of the two Al_2O_3-Fe composites does not have a significant effect on ΔT_c. The reduction in Biot modulus (in the case of the hot pressed composite) and the reduction in Young's modulus of the composites compared to the parent matrix material is thought to be the cause of the decreased thermal shock generated stress intensity factor, and hence the increased ΔT_c. Possible explanations regarding the differences in the estimated values of Biot moduli for the three materials have been proposed.

The increased toughness of the two Al_2O_3-Fe composite materials is thought to be primarily responsible for the greater strength retention properties relative to the monolithic matrix material, although the increased toughness is attributed only partly to the inclusion of metallic particles and the anticipated crack bridging process. Toughening mechanisms of crack blunting and deflection, typically by porous regions and second phase particles respectively, have been shown to occur more readily than plastic deformation of the iron particles.

Table 6.1 Estimated thermal stress resistance parameters for hot pressed monolithic Al_2O_3, hot pressed Al_2O_3-Fe and sintered Al_2O_3-Fe.

	H.P. Al_2O_3	H.P. Al_2O_3-Fe	Sintered Al_2O_3-Fe
σ_f (MPa)	258	356	82
E (GPa)	380	341	258
υ	0.22	0.22	0.22
k (W m^{-1} K^{-1})	20	20	20
α (x 10^{-6} K^{-1})	7.7	7.7	7.7
K_{Ic} (MPa $m^{½}$)	3.1	6.9	8.3
R' (W m^{-1})	**1.38×10^3**	**2.12×10^3**	**0.64×10^3**
R''''(m^{-1})	**0.185×10^{-3}**	**0.482×10^{-3}**	**13.14×10^{-3}**

Table 6.2 Predicted retained strength values for hot pressed monolithic Al_2O_3, hot pressed Al_2O_3-Fe and sintered Al_2O_3-Fe materials. Crack arrest lengths corresponding to various temperature differentials have been taken from points of intersection between the K envelope and the superimposed K_R curve (figures 6.23, 6.25 and 6.26).

	ΔT (^oC)							
	0	190	200	250	300	350	400	500
Hot Pressed Al_2O_3, $\beta=2$								
a	0.042	0.042	0.24	0.40	0.48			
K_{Ic}	3.1	3.1	3.1	3.1	3.1			
$\sigma_{bend.}$	434	434	182	141	128			
Hot Pressed Al_2O_3-Fe, $\beta=1$								
a	0.019	0.019	0.019	0.019	0.019	0.30	0.37	0.46
K_{Ic}	3.1	3.1	3.1	3.1	3.1	3.31	3.38	3.44
$\sigma_{bend.}$	645	645	645	645	645	173	159	145
Sintered Al_2O_3-Fe, $\beta=2$								
a	0.362	0.362	0.362	0.362	0.362	0.41	0.45	
K_{Ic}	3.1	3.1	3.1	3.1	3.1	3.15	3.2	
$\sigma_{bend.}$	148	148	148	148	148	141	137	

where units of a, K_{Ic} and $\sigma_{bend.}$ are mm, MPa $m^{½}$ and MPa respectively.

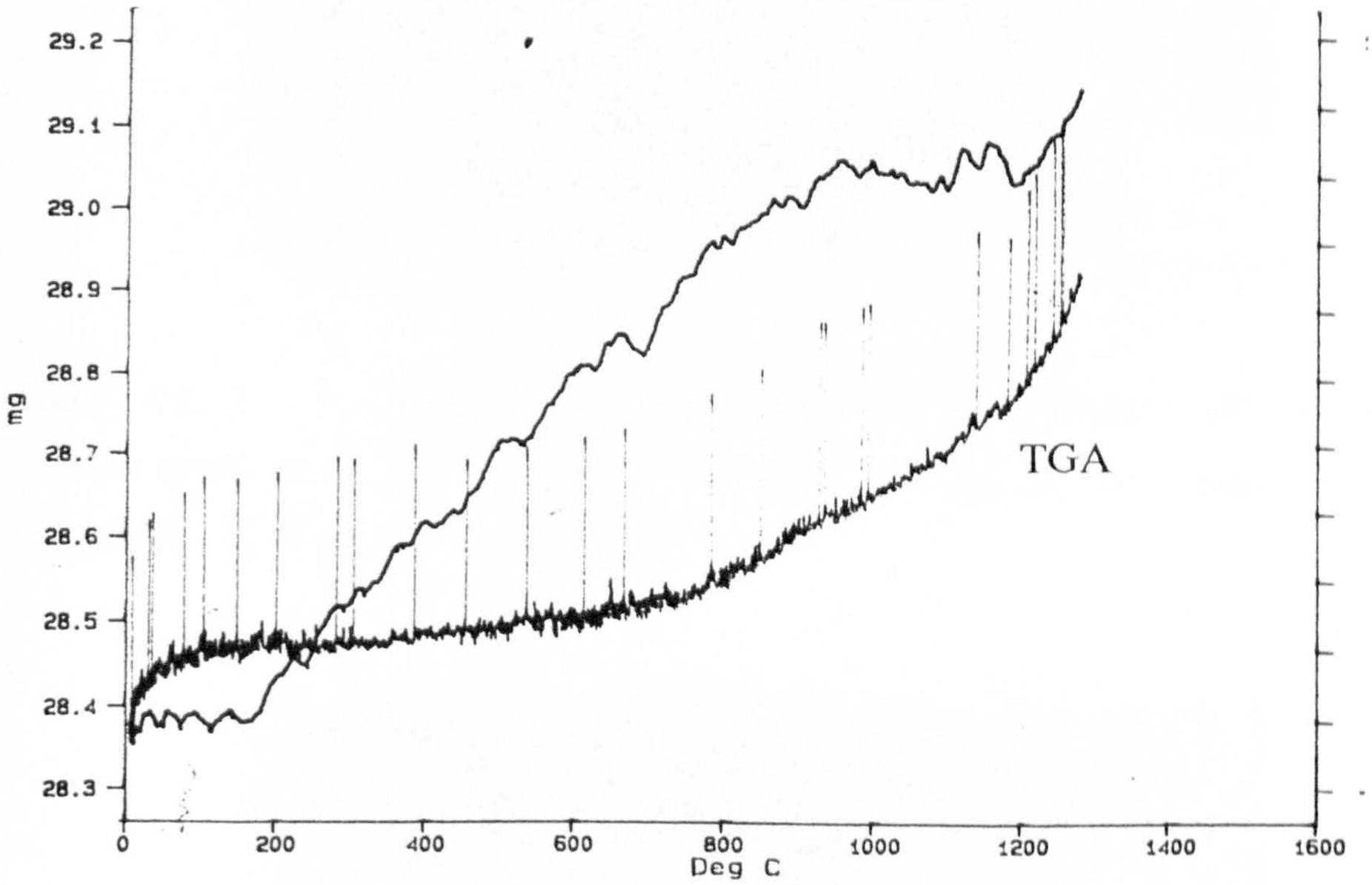

Figure 6.1 Thermal gravimetric analysis read-out of mass versus temperature for 30 mg specimen of hot pressed Al_2O_3-Fe composite. Ramp rate=50 °C min^{-1}. Note the plateau in mass reading between approximately 200 °C and 500 °C.

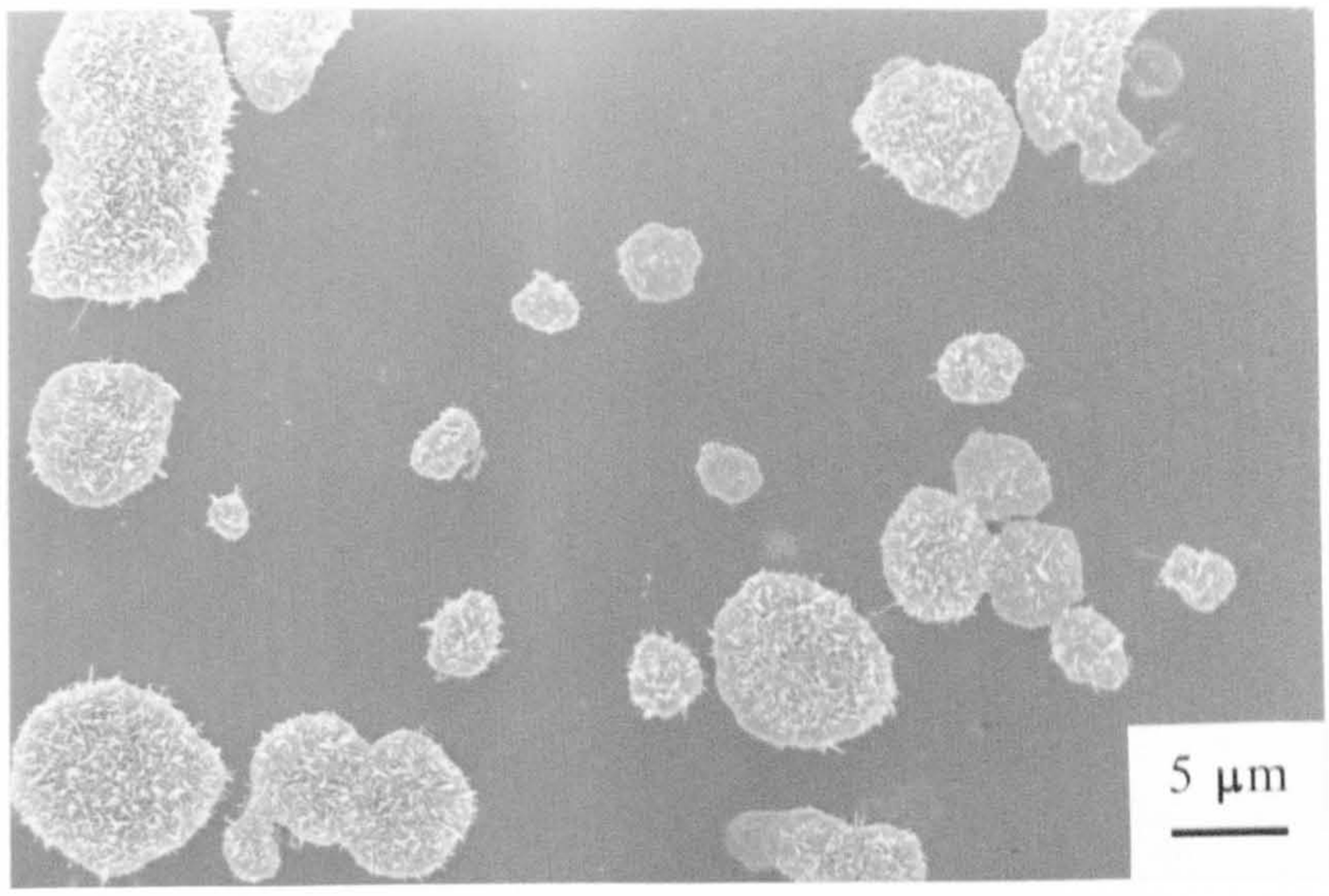

Figure 6.2 SEM photomicrograph (secondary electron image) showing surface appearance of the hot pressed Al_2O_3-Fe composite after exposure to a temperature of 500 °C for 15 minutes.

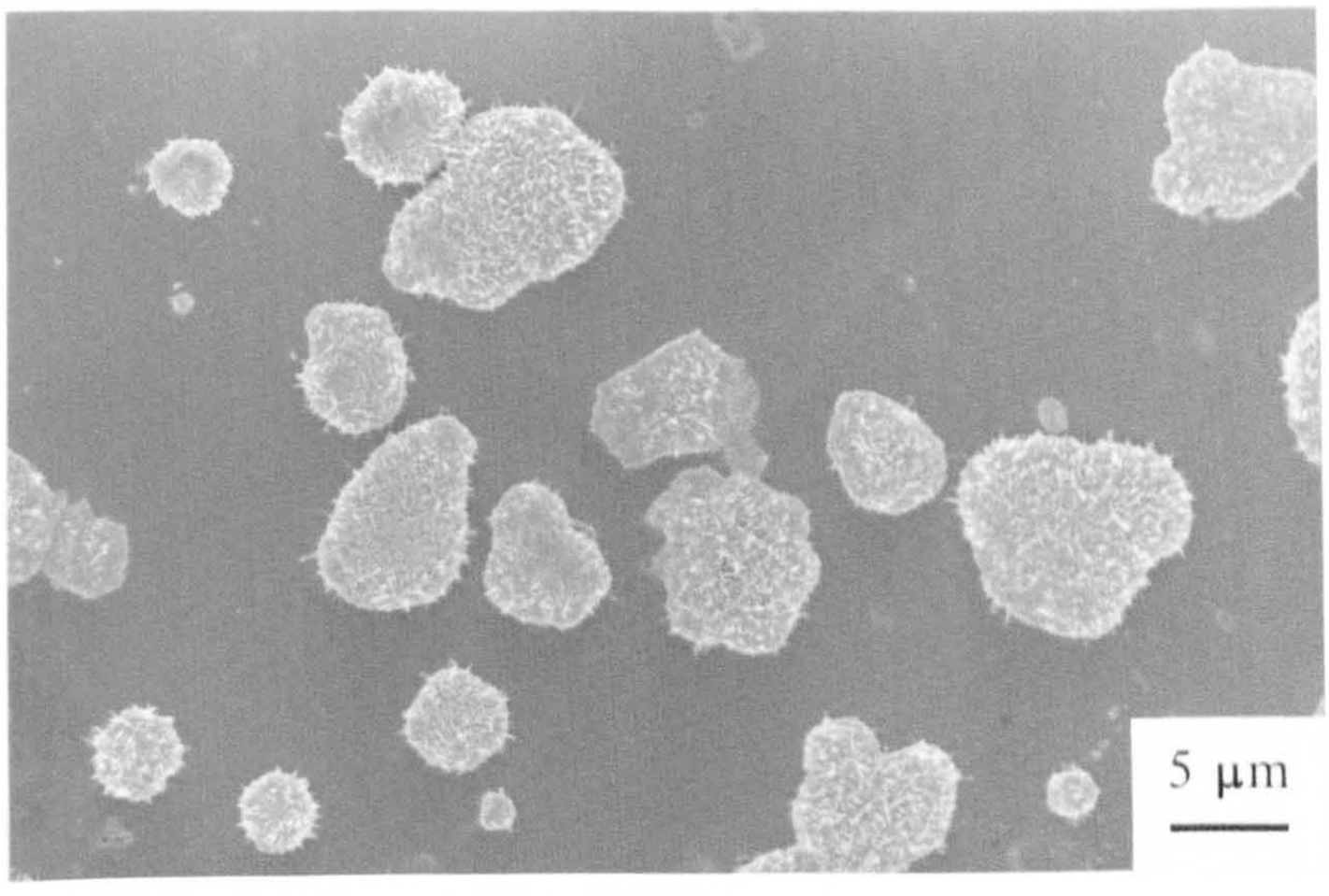

Figure 6.3 SEM photomicrograph (secondary electron image) showing surface appearance of the hot pressed Al_2O_3-Fe composite after exposure to a temperature of 500 °C for 60 minutes.

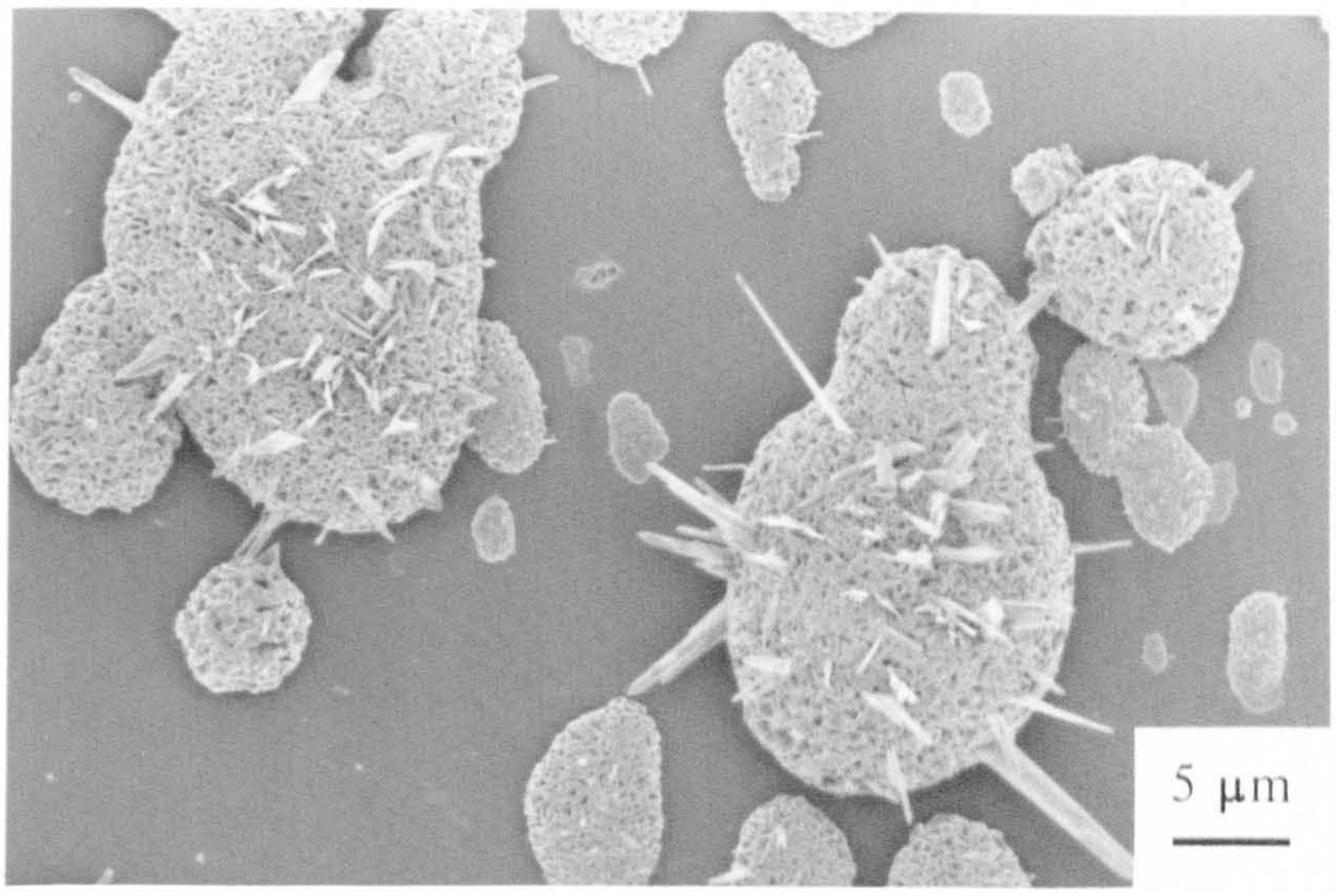

Figure 6.4 SEM photomicrograph (secondary electron image) showing surface appearance of the hot pressed Al_2O_3-Fe composite after exposure to a temperature of 800 °C for 15 minutes.

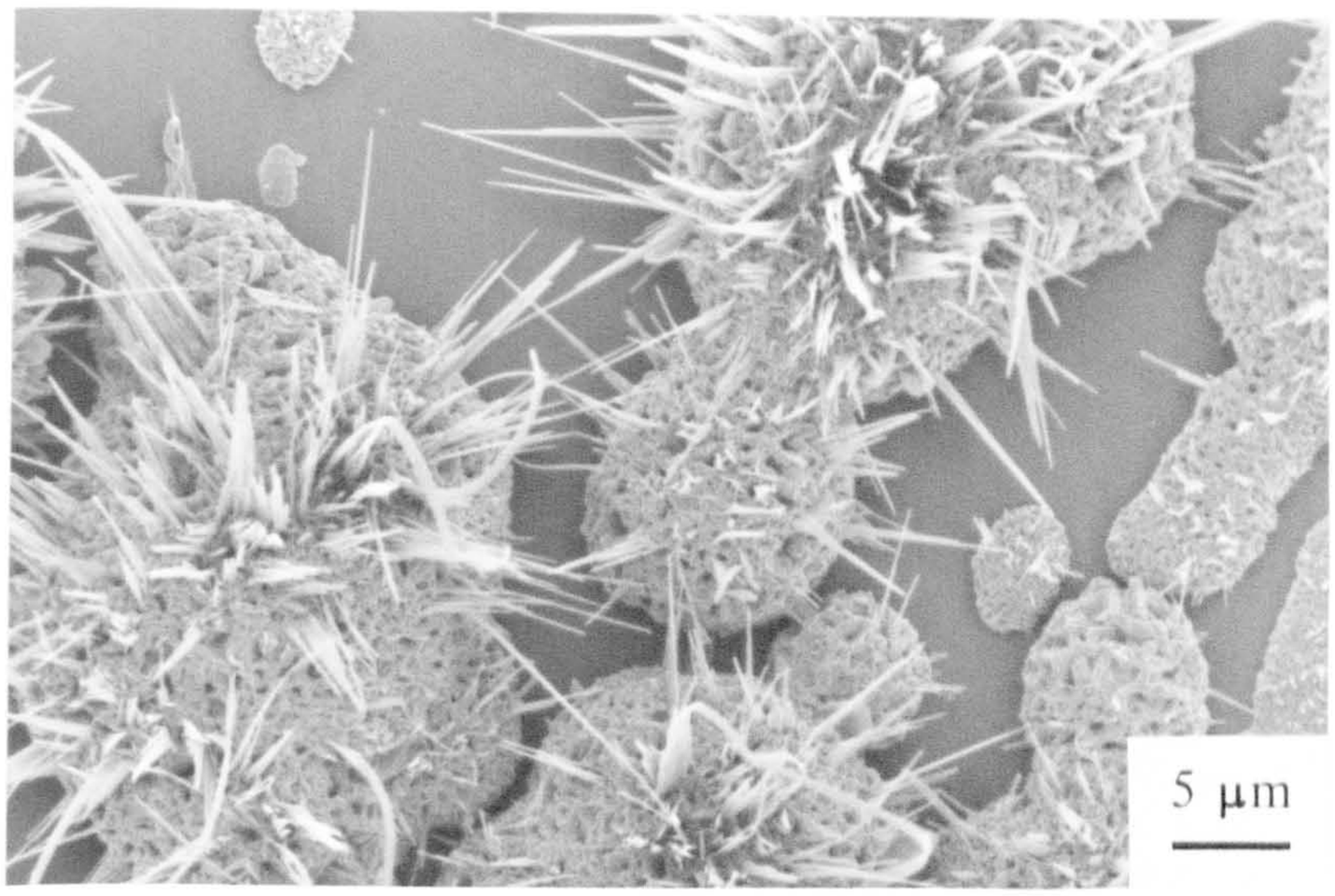

Figure 6.5 SEM photomicrograph (secondary electron image) showing surface appearance of the hot pressed Al_2O_3-Fe composite after exposure to a temperature of 800 °C for 60 minutes.

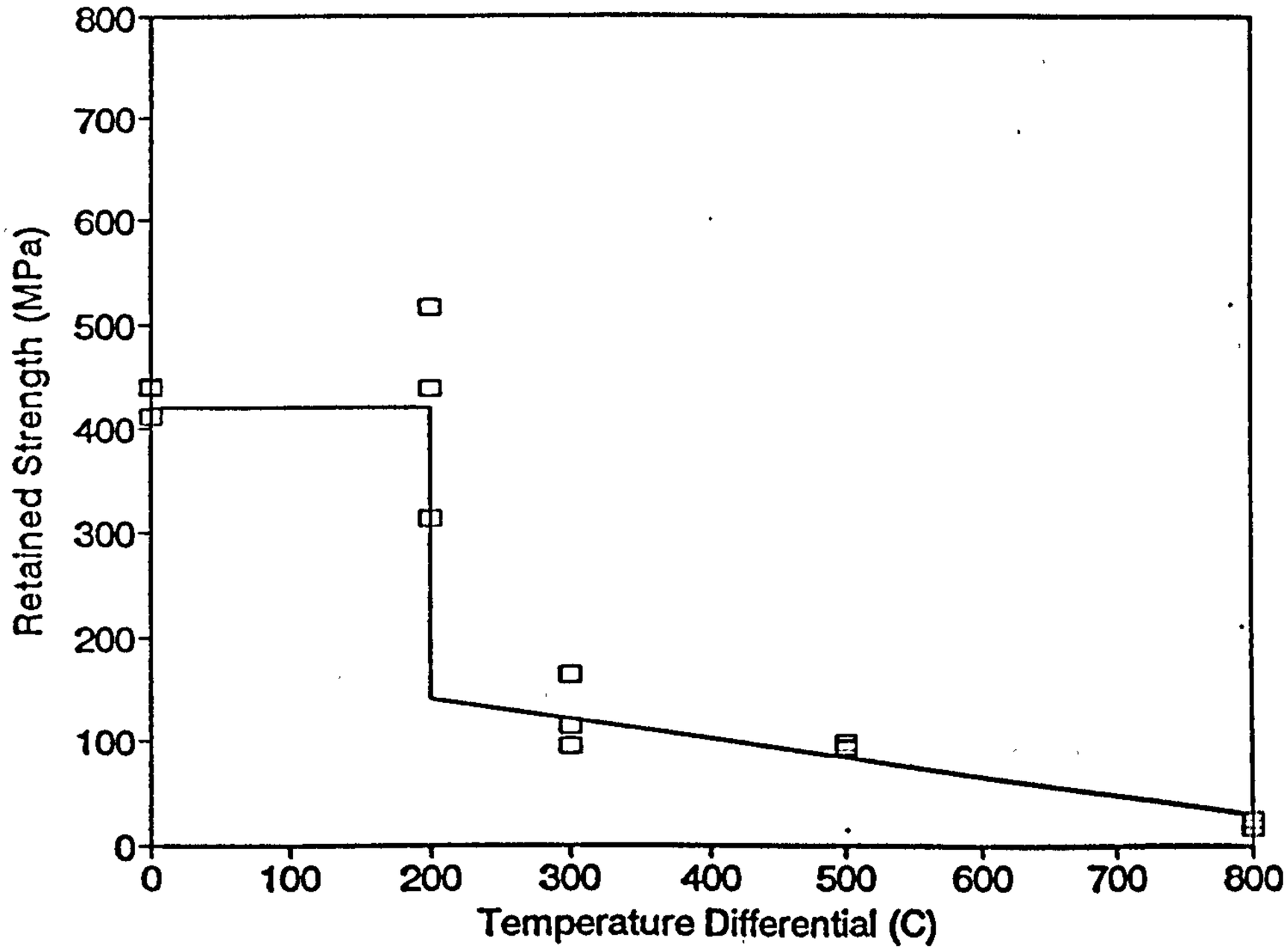

Figure 6.6 Plot of retained flexural strength versus temperature differential for hot pressed monolithic Al_2O_3.

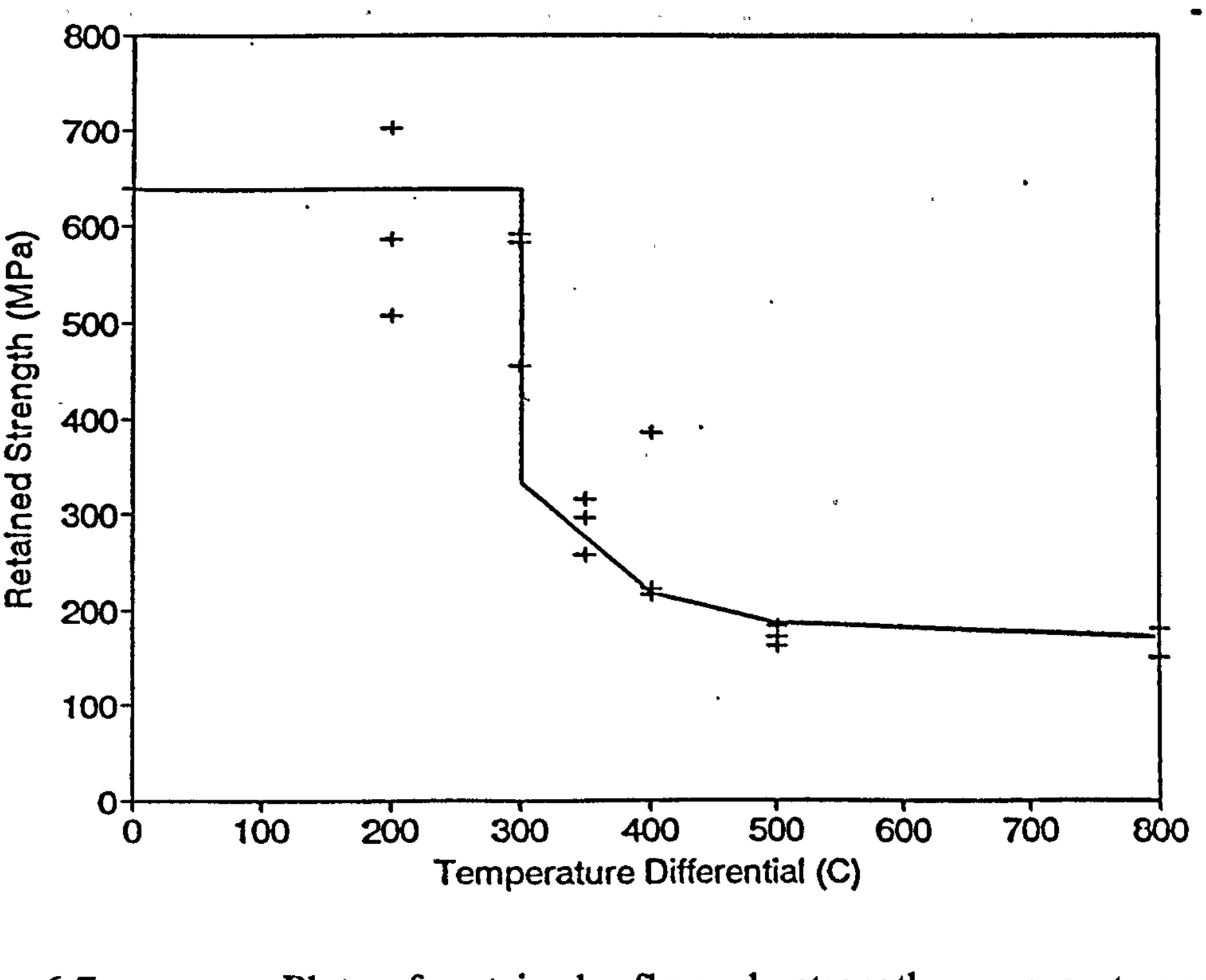

Figure 6.7 Plot of retained flexural strength versus temperature differential for hot pressed Al_2O_3-Fe composite.

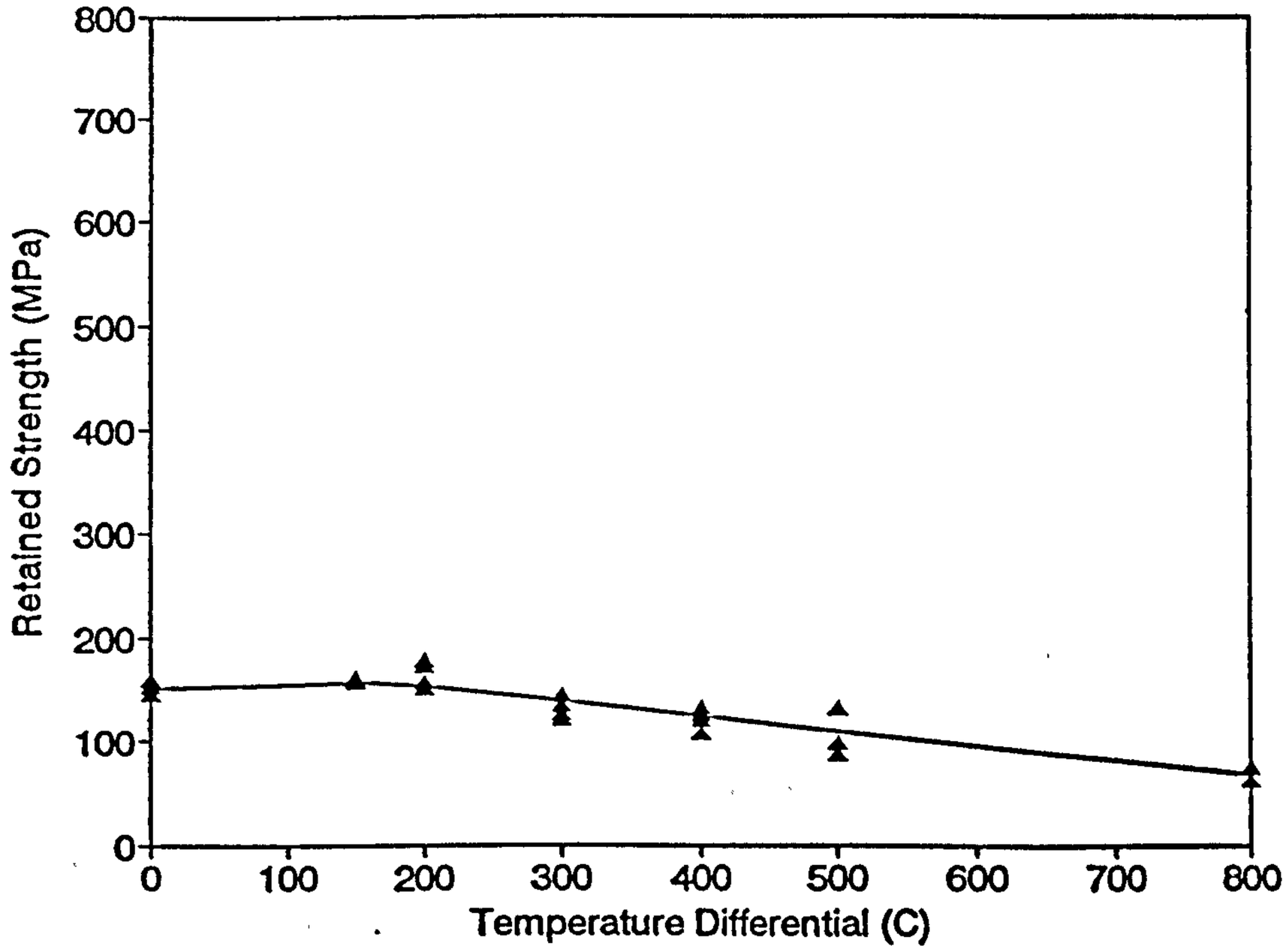

Figure 6.8 Plot of retained flexural strength versus temperature differential for sintered Al_2O_3-Fe composite.

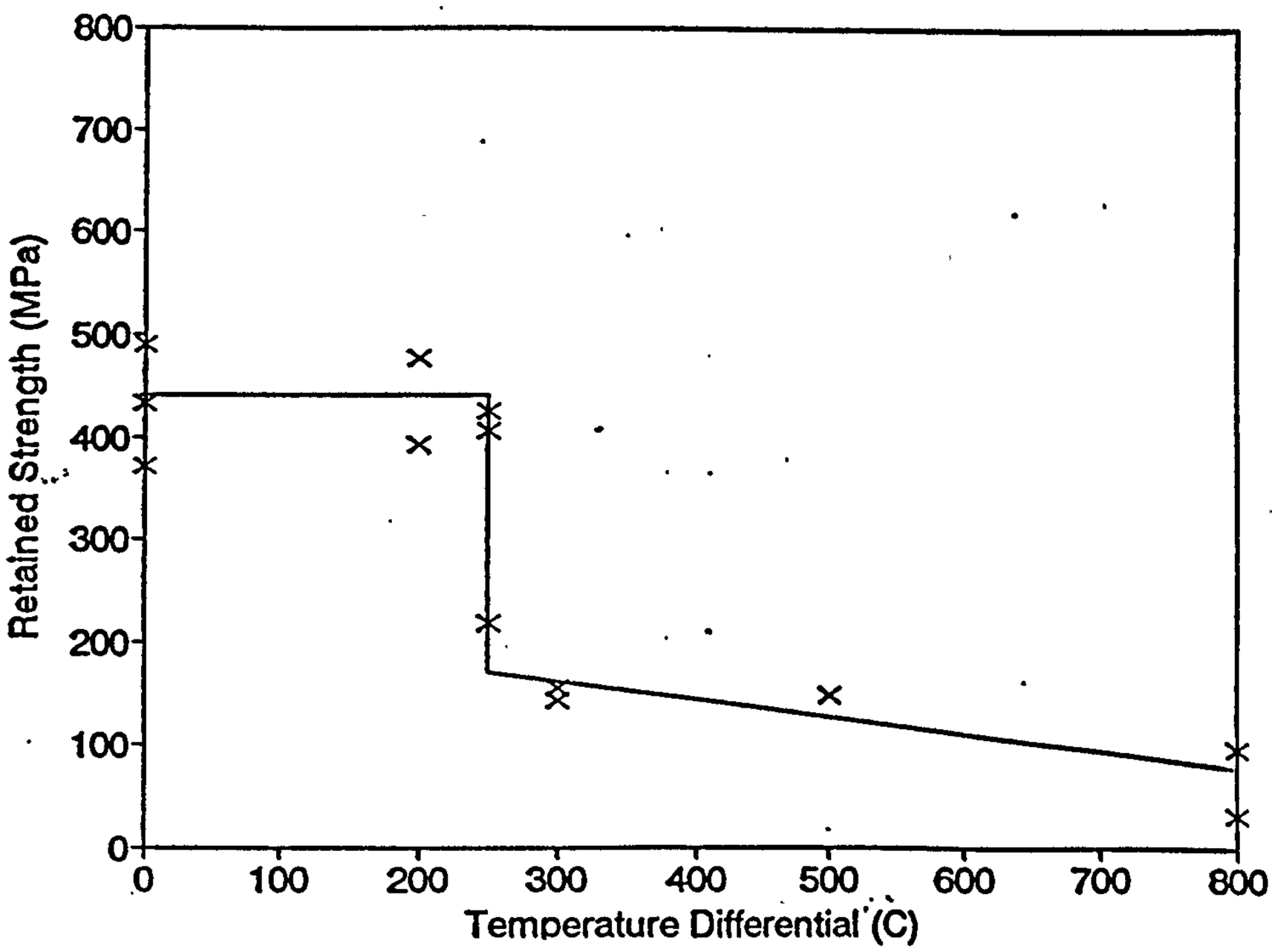

Figure 6.9 Plot of retained flexural strength versus temperature differential for ZTA.

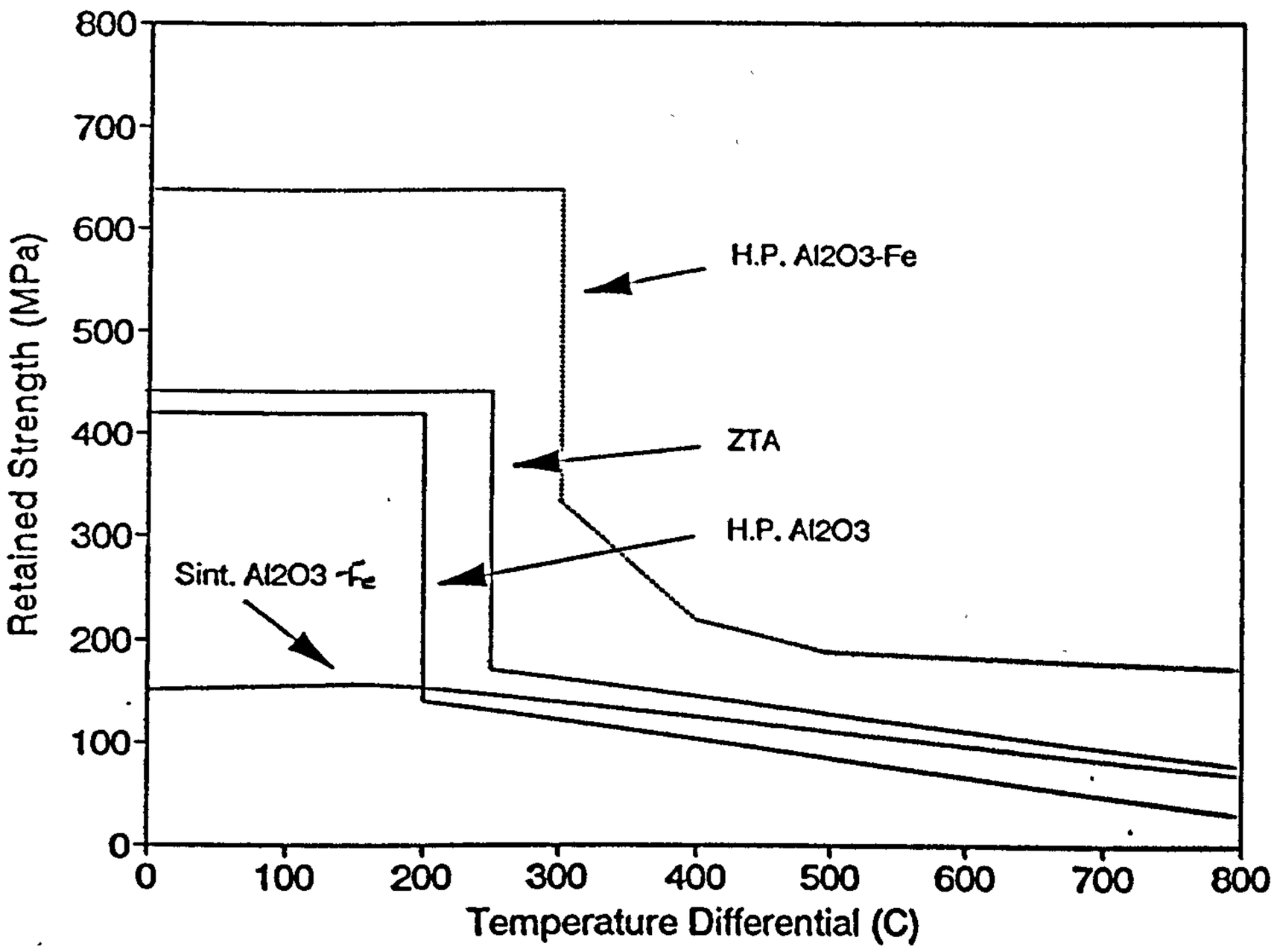

Figure 6.10 Plot of retained flexural strength versus temperature differential for hot pressed monolithic Al_2O_3, hot pressed Al_2O_3-Fe composite, sintered Al_2O_3-Fe composite and ZTA (individual data points have been omitted for clarity).

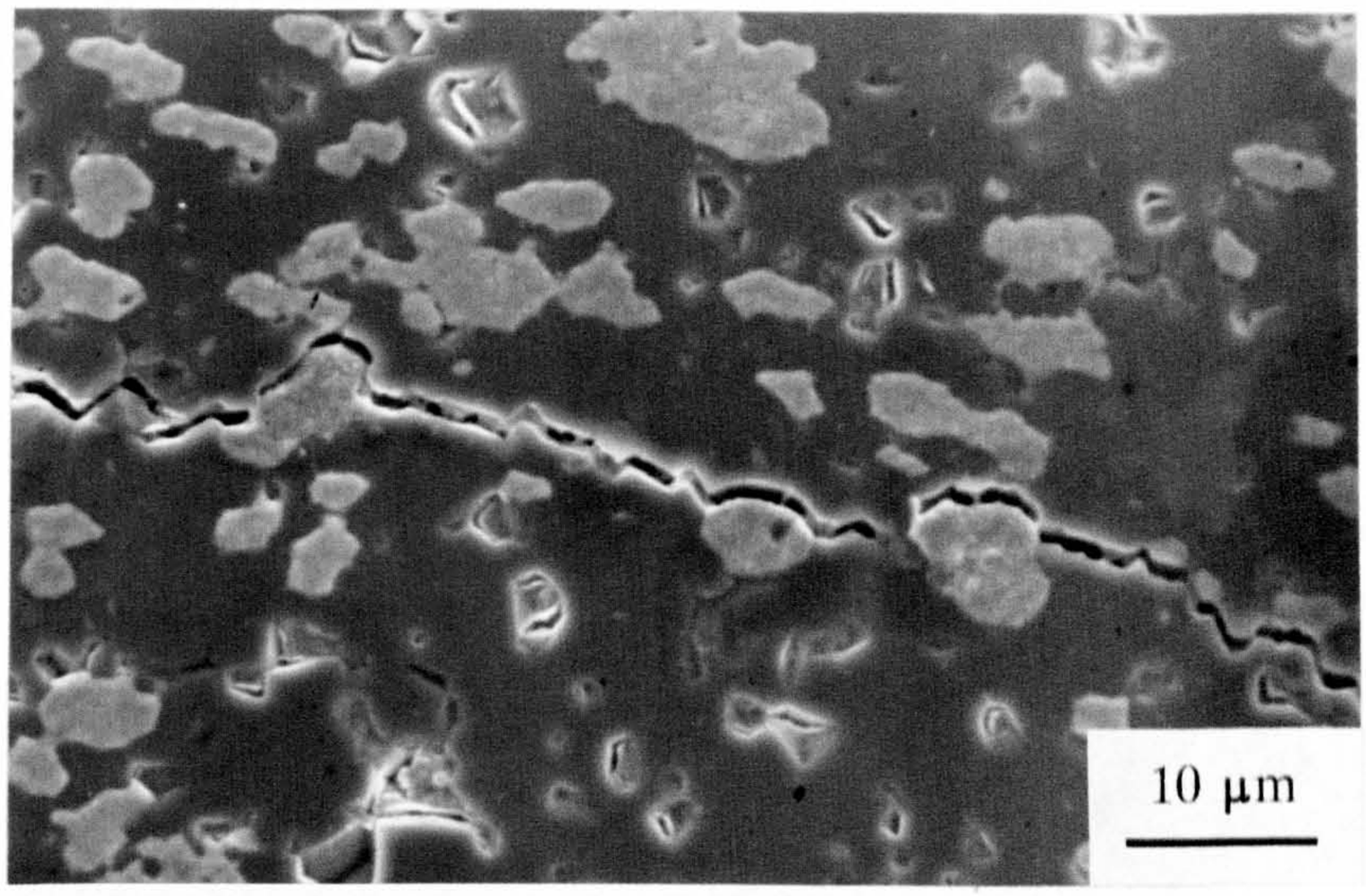

a)

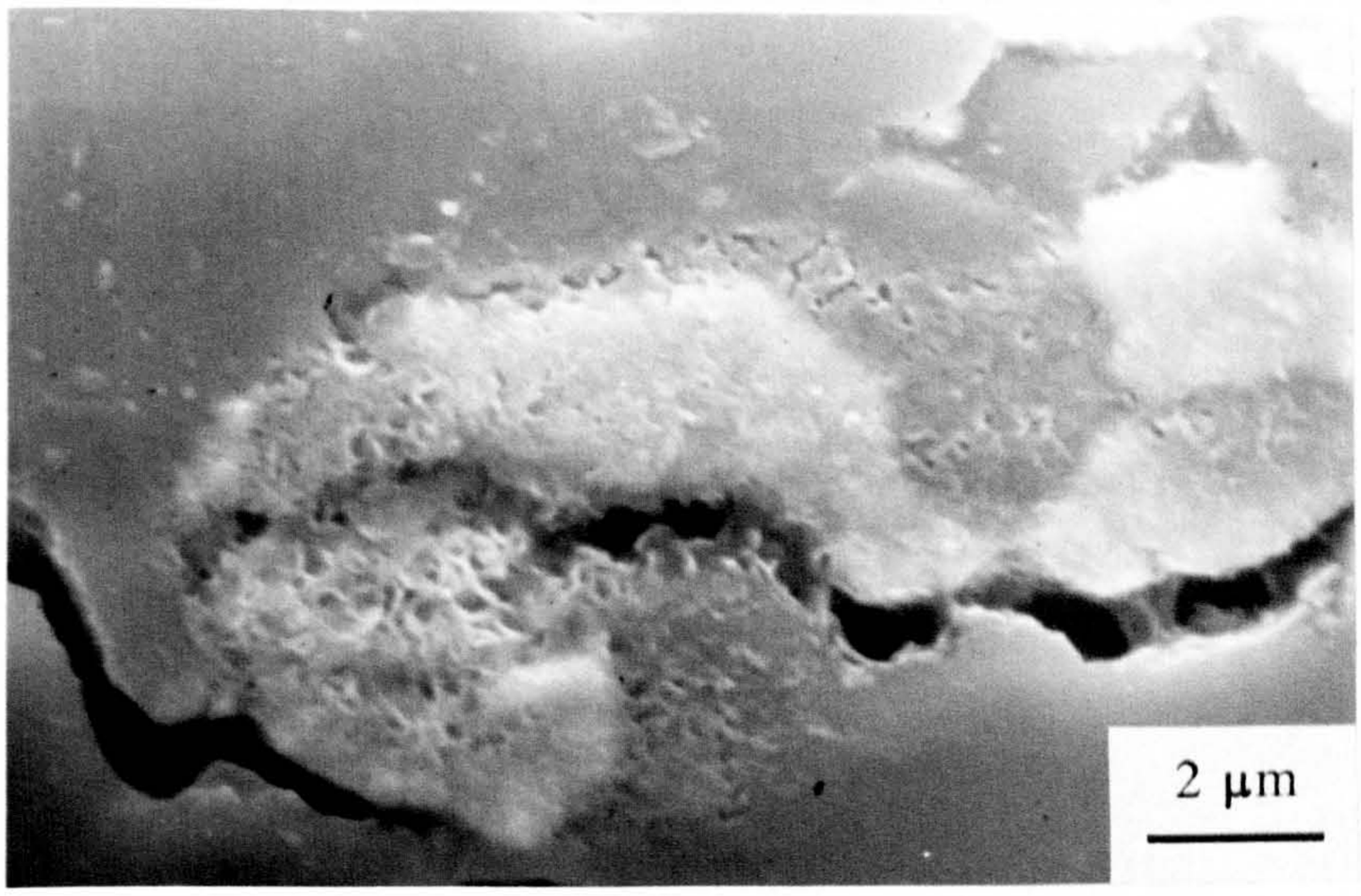

b)

Figure 6.11 Examples of SEM photomicrographs (secondary electron images) showing thermal shock induced fractures within hot pressed Al_2O_3-Fe composite material, subjected to $\Delta T = 400\ ^{o}C$. Crack/particle interactions include **a)** interfacial failure resulting in particle pull-out and **b)** ductile particle bridging by the Fe phase.

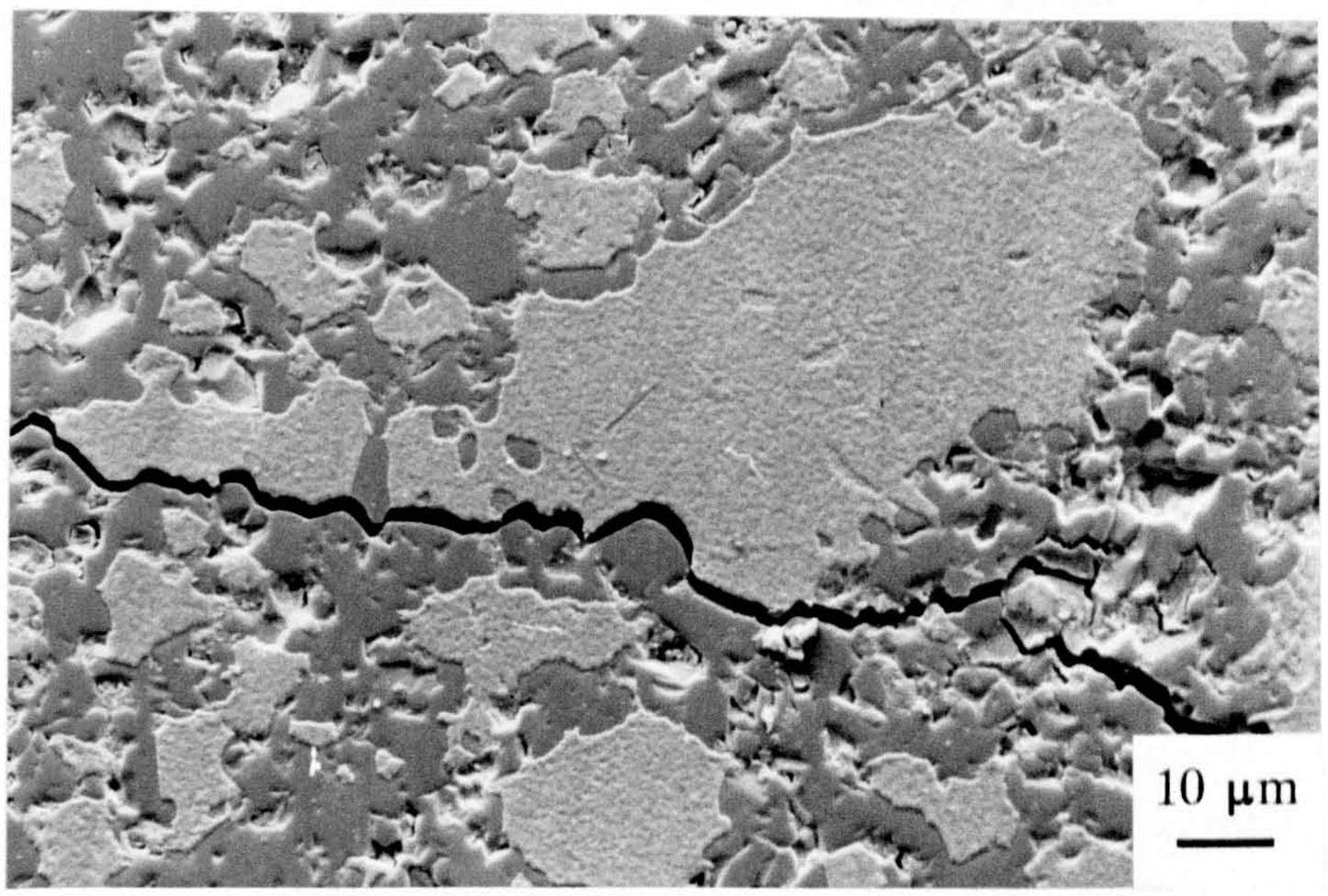

a)

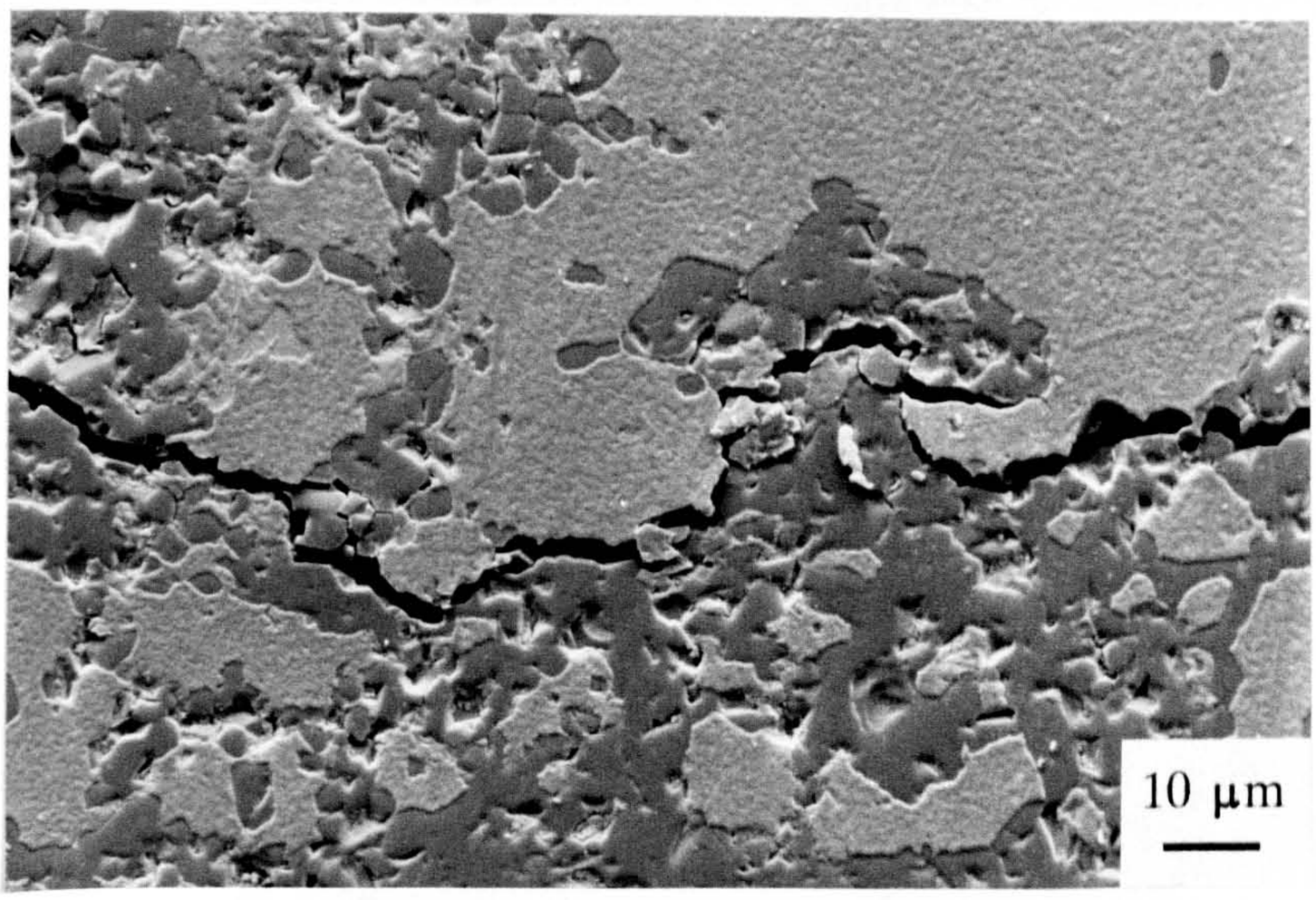

b)

Figure 6.12 Examples of SEM photomicrographs (secondary electron images) showing thermal shock induced fractures within sintered Al_2O_3-Fe composite material, subjected to $\Delta T = 400\,^{o}C$. Crack/particle interactions include **a)** interfacial failure resulting in particle pull-out and **b)** limited ductile particle bridging by the Fe phase.

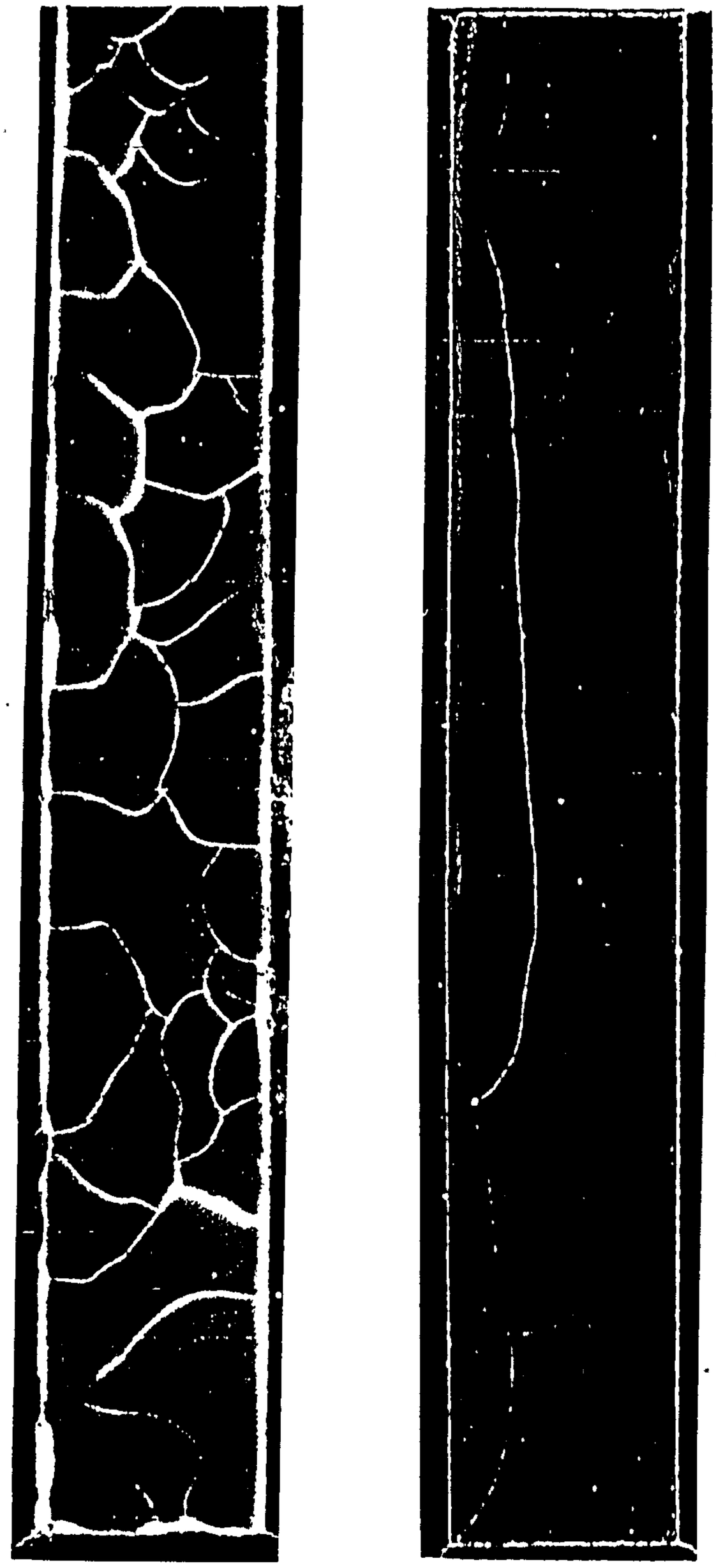

Figure 6.13 Montage of images of surface crack patterns obtained using CSLM and fluorescent dye for a) hot pressed monolithic Al_2O_3 and b) hot pressed Al_2O_3-Fe composite for ΔT=400 °C.

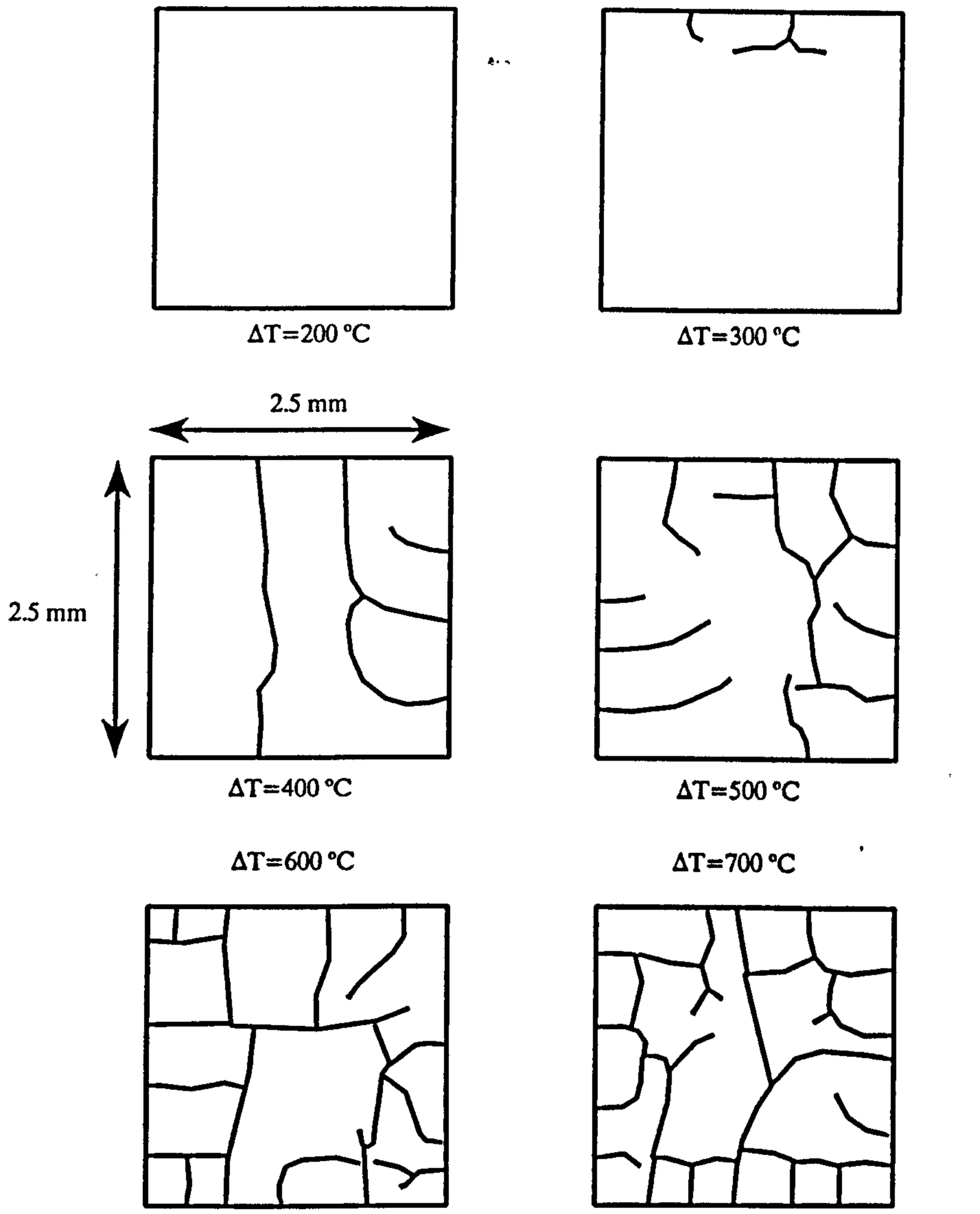

Figure 6.14 Series of schematic illustrations depicting surface crack patterns observed in hot pressed monolithic Al_2O_3 for a range of temperature differentials.

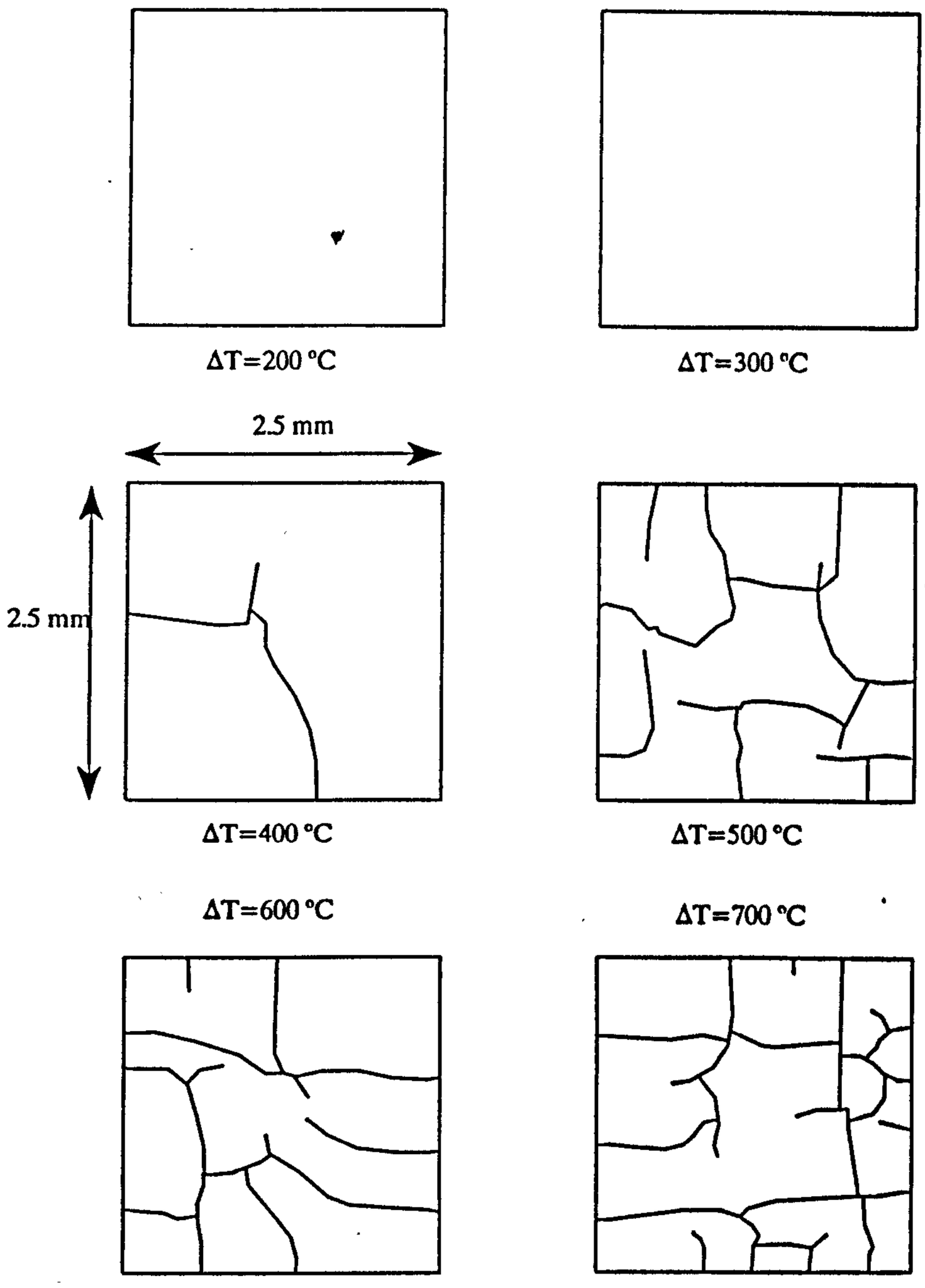

Figure 6.15 Series of schematic illustrations depicting surface crack patterns observed in hot pressed Al_2O_3-Fe composite for a range of temperature differentials.

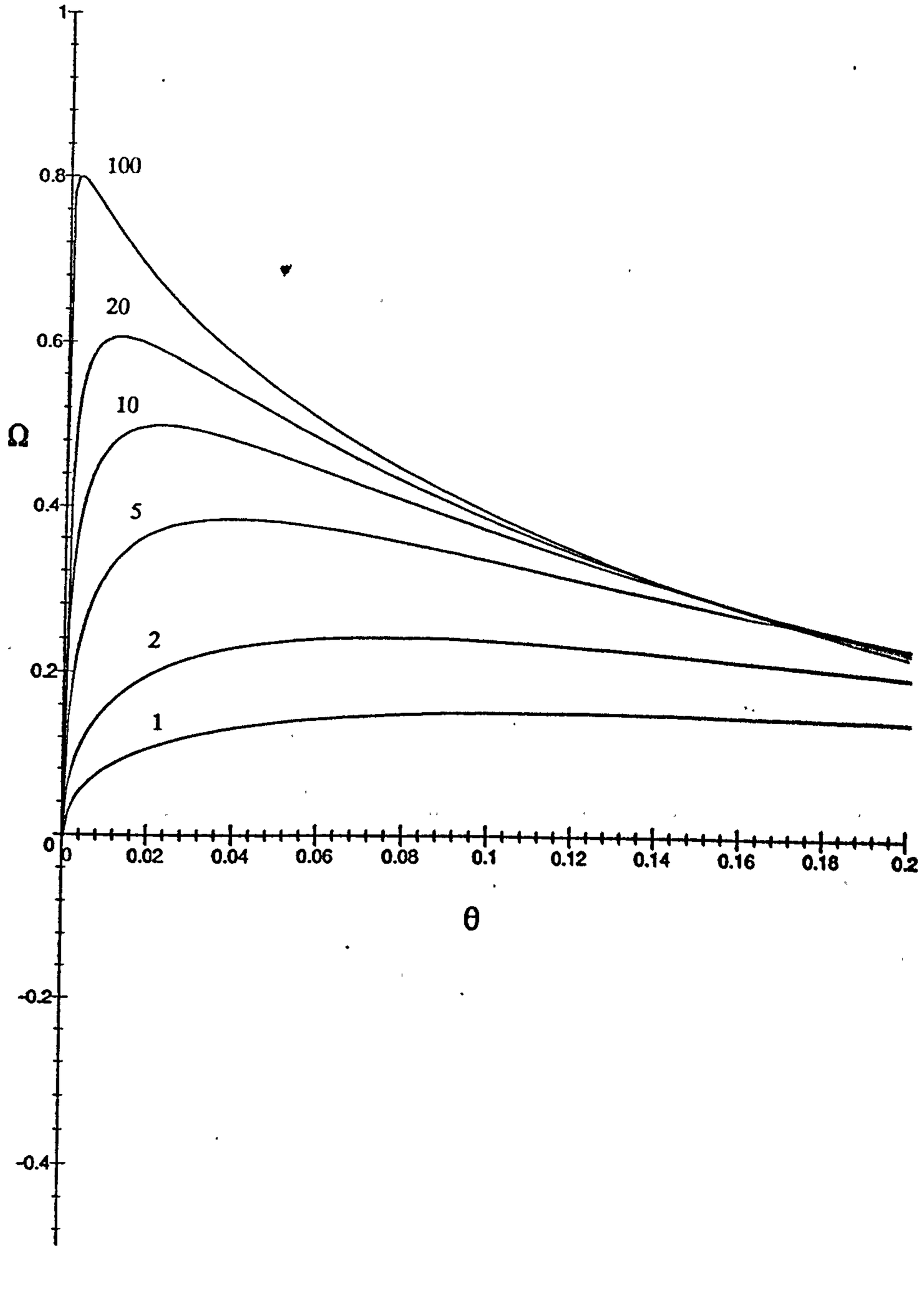

Figure 6.16 Plot of normalised thermal stress versus normalised time for a range of Biot moduli, as stated against each curve.

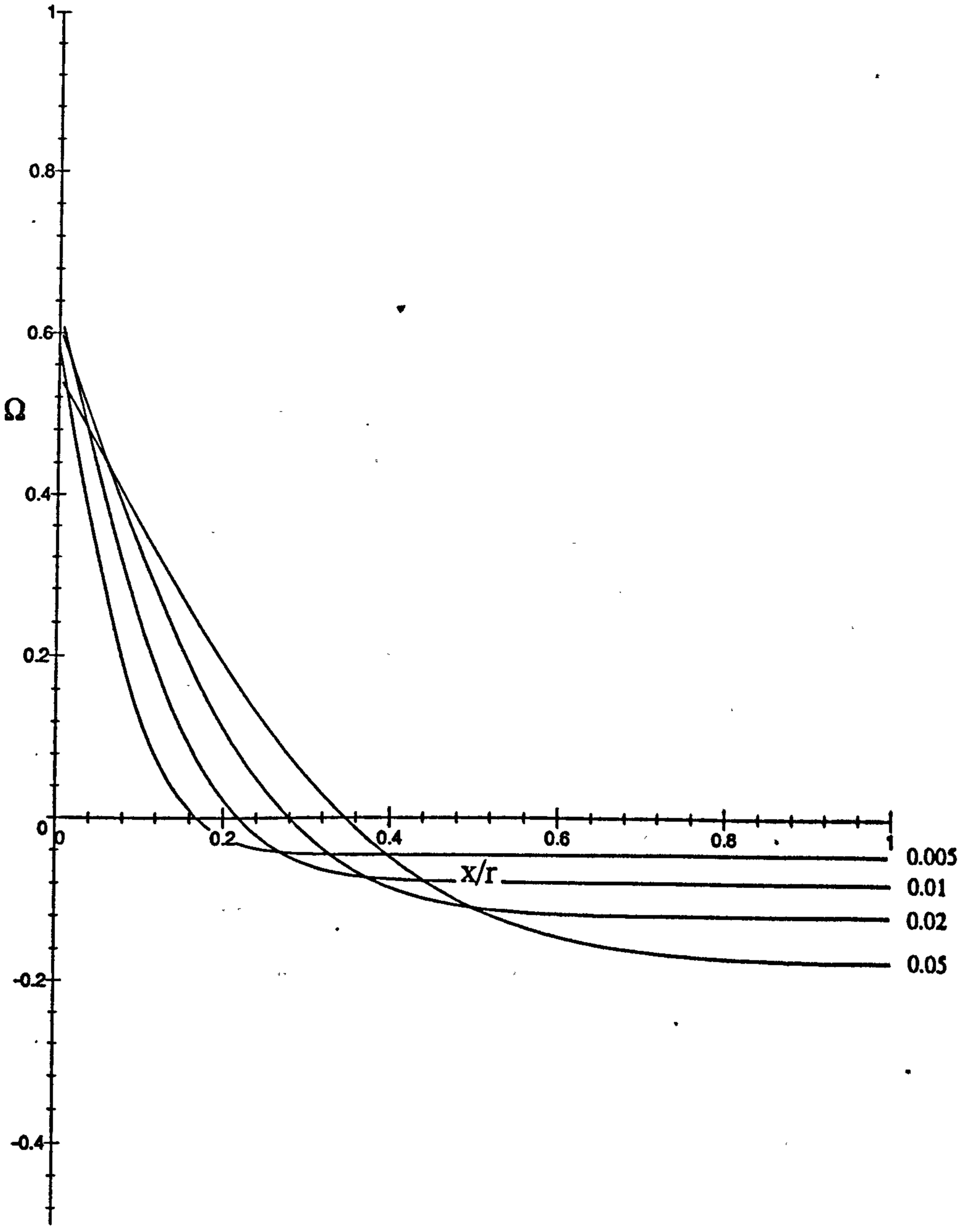

Figure 6.17 Plot showing variation of normalised thermal stress with depth for various values of normalised time (stated against each curve) and a Biot modulus of 20.

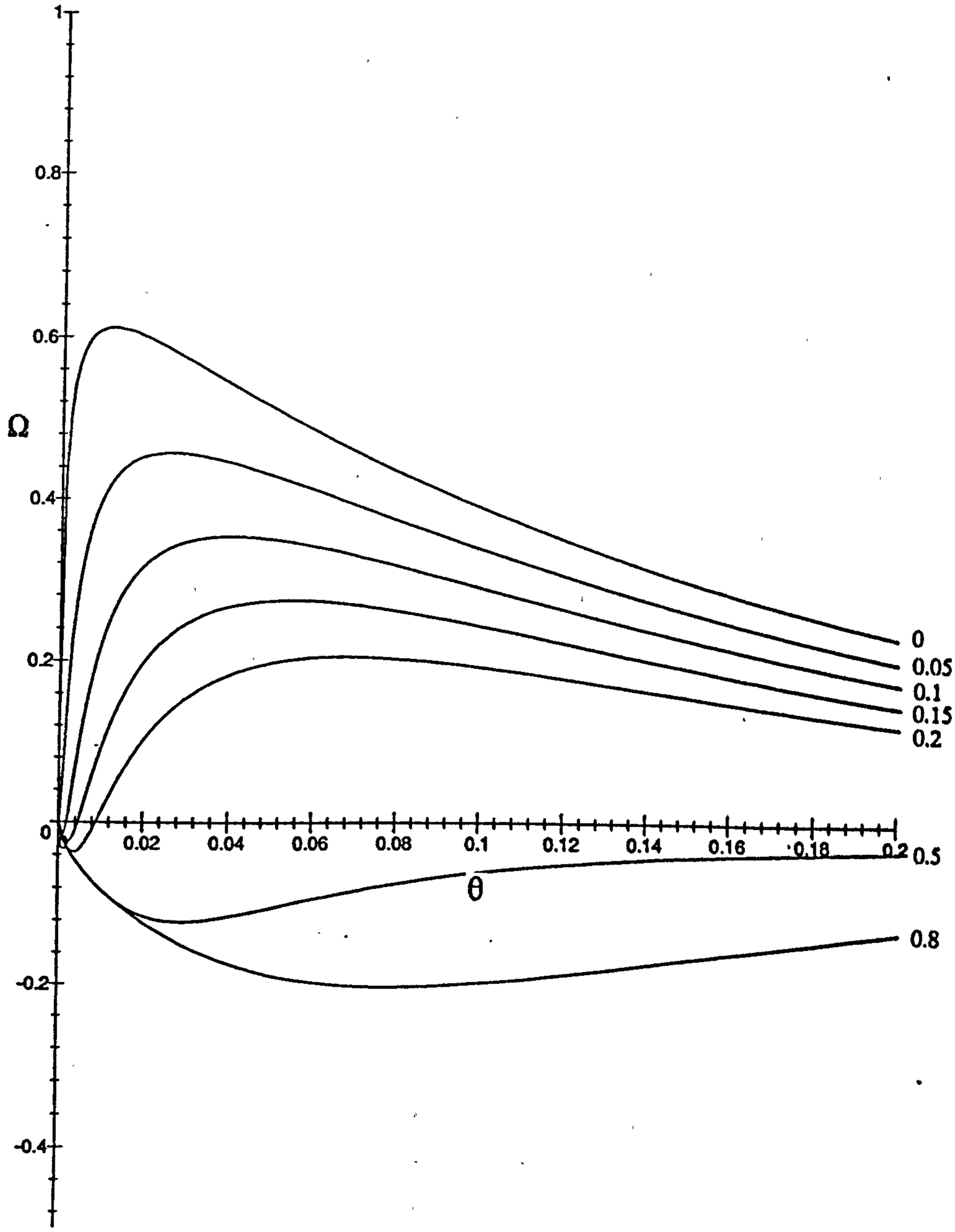

Figure 6.18 Plot showing variation of normalised thermal stress with normalised time for specific values of depth (stated against each curve) and Biot modulus of 20.

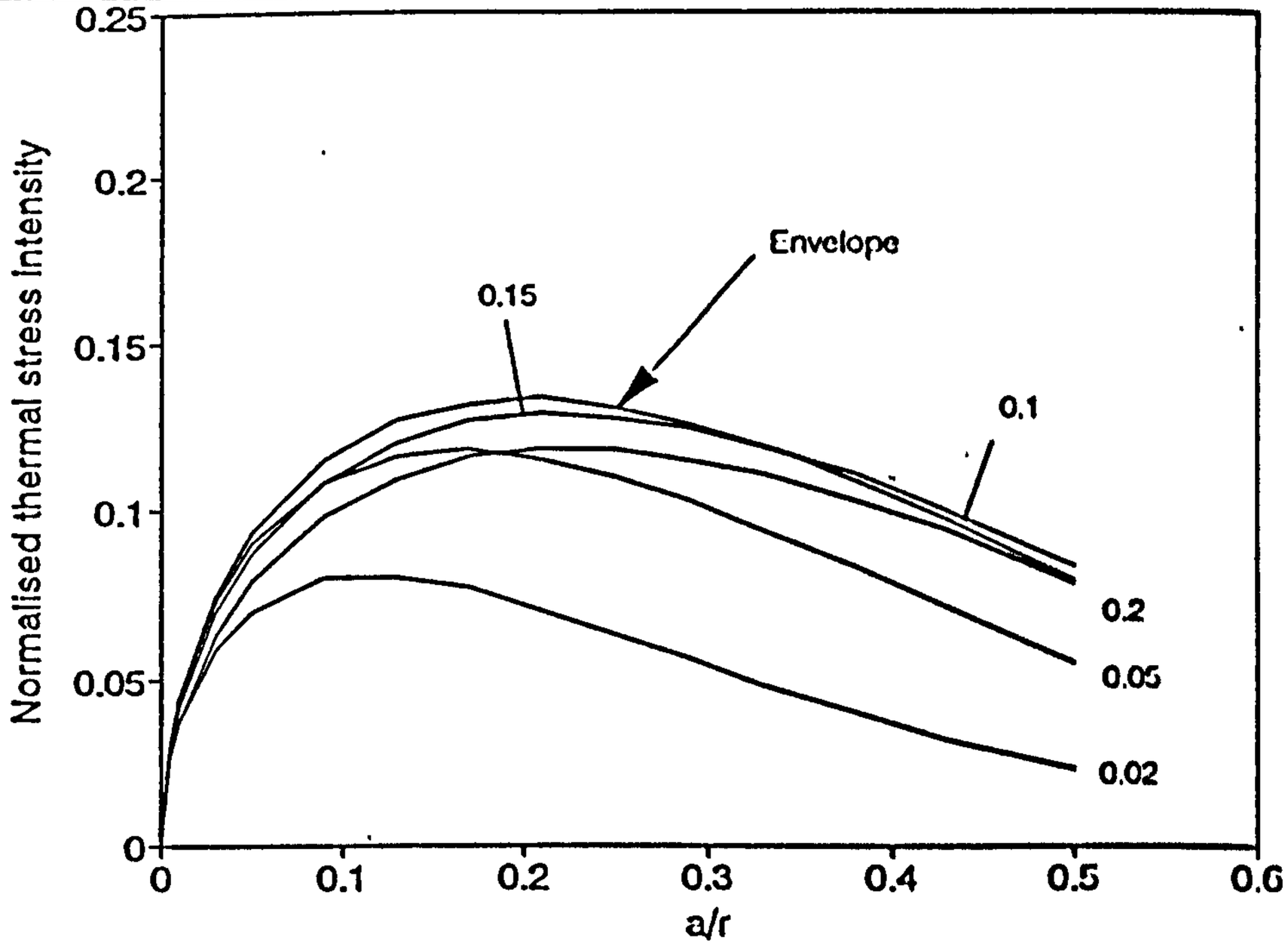

Figure 6.19 Plot of normalised thermal shock generated stress intensity factor versus normalised crack length for various values of normalised time and Biot modulus of 2. Envelope of κ curves is also shown.

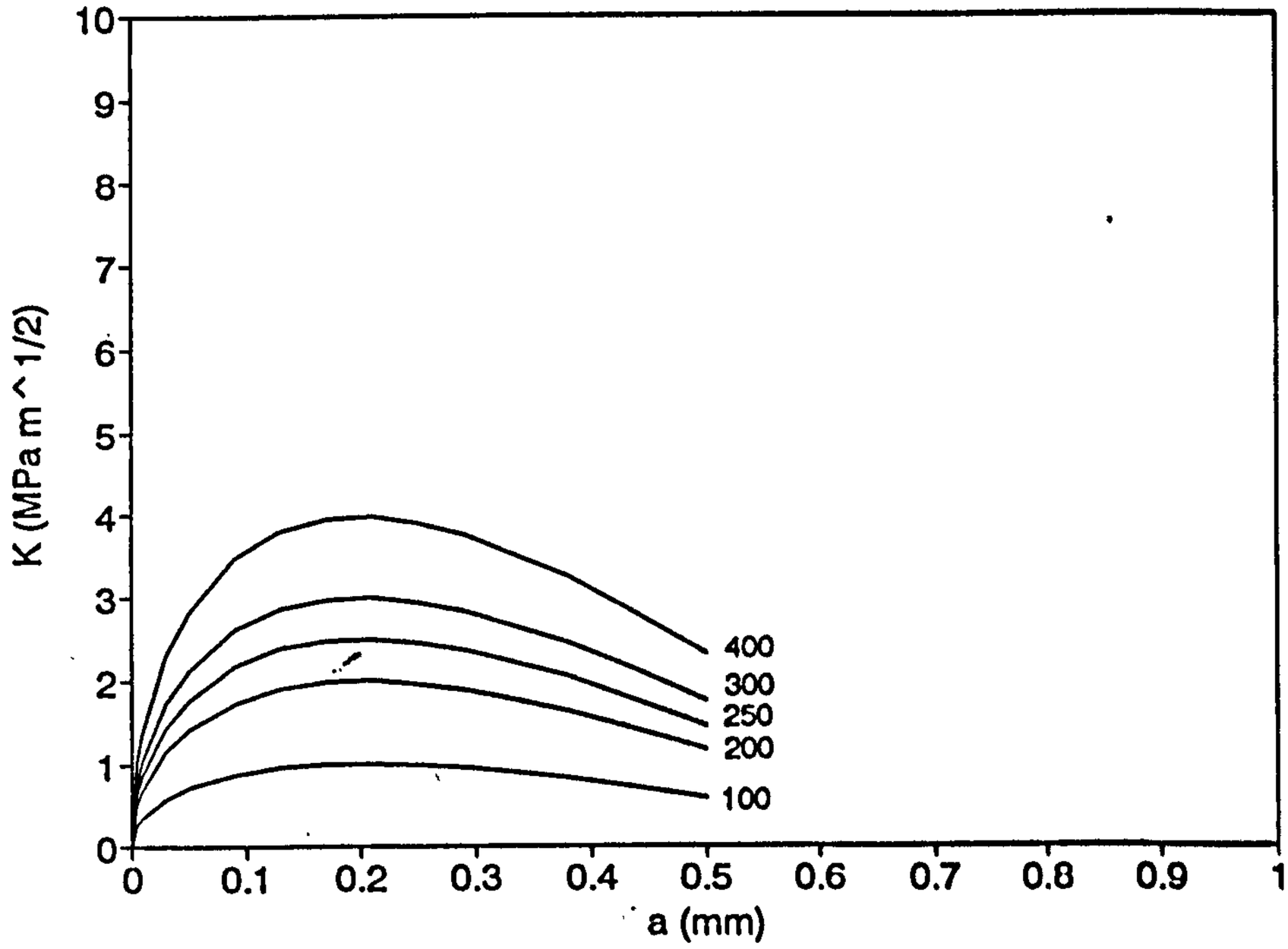

Figure 6.20 Plot of envelope of thermal shock generated stress intensity factor versus crack length for hot pressed monolithic Al_2O_3 subjected to various temperature differentials ($\beta = 1$).

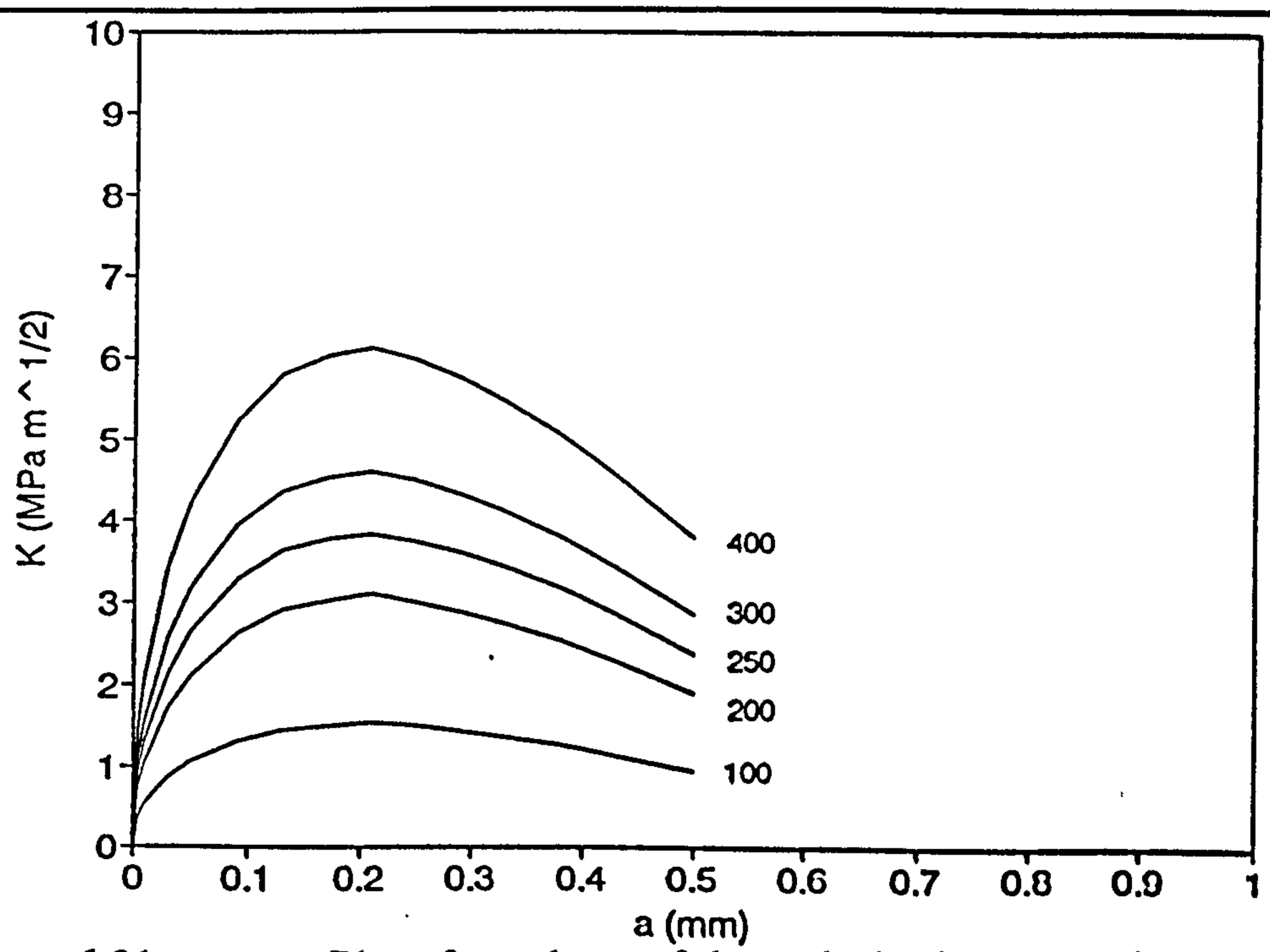

Figure 6.21 Plot of envelope of thermal shock generated stress intensity factor versus crack length for hot pressed monolithic Al_2O_3 subjected to various temperature differentials ($\beta=2$).

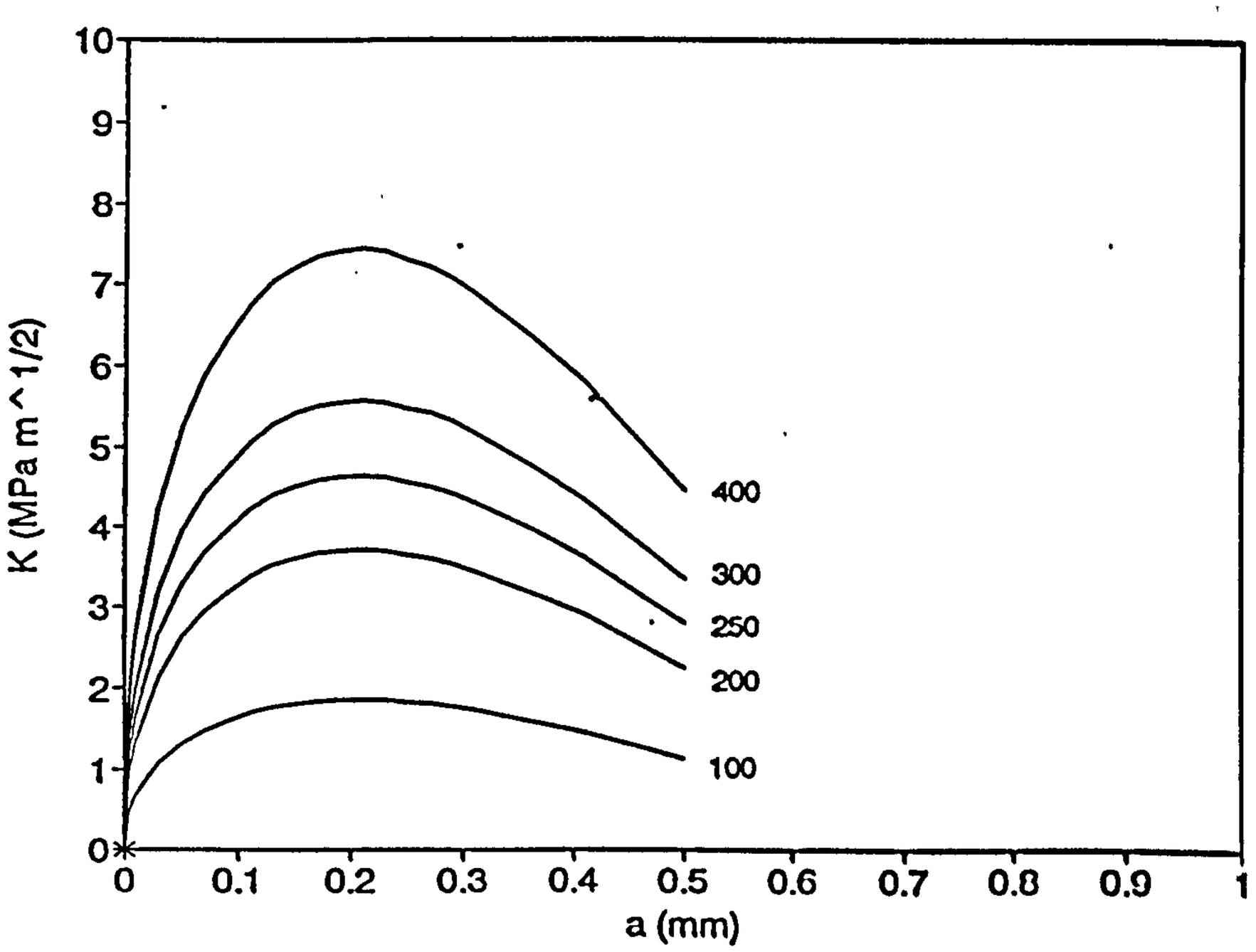

Figure 6.22 Plot of envelope of thermal shock generated stress intensity factor versus crack length for hot pressed monolithic Al_2O_3 subjected to various temperature differentials ($\beta=3$).

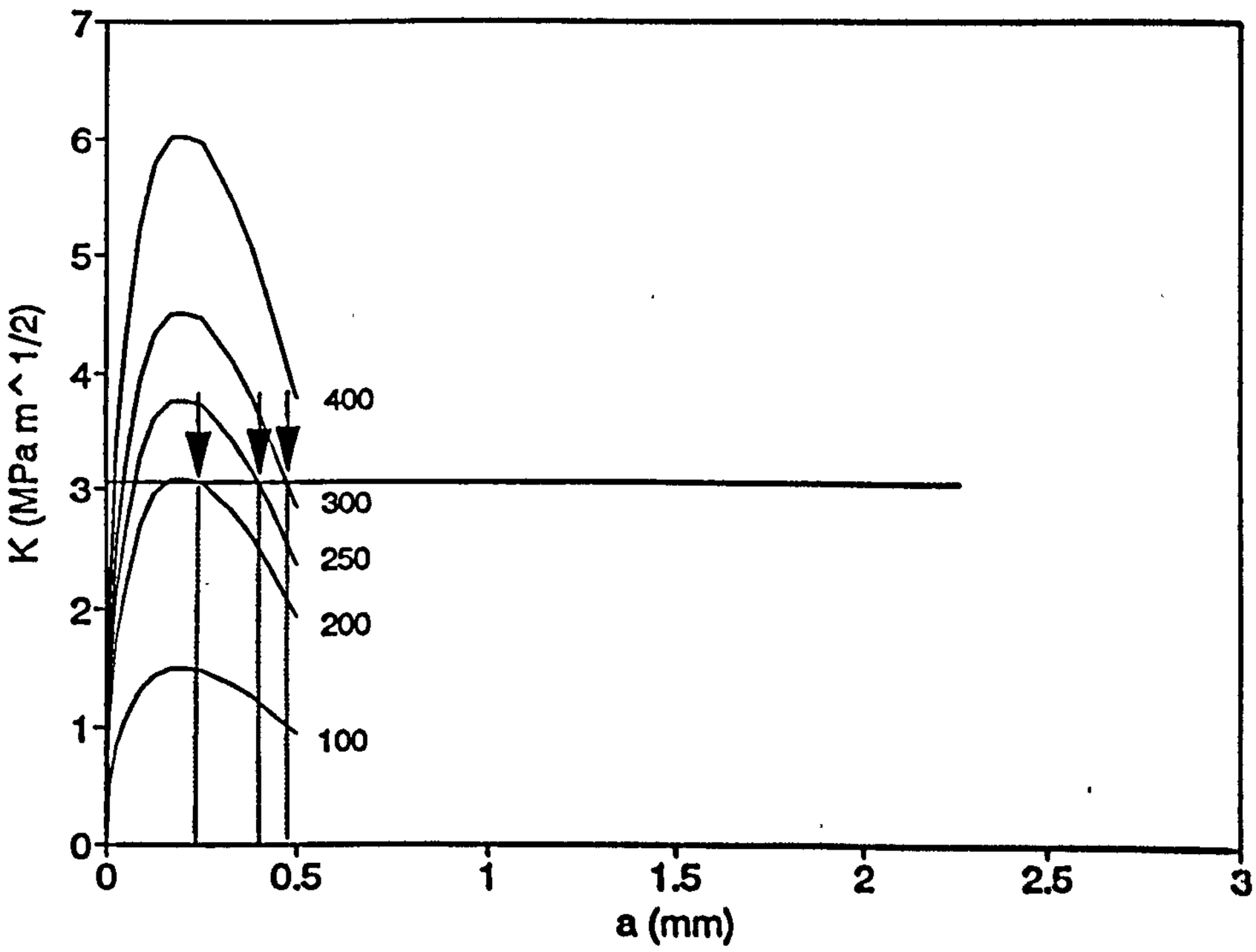

Figure 6.23 Plot showing envelope of thermal shock generated stress intensity factor versus crack length for hot pressed monolithic Al_2O_3 subjected to various temperature differentials. Superimposed is the constant K_R curve and proposed positions of crack arrest (represented by the bold arrows) ($\beta=2$).

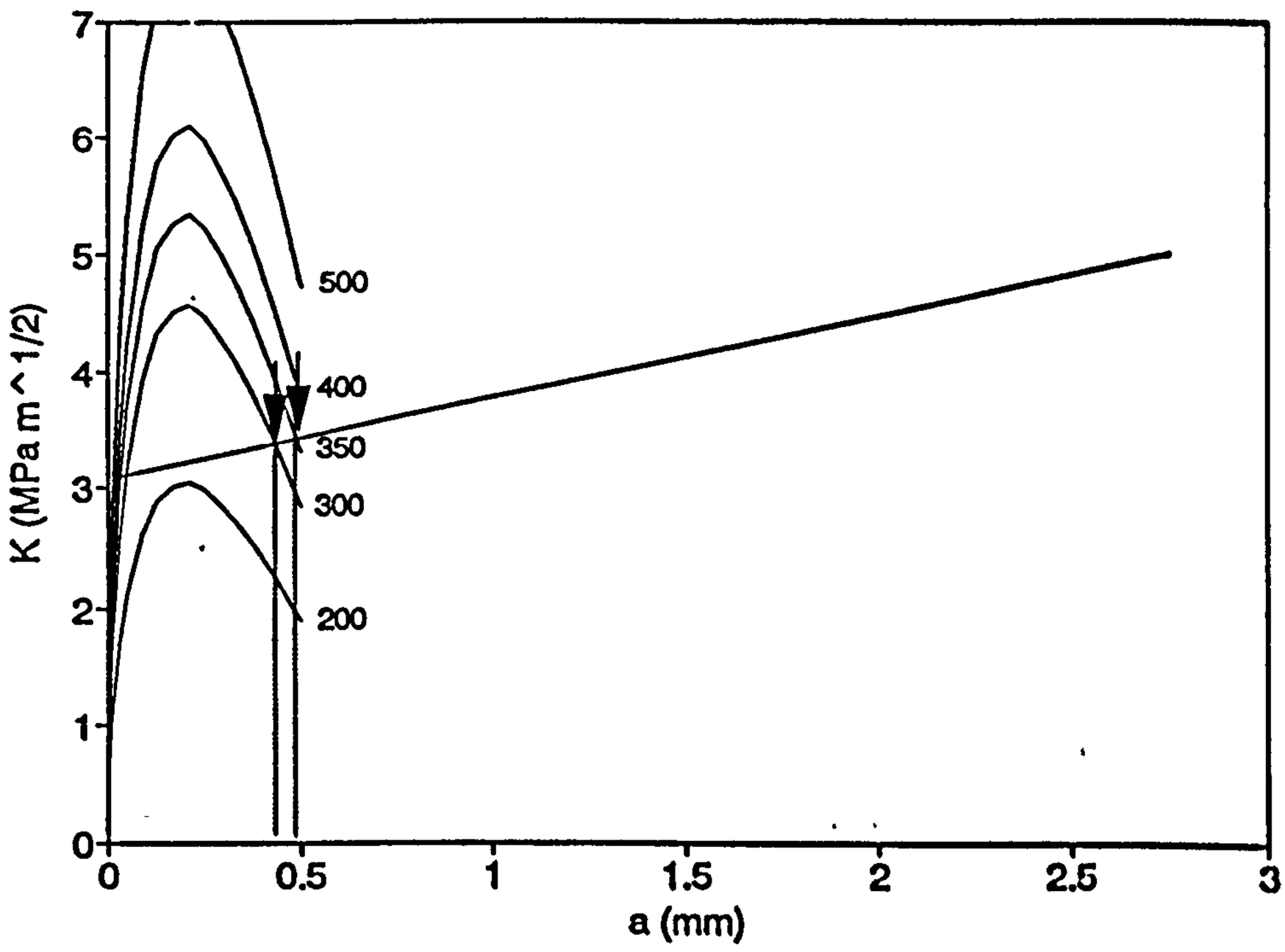

Figure 6.24 Plot showing envelope of thermal shock generated stress intensity factor versus crack length for hot pressed Al_2O_3-Fe composite subjected to various temperature differentials. Superimposed is the K_R curve and proposed positions of crack arrest (represented by the bold arrows) ($\beta=2$).

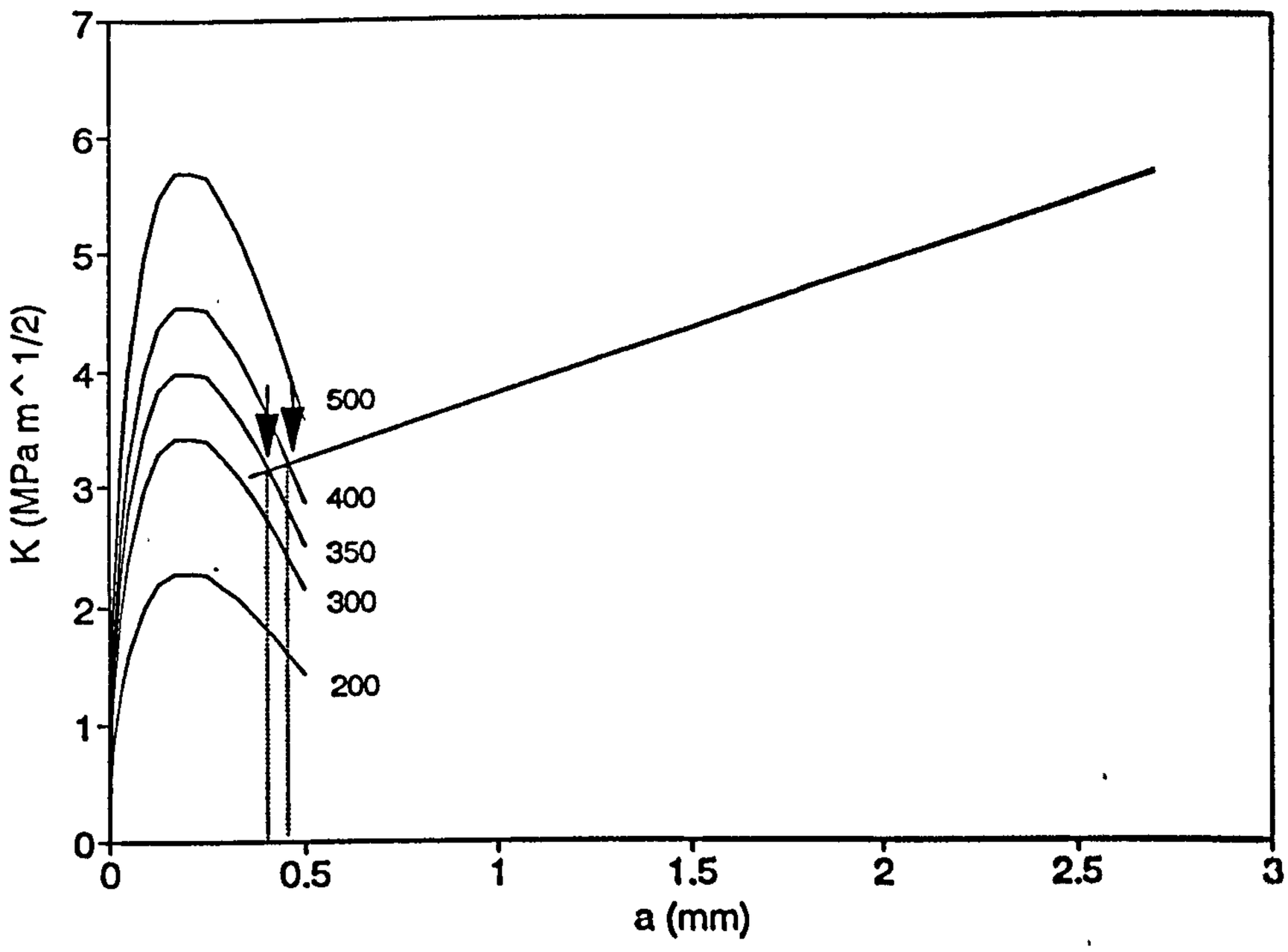

Figure 6.25 Plot showing envelope of thermal shock generated stress intensity factor versus crack length for sintered Al_2O_3-Fe composite subjected to various temperature differentials. Superimposed is the K_R curve and proposed positions of crack arrest (represented by the bold arrows) ($\beta=2$).

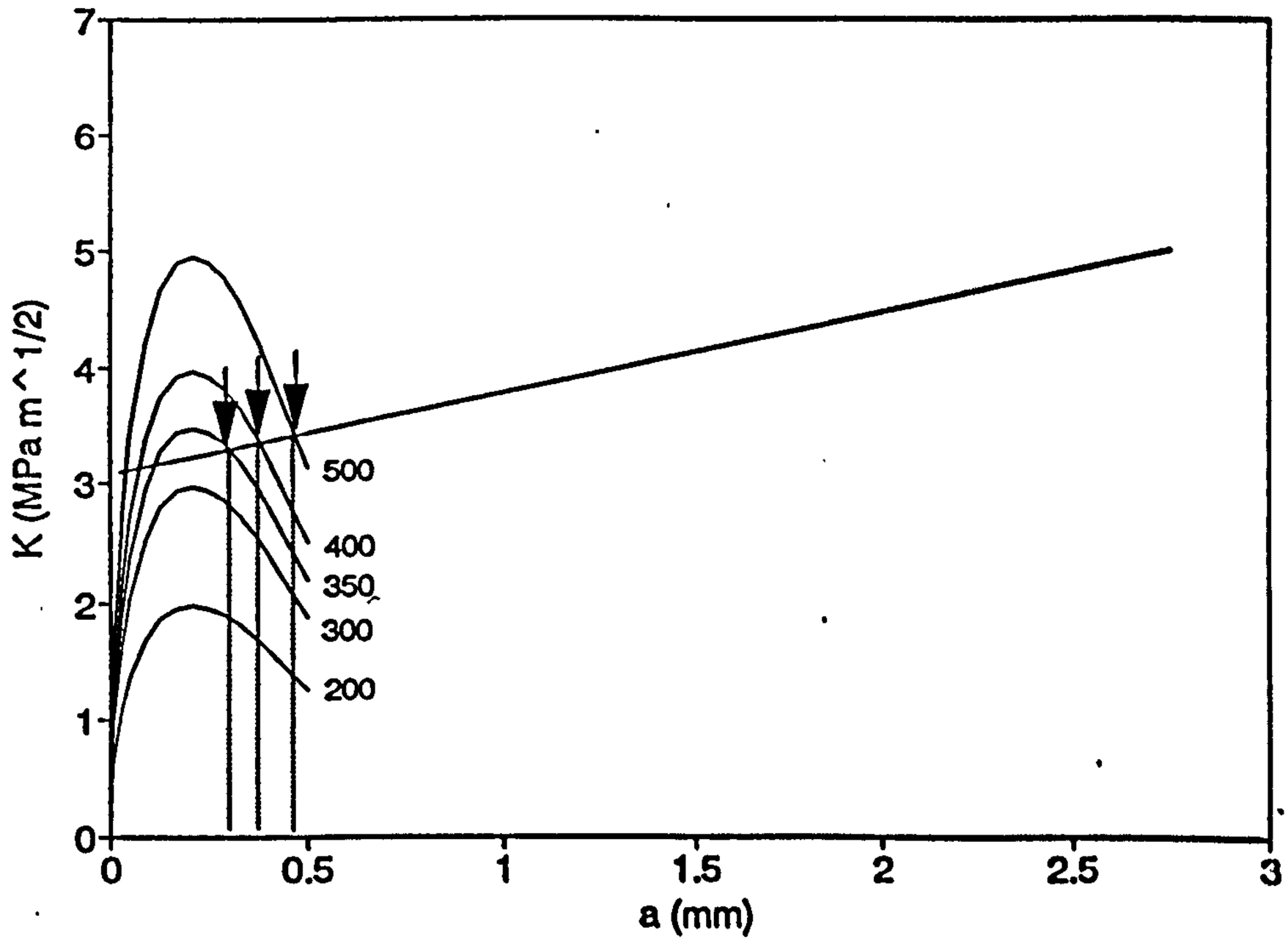

Figure 6.26 Plot showing envelope of thermal shock generated stress intensity factor versus crack length for the hot pressed Al_2O_3-Fe composite subjected to various temperature differentials. Superimposed is the K_R curve and proposed positions of crack arrest (represented by the bold arrows) ($\beta = 1$).

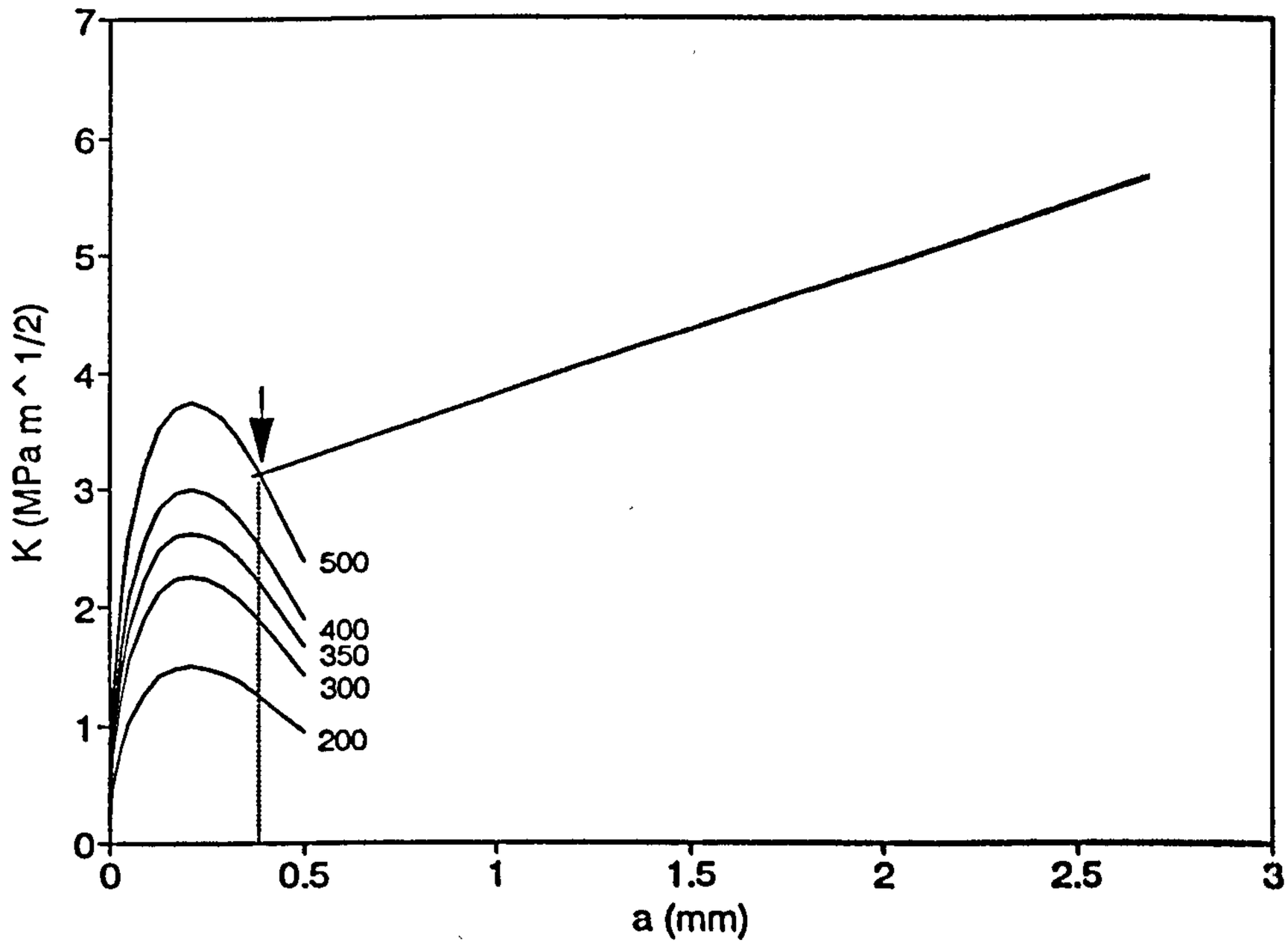

Figure 6.27 Plot showing envelope of thermal shock generated stress intensity factor versus crack length for the sintered Al_2O_3-Fe composite subjected to various temperature differentials. Superimposed is the K_R curve and proposed positions of crack arrest (represented by the bold arrows) ($\beta=1$). Note that only at temperature differentials equal to or greater than 500 °C do the thermal shock generated stress intensity factor curve and the superimposed K_R curve intersect.

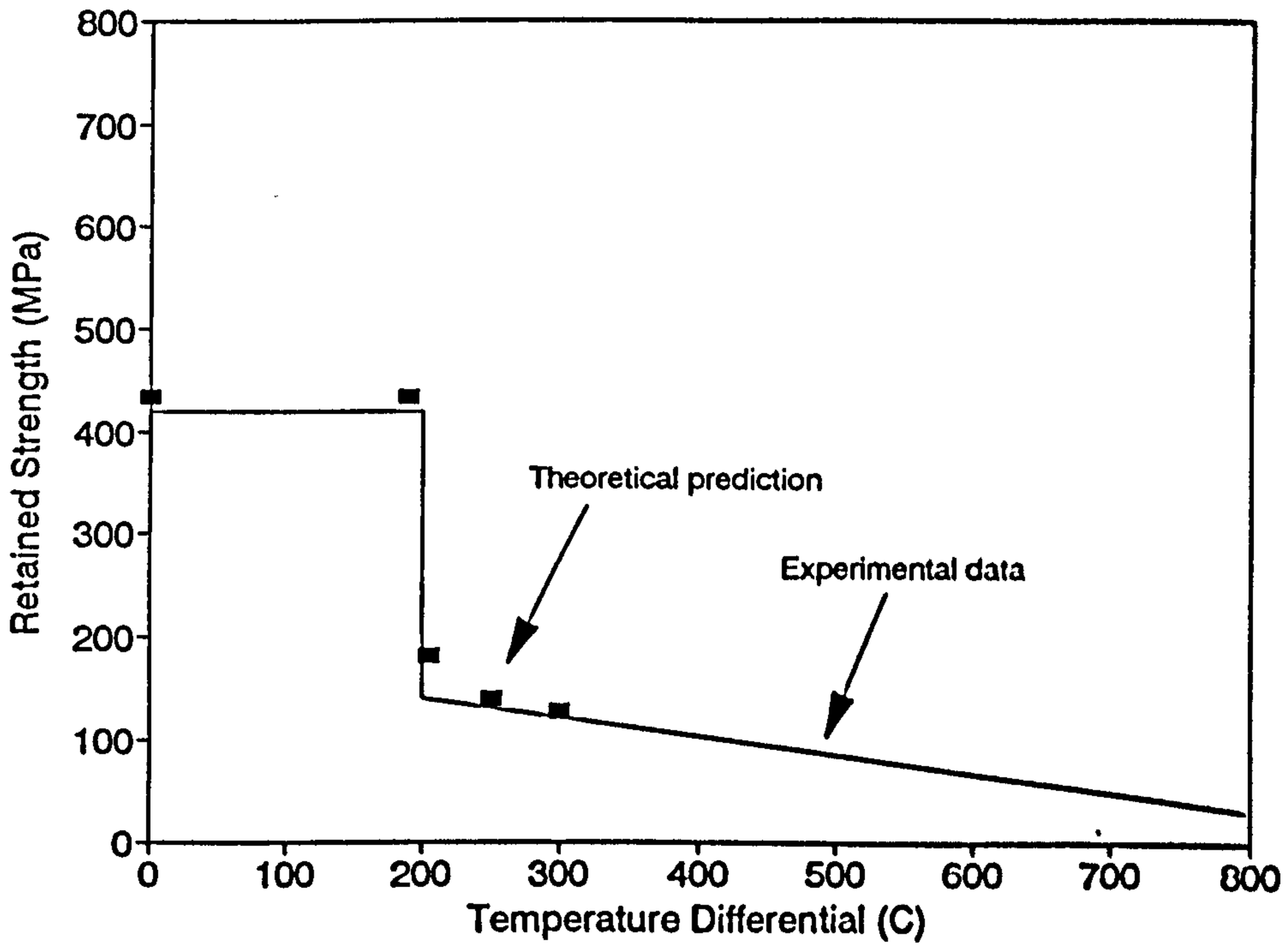

Figure 6.28 Plot of experimentally determined retained flexural strength versus temperature differential for hot pressed monolithic Al_2O_3. Also plotted are the theoretically predicted retained flexural strength values for various temperature differentials, showing good agreement with the experimental data ($\beta=2$).

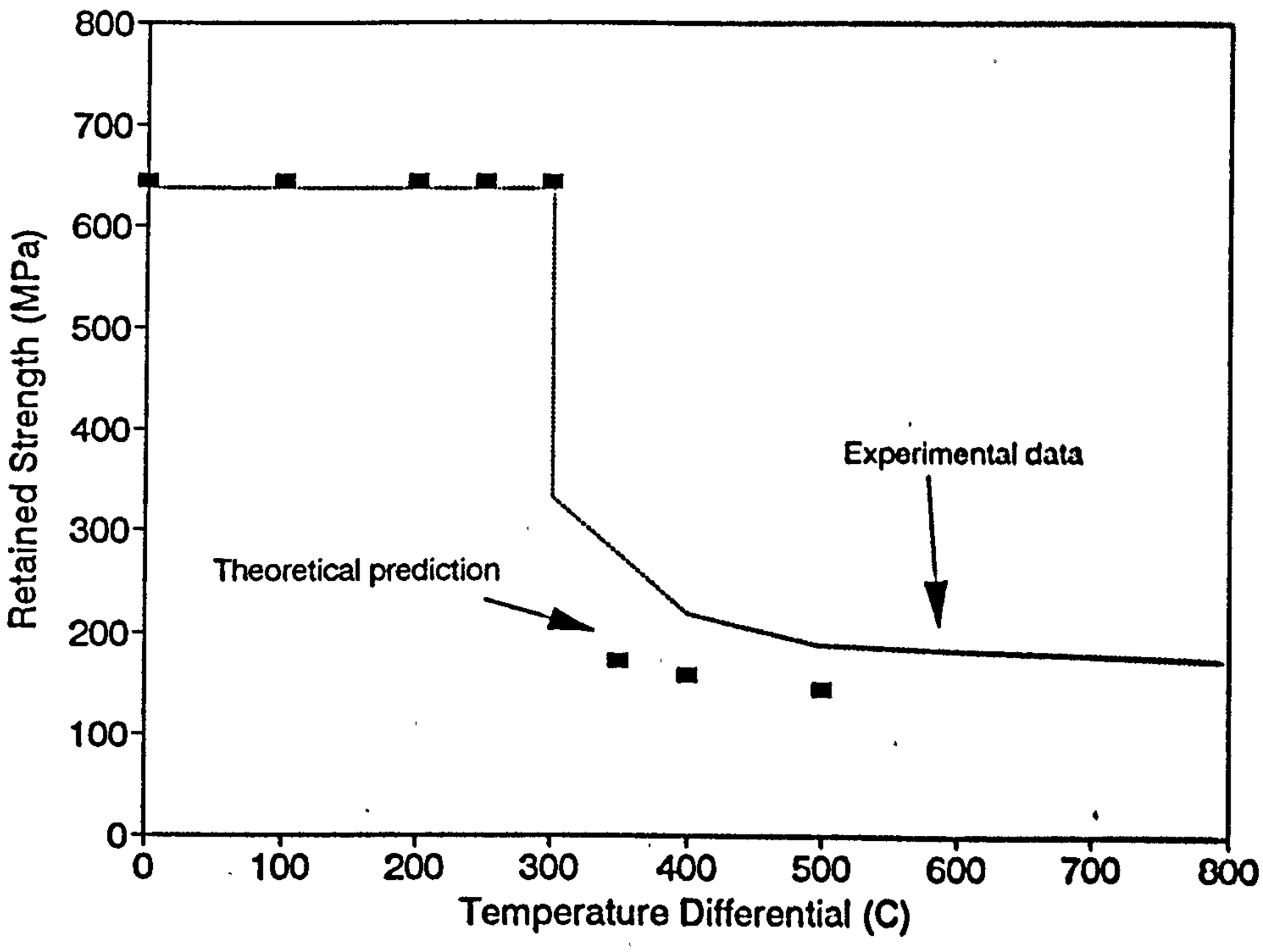

Figure 6.29 Plot of experimentally determined retained flexural strength versus temperature differential for the hot pressed Al_2O_3-Fe composite. Also shown are the theoretically predicted retained flexural strength values for various temperature differentials ($\beta = 1$).

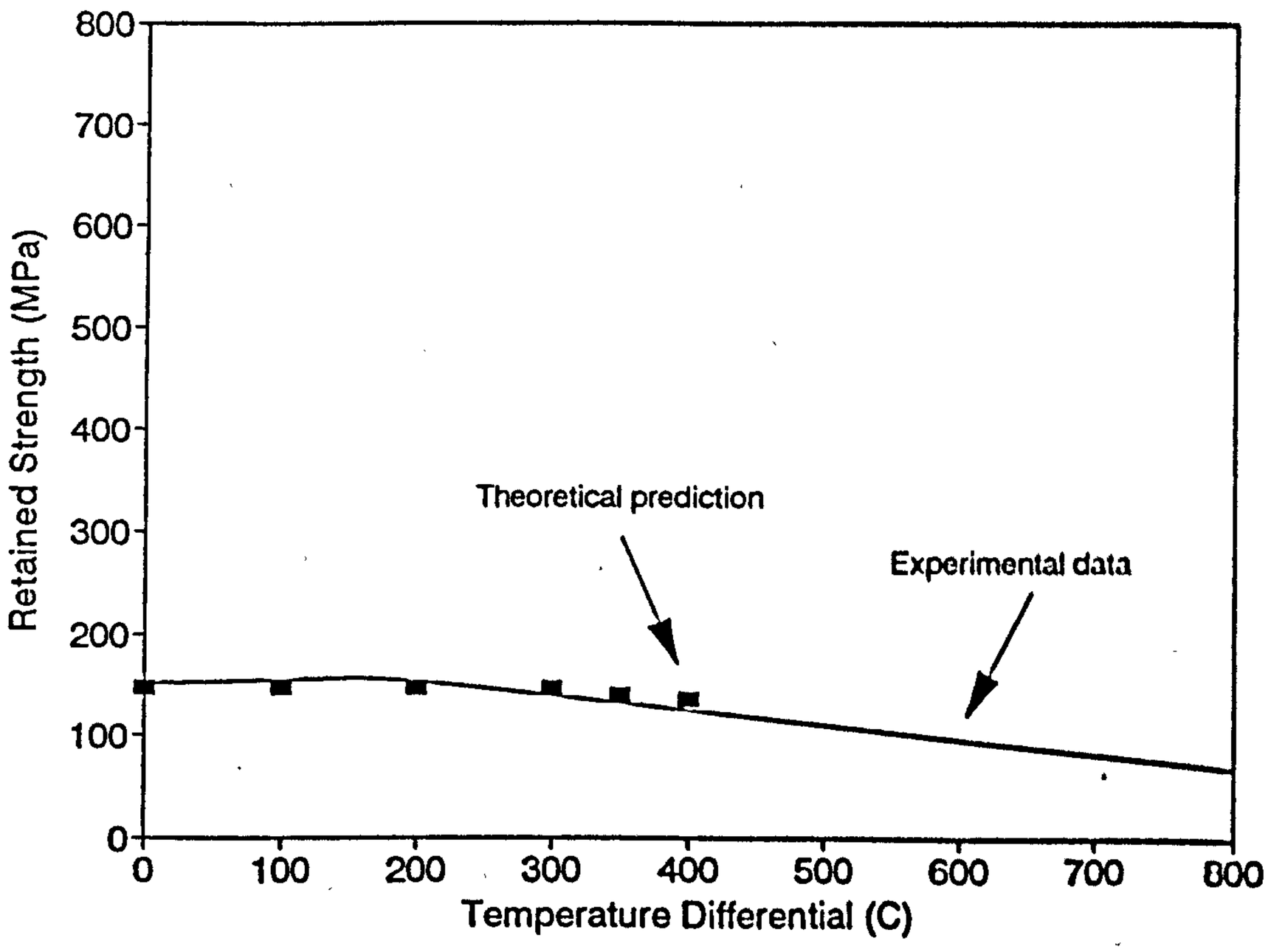

Figure 6.30 Plot of experimentally determined retained flexural strength versus temperature differential for the sintered Al_2O_3-Fe composite. Also shown are the theoretically predicted retained flexural strength values for various temperature differentials ($\beta = 2$).

CHAPTER SEVEN

CONCLUDING REMARKS

7.1 CONCLUSIONS FROM CURRENT WORK

The project involved a study of various aspects of an alumina-20 volume % iron ceramic matrix composite. The primary aim of the work was to determine whether or not the incorporation of the ductile phase led to an improved resistance to thermal shock compared to the monolithic parent matrix material, in particular whether the expected increase in fracture toughness alone resulted in superior performance. This aim has been achieved.

Alumina-iron composites have been successfully fabricated using the techniques of hot pressing and conventional pressureless sintering. The hot pressed composite showed a fully dense, reproducible microstructure of fine matrix grain size, incorporating small, discrete metallic particles of irregular morphology. The sintering process has yet to be optimised. A material of comparatively coarse microstructure and relative density of 95 % theoretical density has been achieved to date. It is envisaged that further work in this area may result in a higher relative density and a microstructure similar to that of the hot pressed composite.

Quantitative thermal shock analysis required the evaluation of the mechanical properties of the composite materials. The fracture toughness and fracture behaviour of the sintered composite has been evaluated using the double

cantilever beam technique. It has been found that the sintered composite exhibits K_R curve behaviour, with the fracture toughness rising linearly with increasing crack length to 8.3 MPa $m^{½}$ for a crack length of 5 mm, and that this is a consequence of the second phase particles. However, the full toughening potential of the ductile phase is not exploited, due to a weak ceramic/metal interface. The increase in fracture toughness with increasing crack length has been attributed to ductile particle crack bridging, crack deflection and subsequent particle pull-out, and crack blunting in areas of porosity. The K_R curve obtained is similar, although slightly more pronounced, than that observed for the hot pressed composite in a previous study. The flexure strength of the composites has been evaluated and compared with that of the matrix material. The strength of the hot pressed composite has been shown to be substantially greater than the monolithic matrix (641 MPa compared with 464 MPa respectively). This has been attributed to the more refined grain structure of the matrix. The strength of the sintered composite, however, was found to be 148 MPa, due to the increased porosity and more coarse matrix grain structure induced by conventional sintering. The Young's moduli of the composites has been estimated to be 344 GPa and 316 GPa for the hot pressed and sintered materials respectively. Subsequent measurement (giving 341 GPa and 258 GPa respectively) showed good agreement for the hot pressed composite. The discrepancy in the case of the sintered composite has been attributed to inferior ceramic/metal interfacial bonding compared with the hot pressed composite.

Evaluation of the thermal shock behaviour of the alumina-iron composites has been approached in several ways. Initially, it was established that exposure of the composites to elevated temperature alone did not affect the flexure strength. Experimental work was then carried out in order to determine the nature and extent of strength degradation following various thermal shock treatments. Specimens were quenched in water from a range of temperatures, and subsequently tested in three point flexure. The high strength hot pressed alumina-iron composite was found to exhibit an increased critical temperature differential

(relative to the monolithic matrix) of approximately 350 °C. More severe treatments resulted in a gradual further loss of strength. In contrast, the low strength sintered alumina-iron composite showed little strength degradation over the range of treatments, with no definite critical temperature differential. The behaviour was characteristic of that typically observed for refractory materials. The thermal shock behaviour of the hot pressed monolithic matrix material and a commercially available zirconia toughened alumina was also evaluated. Both behaved as typical high strength engineering ceramics, showing severe loss of strength for ΔT_c of 200 °C and 250 °C respectively. The calculation of thermal shock parameters for the alumina-iron composites and the monolith supported the experimental findings. Fluorescence microscopy allowed low magnification examination of fracture patterns resulting from thermal shock treatments covering a range of ΔT values, and qualitatively supported the retained strength results obtained for the hot pressed composite and the monolithic matrix material, giving an indication of ΔT_c and the degree of surface cracking. Examination of the interaction of thermal shock induced cracks with second phase particles using scanning electron microscopy showed that the preferred interactions resulted in failure of the ceramic/metal interface.

Quantitative analysis of the thermal shock behaviour of the two alumina-iron composites and the monolithic matrix was performed. A fracture mechanics approach developed by Evans & Charles was adopted. Thermal stresses were calculated using expressions developed by Jaeger. Envelopes of maximum thermal shock generated stress intensity factor, K, versus crack length, a, have been calculated for conditions of varying Biot moduli, for the three materials. The experimentally derived K_R curves were then superimposed, allowing the determination of critical temperature differentials depending on the positions of intersection of the thermal shock generated stress intensity factor curves with the K_R curve. An attempt was also made to calculate the predicted retained flexural strength from the proposed positions of crack arrest, for various temperature differentials for the three materials.

The thermal properties (α, k) of the composite materials were estimated. Several appropriate values of Biot modulus, β, were then chosen for the construction of K versus a curves which best represented the experimentally obtained data, in terms of ΔT_c for the alumina-iron composites and the monolith. Crack arrest lengths were taken from the points of intersection of the calculated K curves with the superimposed K_R curve for each of the three materials. The crack lengths were then used to calculate the approximate retained strengths corresponding to a range of ΔT. The predicted degrees of retained strength show that both the hot pressed monolith and composite behave as high strength engineering ceramics, exhibiting a severe loss of strength at ΔT_c, whereas the sintered composite shows little strength degradation and no definite ΔT_c, typical of a refractory ceramic. The theoretical analysis shows moderate agreement with the experimental results. Further experimental work is required regarding the measurement of the thermal properties of the alumina-iron composite materials, in order to confirm the validity of the assumptions made, and to enable accurate determination of the predicted degree of strength degradation following a given thermal shock treatment.

The inclusion of iron particles in an alumina matrix *has* been found to improve the thermal shock behaviour, both in terms of the increased critical temperature differential and the increased resistance to damage. However, the application of a quantitative analysis has indicated that the increase in the critical temperature differential for the composites is a direct consequence of the decreased Young's modulus and/or a decrease in Biot modulus, both of which result in a decrease in the thermal shock generated stress intensity factor generated for a given temperature differential. The observed increase in toughness of the two alumina-iron composites does not contribute significantly to the increased critical temperature differential determined both experimentally and analytically. However, it is concluded that the increase in fracture toughness of the composites contributes towards the increased damage resistance, but that this is due primarily to the mechanisms of crack blunting and crack deflection, and *not* to the proposed

mechanism of ductile particle bridging utilising the ductility of the metallic phase.

7.2 PROPOSED FURTHER WORK

7.2.1 Processing Development

The conventional pressureless sintering of the Al_2O_3-Fe composite requires additional work in order to optimise the final density and refine the microstructure. This may be achieved by altering several processing variables, including the sintering temperature, the dwell time at maximum temperature, ramp rates and sintering atmospheres. The final sintered composite should be similar in terms of microstructure to the hot pressed composite.

7.2.2 Interfacial Examination

It has been shown that for the alumina-iron composites involved in this study, the ceramic/metal interfacial bond strength is low, thus preventing the full toughening potential of the ductile phase from being exploited. The low strength of the interface is also thought to be detrimental to other properties of the composites, such as strength and stiffness. However, characterisation of the interface has not been included in the current work. Research is therefore required in this area in order to determine the exact nature of the bonding at the alumina/iron interface, and possibilities regarding the improvement of the bonding must be considered.

7.2.3 Accurate Determination of Thermal Properties

The quantitative analysis presented in chapter 6 is based on a fracture mechanical approach, enabling the determination of the thermal shock generated stress intensity factor curves generated for a given thermal shock treatment. The calculation of such data requires the knowledge of several thermal properties of the materials of interest, i.e. the thermal conductivity and heat transfer

coefficient. For the purposes of this study, k and h have been estimated, based on the values reported in the literature for monolithic alumina. It is thought that the estimated values are reasonable approximations. However, measurement of the properties would firstly justify the assumptions made, and secondly enable a more accurate prediction of the thermal shock behaviour of the composite materials.

7.2.4 Other Properties

The increased fracture toughness of the alumina-iron composite materials may lead, whether directly or indirectly, to the enhancement of other properties, such as wear resistance, fatigue and high temperature behaviour. Further work is therefore required in these fields if such composites are to gain wider applicability.

REFERENCES

AGHAJANIAN, M. K., MACMILLAN, N. H., KENNEDY, C. R., LUSZCZ, S. J., ROY, R., "Properties and Microstructures of Lanxide Al_2O_3-Al Ceramic Composite Materials", 1989, ***J. Mat. Sci.***, 24, 658-670.

ANDERSSON, T., ROWCLIFFE, D. J., "Indentation Thermal Shock Test for Ceramics", 1996, ***J. Am. Ceram. Soc.***, 79, [6], 1509-1014.

ARNOLD, M., BOCCACCINI, A. R., ONDRACEK, G., "Theoretical and Experimental Considerations of the Thermal Shock Resistance of Sintered Glasses and Ceramics using Modelled Microstructure-Property Correlations", 1996, ***J. Mat. Sci.***, 31, 463-469.

ASHBY, M. F., BEAUMONT, P. W. R., "Processing of Toughened Alumina", 1992, Technical Report CUED/C-MATS/TR203, Engineering Department, University of Cambridge, U.K.

ASHBY, M. F., BLUNT, F. J., BANNISTER, M., "Flow Characteristics of Highly Constrained Metal Wires", 1989, ***Acta. Met.***, 37, 1847-1857.

ASTM, "Standard Test Method for Flexural Strength of Advanced Ceramics at Ambient Temperature", Designation C 1161 - 90.

BAHR, H. A., BAHR, U., BALKE, H., MASCHKE, H., PETZOLD, A., WEI β, H. J., "Multiple Crack Propagation Under Thermal Load", 1993, Thermal Shock and Thermal Fatigue Behaviour of Advanced Ceramics, Schneider, G. A., and Petzow, G., (eds.), Kluwer Academic Publishers, 143-153.

BANNISTER, M., SHERCLIFF, H., BAO, G., ZOK, F., ASHBY, M. F., "Toughening in Brittle Systems by Ductile Bridging Ligaments", 1992, ***Acta. Met.***, 40, No. 7, 1531-1537.

BARAN, G., DEGRANGE, M., ROQUES-CARMES, C., WEHBI, D., "Fracture Toughness of Metal Reinforced Glass Composites", 1990, ***J. Mat. Sci.***, 25, 4211-4215.

BHATTACHARYA, A. K., PETROVIC, J. J., "Ductile Phase Toughening and R-Curve Behaviour in a B_4C-Al Cermet", 1992, ***J. Mat. Sci.***, 27, 2205-2210.

BECHER, P. F., LEWIS III, D., CARMAN, K. R., GONZALEZ, A. C., "Thermal Shock Resistance in Ceramics: Size and Geometry Effects in Quench Tests", 1980, ***Ceram. Bull.***, 59, No. 5, 542-548.

BORDIA, R. K., RAJ, R., "Analysis of Sintering of a Composite with a Glass or Ceramic Matrix", 1986, ***J. Am. Ceram. Soc.***, 69, [3], C-55-C-57.

BRAUN, L. M., BENNISON, S. J., LAWN, B. R., "Objective Evaluation of Short-Crack Toughness Curvess using Indentation Flaws: Case Study on Alumina-Based Ceramics", 1992, ***J. Am. Ceram. Soc.***, 75, [11], 3049-3057.

BUESSEM, W. R., High Temperature Technology, Chapman and Hall, 1956, 460-469.

CHAKLADER, A. C. D., ARMSTRONG, A. M., MISRA, S. K., "Interface Reactions between Metal and Ceramics: IV, Wetting of Sapphire by Liquid Copper-Oxygen Alloys", 1968, ***J. Am. Ceram. Soc.***, 51, [11], 630-633.

DAVIDGE, R. W., Mechanical Behaviour of Ceramics, Cambridge University Press, 1979, 118-131.

DAVIDGE, R. W., GREEN, T. J., "The Strength of Two-Phase Ceramic/Glass Materials", 1968, ***J. Mat. Sci.***, 3, 629-634.

DAVIDGE, R. W., TAPPIN, G., "Thermal Shock and Fracture in Ceramics", 1967, ***Trans. Brit. Ceram. Soc.***, 66, [8], 405-422.

DUAN, K., MAI, Y.-W., "R-Curve Effect on Strength and Reliability, of Toughened Ceramic Materials", 1995, ***J. Mat. Sci.***, 30, 1405-1408.

EVANS, A. G., "Perspective on the Development of High Toughness Ceramics", 1990, ***J. Am. Ceram. Soc.***,73, [2], 187-206.

EVANS, A. G., CHARLES, E. A., "Fracture Toughness Determinations by Indentation", 1976, ***J. Am. Ceram. Soc.***,59, [7-8], 371-372.

EVANS, A. G., CHARLES, E. A., "Structural Integrity in Severe Thermal Environments", 1977, ***J. Am. Ceram. Soc.***,60, [1-2], 22-29.

FAN, C., RAHAMAN, M. N., "Factors Controlling the Sintering of Ceramic Particulate Composites: 1, Conventional Processing", 1992, ***J. Am. Ceram. Soc.***,75, [8], 2056-2065.

FETT, T., MUNZ, D., THUN, G., "Evaluation of Bridging Parameters in Aluminas from R-Curves by use of the Fracture Mechanical Weight Function", 1995, ***J. Am. Ceram, Soc.***,78, [4], 949-951.

FISCHER, G., BAHR, H. A., "Induziering von Thermoschock-Ri βmustern an einseitig erwärmten Glasproben", 1988, ***Proceedings VIII. Symposium Verformung und Bruch, Teil II, Magdeburg***,51 (as cited by Bahr *et al.* 1993).

FLINN, B. D., RÜHLE, M., EVANS, A. G., "Toughening in Composites of Al_2O_3 Reinforced with Al", 1989, ***Acta. Met.***, 37, No. 11, 3001-3006.

GOGOTSI, G. A., GROUSHEVSKY, Y. L., STRELOV, K. K., "The Significance of Non-Elastic Deformation in the Fracture of Heterogeneous Ceramic Materials", 1978, ***Ceramurgia International***,4, [3], 113-118.

GOVILA, R. K., "Indentation-Precracking and Double-Torsion Methods for Measuring Fracture Mechanics Parameters in Hot-Pressed Si_3N_4", 1980, ***J. Am. Ceram. Soc.***,63, [5-6], 319-326.

GUPTA, T. K., "Strength Degradation and Crack Propagation in Thermally Shocked Al_2O_3", 1972, ***J. Am. Ceram. Soc.***,55, [5], 249-253.

HAN, D., MECHOLSKY Jr., J. J., "Fracture Analysis of Cobalt-Bonded Tungsten Carbide Composites", 1990, ***J. Mat. Sci.***,25, 4949-4956.

HASSELMAN, D. P. H., "Unified Theory of Thermal Shock Fracture Initiation and Crack Propagation in Brittle Ceramics", 1969, *J. Am. Ceram. Soc.*, 52, [11], 600-604.

HASSELMAN, D. P. H., "Strength Behaviour of Polycrystalline Alumina Subjected to Thermal Shock", 1970, *J. Am. Ceram. Soc.*, 53, [9], 490-495.

HING, P., GROVES, G. W., "The Strength and Fracture Toughness of Polycrystalline Magnesium Oxide Containing Metallic Particles and Fibres", 1972, *J. Mat. Sci.*, 7, 427-434.

HODKINSON, P. H., NADEAU, J. S., "Slow Crack Growth in Graphite", 1975, *J. Mat. Sci.*, 10, 846-856.

HSUEH, C.-H., BECHER, P. F., "Determination of the R-Curve from the Strength-Indentation Load Relation", 1995, *J. Am. Ceram. Soc.*, 78, [8], 2237-2239.

JAEGER, J. C., "On Thermal Stresses in Circular Cylinders", 1945, *Philosophical Magazine*, 36, [257], 418-428.

JANSSEN, R., SCHÖN, PRIELIPP, H., CLAUSSEN, N., "Multifunctional Ceramics for Thermal Shock Applications", 1993, Thermal Shock and Thermal Fatigue of Advanced Ceramics, Schneider, G. A., Petzow, G., (eds.), Kluwer Academic Publishers, 521-529.

JESSEN, T. L., "Fracture Toughness of Graded Metal-Particulate/Brittle-Matrix Composites", 1990, *J. A. Ceram. Soc.*, 73, [5], 1405-1408.

KENDALL, K., McNALFORD, N., TAN, S. R., BIRCHALL, J. D., "Influence of Toughness on Weibull Modulus of Ceramic Bending Strength", 1986, *J. Mat. Res.*, 1, [1], 120-123.

KINGERY, W. D., "Factors Affecting Thermal Stress Resistance of Ceramic Materials", *J. Am. Ceram. Soc.*, 38, [1], 1955, 3-15.

KOVAR, D., READEY, M. J., "Grain Size Distributions and Strength Variability of High Purity Alumina", 1996, *J. Am. Ceram. Soc.*, 79, [2], 305-312.

KRSTIC, V. V., NICHOLSON, P. S., HOAGLAND, R. G., "Toughening of Glasses by Metallic Particles", 1981, ***J. Am. Ceram. Soc.***, 64, [9], 499-503.

LAWN, B. R., SWAIN, M. V., "Microfracture beneath Point Indentations in Brittle Solids", 1975, ***J. Mat. Sci.***, 10, 113-122.

LI, J. F., WATANABE, R., "Fracture Toughness of Al_2O_3-Particle Dispersed Y_2O_3-Partially Stabilized Zirconia", 1995, ***J. Am. Ceram. Soc.***, 78, [4], 1079-1082.

LOEHMAN, R. E., EWSUK, K., TOMSIA, A. P., "Synthesis of Al_2O_3-Al Composites by Reactive Metal Penetration", 1996, ***J. Am. Ceram. Soc.***, 79, [1], 27-32.

LUTZ, E. H., SWAIN, M. V., CLAUSSEN, N., "Thermal Shock Behaviour of Duplex Ceramics", 1991, ***J. Am. Ceram. Soc.***, 74, [1], 19-24.

LUTZ, E. H., SWAIN, M. V., "Interrelation between Flaw Resistance, R-Curve Behaviour and Thermal Shock Strength Degradation in Ceramics", 1991, ***J. Am. Ceram. Soc.***, 74, [11], 2859-2868.

LUTZ, E. H., SWAIN, M. V., "Mechanical and Thermal Shock Properties of Duplex-Ceramics - A Review", 1991, ***Materials Forum***, 15, 307-323.

MARSHALL, D. B., SWAIN, M. V., "Crack Resistance Curves in Magnesia-Partially-Stabilized Zirconia", 1988, ***J. Am. Ceram. Soc.***, 71, [6], 399-407.

MIGNARD, F., OLAGNON, C., SAADAOUI, M., FANTOZZI, G., "Thermal Shock Behaviour of a Coarse Grain Porous Alumina", 1996, ***J. Mat. Sci.***, 31, 2437-2441.

MOORE, R. H., KUNZ, S. C., "Metal Particle-Toughened Borosilicate Sealing Glass", 1987, ***Ceram. Eng. Sci. Proc.***, 8, [7-8], 839-847.

MORRELL, R., "Thermal Stress and Thermal Shock in Ceramics - A Survey of Industrial Problems and a Review of Test Methods and Thermal Stress Theory", N.P.L. Report Chem 66, April 1977, 55.

MORRELL, R., Handbook of Properties of Technical & Engineering Ceramics, Part 1: an Introduction for the Engineer and Designer, National Physical Laboratory, 1985, 94-97.

NISHIDA, T., HANAKI, Y., "Measurement of Rising R-Curve Behaviour in Toughened Silicon Nitride by Stable Crack Propagation in Bending", 1995, *J. Am. Ceram. Soc.*, 78, [11], 3113-3116.

Nuffield Book of Data, (ed. H. Ellis), 1984, Longman Group Ltd., Essex England, 130-131.

POMPE, W. E., "Thermal Shock Behaviour of Ceramic Materials - Modelling and Measurement", 1993, Thermal Shock and Thermal Fatigue Behaviour of Advanced Ceramics, Schneider, G. A., Petzow, G., (eds.), Kluwer Academic Publishers, 3-14.

POMPE, W. E., BAHR, H.-A., SCHNEIDER, G., WEI β, H.-J., "Modelling and Measuring of Thermal Shock Behaviour of Ceramics", 1993, *Ceramic Forum International*, 70, No. 3, 79-84.

PONTON, C. B., RAWLINGS, R. D., "Dependence of the Vickers Indentation Fracture Toughness on the Surface Crack Length", 1989, *Br. Ceram. Trans.*, 88, 83-90.

QUINN, G. D., MORRELL, R., "Design Data for Engineering Ceramics: A Review of the Flexure Test", 1991, *J. Am. Ceram. Soc.*, 74, [9], 2037-2066.

RITLAND, M. A., READEY, D. W., "Alumina-Copper Composites by Vapour Phase Sintering", 1994, *Ceram. Eng. Sci. Proc.*, 14, [9/10], 896-907.

RÜHLE, M., EVANS, A. G., "High Toughness Ceramics and Ceramic Composites", 1989, *Prog. Mat. Sci.*, 33, 85-167.

SALAS, O., NI, H., JAYARAM, V., VLACH, K. C., LEVI, C. G., MEHRABIAN, R., "Nucleation and Growth of Al_2O_3/Metal Composites by Oxidation of Aluminium Alloys", 1991, *J. Mat. Res.*, 6, No. 9, 1964-1995.

SCHNEIDER, G. A., "Thermal Shock Criteria for Ceramics", 1991, ***Ceramics International***,17, 325-333.

SELSING, J., "Internal Stresses in Ceramics", 1961, ***J. Am. Ceram. Soc.***,44, [8], 419.

SHERCLIFF, H. R., VEKINIS, G., ASHBY, M. F., BEAUMONT, P. W. R., "Processing of Toughened Alumina", 1992, Technical Report CUED/C-MATS/TR203, Engineering Department, University of Cambridge, U.K.

SHERCLIFF, H. R., VEKINIS, G., SOFIANOPOULOS, M., MUNDAY, M., FERNANDES, J., "Novel Processing of Ni-Toughened Alumina and Characterisation of Fracture Behaviour", 1994, Technical Report CUED/C-MATS/TR221, Engineering Department, University of Cambridge, U.K.

SINGH, J. P., TREE, Y., HASSELMAN, D. P. H., "Effect of Bath and Specimen Temperature on the Thermal Stress Resistance of Brittle Ceramics Subjected to Thermal Quenching", 1981, ***J. Mat. Sci.***, 16, 2109-2118.

SIGL, S., MATAGA, P. A., DALGLEISH, B. J., McMEEKING, R. M., EVANS, A. G., "On the Fracture Toughness of Brittle Materials Reinforced with a Ductile Phase", 1988, ***Acta. Met.***, 36, No. 4, 945-953.

STECH, M., RÖDEL, J., "Method for Measuring Short-Crack R-Curves without Calibration Parameters: Case Studies on Alumina and Alumina/Aluminium Composites", 1996, ***J. Am. Ceram. Soc.***, 79, [2], 291-297.

SUN, X., "Aspects of the Processing and Properties of Nickel Particle Toughened Alumina", 1993, Ph. D. Thesis, University of Surrey, U.K.

SUN, X., TRUSTY, P. A., YEOMANS, J. A., SHERCLIFF, H. R., "The Fabrication and Properties of Alumina-Ductile Metal Particle Composites", ***Proc. ICCM/VIII***,Honolulu, 15-17 July, 1991, edited by Tsai, S. W., Springer, G. S., 17J, 1-10, published by SAMPE.

SUN, X., YEOMANS, J. A., "Influence of Particle Size Distribution on Ductile-Phase Toughneing in Brittle Materials", 1996, ***J. Am. Ceram. Soc.***, 79, [2], 562-564.

SWAIN, M. V., "R-Curve Behaviour and Thermal Shock Resistance of Ceramics", 1990, ***J. Am. Ceram. Soc.***, 73, [3], 621-628.

SWAIN, M. V., "Quasi-Brittle Behaviour of Ceramics and its Relevance for Thermal Shock", 1991, ***Eng. Fract. Mech.***, 40, No. 4/5, 871-877.

THOMPSON, I. R., RAJ, R., "In-Situ Stress-Strain Response of Small Metal Particles Embedded in a Ceramic Matrix", 1994, ***Acta. Met.***, 42, No. 7, 2477-2485.

THOMPSON, I., RAWLINGS, R. D., "Monitoring Thermal Shock of Alumina and Zirconia-Toughened Alumina by Acoustic Techniques", 1991, ***J. Mat. Sci.***, 26, 4534-4540.

TRUMBLE, K. P., "Thermodynamic Analysis of Aluminate Formation at Fe/Al_2O_3 and Cu/Al_2O_3 Interfaces", 1992, ***Acta. Met.*** 40, Suppl., 5105-5110.

TRUSTY, P. A., "The Influence of Microstructure on the Fracture Toughness of Alumina-Iron Ceramic Matrix Composites", 1994, Ph.D. Thesis, University of Surrey, U.K.

TUAN, W. H., WU, H. H., YANG, T. J., "The Preparation of Al_2O_3/Ni Composites by a Powder Coating Technique", 1995, ***J. Mat. Sci.***, 30, 855-859.

TUAN, W. H., BROOK, R. J., "Processing of Alumina/Nickel Composites", 1992, ***J. Eur. Ceram. Soc.***, 10, 95-100.

TUAN, W. H., CHEN, W. R., "Mechanical Properties of Alumina-Zirconia-Silver Composites", 1995, ***J. Am. Ceram. Soc.***, 78, [2], 465-469.

VEKINIS, G., "Metal Alloy-Reinforced Al_2O_3 for High Impact Energy Absorption", 1992, ***Proc. Props. Mat.***, Sept., 7-10.

WACHTMAN, J. B., "Elastic Deformation of Ceramics and other Refractory Materials", 1969, Mechanical and Thermal Properties of Ceramics, (ed. J. B. Wachtman), NBS Special Publication 303, p. 139. National Bureau of Standards, Washington, [23, 27] (as cited by Davidge 1979).

WANG, J., PONTON, C. B., MARQUIS, P. M., "Silver-Toughened Alumina Ceramics", 1992, ***Br. Ceram. Trans.***, 92, 67.

WANG, B., LIU, Y., YU, S., HUANG, K., "The Crack-Bridging Model with the Consideration of Residual Stress in Particulate-Reinforced Ceramics", 1991, ***Eng. Fract. Mech.***, 38, No. 2/3, 207-214.

WURST, J. C., NELSON, J. A., "Lineal Intercept Technique for Measuring Grain Size in Two-Phase Polycrystalline Ceramics", 1972, ***J. Am. Ceram. Soc.***, 55, [2], 109.

XU, H. H. K., OSTERTAG, C. P., KRAUSE Jr., R. F., "Effect of Temperature on Toughness Curves in Alumina", 1995, ***J. Am. Ceram. Soc.***, 78, [1], 260-262.

ZHANG, X.-M., "Processing and Mechanical Properties of Nickel (Titanium)/Alumina and Metal/Hydroxyapatite Composites", 1995, Ph. D. Thesis, Eindhoven University of Technology, The Netherlands.

ZHANG, X., LU, G., HOFFMAN, M. J., METSELAAR, R., "Properties and Interface Structures of Ni and Ni-Ti Alloy Toughened Al_2O_3 Ceramic Composites", 1995, ***J. Eur. Ceram. Soc.***, 15, 225-232.

APPENDIX 1

ASTM FLEXURE TEST STANDARD

All flexure testing was performed according to the ASTM Standard Test Method for Flexural Strength of Advanced Ceramics at Ambient Temperature (Designation: C 1161 - 90). The requirements stated in the procedure were followed as closely as possible. The appropriate sections of the preparation and testing procedure relevant to three point loading are given below.

Configuration A was adopted due to the small amounts of material available. Specimen sizes were therefore required to be 2 mm in width, 1.5 mm in depth *and 25 mm* long, with a loading span of 20 mm. Fixed bearing diameters were 2.0-2.5 mm in diameter. The cross-head loading *rate was as low as possible* (0.5 mm min^{-1}).

Specimens were ground and polished to a 3 μm surface finish on one long face only. This face was subjected to a tensile stress during subsequent flexure testing. The long edges of the specimens were not chamfered or rounded.

Flexural fracture stress, $\sigma_{bending}$, is then given by

$$\sigma_{bending} = \frac{3PL}{2bd^2}$$

where P is the load at fracture, L is the span, b and d are the thickness and width of the specimen respectively.

APPENDIX 2

COMPUTER ROUTINE

Maple V commands necessary for computation of normalised thermal stress values are given below. The example shown is for $\beta=2, \theta=0.01, a/r=0.1$. The integral is an approximation from 0 to 0.999, due to limitations concerning the hardware available. In each case, the first 10 Bessel function roots have been taken into account. Figure A2.1 shows a plot of the Bessel function used in this case (first 20 solutions shown).

```
theta:=0.01;

r:=1;

a:=0.1;

f:=B*BesselJ(1,B)- β*BesselJ(0,B);

β:=2;

for j from 1 to 10

bvals[j]:=fsolve(f, B, (j-3)*3.1+2..j*3.1+3)

od;
```

```
brack:=BesselJ(1,bvals[i])+(r/(1-(a*y)))*BesselJ(1,((a*y))/r)*bvals[i])
bvals[i]*BesselJ(0,((1-(a*y))/r)*bvals[i]);

divis:=bvals[i]*(B^2+bvals[i]^2)*(BesselJ(0,bvals[i]));

top:=2*B*exp(-theta*(bvals[i]^2));

omega:=sum(top*brack/divis,i=1..10);

F(y):=(1-y)*(0.2945-0.3912*y^2+0.7685*y^4-0.9942*y^6+0.5094*y^8);

bott:=(1-y^2)^0.5;

topp:=omega*(1+F(y));

integ:=int((topp/bott),y=0..0.999);

k:=((2*(a/r)^0.5)/(3.141592654^0.5))*integ;

evalf(");
```

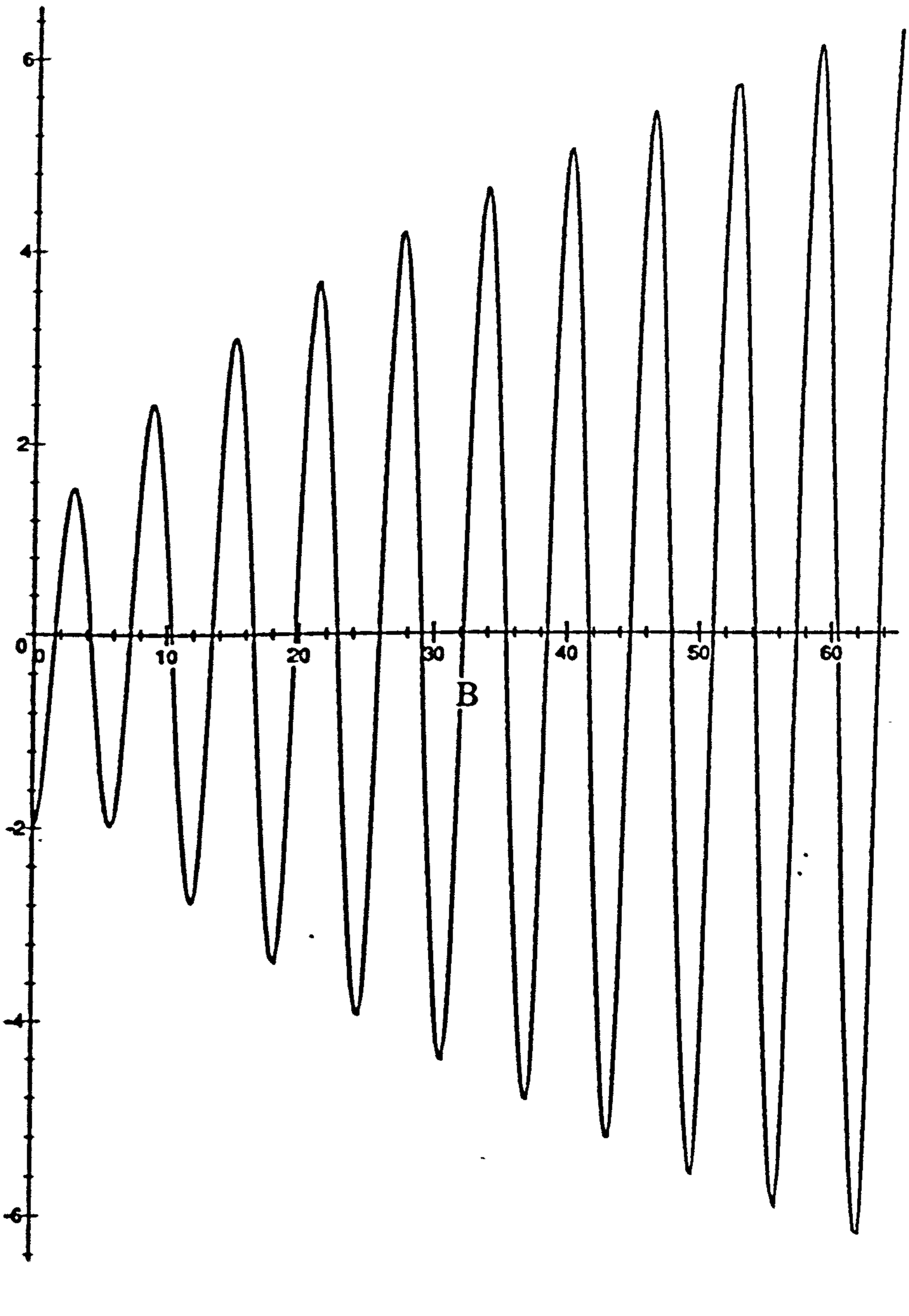

Figure A2.1 Plot of Bessel function $f = B\ Bessel\ J\ (1,B) - \beta\ Bessel\ J\ (0,B)$.
First 20 roots shown for Biot modulus, β, of 2.